Development of a new steam explosion model for the MC3D software

Linkai Wei

Development of a new steam explosion model for the MC3D software

Développement d'un nouveau modèle d'explosion de vapeur pour le logiciel MC3D

Linkai WEI

Une thèse en vue de l'obtention du

DOCTORAT DE L'UNIVERSITE DE LORRAINE

Spécialité: Energie et Mécanique

Ecole doctorale :

Sciences et Ingénierie des Molécules, des Produits, des procédés, et de l'Energie (SIMPPE)

Soutenue publiquement le 17 mars 2023 devant le jury composé par :

Président de jury et rapporteur	M. Daniel FUSTER	Directeur de recherche, CNRS, Paris
Rapporteur :	M^{me} Nathalie SEILER	Docteur-ingénieure, HDR, CEA, Saint-Paul-Lez-Durance
Examinateurs :	M^{me} Véronique ROIG	Professeure, IMFT, Toulouse
	M. Erik De MALMAZET	Docteur-ingénieur, EDF, Chatou
Directeur de Thèse :	M. Nicolas RIMBERT	Professeur, Université de Lorraine, Vandœuvre-lès-Nancy
Co-directeur de Thèse	M. Renaud MEIGNEN	Docteur-chercheur, IRSN, Saint-Paul-Lez-Durance
Membre invité	M. Pascal PILUSO	Docteur-ingénieur, HDR, CEA, Saint-Paul-Lez-Durance

Laboratoire Energies et Mécanique Théorique et Appliquée (LEMTA) — UMR 7563

Laboratoire d'Etude de la Physique du Corium (LEPC) — IRSN/PSN-RES/SAM/LEPC

DEVELOPPEMENT D'UN NOUVEAU MODELE D'EXPLOSION DE VAPEUR POUR MC3D

RAPPORT DE THESE

Linkai Wei

SUMMARY

LIST OF FIGURES AND TABLES

Figures

Tables

Acknowledgments

My PhD program would not have been possible without the support of many people. I would like to acknowledge their support and thank them all.

First of all, I would like to express my sincere gratitude to my supervisor, Dr. MEIGNEN Renaud, for his regular guidance and help all these last years, from the application of the doctoral program to the manuscript writing. I would also like to thank my thesis director, Pro. RIMBERT Nicolas, for his advice and encouragement from the beginning to the end of my thesis and his revision of my manuscript.

I would also like to acknowledge Dr. FUSTER Daniel and Dr. De MALMAZET Erik, who are my CSI and Ph.D. defense committee members, for their valuable discussions and suggestions on my Ph.D. topic. I would also like to thank Dr. SEILER Nathalie and Pro. ROIG Véronique for taking the time to serve on my Ph.D. committee.

Special thanks to Dr. POPINET Stephane and other developers for sharing the open-source Basilisk code, and to the MC3D group, in particular, Dr. PICCHI Stéphane for his technical support in the use of MC3D and the development of MC3D patches.

I would like to thank IRSN for funding this PhD program. I am also grateful to the head of the laboratory, Dr. RICAUD Jean-Marc, and the secretary, Mrs. BURLE Laetitia, for all the administrative procedures that facilitated my work at IRSN.

I also cannot underestimate the support of my friends and family. Their support has been important to my ability to complete this work.

Abstract

Steam explosion is one of the most critical and complex phenomena that may occur during severe accident in a Nuclear Power Plant. This explosive phenomenon is analogous to a detonation and is due to the fragmentation of the molten fuel, the passage of the shock wave and the very fast release of the associated energy. The MC3D computer code is recognized as reference for the evaluation of this phenomenon. However, the precise mechanisms of the process of pressurization are still very uncertain and are the subject of works carried out under the program RSNR-ICE (2014-2023). The program validated the general principle of MC3D-EXPLO model, based on a principle of direct boiling around the surface of the corium fragments, i.e., the heat transfer is evaluated by a film boiling mechanism and directly contributions to vaporization. However, it appears that the fragmentation seems, under certain conditions, to be achieved without a significant dispersion of the fragments in the water, in a so-called Micro-Interaction (MI) process, which is contrary to what the current MC3D model assumes. The aim of the thesis is to finalize these works through an in-depth analysis of the current model and supplementary DNS simulations of combined heat transfer and fragmentation to propose an improved modeling of the explosion for MC3D.

Following an extensive bibliography of the steam explosion phenomenon, a detailed analysis of the behavior of the current MC3D model is performed, using a simple and ideal test-case. Despite the simplicity of the data set, the analysis can be directly applied to experiments with one-dimensional geometry such as KROTOS. The detailed mechanisms of the pressure escalation are evidenced. The crucial role of initial and created void (volume fraction of vapor) is highlighted: the initial void may easily damp the trigger shock and avoid the escalation, whereas the void creation process is highly sensitive to unclear parameters. Some numerical deficiencies are highlighted, and the major needs for improved understanding and modeling are outlined.

The Basilisk software was then used to perform DNS simulations to get details of combined fragmentation and heat transfer and verify the MC3D modeling assumptions. Comprehensive analysis about fragmentation regimes, statistics including Sauter Mean Diameter and Probability Density Function of fragment mass, the transient Nusselt number and drag coefficient were conducted. The simulations highlight the heat transfer mechanisms, indicating that heat is transferred mostly at the front of the fragmenting drop and transported to the rear in the wake. Then, in contrast with MI models, this micro-interaction zone does not seem to be strongly active for the heat transfers. Nevertheless, this conclusion holds for the simulated conditions without solidification of the melt. The modeling in MC3D should be able to account also for heat transfers occurring in the wake. Results for the same test-case using MC3D are then compared with that of Basilisk, indicating the main needs of modification of MC3D model.

Finally, the main lines of a proposed new model are presented and discussed. Those that can be validated from the DNS results were implemented in the current MC3D version. This concerns, in particular, the introduction of a Non-Equilibrium Micro-Interaction (NEMI), by improving the model of the entrainment processes and by considering the effect of deformation on the heat transfers. The other proposals concerning the behavior of the void may be implemented in the future version (V4) of the code. Indeed, the DNS simulations are limited to non-boiling conditions so that the void creation process, i.e., the coalescence of the small bubbles into a large one, remains to be clarified. The analysis suggests improvements of modeling in this direction. Similarly, the DNS cannot simulate solidification with the current tool, but the present analysis highlights the heat mixing and diffusion processes and indicates that large crust growth should not be possible, and a bulk solidification process seems more plausible.

KEYWORDS

Fuel-Coolant Interaction, Steam Explosion, micro-interaction, secondary fragmentation, heat transfer, MC3D, RSNR-ICE project

Résumé de la thèse

Lors d'un accident grave dans un centrale nucléaire, le cœur du réacteur peut fondre, formant un mélange à haute température (~3000K) appelé corium. Le corium peut pénétrer dans des régions contenant de l'eau liquide (fond de cuve, puits de cuve), ce qui entraîne une interaction entre le corium et l'eau (ICE). Au cours de l'ICE, une explosion de vapeur énergétique peut alors se produire et menacer l'intégrité du confinement. La compréhension et la modélisation de l'interaction entre le corium et l'eau en général et de l'explosion de vapeur en particulier restent l'une des questions les plus difficiles et les plus critiques pour la sûreté nucléaire.

Il y a trois principales étapes pour l'ICE. Tout d'abord, le PREMELANGE (premixing) est caractérisé par une fragmentation primaire du jet continu de combustible fondu en gouttes de quelques millimètres, générant un mélange grossier de combustible et de réfrigérant. Il donne la condition initiale et détermine la puissance de l'explosion de vapeur, si elle se produit. En effet, l'explosion nécessite un processus de déclenchement, ou «trigger», c'est-à-dire une perturbation locale de l'écoulement qui peut initier l'explosion. Elle peut être due à un événement externe, mais l'explosion peut aussi être auto-initiées. L'EXPLOSION est similaire à un processus de détonation et est due à la très forte augmentation du transfert de chaleur par la fragmentation fine des gouttes en fragments (~50-100 µm) provoquée par le passage de l'onde de choc à travers le mélange grossier de corium et de l'eau. Cette fragmentation fine augmente fortement la surface d'échange, ce qui va provoquer une vaporisation violente et entretenir l'onde de pression de choc.

L'ICE est modélisé dans le code d'écoulement thermo-hydraulique multiphasiques MC3D, développé par l'IRSN, à travers deux modules (applications) différents : PREMIX pour le prémélange et EXPLO pour l'explosion.

Suite à l'accident de Fukushima, l'Agence Nationale pour la Recherche (ANR) a lancé un programme (RSNR) d'amélioration de la sûreté nucléaire, parmi lequel le projet ICE (Interaction Corium-Eau), dédié à l'amélioration de la compréhension et de la modélisation de l'ICE et de l'explosion de vapeur (2014-2023). Parmi les résultats du projet, les travaux ont permis de mieux comprendre la phénoménologie générale et de valider le principe général de MC3D, basé sur un principe d'ébullition directe autour de la surface des fragments de corium via un mécanisme d'ébullition en film. Cependant, il apparaît que les processus de fragmentation semblent, dans certaines conditions, se réaliser sans une dispersion significative des fragments dans l'eau, ce qui est contraire à ce que présuppose le modèle MC3D actuel. Un processus de « Micro-Interaction », selon la terminologie employée par Theofanous, semble donc se mettre en place, sans que les détails de ce processus ne puisse être mis en évidence.

L'objectif de la présente thèse est de confirmer et consolider les connaissances acquises durant le projet RSNR-ICE, en particulier les processus de transfert de chaleur combinés à la fragmentation, et de proposer une modélisation améliorée de l'explosion pour MC3D.

La thèse est divisée en plusieurs chapitres.

Chapitre 1 : il présente le contexte, les objectifs et le plan de la thèse.

Chapitre 2 : Revue de la littérature sur la phénoménologie et la modélisation. Nous passons d'abord en revue les activités expérimentales et discutons en particulier les diverses difficultés rencontrées pour mener des expériences d'explosion, ce qui permet de prendre conscience des difficultés de compréhension même du phénomène et des incertitudes pour la modélisation. Celle-ci est ensuite abordée, en commençant par les modèles simples de thermodynamiques, qui tentent d'estimer l'énergie de l'explosion mais qui donnent en général des estimations très conservatives et inutilisables en pratique. Les modèles de type détonation sont ensuite présentés et discutés. Même si les modèles de détonation partagent toujours la même hypothèse avec les modèles thermodynamiques selon laquelle un état d'équilibre homogène des différentes phases est créé et maintenu pendant l'interaction, il peut être considéré comme un progrès essentiel puisqu'il permet de saisir la phénoménologie générale de l'explosion en identifiant le rôle clé de la fragmentation et en expliquant théoriquement comment une explosion stable peut se maintenir si elle se produit. Cependant, ces modèles restent qualitatifs, limités d'une part par les hypothèses de résolution, et d'autres part par les connaissances très faibles des caractéristiques intimes de l'explosion.

Pour aller plus loin dans des évaluations plus précises, les détails des processus de fragmentation, du transfert de chaleur et de l'ébullition jouent un rôle vital et doivent être mieux décrits. C'est pourquoi des codes multidimensionnels de thermo hydraulique, dont MC3D, ont été développés, bien que la physique de la fragmentation et du transfert de chaleur soit loin d'être entièrement comprise. Les modèles ont cependant pris deux directions différentes. Yuen et Theofanous (1999) ont d'un côté proposé l'idée de "Micro-Interaction", conservant le principe d'équilibre, mais estimant que seule une fraction de l'eau peut être en équilibre avec les fragments et la vapeur, dans un champ unique nommé "m-fluide", et obtenus des prédictions plus raisonnables. D'un autre côté, des modèles plus mécanistes, visant une description plus précise des mécanismes, ont été proposés, tels que le code MC3D. Les hypothèses et modèles de base utilisés dans la modélisation de la fragmentation et du transfert de chaleur pendant l'explosion sont présentés et discutés.

Chapitre 3: Analyse de sensibilité de MC3D-EXPLO. Les impacts de la modélisation actuelle et des différents paramètres associés de l'EXPLO sont ensuite analysés par le détail grâce à un simple cas-test unidimensionnel. Cette analyse a en fait un double objectif. Le premier est de mieux caractériser le comportement actuel du modèle. D'autre part, elle peut également être utilisée pour mieux comprendre les résultats des essais unidimensionnels, notamment les essais KROTOS, menés en premier lieu à ISPRA, puis par le CEA, dans le cadre du projet ICE en particulier. L'objectif est donc d'analyser la réponse d'un prémélange donné à un déclenchement par un trigger du même type que celui utilisé dans KROTOS (capsule de gaz sous pression).

Cette étude est initiée par l'analyse de la réponse pour un écoulement monophasique, puis pour un écoulement diphasique eau/vapeur. On constate que la présence de vapeur provoque une atténuation très rapide de l'onde de choc. Une analyse de sensibilité de plusieurs paramètres est ensuite réalisée pour un mélange triphasé, notamment la fraction de vapeur initiale, la fraction de gouttes de corium, le diamètre des bulles de vapeur et le diamètre des fragments. L'analyse permet une compréhension détaillée de l'imbrication des effets des modèles (la fragmentation engendre l'ébullition qui engendre la pression qui détermine la fragmentation). Il s'avère que certains paramètres ont une influence cruciale, sur le comportement et la fiabilité des résultats et doivent être traités avec précaution. Elle a conduit aux conclusions les plus importantes suivantes:

1. Le vide initial dans le mélange a une importance considérable sur la propagation de l'onde de choc par son fort effet d'amortisseur. Si le corium au front de la zone de prémélange est solidifié, les bulles présentes peuvent provoquer une chute de la pressurisation et empêcher une explosion. Ceci peut déjà aider à comprendre le comportement de certains essais KROTOS.
2. L'évolution et la configuration/environnement local des "bulles" générées par la vaporisation lors de la fragmentation fine sont mal prises en compte par le modèle actuel et constituent le premier axe d'amélioration. Dans certains cas, cela peut conduire à une forte condensation et à une sous-estimation considérable de l'explosion. Néanmoins, les améliorations nécessaires semblent assez complexes, nécessitant probablement l'emploi d'un champ numérique dédiée.
3. Malgré les grandes incertitudes dues au très petit nombre de données expérimentales précises, il semble que le modèle de fragmentation soit qualitativement correct, mais nécessite quelques améliorations pour une meilleure précision.
4. Un résultat important est que l'hypothèse d'un champ de température unique pour tous les fragments doit être revue. Lorsque les fragments sont petits, ils perdent rapidement leur chaleur de sorte que les fragments "chauds" nouvellement générés peuvent être mal pris en compte dans un processus de moyenne : en dessous d'une température minimum, les fragments échangent directement avec l'eau, sans ébullition du film.

Par ailleurs, l'analyse confirme les difficultés déjà soulevées dans les documents de validation du code, relatif au processus de solidification durant l'explosion qui semble limiter la réduction de la taille des fragments avec la puissance de l'explosion. Ce processus nécessite en premier lieu une meilleure compréhension.

Cette analyse confirme la nécessité de poursuivre les travaux de simulation à petite échelle de la fragmentation d'une goutte chaude dans un autre liquide afin de mieux comprendre les interactions dynamiques et thermiques au cours du processus de fragmentation.

Dans ce but, **le chapitre 4 : simulation « directe » de la fragmentation d'une goutte,** a été réalisée. A cet effet, une simulation fine avec le logiciel Basilisk a été engagée. L'objectif principal est d'apporter des informations sur

les processus de transfert de chaleur combinés à la fragmentation et de vérifier le principe de modélisation dans MC3D où les particules sont des sphères qui agissent avec le fluide environnant de manière indépendantes. Dans le modèle Basilisk mis en œuvre, la température est considérée comme un scalaire passif, sans effet de rétroaction par les modifications des propriétés physique. L'ébullition ne peut être prise en compte du fait du cout prohibitif que cela engendrerait pour des simulations tridimensionnelles. Il est cependant estimé que, du fait des très hautes pressions pendant l'explosion, son impact, au moins pour les premières phases, doit être secondaire et ne modifie pas qualitativement les processus.

Le travail avec Basilisk commence, après la mise en place du modèle, par le test et la vérification de l'approche utilisée dans nos simulations. Dans ce but, des calculs d'un écoulement monophasique autour d'un cylindre chauffé (ou d'une sphère en 3D) ont été effectués. Les nombres de Nusselt issus de la simulation sont comparés aux corrélations classiques de Whitaker pour vérifier la convection et diffusion du champ de température ainsi que les couches thermiques sont bien résolues dans la simulation.

Ensuite, les caractéristiques transitoires du transfert de chaleur d'une goutte soumise à un saut de vitesse sont étudiées pour différents nombres initiaux de Weber. Les simulations sont réalisées sur le calculateur TGCC du CEA, nécessitant jusqu'à environ 30 000 processeurs de calculs. L'analyse de sensibilité du maillage limite les calculs en termes de nombre de Weber de l'écoulement, c'est-à-dire de taille des fragments. Le nombre de Weber maximal de 2560 est néanmoins suffisant pour dévoiler les processus à l'échelle micronique mise en œuvre dans une explosion. A cet égard, la taille des fragments est inférieure à la limite basse des mesures expérimentales dans les essais KROTOS, indiquant qu'en tout état de cause, la solidification devrait être prise en compte pour les très hauts nombres de Weber.

L'analyse concerne en premier lieu les aspects dynamiques de la fragmentation, étendant ainsi certains travaux de simulation, dont ceux de Castrillon-Escobar (2016). Le diamètre moyen de Sauter (SMD) est un paramètre important pour caractériser le résultat du processus de fragmentation et valider les modèles MC3D. Les valeurs du diamètre moyen de Sauter de nos simulations coïncident bien avec les résultats expérimentaux (cf. Figure 1).

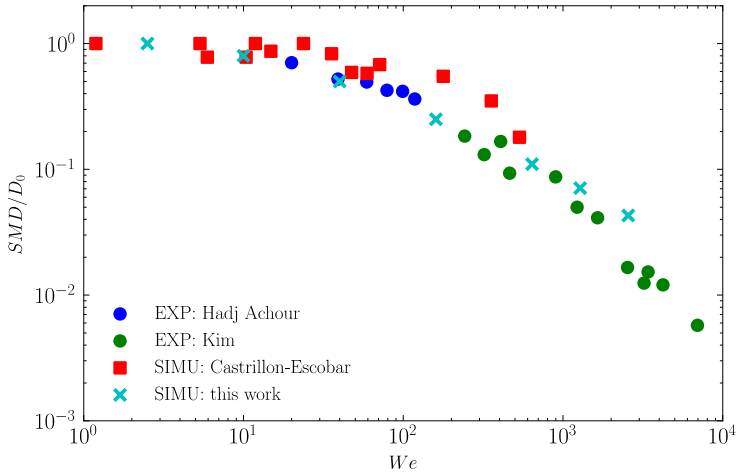

*Figure 1: Diamètre moyen de Sauter (**SMD / D0**) dans nos simulations, en fonction du nombre de Weber, comparés aux résultats expérimentaux. Les résultats des simulations de Castrillon-Escobar (2016), à plus bas Weber, sont également présentées.*

Confirmant les résultats précédents, les simulations montrent clairement que la durée de la fragmentation est liée au temps caractéristique dit de Ranger & Nicholls $t_{RN} = \frac{D_d}{\Delta V_{dc}} \cdot \sqrt{\frac{\rho_d}{\rho_c}}$, l'indice d étant relatif à la goutte (drop) et le c au fluide continu environnant. On assite d'abord à une déformation plus ou moins forte, puis à la fragmentation, de sorte que, contrairement aux modèles, en particulier celui de MC3D, la fragmentation n'est pas un processus continu et régulier.

Différents nombres de Weber conduisent à différents régimes de fragmentation pour le système liquide/liquide, voir la Figure 2.

1. Un faible nombre de Weber (1~7) conduit à une simple oscillation de la goutte avec une fréquence spécifique sans aucune rupture. (Figure 2-a)
2. Contrairement au système liquide/gaz, l'augmentation du nombre de Weber (~10) ne conduit pas à une pulvérisation par rupture du sac mais à une rupture en deux gouttes filles par élongation. (Figure 2-b).
3. L'augmentation du nombre de Weber (~40, Figure 2-c), n'induit pas, contrairement au cas liquide/gaz, de changement de configuration de la déformation. Si la déformation finit par produire un sac, celui-ci est orienté de manière « inverse », concave plutôt que convexe. La déformation reste liée au cisaillement à la surface de la goutte par l'eau environnante, plutôt que par des effets de pression de type Rayleigh-Taylor dans le cas liquide/gaz. Cependant, ce sac ne représente qu'une petite proportion de la masse totale, et la plupart de la masse est accumulée dans un anneau toroïdal perpendiculaire au fluide porteur. L'anneau toroïdal se désintègre en un plus petit nombre de fragments de la même taille que l'épaisseur de l'anneau, donc en raison des effets capillaires, après la rupture du sac. Ainsi, contrairement au cas liquide-gaz, il y a une continuité dans la taille des fragments vis-à-vis du nombre de Weber.
4. Pour les cas de nombre de Weber plus élevé (~160, Figure 2-d), le même mécanisme de sac se forme, mais de grandes instabilités tangentielles dues à la force de cisaillement à l'interface (donc de type Kelvin-Helmholtz) se développent en face avant. Ensuite, des modulations azimutales transversales de l'onde 2D sont observées, formant de fines "feuilles". En raison de l'étirement des crêtes d'ondulation de l'interface, des ligaments sont générés et entraînés dans le sac. Enfin, les ligaments et le sac restant se brisent en fragments de différentes tailles.
5. Pour un nombre élevé de Weber, (640~1280, Figure 2-e), le mécanisme typique d'amincissement des feuilles << sheet stripping>> est confirmé. La goutte est rapidement déstabilisée par des ondes 2D longueur d'onde de plus en plus courte, puis en ondes 3D. De multiples couches minces parallèles sont formées perpendiculairement au fluide d'entrée, puis les couches se transforment en petites feuilles et se détachent de la goutte. Les petites feuilles sont dues à l'effet combiné du cisaillement et des effets Rayleigh-Taylor locaux. Les fragments sont maintenant directement formés à l'avant et entraînés vers l'arrière. Dans le même temps, la goutte elle-même se déforme progressivement en un sac creux, puis se fragmente. Comme les fragments sont principalement créés par la désintégration des feuilles minces, leur taille et leur densité de surface sont relativement faibles.

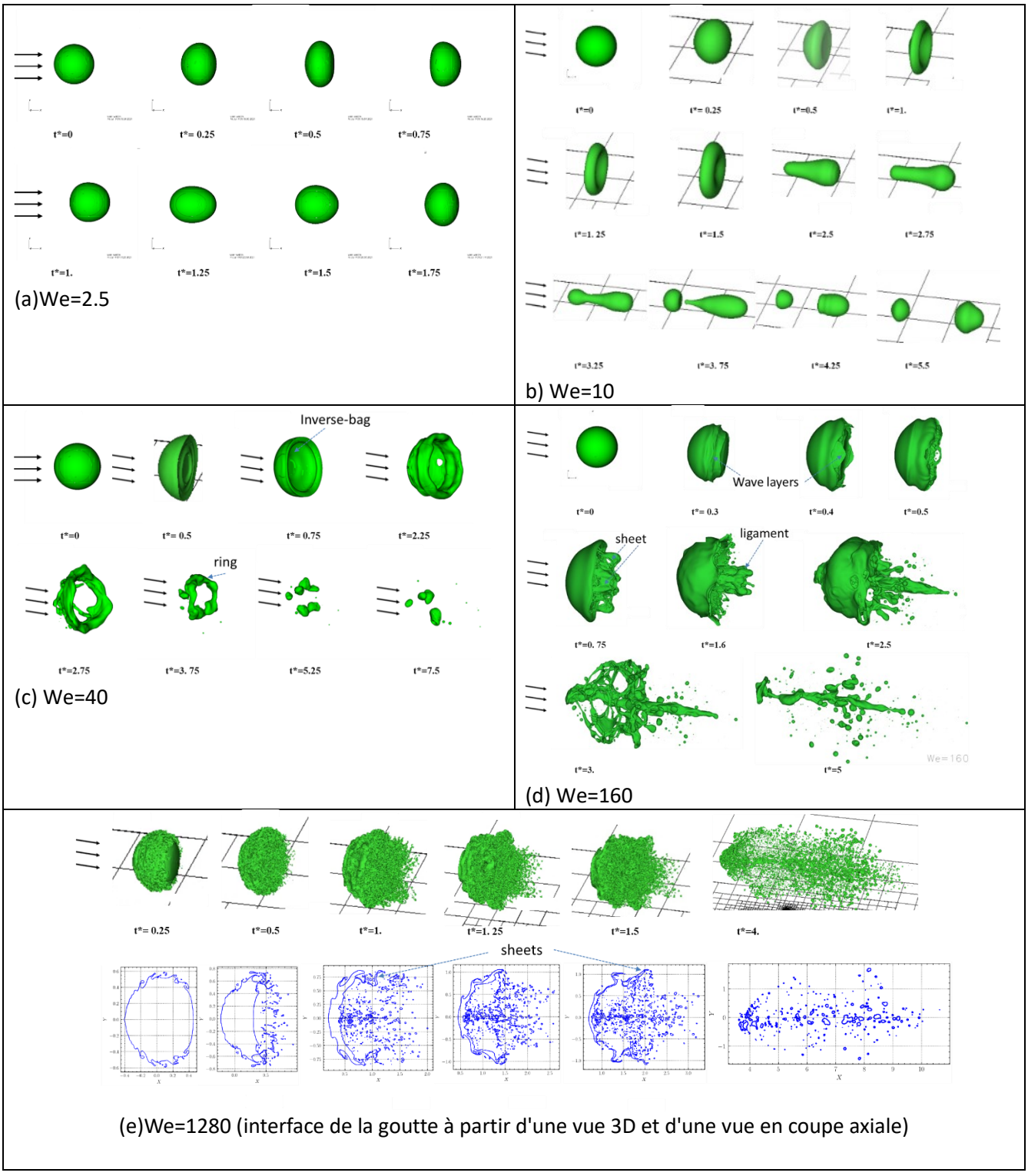

Figure 2: Morphologie de la déformation et de la rupture des gouttes

Le coefficient de traînée de la goutte se déformant et se fragmentant est un paramètre très important pour modéliser l'interaction dynamique particules-écoulement pour MC3D. En effet, le code ne dispose pas de loi spécifique pour des conditions aussi transitoires. Lorsqu'une goutte émerge dans un écoulement en mouvement à vitesse d'entrée constante, elle est affectée par l'écoulement. La distribution de la pression statique autour de la goutte n'est pas uniforme, ce déforme et comprime la goutte dans le sens de l'écoulement. Pendant un tel processus transitoire, le coefficient de traînée instationnaire de la goutte peut changer de manière significative.

Le coefficient de traînée estimé est présenté à la Figure 3. Après un très court instant transitoire, le coefficient a dans tous les cas une valeur proche de 0,45, ce qui correspond à une sphère indéformable (ligne bleue pointillée).

De même, pour le plus petit nombre de Weber, c'est-à-dire une goutte oscillante, le coefficient de traînée oscille autour de cette valeur. Dans les autres cas, la déformation de la goutte dans le plan perpendiculaire contribue à l'augmentation forte du coefficient de traînée. Pour le régime dit « Cap-bubble », l'analyse classique indique que le coefficient de traînée maximal est d'environ 8/3 (cf. ligne rouge pointillée sur la Figure 3 Cette valeur correspond en fait à une distorsion critique de la goutte au-delà de laquelle la fragmentation se produit. On remarquera que pour le cas We=10, cette valeur critique de 8/3 est atteinte jusqu'au moment où la goutte s'allonge dans le sens du courant. Pour les autres cas, la déformation est suivie d'une fragmentation, et il n'est alors pas étonnant que la traînée dépasse 8/3. Les trois cas We =160 à 1280 semblent converger et une valeur du coefficient de traînée entre 6 et 8, indépendant du nombre de Weber, qui peut donc être utilisée dans la modélisation MC3D lorsque la goutte se fragmente.

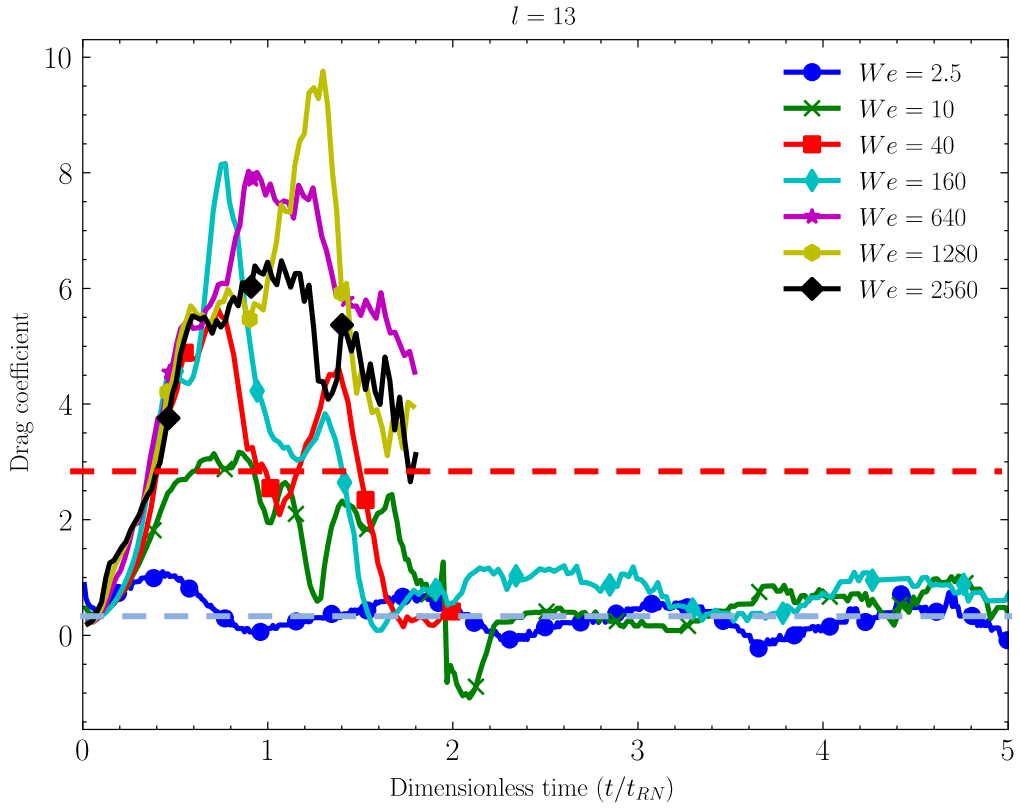

Figure 3: Coefficient de traînée pour différents cas de Weber

L'analyse dans le chapitre 4 est ensuite consacré aux aspects thermiques.

La température moyenne de la goutte est indiquée dans Figure 4. Nous constatons tout d'abord que le temps caractéristique du refroidissement n'est pas précisément t_{RN} , c'est-à-dire uniquement lié à la fragmentation. En effet, s'ajoute un temps caractéristique pour le refroidissement lui-même, dépendant de la taille des fragments, ainsi que de la différence de vitesse avec le fluide porteur. Après un moment de faible transfert, lié au temps de déformation de la goutte, le refroidissement devient très rapide pendant environ 1 t_{RN}, puis devient plus modéré et diminue graduellement. Cette diminution est liée probablement à l'entrainement des fragments avec l'eau, diminuant la vitesse relative, et donc l'échange. Cela pourrait également être dû à l'accumulation des fragments dans le sillage de la goutte (zone de micro-interaction), où les écarts de vitesse sont faibles. On constate que au bout de 5 t_{RN}, temps typique de fragmentation dans tous les cas, le refroidissement est non seulement plus rapide à haut Weber, mais également en proportion plus importante. L'explosion étant lié à la cinétique du transfert thermique, cela introduit donc une notion d'efficacité (rendement) de la fragmentation dans le processus. Pour les nombres de Weber modérés, le refroidissement est incomplet. Il est de l'ordre de 90 % pour un Weber de 1000.

Le refroidissement comparativement plus rapide à des nombres de Weber élevés signifie également en particulier que la solidification devrait intervenir plus rapidement dans ces situations. Les résultats de MC3D

montrent également une tendance similaire, due au fait que la chaleur est transférée à partir de fragments plus petits, mais que le refroidissement est beaucoup plus lent. Dans MC3D, le transfert de chaleur du combustible au liquide de refroidissement se fait principalement par le refroidissement des fragments en raison de leur plus grande surface interfaciale. Ainsi, la description précise de la dynamique de fragmentation est très importante pour modéliser ce processus. Comme une grande incertitude demeure pour le temps de fragmentation, le temps de refroidissement caractéristique peut être considéré comme un meilleur critère pour définir correctement ce coefficient de fragmentation.

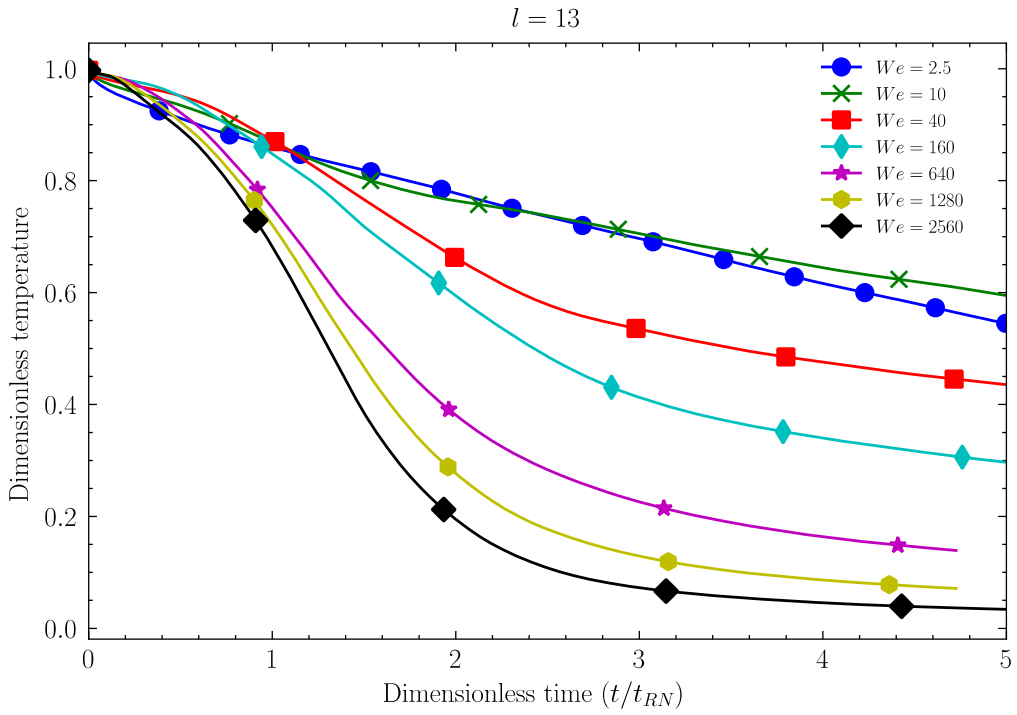

Figure 4: Température moyenne de la goutte (sans dimension) pour différents cas de Weber

Sur le plan phénoménologique, les simulations révèlent les détails des processus de diffusion thermique au sein de la goutte et du fluide environnant (Figure 5). Il apparait qu'en tout état de cause, la phénoménologie générale soit la même, quel que soit le nombre de Weber : l'échange a principalement lieu en face avant et les couches refroidies sont transportées au fur et à mesure le long de l'interface jusqu'à s'accumuler aux crêtes des vagues ou, à Weber modéré, dans l'anneau (ou, en l'absence de fragmentation) ou même dans la partie arrière de la goutte en régime d'oscillation. Les vortex internes jouent donc un rôle très important dans les processus de diffusion de la chaleur au sein de la goutte, et donc de possible apparition de la solidification, ce que ne font pas les divers modèles de solidification employés dans les codes d'ICE. De même pour le liquide environnant, les couches chauffées sont transportées et s'accumulent dans la zone de sac derrière la goutte.

Ainsi, dans les simulations, les fragments sont formés relativement froids et l'interaction thermique dans le sac est finalement de faible ampleur, contrairement au principe du concept de Micro-Interaction. Néanmoins, dans une situation plus réaliste pour l'application à l'explosion de vapeur, la fragmentation a nécessairement lieu à une température élevée, sinon elle serait bloquée par la solidification. Les échanges entre fragments et fluides environnant devraient donc avoir une part plus importante en condition d'explosion de vapeur, que dans nos simulations.

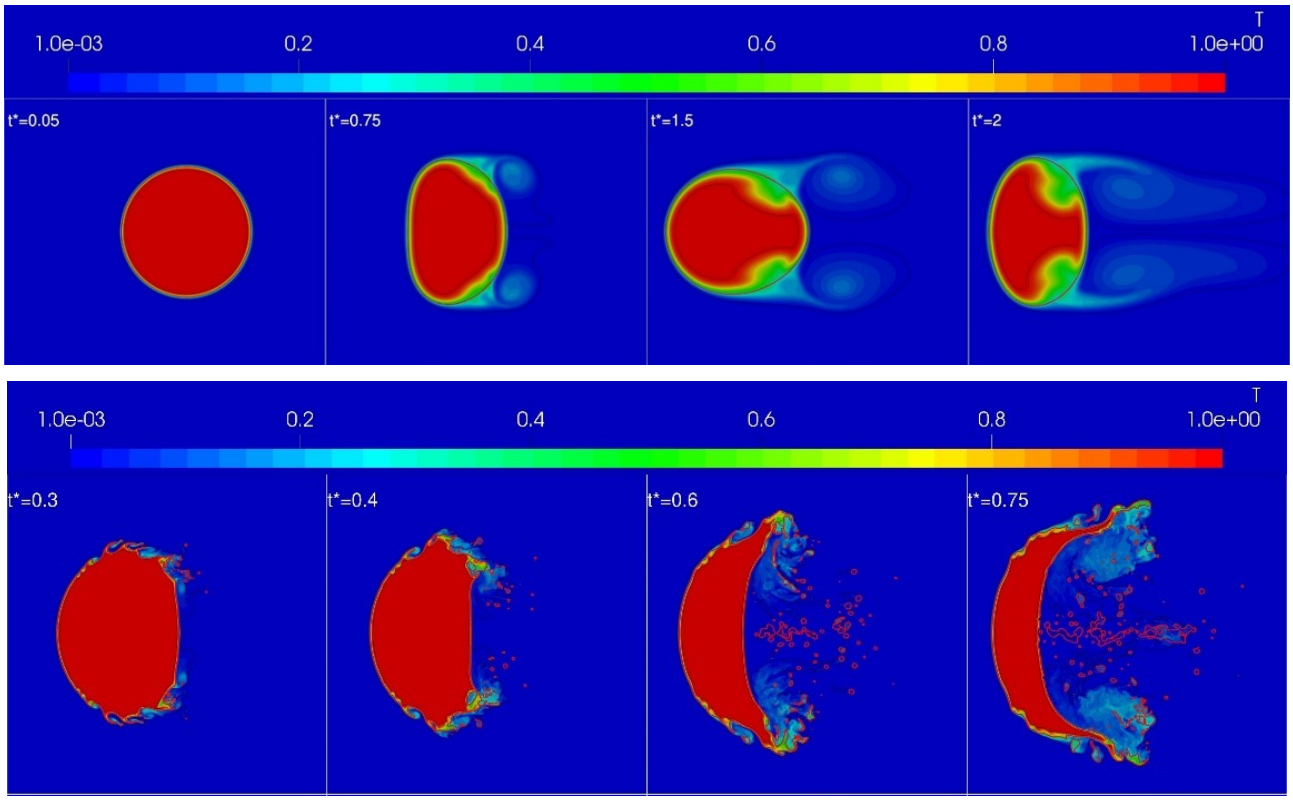

Figure 5: Temperature field (axial cut) at different time step for the case We = 2.5, top, and We = 640, bottom. The red solid line represents the drop-liquid interface. The black solid line inside the drop represents the iso-temperature contour 99% of the initial drop overheat. Illustration du processus de transport des couches refroidies et accumulation, soit en arrière de la goutte, en régime d'oscillation, soit en crête des ondes d'instabilités.

Les simulations de Basilisk ont aussi conduit aux conclusions suivantes :

1. Le processus d'interaction entre les 2 fluides est mis en évidence, avec une faible dispersion des fragments résultants, contrairement à la situation liquide-gaz. La fragmentation produit un mélange des deux fluides à l'arrière de la goutte, dans le sac, avec un volume égal à environ 15 fois celui de la goutte initiale. Ceci peut donner au premier ordre le volume de l'eau entraînée et interagissant avec la masse fondue.
2. En l'absence de fragmentation, le mouvement interne du fluide semble suffisant pour assurer un mélange interne assez important, ce qui rend fragile l'hypothèse couramment faite que la solidification se développe sous forme de "croûte" assez fragile. Plus précisément, la couche limite thermique à l'intérieur de la surface se déplace continuellement vers le centre de la goutte, refroidissant la goutte. Si une solidification a lieu, elle ne peut se développer en face avant que sous une forme de croûte très fine sans tenue mécanique (et avec des propriétés mécaniques probablement très complexes). Elle pourrait cependant avoir un impact sur le développement des instabilités et la taille des fragments.
3. La température de l'eau entraînée dans le mélange est loin d'être homogène, notamment aux nombres de Weber faibles et modérés, et les caractéristiques du chauffage de ce volume dépendent fortement de We, contrairement aux modèles de micro-interaction existants.

Chapitre 5 : Proposition de nouveau modèle. D'après les résultats décrits ci-dessus, il semble que les principes du modèle EXPLO doivent être partiellement révisés au moins sur pour ce qui concerne les aspects dynamiques. En effet, pendant un temps donné, les fragments sont piégés dans le sillage des gouttes qui se fragmentent, avec une quantité importante d'eau. Puisque les principes de transfert thermique en déséquilibre sont conservés, nous nous orientons vers un modèle mixte que l'on appellera le modèle de "Micro-interaction en déséquilibre" (NEMI), illustré sur la Figure 6.

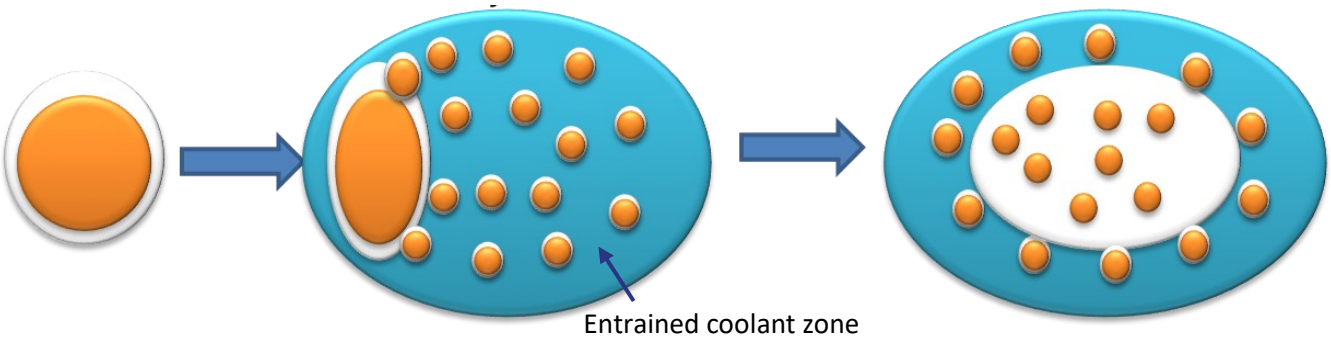

Figure 6: Concept de Micro-interaction en déséquilibre

Les efforts de modélisation sont restés concentrés sur les aspects qui peuvent être directement comparés avec les simulations. Pour cela, nous avons caractérisé les résultats importants en grandeurs caractéristiques facilement comparables :

- diamètre moyen de Sauter ;
- temps de fragmentation ;
- entrainement de la goutte (vitesse relative) à des temps caractéristiques de 1 et 3 t_{RN} ;
- refroidissement global de la goutte aux mêmes instants de 1 et 3 t_{RN}.

Tout d'abord, la modélisation des frottements a été revue pour prendre en compte les aspects liés à la fragmentation. Ensuite, le processus de « piégeage » des fragments produits avec le reste de la goutte est pris en compte par une modification « numérique » du modèle : les fragments produits ne sont plus placés dans le champ « FRAGMENTS » du code, mais dans un des champs « DROPS » disponibles dans le représentation dite MUDROPS (modèle MUSIG) où chaque champ correspond à une « classe » avec un diamètre précis. Puisque tous les champs DROPS ont la même vitesse (par construction), fragments et gouttes vont à la même vitesse. L'entrainement d'une fraction dans le sillage a été modélisée d'une manière simplifiée via la notion de « masse ajoutée », le « volume ajouté » correspondant approximativement au volume du sillage (sac).

Concernant les transferts thermiques, il a été choisi de ne pas modifier le transfert particulier par convection hors ébullition, mais d'effectuer des modifications liées à la configuration de l'écoulement. L'idée est pour cela d'ajouter un coefficient multiplicateur lié à la déformation. Il est fait l'hypothèse que ce coefficient est lié au coefficient de frottement. Il n'a pas été possible d'ajuster précisément les divers paramètres, par manque de temps. Seuls des calculs d'illustration sont présentés. Le refroidissement global de la goutte et des fragments est illustré en Figure 7. Ce refroidissement est plutôt correct à l'issue 3 temps t_{RN} caractéristique du refroidissement global après fragmentation, donc après interaction. Le résultat moins bon après 1 t_{RN} illustre le fait que la dynamique précise de la fragmentation est mal prise en compte. Il n'est pas certain que cela soit très important pour décrire l'explosion, mais une piste d'amélioration est proposée.

Pour ce qui est de l'évolution du taux de vide au cours de l'interaction, nous sommes obligés d'effectuer des hypothèses, mais il semble que nous devions passer par une description numérique plus précise : nous proposons de séparer les champs numériques pour le gaz préexistant et de celui créé pendant l'interaction (vapeur mais également hydrogène en cas d'oxydation). Cela permettra de moduler plus facilement les caractéristiques des bulles, dont la dimension est un paramètre très important dans certaines conditions.

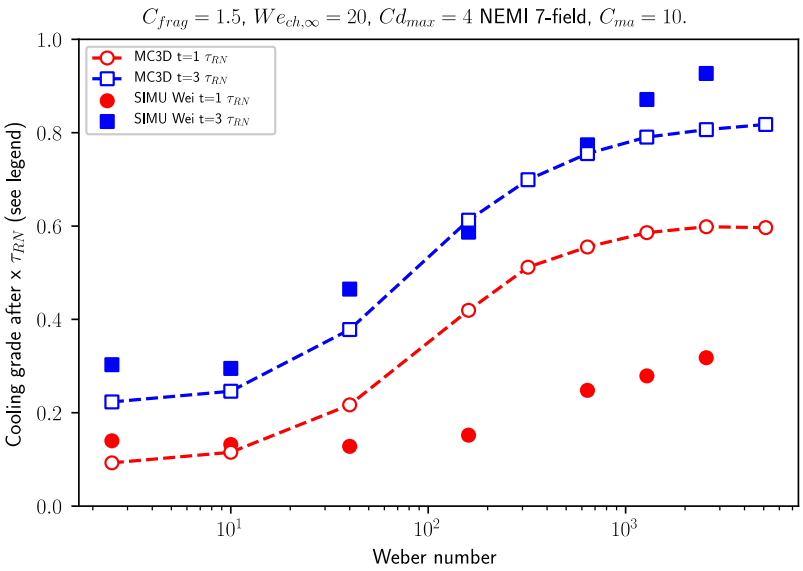

Figure 7: Cooling grade for the same calculation as the one for Figure 148, except a number of classes =7

Nomenclature

A	Interfacial area between melt and coolant
A_{fl}	Interfacial area between fragments and liquid
α_d	Volume fraction of drop
α_m	Volume fraction of mixture m.
c	Speed of sound
C_{frag}	Coefficient of fragmentation
C_p	Heat capacity at constant pressure
C_D	Drag coefficient of melt
D_d	Diameter of drop
D_f	Diameter of fragment
δ_s	Dirac fonction at interface
Δh_{lv}	Latent heat of vaporization
ΔP	Pressure jump during the passage of shock wave
ΔV_{dc}	Velocity difference between drop and coolant
Δv	Velocity jump between drop and liquid
Δx	Mesh size in x-direction
f	Body force/acceleration
Γ_f	Volumetric fragmentation rate
Γ_k	Volumetric mass transfer from/to the component k
Γ_{lv}^f	Volumetric vaporization rate due to film boiling
h	Local heat transfer coefficient
h_l / $h_{v,sat}$	Local enthalpy of the liquid coolant/enthalpy of the vapor at saturation conditions
h_{film}	Film boiling heat transfer coefficient
h^{EH}	Film boiling heat transfer coefficient using Epstein-Hauser correlation
k	Curvature at interface
λ	Thermal conductivity
$\boldsymbol{\mu}$	Viscosity
n	Unit and normal vector at interface
ν_a	Artificial viscosity
P	Pressure
$\Phi_{film,fi}$	Film boiling heat flux leaving the fragment and arriving to the film interface

$\Phi_{ra,fi}$	Radiation heat flux from fragment and arriving to the interface
$\Phi_{cv,il}$	Convection heat flux leaving from interface to liquid
Pr	Prandtl number of the drop
Re	Reynolds number of the drop
ρ	Density
σ	Surface tension
t	Time
$T_f / T_{sat} / T_l$	Temperature of fragment / saturation / liquid
t_f^*	Characteristic dimensionless fragmentation times
τ_{RN}	Ranger & Nicholls characteristic time
$(\quad)^T$	Matrices transport operator
U	Velocity vector
We_{ch}	Characteristic Weber number of fragmentation

1. Introduction and objectives

1.1. Nuclear energy and severe accidents

Nuclear energy, as a clean and carbon-free source, has been widely used among the world and considered as one of the safe sources after its application. However, the great damages caused by nuclear accidents like Three-mile islands (USA, 1978) and Chernobyl (Soviet Union, 1981) made nuclear scientists and engineers realize its potential risks and danger. Especially after Fukushima nuclear accident (Japan, 2011), the safety of nuclear power station has once again drawn people's attention and been questioned. These nuclear accidents made nuclear safety analyses and improvements become one of the biggest concerns for nuclear research and design.

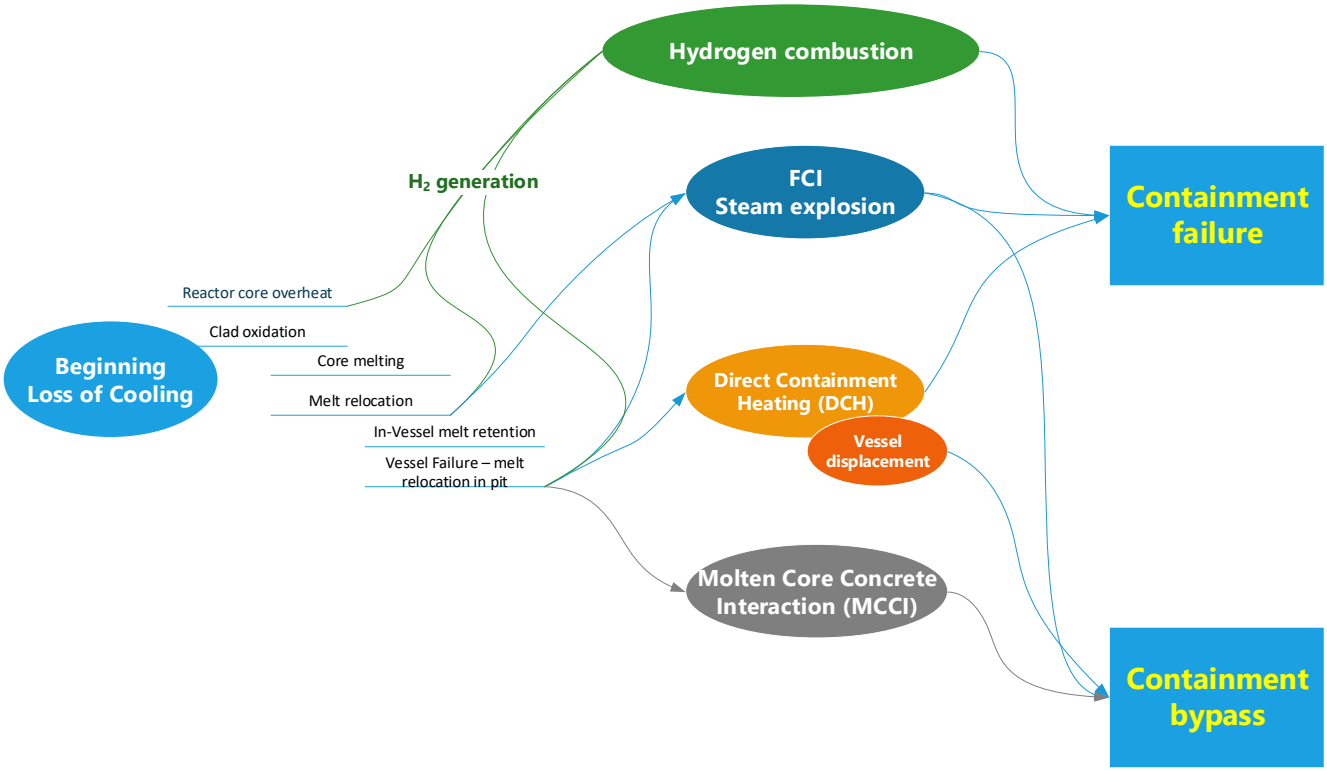

Figure 8: Severe accident sequence and relative phenomena

A nuclear accident could be initiated by many reasons, operation errors introduced by human or system, the failure of important structure, violent transition etc. If we look back how severe accident are developed from normal state, several important stages may be experienced by the reactor core (the major source of nuclear radiation), as depicted in Figure 8. Initiated by loss of cooling capabilities (station black-out, loss of coolant through breaks, natural disaster, human error …) and its relative reactivity, the reactor core may be overheated. The oxidation of the zirconium clads, the first barrier of nuclear safety, caused by its high temperature, would generate large amounts of hydrogen, which may rapidly be transported out of the primary loop though existing breaks, in the containment. In fact, hydrogen may be produced all along the corium progression, until its complete cooling. Following the clad oxidation, the reactor core may melt down if effective measures are not taken in time. Under such situation, the molten core, i.e., mixture of fuel and structures, called also "corium" will fall down and relocate in the Reactor Pressure Vessel (RPV) plenum, which should be filled with water. In such situation, an energetic explosion may occur from the Fuel-Coolant Interaction, specified as In-vessel Steam Explosion. The risk of containment failure by impact of the upper head of the reactor vessel to the upper dome of containment was identified as the so-called α-mode failure (Nuclear Regulatory Commission, 1975). Although the α-mode failure has been considered as physically unreasonable by recent researches (Theofanous and Yuen, 1995; Turland et al., 1995), in-vessel steam explosion is still a concern but it may only lead to a failure of the vessel. The analysis in the frame of SERNA-1 project (Sairanen et al., 2007) recognized nevertheless that the levels of loads caused by the in-vessel explosion would not challenge the integrity of the RPV if the RPV does not suffer the pre-existing thermal loads and estimated that resolving in-vessel explosion was not a first priority. The corium

relocation in the RPV plenum would be accompanied by considerable hydrogen production and generate a debris bed or melt pool. In case that melt pool cannot be effectively cooled down, the RPV plenum may melt through. Once the RPV, the second barrier of nuclear safety, fails, the corium would pour out into reactor pit (also called cavity), which may be filled with water, depending of the Severe Accident Management of the reactor. Then, the Ex-vessel Steam Explosion could happen and threat the integrity of containment, which is the last barrier of nuclear safety, and lead to release of radioactive materials to the environment. In the absence of water, a supplementary phenomenon called Direct Containment Heating, may be involved by a High-Pressure Melt Ejection, if the vessel depressurization is not sufficient, this involves fine fragmentation and dispersion of the melt in the containment, accompanied by fast and almost complete hydrogen production. This provokes the combustion of the pre-existing and produced hydrogen which may endanger the containment.

In the meantime, the hydrogen generated by melt oxidation during the whole process could also explode, which is also an important risk for containment integrity. Finally, if the corium takes contact with the containment ground, the Melt Corium Concrete Interaction (MCCI) might occur. This may provoke a break-through of the basemat and leakage to the environment.

As for the Ex-Vessel steam explosion, the SERENA project confirmed that the level of loads may cause some damage to the cavity and eventually the containment integrity. As a result, the studies of steam explosion risk are mainly focused on potential Ex-vessel case.

The main difficulties come from its highly coupled nature and extreme condition:

- multi-component (corium, coolant, and incondensable gas)
- multi-phase (solid, liquid and gases)
- Multiphysics (film boiling, fragmentation, solidification, oxidation, and compressibility/shock wave)
- supercritical temperature and pressure and short timescale (complexities for experiments)

In this context, the understanding and modelling of the Fuel-Coolant Interaction in general and steam explosion in particular is one of the most challenging and critical issues for nuclear safety analysis in case of severe accident.

Following the Fukushima accident and the SERENA-2 project, a national French project called ICE was launched with the objectives to improve knowledge, understanding and modeling of steam explosion, a phenomenon subject to strong confusions. The current research is linked with this project, and somehow concludes it. Our attention is focused on the Steam Explosion understanding in order to provide an improved modelling of the phenomenon in the MC3D computer code, developed by IRSN.

1.2. Steam explosion

To be specific, the distinction of concept between Fuel-Coolant Interaction (FCI) and Steam Explosion is made in this work. Fuel-Coolant Interaction (FCI) describes all the process from the contact of melt/coolant to the final explosion while Steam Explosion means only a possible transient phase of the FCI, including pressurization, pressure escalation and propagation.

Steam explosion, or more generally vapor explosion, refers to the potential energetic explosion when a hot liquid (melt) contacts a cooler volatile liquid (Buchanan, 1974; Fletcher and Theofanous, 1997). In fact, the studies on steam explosion started from the metal casting industry, where there is also the potential contact between a hot liquid (metal) whose temperature is much higher than the saturation temperature of a cold volatile liquid. Steam explosions also occur in submarine volcanos (Berthoud, 2000a; Fletcher and Theofanous, 1997; Head and Wilson, 2003; Wohletz, 2002). In nuclear industry, steam explosion studies started in fact for the development of fast breeder reactors with coolant as sodium (PHENIX, SUPERPHENIX in France). Thus, we may speak more generally of “vapor explosions”. The 1978 Three-mile islands accident led to consider that the phenomenon could also happen and be destructive for water cooled reactors (PWRs, BWRs, then CANDU …).

According to previous researchers, some “implicit” conditions should be filled for the occurrence of an explosion, so additional terms are emphasized to describe steam explosion (Berthoud, 1987, 2000a; Corradini et al., 1988):

- generation of fine melt debris by rapid fragmentation;
- intense and fast heat transfer from the melt and coolant vaporization;
- generation of shock waves (timescale for vaporization is shorter than that for pressure relief), thus generating fine fragmentation.

A steam explosion may then arise anytime when the liquid melt is contacting liquid water. However, it’s generally believed that powerful explosions able to damage the reactor structure and safety equipment may occur only in the situation when the melt is penetrating water. The situation of water penetrating melt seems unlikely in the nuclear context and is expected to lead only to moderate interactions. A particular attention may be put on the so-called “stratified” configuration, which may occur from two situations:

- water application on top of a molten pool: experimental analyses indicated to possibility of triggering an explosion only if the surface of the pool is made of unoxidized metal (Yang et al., 2023)
- melt spreading under water: the fragmentation of the melt during its penetration in the water may be uncomplete and liquid melt may then spread on the bottom surface.

This second possibility is still the subject of debate and research work (Huhtiniemi and Magallon, 2001; Konovalenko et al., 2012). The current OECD ROSAU program investigates in particular underwater melt spreading (MST tests) with particular caution to avoid steam explosion (nearly saturated water).

The stratified situation is out of the scope of the present work. In the case of melt penetrating water, three main phases named premixing, triggering and explosion are identified (Figure 10). The **premixing** is characterized by primary coarse fragmentation from continuous melt fuel jet into drops of some millimeters, thus generating a coarse fuel-coolant mixture, which gives the initial condition and determines the strength of a steam explosion, if it occurs. Indeed, the explosion needs a **triggering** process, i.e., a local perturbation of the flow, to initiate the explosion. The trigger can be spontaneous (local destabilization of the flow) or introduced by the external events. The **explosion** is similar to a detonation process and is due to a self-sustained secondary fine fragmentation of the primary drops into fragments (~50-100 µm), generated by the passage of the shock wave in the coarse fuel-coolant mixture. The fast and fine fragmentation strongly increases the melt interfacial area and thus enhances the heat transfer between the melt (of temperature ~3000 K) and water, which will cause violent vaporization and sustain the shock pressure wave.

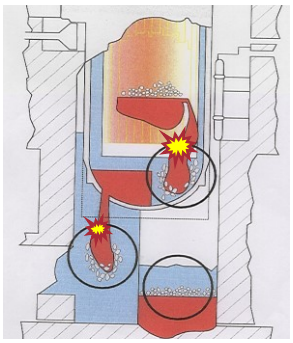

Figure 9: Illustration of possible Fuel-Coolant Interaction locations

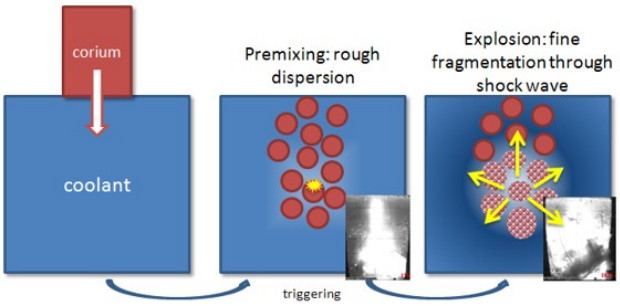

Figure 10: Major stages of steam explosion

The FCI is modeled in the MC3D thermal-hydraulic multiphase flow code, through two separate models (application): PREMIX for the premixing and EXPLO for the explosion. It is noticed that the triggering process is not modeled, being too local and stochastic in nature. The EXPLO model is then not fully predictive but may give rather the potential for steam explosion, for a given premixture, as a function of the triggering event.

Even if general phases of FCI are identified, there are still some important uncertainties and lack of understanding. This leads to recognition of serious difficulties and uncertainties for the relative to numerical modelling. In fact, the simulation results should always be considered with caution because of the difficulties and uncertainties to model numerically such a complex phenomenology which involves strong coupling processes. To get an accurate estimation of magnitude and location of pressure loads, it is necessary to identify, understand and model decisive phenomena and relative mechanisms. Figure 11 gives a quick capture about the coupling nature of FCI. Accompanied by violent vapor production, the pressurization process is the crucial phenomenon directly determining the explosion strength. In one hand, the pressurization is indeed caused by film boiling from massive amounts of fine fragments of melt drops by strong shock waves (some hundreds of bars). which are generated from fine fragmentation. On the other hand, pressurization itself would increase local pressure and void, changing the fluid dynamic which plays a crucial role on fine fragmentation. Thus, the pressurization, fine fragmentation and multi-phase dynamic are highly coupled.

The pressurization is caused by coolant **vaporization**, which is a mass transfer process and related to heat transfer by film boiling. Thus, specific vaporization model should be built to evaluate the quantity of generated vapor during explosion. The results in this work (discussed in section 3.3) indicate that the possible bubble condensation in some cases can also influence the global vaporization. In fact, the heat transfer process during pressurization can change instantaneously due to **fragmentation**, by modifying the interfacial area between melt and coolant. The fragmentation is a mass transfer process, and kinetic model for fragmentation are expected to be implanted. Even thermal and hydrodynamic fragmentation could exist along steam explosion, the hydrodynamic fragmentation is expected to have a key role, which depends on the relative velocity between the melt liquid drop and its surrounding coolant. To identify this relative velocity, the **multiphase fluid dynamic** should be resolved. It is momentum transfer in nature, and adapted flow configuration/map and friction closure between different phases (e.g., dispersed melt drop, fragments and vapor with continuous water) should be modelled to close the system. It is also important to point out that the local phenomena like oxidation and solidification can also have a considerable effect (Loisel et al., 2019; Uršič, 2011; Uršič et al., 2011). The **oxidation** could influence the fluid dynamic by producing non-condensable gas and vaporization by providing additional

chemical heat source to the system. The **solidification** may change the fluid dynamic because of different friction and fragmentation by varying the drop stiffness.

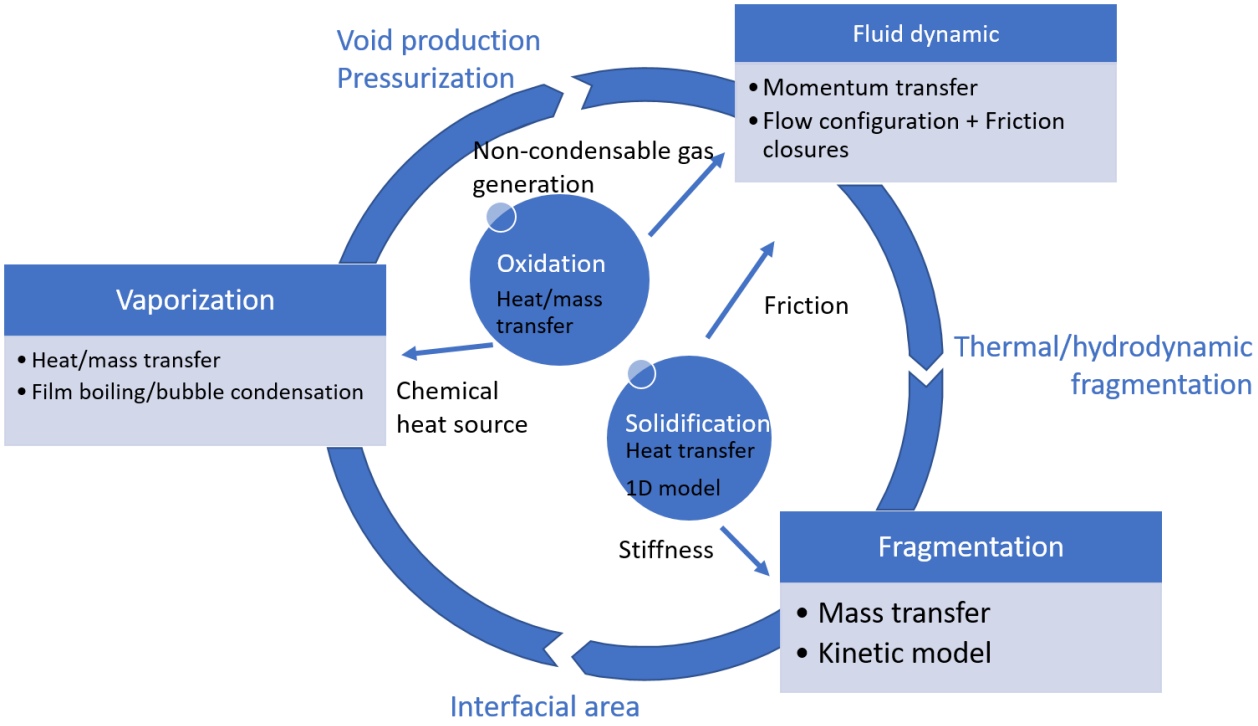

Figure 11: Major phenomena and links for Fuel-Coolant Interaction modelling

1.3. Objectives of the thesis and outline of the thesis

Following the Fukushima accident, the "Agence National pour la Recherche" (ANR) launched a program for improving nuclear safety (Recherche en Sureté Nucléaire et Radioprotection, RSNR), among which the project ICE (Interaction Corium-Eau), dedicated to the improvement of understanding and modelling of FCI and steam explosion (2014-2019). Among the project outcomes, the works led to a substantial improvement of the understanding of the local phenomena related to the fine fragmentation and vaporization process during the explosion.

The objective of the present PhD thesis is to confirm these outcomes and improve the link between fragmentation and heat transfers and consider the new insights gained from the analysis to propose a new modeling for the V4 version of MC3D (new rebuilt version currently under development) and implement exploratory simplified models in the V3 MC3D-EXPLO application.

In the second part of this thesis manuscript, a detailed bibliography allows to characterize the important processes of the phenomenon. A quick description of the current treatment (version 3.10) in MC3D is presented, with a perspective on the work carried out in the framework of the research project RSNR-ICE (ANR).

The current (V3.10) modelling of the EXPLO application and the various parameters associated are then analyzed in detail via a simple one-dimensional test-case. The first aim is to better characterize the current behavior of the model and highlight supposed deficiencies and needs for improvements. The analysis is related to the physical modeling as well as to the numerical behavior. The study can also be used to better understand or anticipate the results of one-dimensional tests, in particular the KROTOS tests conducted first by the Joint Research Center at Ispra (Italy) and then by the CEA, in the SERENA (OECD) or ICE frameworks. The test-case is also used to evaluate the impact of proposed model changes. This analysis also confirms the need for further small-scale simulation work (drop) within the ICE project to better understand the dynamic and thermal interactions during the fragmentation process.

For this purpose, simulation of the fragmentation of a drop has been carried out in part IV. A main objective is to provide information on the heat transfer processes. The work with Basilisk starts with the testing and verification of the approach used in our simulations. Next, the transient heat transfer characteristics of a drop subjected to a velocity jump are studied for different initial Weber numbers. Five different breakup mode, so called oscillation, elongation breakup, cap breakup, cap-ligament breakup and sheet stripping are observed increasing the weber number. Detailed transient behavior during the deformation and fragmentation process are quantitatively identified. As for thermal aspects, we find at first that the characteristic time for cooling is not scaling with fragmentation. Cooling is comparatively more rapid at high Weber numbers, which means solidification should get involved more rapidly at high Weber numbers. The increase of the interfacial area has a dominant effect on the enhancement of heat transfer during fragmentation.

The last part of the report provides proposals for an improvement of the EXPLO model in MC3D by introduction of a Non-Equilibrium Micro-Interaction (NEMI).

2. Literature review

Important physical and numerical models of steam explosion will be discussed in the part.

The explosion modelling needs to answer two questions:

- At small scale, when a liquid melt drops of high temperature fall into water whose saturation temperature is much lower, we want to understand and describe and further model the fragmentation of drop, the heat transfer and boiling process, especially under an extreme condition with high and transient pressure and temperature.
- At large scale, in a zone filled with liquid drops, water and vapor, we want to understand and describe and further to model the detail of explosion escalation and propagation, which are generally caused by the previous small-scale interaction. Further, to identify and model the crucial factors which have dominant effect on the prediction of explosion behavior.

Around these two aspects, different models have been proposed by researchers, the evolution of which is following the knowledge acquired through experimental activities, first, and more recently, small-scale simulation studies to supplement the experimental difficulties at this scale.

The industry applications, for example, to estimate the risk of steam explosion for a new type of reactor, can only be performed in the large scale, where we are more interested in the global impact. However, the closure/constitutive models (or the sub-mesh models) used in large scale are generally based on the derivation, extrapolation from the behavior observed on the small scales. Clearly, the accuracy of large-scale codes highly depends on sub-mesh models employed. To improve the accuracy of large-scale model, we need to have a better understanding of phenomenology in smaller scale.

2.1. Short review of experimental activities and major results

Table I summarizes the main experimental programs related to explosion study using corium or other simulant materials. These experimental results were used as the basis for the development and qualification of computational models.

- The FITS program conducted numerous experiments, in various configurations and with various materials. Spontaneous and violent explosions were observed with corium made of a UO2 + Zr02-steel mixture. However, these experiments are not used for software qualification because the experimental conditions of fluid contact are often poorly known and can hardly be reproduced in the calculations.
- The KROTOS program was aimed to study the explosion on a smaller scale (volume of fuel of the order of one liter). This program showed a lower propensity for explosion as well as lower pressure loads for a UO2 + Zr02 "oxide corium" compared to cases with Al203 alumina.
- The ZREX tests showed a very significant increase in the intensity of the explosion due to the oxidation of the zirconium contained in Zr + Zr02 and Zr-steel mixtures.
- The TROI program has confirmed the possibility of spontaneous explosions with corium.

Table I: Experimental program related to explosion study

Program	Laboratory	Stages involved	Material	Remarks
FITS (Berman, 1981) (Berman, 1982) (Mitchell and Corradini, 1981)	Sandia (USA)	Explosion	Thermite Al_20_3-Fe Or Corium	• Test series with corium: spontaneous explosion with a thermal to mechanical energy conversion efficiency of 2% • Test series with thermit: observation of high energy conversion efficiency (8-15%)
KROTOS(Huhtiniemi and Magallon, 2001) (Huhtiniemi et al., 1999, 1997; Magallon, 2006)	JRC in Ispra (EU)	Explosion	Sn of temperature 1000°C Al_20_3 of temperature 2300~2800°C $UO_2 + ZrO_2$ of temperature 2800°C	• Reference for the qualification of models used in Explosion codes • One dimensional test • Effect of material composition (Alumina or corium of UO2 + ZrO2) • No spontaneous explosion with Corium
ZREX and ZRSS (Cho et al., 1998, 1997)	Argonne (USA)	Explosion	Mixture of $Zr+ZrO_2$ Zr-steel	• Triggered explosions • Strong effect of Zr fraction on the energy conversion efficiency
TROI(Song et al., 2002)	KAERI, South Korea	Premixing Explosion	$UO_2 + ZrO_2$ ~10kg	• Spontaneous explosion • weak energy conversion efficiency • Effect of material composition

It may be at first highlighted the extreme challenge that experimentalists must face to simulate steam explosion during a severe accident. Here below, the major experimental activities and results are rapidly reviewed with this perspective, discussing the various challenges and major experimental techniques used to address the problem, and presenting the major results obtained with these techniques.

- Selecting representative corium compositions, which depends strongly on the knowledge of the accident progression (core degradation, vessel ablation, and thermodynamics of the numerous involved chemical components (U, Zr, Fe and the various fission products).
    - The so-called prototypical corium composition is a (UO_2-ZrO_2) fully oxidized composition. The representativeness of such a composition is discussed later in this section. The proportion of U and Zr is a matter of representation of a particular class of reactor, mainly PWR and BWR, which have different proportions of fuel and structures in the core.

- Several other compositions have been used, from (UO_2-ZrO_2) + steel (e.g. CCM tests (Spencer et al., 1994)) to various simulants as
  - Alumina (Al_2O_3, oxide with representative solidification temperature, but low density);
  - Mixtures Fe/Al_2O_3 (from a thermite reaction, involving oxidation of iron);
  - Various oxides with representative physical properties but at intermediate solidification temperatures (e.g. the binary oxide mixtures CaO-B_2O_3 melt used at KTH (Paladino et al., 2002)).
- The thermodynamics of such complex melts is a particular issue. The real representativeness of simulants is always subject to discussion, and results must be considered with caution.

- Heating this composition up to, at least, the liquidus temperature, that is about 3000 K (UO_2-ZrO_2) melts; several specific technics have been elaborated:
  - thermite reaction: this was the privileged technique in the first experiments elaborated in the US in Sandia (SNL) and Argonne (ANL) laboratories (FITS2G & MDC (Berman, 1981) ,FITSB (Berman, 1982) and MD & FITS-A (Mitchell and Corradini, 1981) at Sandia, ZREX and ZRSS (Cho et al., 1998, 1997) at ANL);
    - the thermite reaction technique is limiting the choices of the melt composition, since it is the product of a chemical reaction;
    - the most used one is the reaction Fe_2O_3 + Al -> Fe + Al_2O_3 +Q;
    - ANL and SNL also used thermite reaction yielding more representative melts with U, Zr compositions.
  - direct heating in a crucible: the later must sustain the large temperature; tungsten is used in the KROTOS experiments(Huhtiniemi et al., 1999, 1997; Magallon, 2006); in principle the technique is less limiting regarding the selection of mixtures, however, chemical interactions between the melt and crucible must be avoided and the technique has, up to now, shown strong difficulties to integrate unoxidized compositions, in general due to interaction with zirconium.
- Measuring such high temperatures necessitates itself specific complex techniques: in general, the measure is indirect through pyrometers: measure of top mixture surface in the crucible (TROI) or measure of the crucible temperature itself (KROTOS).
- Injecting this high temperature liquid into a water pool; this means designing an injection system which allows a sufficient characterization of the main parameters: diameter, velocity. This is in general a major difficulty and weakness of the experimental devices. The vessel receiving the water must be sufficiently resistant against an explosion (no elastic deformation) if pressure measurements are foreseen.
- Characterizing the mixing stage: containers with glass or transparent walls allow a global visualization of the mixing (KROTOS(Huhtiniemi and Magallon, 2001), Figure 12, TROI(Song et al., 2002), Figure 13). Recently, the CEA has developed a technique based on X-rays allowing an indirect visualization of the flow (Figure 14). In any case, the explosion itself cannot be precisely characterized even with fast image acquisition, although:
  - KROTOS test in Figure 12 allows to identify the shock and the expansion through some few images;
  - TROI test in Figure 13 gives indication of the location of the initiating event of a spontaneous explosion (melt accumulating and spreading on the bottom of the test section).

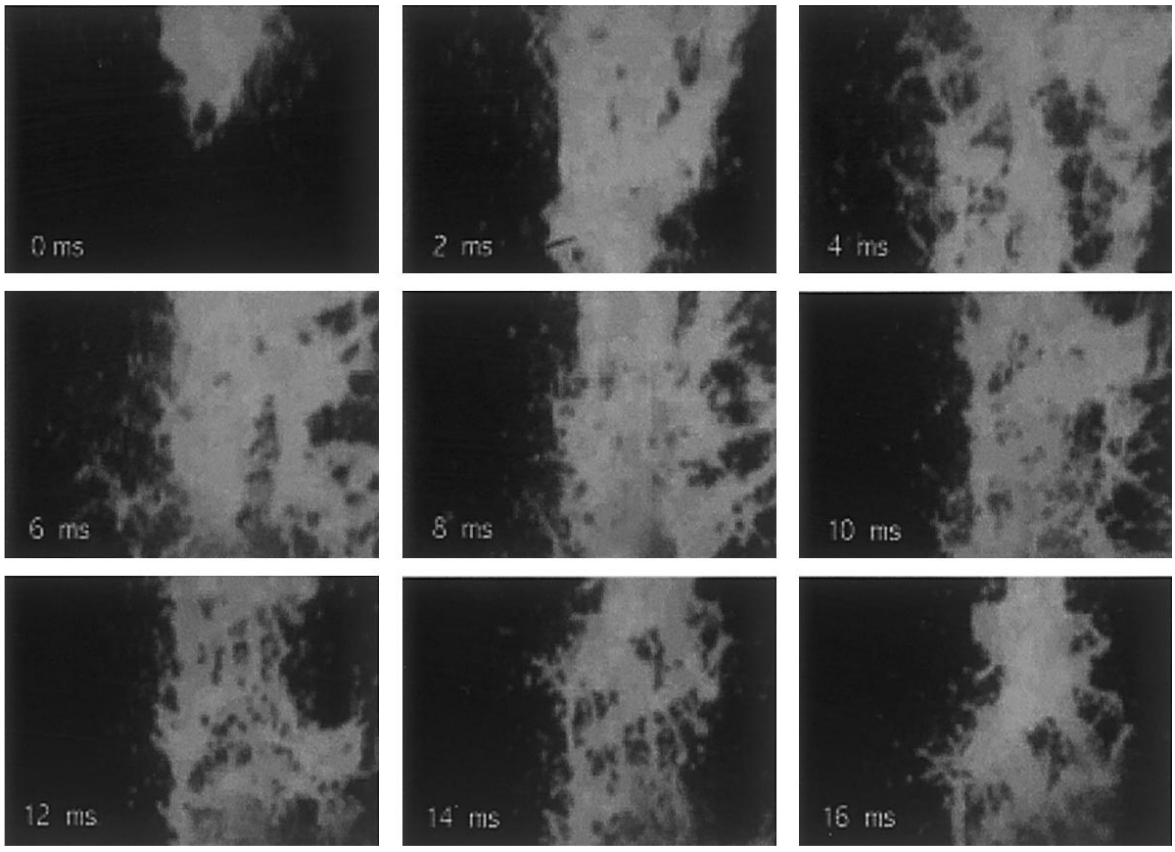

Figure 12: Visualization of the development of the pre-mixture in an early KROTOS test (Huhtiniemi and Magallon, 2001)

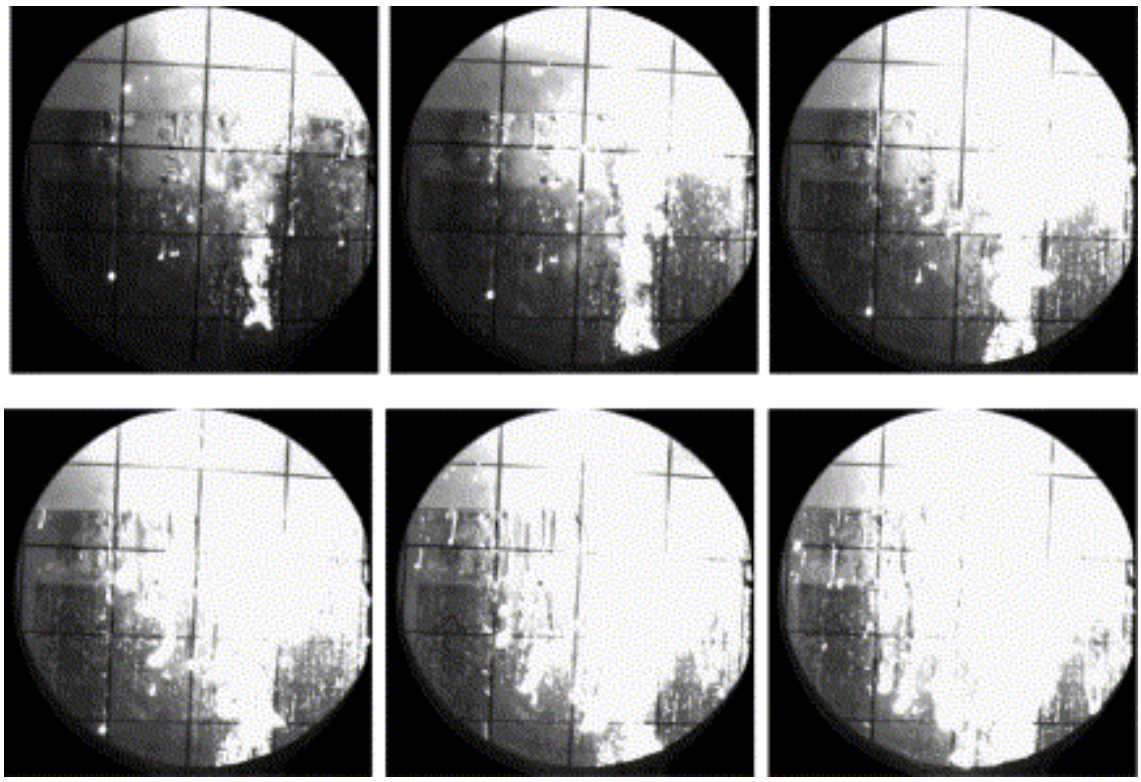

Figure 13: Visualization of the development of the pre-mixture in a TROI test (time interval, 0.01 s). (Song et al., 2002)

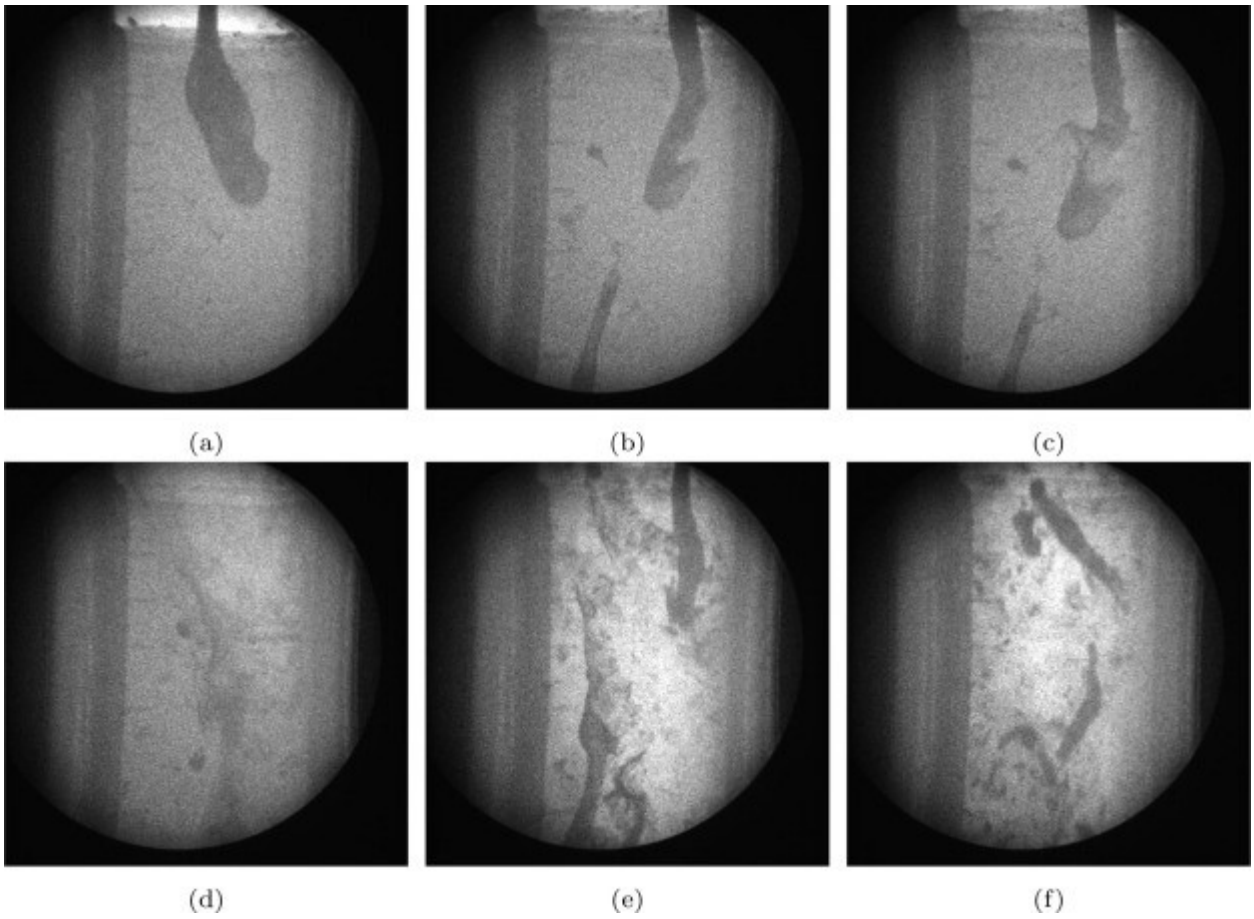

Figure 14: Visualization of the development of the pre-mixture in a recent KROTOS test using X-ray technique (Johnson et al., 2021)

In the absence of visualization, the melt penetration is usually obtained with sacrificial sensors, a technique which leads however to quite uncertain results. There have also been attempts to characterize the mixture extent with local measurements of the void through a grid of sensors (ECO)(Cherdron et al., 2005).

The particle size is obtained from post-mortem granulometry. The current X-Ray techniques do not yet have a sufficient resolution to provide precise data. Post-mortem granulometry has two important drawbacks:

- gives only the final stage;
- is very imprecise for debris with irregular shape.

The particle shape and morphology should give information on the fragmentation process: a large number of the debris have irregular shapes with sharp angular, meaning they have been formed by a thermal cracking process while solidified, thus not relevant for analyzing the fragmentation during liquid stage (we are mostly interested in liquid melt, which should mostly participate in the explosion.

- Elaborating a triggering device: This is a key point for steam explosion experiments. In most of the cases, a small amount of an explosive is used, e.g., FARO, TROI. This seems to generate in general a sharp and strong pressure peak (Figure 15). In 3D geometries, the peak is rapidly decreasing. The question of the actual perturbation generated to the drop has never been discussed. In the KROTOS test (JRC and CEA) a pressurized gas capsule is used (Figure 16). The pressure peak is larger in this case. Despite the gas pressure is 120 bars, the actual propagating pressure is about 50 bars.

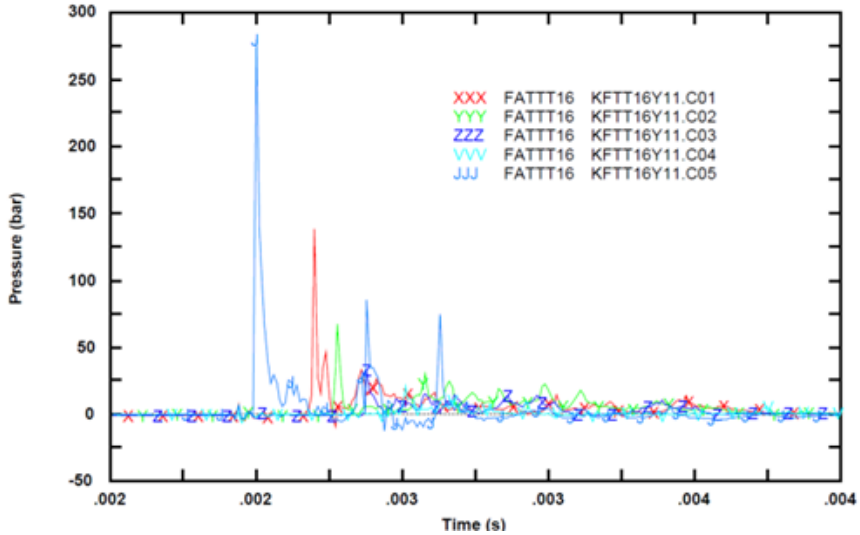

Figure 15: Pressure peak generated by the trigger in pure water for FARO L-33 test, at the wall, for 5 successive distances. The geometry of FARO is 3D, which explains the fast decreasing.

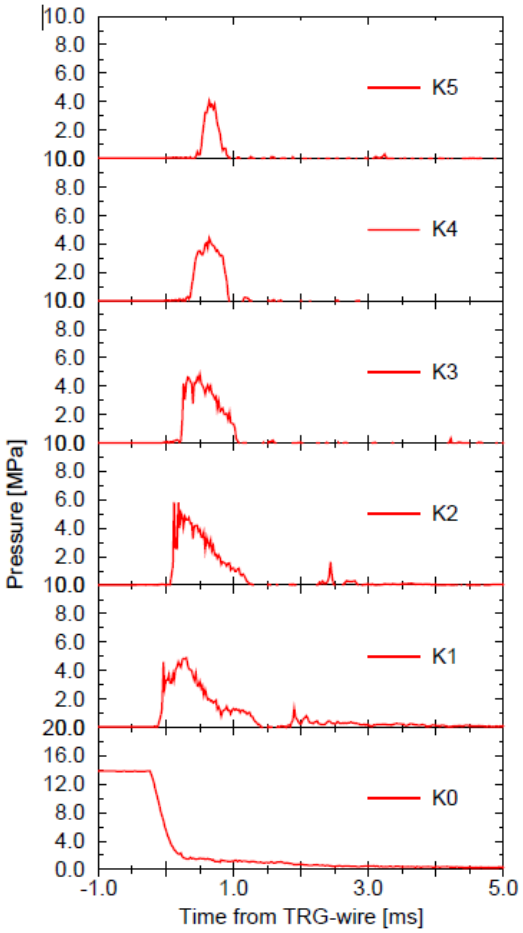

Figure 16: Pressure peak generated by the gas capsule used in the KROTOS test (~1D), pressure history in different height when trigger propagates in pure water at 20°C (Moriyama et al., 2006), K0 on the bottom (h=0m), K1 (h=15cm), and K1, K2, K3, K4, K5 are placed at a distance of 20cm

– Measuring accurately the pressure evolution during the explosion: This necessitates particular types of sensors with fast acquisition. However, pressure sensors are known to be very sensible to the

temperature and it seems that the measurements are not very accurate after some time (giving often negative pressure). The pressure measurements must then be considered with caution, particularly in the long-term, for evaluating the expansion stage.

- Characterizing oxidation: Oxidation seems to occur systematically for the interaction with water, even for UO_2-ZrO_2 mixtures. The issue is threefold:
  - modification of the melt characteristics and properties, in particular solidification;
  - energy input for some metals as zirconium or aluminum (oxidation of Fe is not very energetic);
  - H_2 production, which has an impact on the void in the mixture.

The experimental techniques have strongly evolved with time to provide more precise measurements. Nevertheless, it must be emphasized that the available experiments still have important bias to consider for the analysis:

- geometry: all experiments involve 2D axisymmetric geometries with a vertical melt injection at the center of a water pool: in reality, such a condition is very unlikely and 3D aspects (no vertical jets, no central injection) should be important;
- composition: most of the experiments used fully oxidized UO_2-ZrO_2 mixtures; it is known and accepted that the unoxidized metals should be separated so that the corium should in fact be a composition of one (at least) oxidized mixture and one (or two) metallic mixtures that may oxidize.

2.2. Thermodynamic models

Due to complexities of phenomenology and limits of experimental support, the early investigations started from evaluation of damage potential caused by steam explosion. These models do not take into account the transient and kinetic process like heat transfer and fragmentation but focus on the initial and final state from energetic point of view and try to evaluate the work done by steam explosion between these two states.

2.2.1. Model description

The first remarkable thermodynamic model was originally developed by Hicks & Menzies in 1965 (Hicks and Menzies, 1965) to estimate the work potential during severe accident for sodium fast reactor.

Hicks and Menzies supposed that the fuel and coolant are submitted firstly to an isochoric and adiabatic compression with a fuel-coolant mixture assumed to attain instantaneously its thermal equilibrium. Then the mixture follows an isentropic expansion.

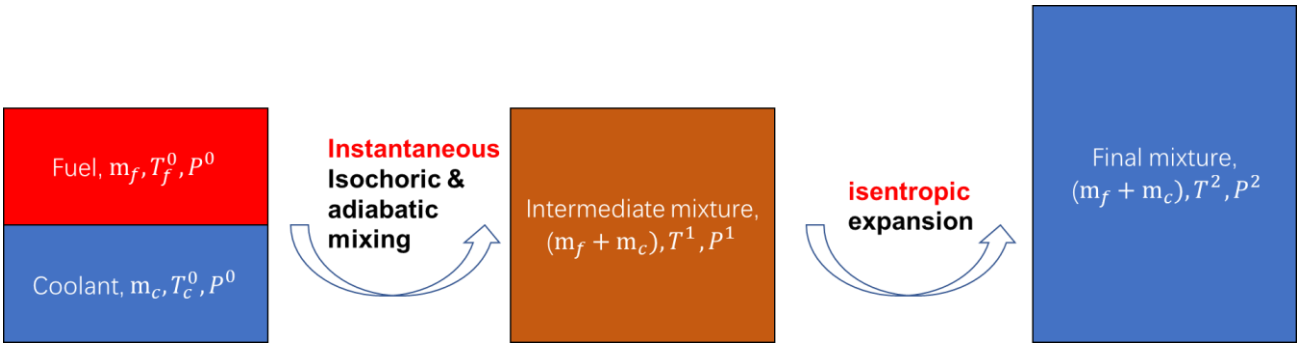

Figure 17: Schematic process in Hicks & Menzies's thermodynamic model

For mixing phase, the two unknowns (the temperature T^1 and pressure P^1 of mixture) are solved by the following equations (taking the whole system as control volume):

- Conservation of total volume (isochoric):

$$\frac{m_f}{\rho_f(T_f^0, P^0)} + \frac{m_c}{\rho_c(T_c^0, P^0)} = \frac{m_f}{\rho_f(T^1, P^1)} + \frac{m_c}{\rho_c(T^1, P^1)}$$

- Conservation of total internal energy ($dU = \delta Q$ (adiabatic)+δW(isochoric) =0):

$$m_f\ u_f(T_f^0, P^0) + m_c u_c(T_c^0, P^0) = m_f\ u_f(T^1, P^1) + m_c u_c(T^1, P^1)$$

For the **expansion** phase, the only unknown temperature T^2 of final mixture can be calculated by employing the conservation of entropy (isentropic):

$$m_f\ s_f(T^1, P^1) + m_c s_c(T^1, P^1) = m_f\ s_f(T^2, P^2) + m_c s_c(T^2, P^2)$$

Here, the entropy S, density ρ and internal energy u are all equation of state in function of temperature and pressure.

Finally, the work done during expansion is evaluated by the following equation:

- $\delta Q = 0$ during the whole reaction, (adiabatic in mixing, the isentropic means the expansion is at the same time adiabatic and reversible), $dU = \delta W$:

$$|W| = -\Delta U = m_f\big(\ u_f(T_f^0, P^0) - \ u_f(T^2, P^2)\big) + m_c(\ u_c(T_c^0, P^0) - \ u_c(T^2, P^2))$$

- one way to define the energy conversion efficiency of thermal energy to mechanical work is as follow:

$$\eta = \frac{|W|}{m_f\big(\ u_f(T_f^0, P^0) - \ u_f(T_c^0, P^0)\big)}$$

The hypothesis that mixture is subjected to isentropic expansion (do not consider energy loss caused by irreversible process) maximizes the work done during expansion. Thus, it can give an upper bound of the conversion efficiency of thermal energy to the mechanical work.

However, it was found that this bound is much higher than that measured in the experiments (Brayer and Berthoud, 1991). Figure 18 demonstrates the conversion efficiency calculated by Hicks and Menzies' model for fuel-coolant interaction under typical condition, on function of coolant to fuel ratio. The conversion efficiency can even attain about 50 % in order of magnitude, which is unrealistic for most of the cases as the heat transfer cannot be instantaneous. But it can be a rough and representative index in case of rapid heat transfer for study of extremely complex problem.

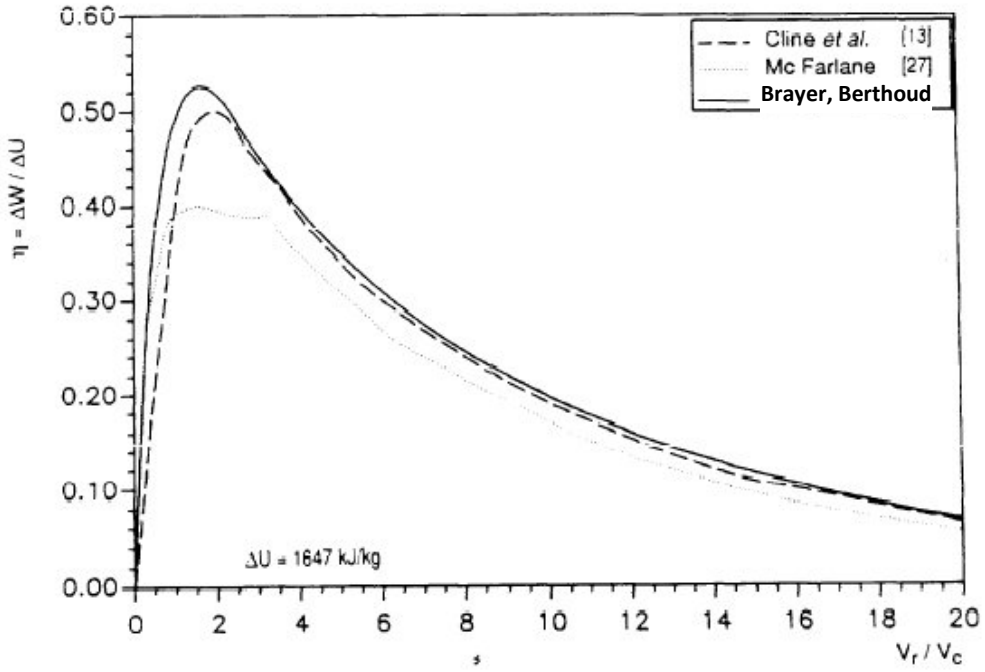

Figure 18 Conversion efficiency for fuel-coolant interaction under typical condition with Hicks and Menzies' model, on function of coolant-fuel volume ratio (Brayer and Berthoud, 1991)

Hall (Buchanan, 1974) proposed an improved model to get a qualified lower limit of conversation efficiency, relaxing the assumption of isentropic expansion. The key idea is to estimate the work done by mixture expansion from an isentropic compression of cover gas which is supposed to be confined with mixture in a fixed volume (can be RPV or containment). As the gas compression is considered reversible, all the irreversibility is then shifted to mixture expansion, which minimizes the work done by mixture expansion[1]. Hence, the model could help to find a conversion efficiency lower than that of Hicks and Menzies'.

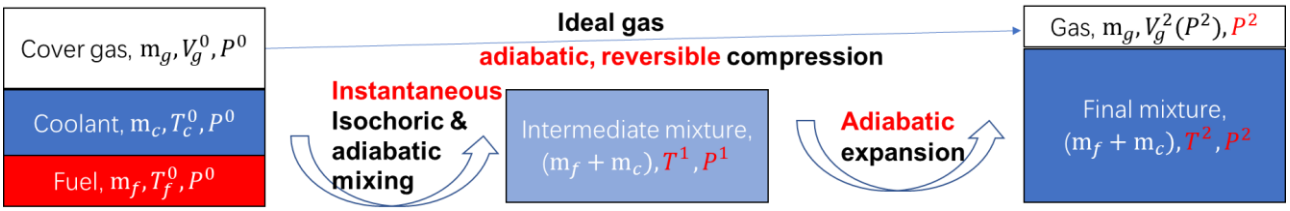

Figure 19: Schematic process in Hall's thermodynamic model

If we study the whole process neglecting the intermediate mixture, we have two unknowns to solve, the final pressure P^2 and temperature T^2. Thus, we need two equations to solve the system:

Conservation of total volume:

- For the cover gas compression: (considered as ideal gas submit adiabatic and reversible compression, Laplace law $PV^\gamma = cst$). The variation of volume: (V_g^2 and V_g^0 donate the final and initial volume of cover gas)

$$V_g^2 - V_g^0 = V_g^0 \left(\left(\frac{P^0}{P^2} \right)^{1/\gamma} - 1 \right)$$

- On the other hand, the variation of volume ΔV for mixture during the whole process:

[1] Minimum for this type of thermodynamic analysis, which cannot be exactly the minimum in the reality without the adiabatic hypothesis.

$$\Delta V = \frac{m_f}{\rho_f(T^2,P^2)} + \frac{m_c}{\rho_c(T^2,P^2)} - \frac{m_f}{\rho_f(T_f^0,P^0)} - \frac{m_c}{\rho_c(T_c^0,P^0)}$$

- As there is total volume conservation, we get the first equation:

$$V_g^0\left(\left(\frac{P^0}{P^2}\right)^{1/\gamma} - 1\right) = \frac{m_f}{\rho_f(T_f^0,P^0)} + \frac{m_c}{\rho_c(T_c^0,P^0)} - \frac{m_f}{\rho_f(T^2,P^2)} - \frac{m_c}{\rho_c(T^2,P^2)}$$

Conservation of total internal energy (isochoric and adiabatic):

- For the cover gas compression, the variation of internal energy: ($dU = \delta W + \delta Q = \delta W$, adiabatic)

$$\Delta U_g = W_g = -\int_{V_g^0}^{V_g^2} PdV = \frac{P^0 V_g^0}{\gamma - 1}\left(\left(\frac{P^2}{P^0}\right)^{(1-\frac{1}{\gamma})} - 1\right)$$

- on inverse, the variation of internal energy ΔU_m for mixture during the whole process:

$$\Delta U_m = m_f\left(u_f(T^2,P^2) - u_f(T_f^0,P^0)\right) + m_c\left(u_c(T^2,P^2) - u_c(T_c^0,P^0)\right)$$

- As the total internal energy is preserved, we get the second equation:

$$\frac{P^0 V_g^0}{\gamma - 1}\left(\left(\frac{P^2}{P^0}\right)^{(1-\frac{1}{\gamma})} - 1\right) = m_f\left(u_f(T_f^0,P^0) - u_f(T^2,P^2)\right) + m_c\left(u_c(T_c^0,P^0) - u_c(T^2,P^2)\right)$$

After resolving the final state, the work done during expansion is evaluated by the following equation:

- $\delta Q = 0$ (adiabatic), $dU = \delta W$:

$$|W| = -\Delta U = m_f\left(u_f(T_f^0,P^0) - u_f(T^2,P^2)\right) + m_c\left(u_c(T_c^0,P^0) - u_c(T^2,P^2)\right)$$

The energy conversion efficiency is defined in the same way as that in Hicks and Menzies'. The final temperature of fuel and coolant in the model discussed above are supposed to be the same, which means the heat transfer between the fuel and coolant is active during the mixture expansion. This mode is called "no cutoff" expansion.

In fact, for a further conservative estimation of the work during mixture expansion, we can remove the heat transfer during the mixture expansion, which means the final temperature of fuel T_f^2 would be different that of coolant $T^2$and rests constant after the mixing, i.e., $T_f^2 = T^1$. This mode is called "cutoff" expansion. A schematic illustration of this mode is given in Figure 20.

Different from the "no cutoff" model, the intermediate state T^1 and P^1 should also be calculated in this case by the same way discussed in Hicks and Menzies' model. Then, two similar equations could be obtained to deduce the final temperature T^2 and pressure P^2.

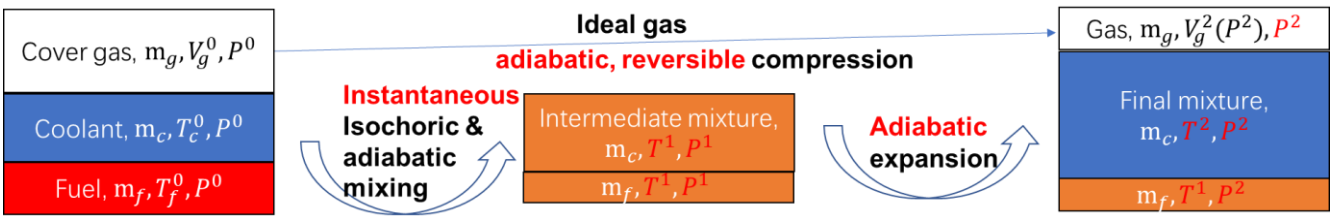

Figure 20 Schematic process in Hall's thermodynamic model, "cut off" mode

The equation set for the "cut off" mode is thus as follows:

- Mixing phase: two unknowns, the temperature T^1 and pressure P^1 of intermediate mixture

$$\frac{m_f}{\rho_f(T_f^0,P^0)} + \frac{m_c}{\rho_c(T_c^0,P^0)} = \frac{m_f}{\rho_f(T^1,P^1)} + \frac{m_c}{\rho_c(T^1,P^1)}$$

$$m_f\ u_f(T_f^0, P^0) + m_c u_c(T_c^0, P^0) = m_f\ u_f(T^1, P^1) + m_c u_c(T^1, P^1)$$

- For the whole process: two unknowns, the temperature T^2 of expanded coolant and final pressure P^2

$$V_g^0\left(\left(\frac{P^0}{P^2}\right)^{1/\gamma} - 1\right) = \frac{m_f}{\rho_f(T_f^0, P^0)} + \frac{m_c}{\rho_c(T_c^0, P^0)} - \frac{m_f}{\rho_f(T^1, P^2)} - \frac{m_c}{\rho_c(T^2, P^2)}$$

$$\frac{P^0 V_g^0}{\gamma - 1}\left(\left(\frac{P^2}{P^0}\right)^{(1-\frac{1}{\gamma})} - 1\right) = m_f\left(u_f(T_f^0, P^0) - u_f(T^1, P^2)\right) + m_c\left(u_c(T_c^0, P^0) - u_c(T^2, P^2)\right)$$

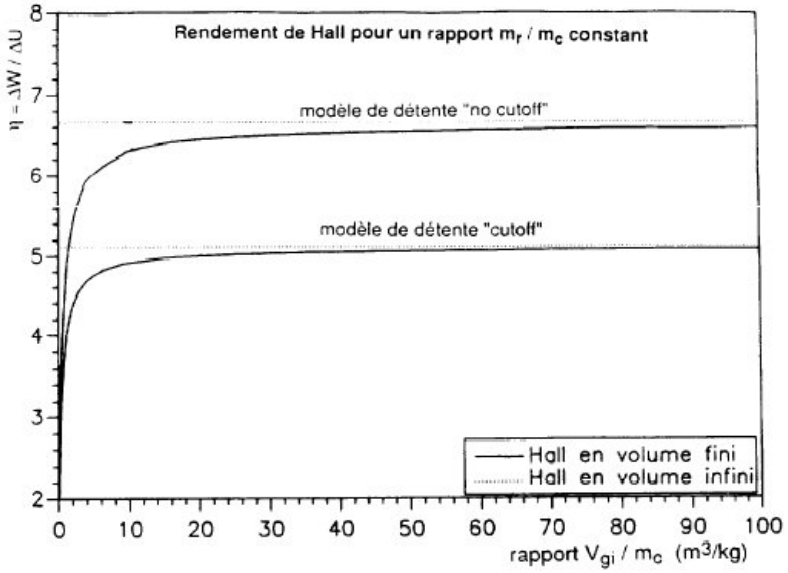

Figure 21: Conversion efficiency for fuel-coolant interaction under typical condition with Hall' model, on function of cover gas volume to fuel mass ratio(Brayer and Berthoud, 1991)

Figure 21 illustrates the conversion efficiency calculated by Hall's model for fuel-coolant interaction under typical condition, on function of cover gas volume to fuel mass ratio. The calculated conversion efficiency is about 5-7% in order of magnitude, which is much smaller than that of Hick and Menzies's model. The "cutoff" model could give a more conservative and smaller estimation.

2.2.2. Remarks

These thermodynamic models can be regarded as the first attempts for explosion energy evaluation. They are easy to use, and they can be helpful to place useful bounds on physical behavior. It should be noticed that these models estimate generally the work done during the mixture expansion, i.e., integral of pressure respect to volume, but the experiments give rather the impulse, i.e., integral of pressure respect to time. Special attention should be taken in case of direct comparison of results between the model and experiments.

It is found that the model of Hicks and Menzies would overestimate the potential work done by a factor of 10, thus giving in general very conservative estimates. While, the results from model of Hall are coincident with order of magnitude of the experiment when the experimental setup is compatible with the hypotheses of the model (Brayer and Berthoud, 1991) (homogeneity of the premixing,…etc.), thus providing in some way a more realistic evaluation.

Nevertheless, these models cannot illustrate the transient and dynamical responses during steam explosion due to lack of kinetic description of flow configuration (amount of melt and water), heat transfer, fragmentation, and shock propagation. They are not compatible with issues related to nuclear safety as being too simplified and approximate, yielding, in a conservative approach, much too large loads. Thus, they cannot be used for the precise analysis of potential damages and evaluation of mitigation strategies.

2.3. Thermal detonation models

2.3.1. Board, Hall and Hall model

By making an analogy between chemical detonations and steam explosion, a simple 0D model for one-dimensional steady explosions was firstly proposed by Board and Hall in 1974 (Board et al., 1975). The structure of a thermal interaction propagating stably behind a shock front is illustrated in Figure 22 (from (Board et al., 1975)). Because the steady explosion must satisfy the so-called Chapman-Jouguet (C-J) stability condition (Figure 23, Figure 24), the propagation velocities and pressures may be predicted without a detailed knowledge of the fragmentation and energy transfer processes.

The interest of this model is that it provides a first insight about explosion structure and a very simple and analytical description of explosion propagation, Figure 22:

- Undisturbed region, before shock front:
  - coarse mixture of fuel and coolant (homogeneous mixed);
  - with initial thermodynamic state (P1, V1) (see example pressure-density in Figure 24).
- On passing the front, the mixture will evolve instantaneously and adiabatically along a so called "Hugoniot shock adiabatic" curve in the PV plane.
- Fragmentation/reaction zone, between shock font and C-J plan:
  - the shock induces a differential of fuel and coolant velocities, which causes rapid fragmentation of the fuel;
  - fuel and coolant are in thermal equilibrium (infinite heat transfers) so that the fragmentation zone is equivalent to the reaction zone in chemical detonations;
  - this detailed state in this zone is not modelled, but used to understand the phenomenology.
- At the CJ point, the mixture reaches a second adiabatic curve. Following chemical detonation theory, the tangent of this second adiabatic from the initial point (P1, V1) defines the CJ point:
  - The CJ point has the sonic velocity with respect to the front (inversely, the front propagates at the speed of sound of the mixture at the CJ point).
- Expansion zone (after CJ plan):
  - The mixture has attained full thermal equilibrium at high pressure, and is expanding as the pressure is relieved, thus driving the front forward.
- Stable zone:
  - Region where the velocities have come back to zero.

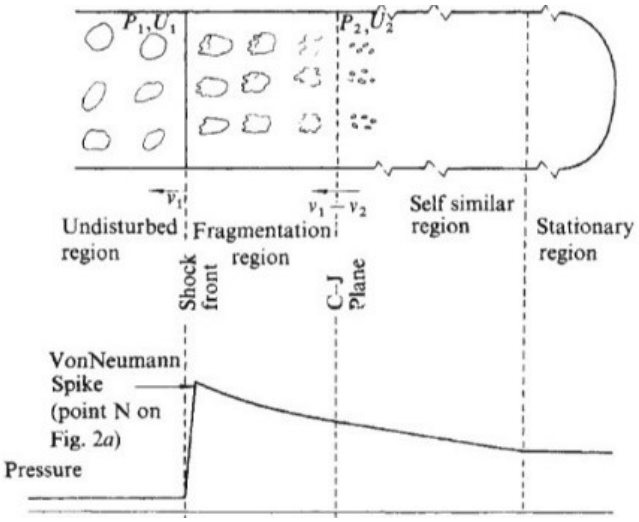

Figure 22: Geometry and schematic pressure profiles of a one- dimensional explosion (from(Board et al., 1975))

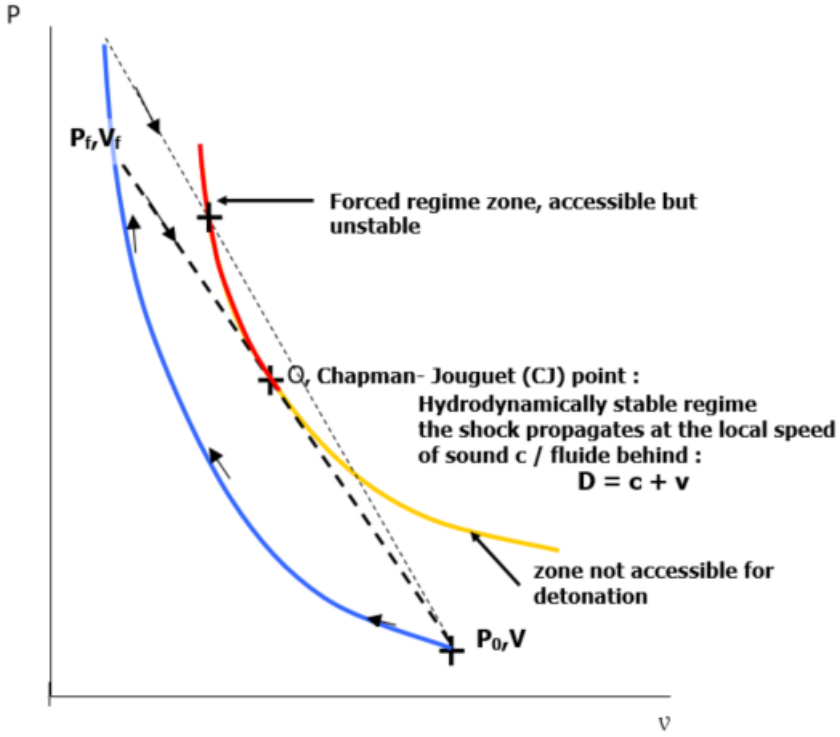

Figure 23: Schematic representation of detonation: on passing the shock, the system will evolve adiabatically (curve blue). After the reaction zone, the system will evolve on a second adiabatic curve (equilibrium Hugoniot adiabatic, red). Only the CJ point is thermodynamically stable

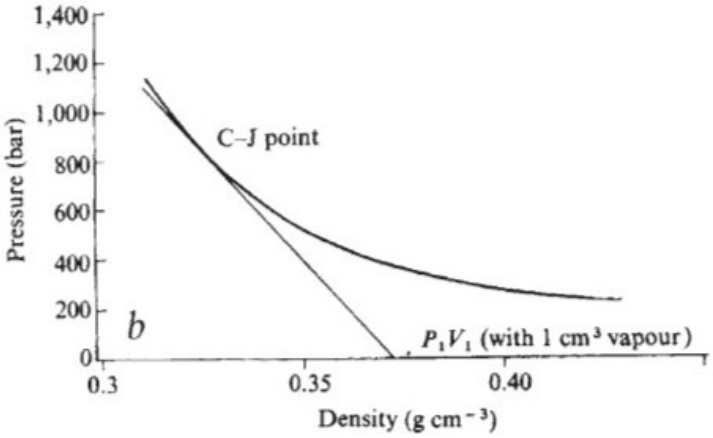

Figure 24: Shock adiabatic for an initial mixture of equal volumes of tin at 1,000°C, water at 100°C and steam (from(Board et al., 1975)).

Compared with the thermodynamic model, the thermal detonation model shares always the same hypothesis that a homogeneous equilibrium state was sustained before and after explosion, and only these two states are numerically modeled in the model. But the thermal detonation model could be regarded as a progress to thermodynamic model and start to capture the phenomenology of explosion by identifying the key role of fragmentation and explaining theoretically how a steady explosion can sustain if it occurs. However, the assumption of homogeneous equilibrium state after shock means that fragmentation and heat transfer should be extremely fast and violent, even instantaneous, to be completed along a very short distance (the reaction zone).

With the further understanding of steam explosion, the kinetics of fragmentation and local disequilibrium between phases were firstly identified as the crucial factor for correct estimation of explosion strength. Therefore, two directions to improve thermal detonation modelling is either to add an additional description of fragmentation kinetic or to relax the assumption of local equilibrium by supposing one or more phases (vapor, liquid, and melt) are no longer in thermal and mechanical equilibrium.

2.3.2. Use and limits of the model

Several variants were built with various improvements. One the most representative work to improve this model was firstly developed by Cho & et al (Cho et al., 1972, 1971) by considering the dynamics of fragmentation which clearly could not be instantaneous.

Scott and Berthoud (Edouard SCOTT,Berthoud G., 1978) built a multiphase 1-dimensional model to describe the reaction zone more precisely. They considered 3 phases: the melt drops, the fragments, and the coolant and included a detailed fragmentation model. However, a basic remaining hypothesis is the thermal equilibrium between the created fragments and the coolant, treated as a single phase.

These models have been used extensively. However, relaxing equilibrium hypotheses led to strong numerical difficulties, as was recognized by Scott himself. One reason is the shape of the Hugoniot curve which is not as "nice" as shown above, when considering more realistic initial conditions(Frost et al., 1991), see e.g., Figure 25. Thus, researchers were facing a simple modelling by its simplifying hypotheses, but complex to build and use.

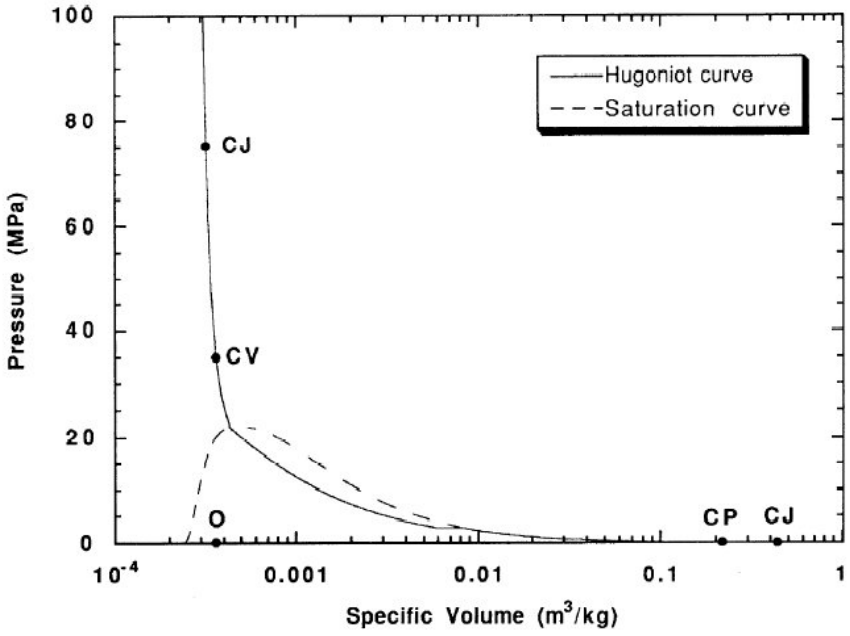

Figure 25: Example of Hugoniot curve as computed by Lee & Ciccarelli for a calculation of a tin/water interaction (Frost et al., 1991)

2.3.3. Extension: the micro-interaction model

One the most representative work to improve this model was proposed by Yuen & Theofanous (Yuen and Theofanous, 1999) by separating non equilibrium/non-participating coolant from the rest of the mixture, treated, still, with a condition of thermodynamic equilibrium. Compared to the Scott & Berthoud model, the fragments are in equilibrium with only a fraction of the water and the vapor, in a single field named "m-fluid".

Applying the Board et al. model (Board et al., 1975), they concluded that pre-mixtures with low fuel fraction can hardly detonate to supercritical pressures. They then concluded that, from the Board et al. model, explosions cannot propagate unless with a rich pre-mixture and unreasonably high fragmentation rates. Based on experiment results (Chen et al., 1999), they supposed that only a part of the liquid is in equilibrium with fragments (shown in Figure 26). By doing so, they obtained more reasonable results (Figure 27). This local thermal equilibrium[2] (only part of water is entrained and in equilibrium with corium) concept was then introduced in their dynamic code ESPROSE and further denominated the "Micro-Interaction model".

We might here emphasis that we must consider separately:

- the process of local micro-interaction, that must be studied and characterized;
- the "MI model" proposed by Theofanous and extended by several authors (e.g. Bürger(Buck and Bürger, 1997)).

[2] In their original paper, Yuen and Theofanous called their improvement 'micro-interaction' model in the meaning that only water in a confined region (part of water) interacts with fuel. No specific model was proposed to evaluate this limited water quantity. In the author's opinion, it is not really a mechanist model but more like an engineering and parametric approach. To make the difference between the Non-equilibrium Micro-Interaction model that we work on, Yuen and Theofanous' model here are called local thermal equilibrium concept.

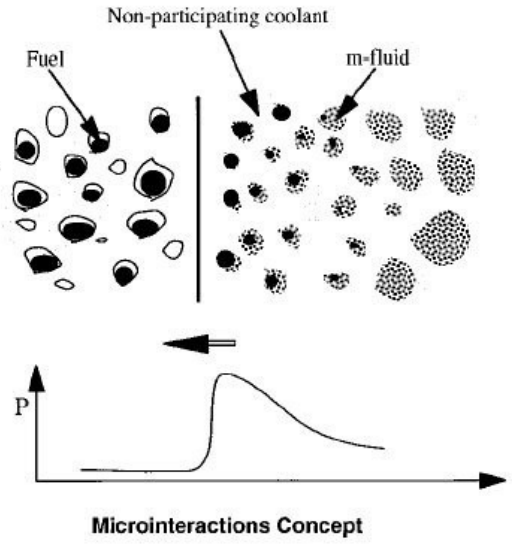

Figure 26: The local thermal equilibrium concept. The 'non-participating' coolant is compressed behind the shock, but it does not react thermally with the fragments.(Yuen and Theofanous, 1999)

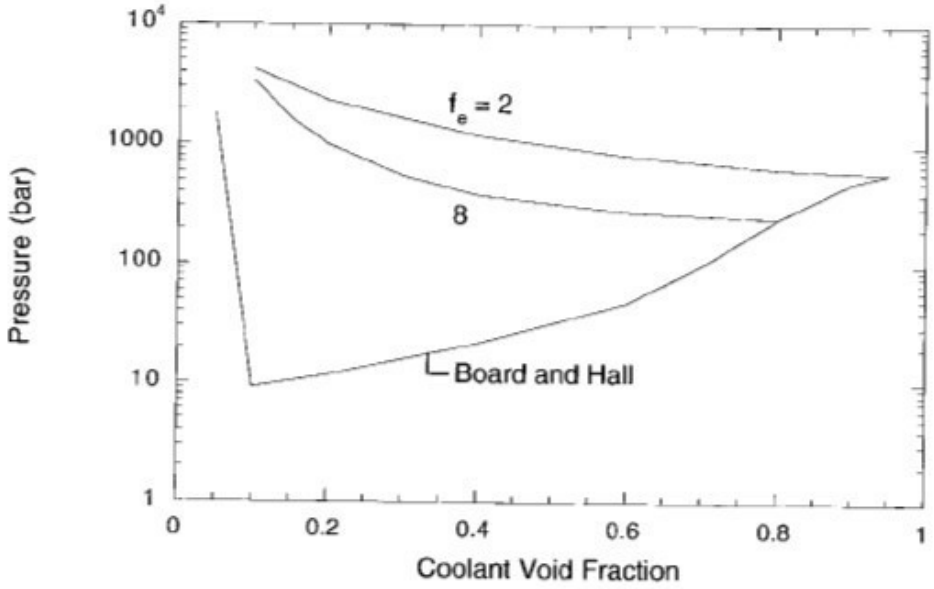

Figure 27: Solutions of the micro-interaction's thermal detonation model, here f_e volume of entrained coolant per unit volume of fuel (Yuen and Theofanous, 1999)

Some similar and generalist work was done by Huang & Kolev (Hulin and Kolev, 2000; Kolev, 2015) and Iskihakov (Iskhakov et al., 2019) considering more disequilibrium between phases by separating non-entrained steam, non-entrained water and non-entrained corium from the homogenous mixture.

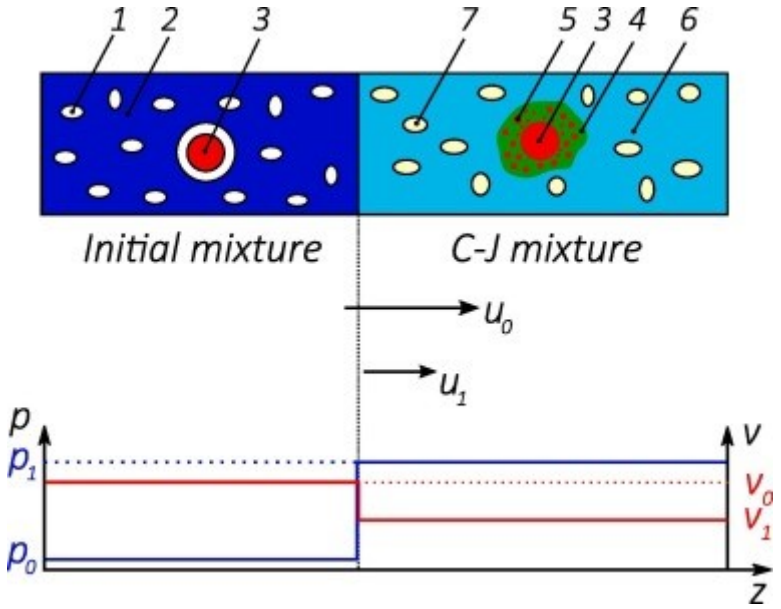

Figure 28: Multiphase thermal detonations model. Initial mixture: 1 – steam, 2 –water, 3 – melt droplet. C-J mixture: 4 – entrained coolant (water and steam), 5 - melt fragment, 6 – non-entrained water, 7 – non-entrained steam. (Iskhakov et al., 2019)

2.3.4. Conclusion for thermal detonation model

These models are important for understanding the basic features of the explosion phenomena and the biggest advantage of this kind of analysis is that it can predict propagation velocities and characteristic pressures without a detailed knowledge of the fragmentation and energy transfer processes. On the other hand, despite quite crude approximations, they become rapidly very complex to develop and use, thus with a clear limit for improvements.

To go further for more precise evaluations, the details of fragmentation processes and heat transfer play a vital role and must be better described.

Also, the initial conditions of the explosion needed to be defined with some precision, at least the amount of melt and vapor in the mixture. Such issue seemed out of reach with simple models, although simplified 1-D models can be built, in general for specific purposes (e.g. THIRMAL (Wang et al., 1989) and COSTA (Meignen, 1995) models).

To better catch the implications of more detailed modelling, researchers started in the 90's to develop multidimensional thermal-hydraulics models, although the physics of fragmentation and heat transfer was far from being fully understood. Indeed, 30 years later, there are still room for improvements, particularly concerning the boiling characteristics and the impact of solidification.

2.4. Multi-dimensional thermal-hydraulic models

2.4.1. A general status at the time of the OECD SERENA program

Various models have been built but many of them have also been abandoned more or less rapidly. The OECD program SERENA (2000-2005) aimed at establishing a state of the art of understanding and capabilities of the computed codes. The programmed involved 13 organizations, see Table 2

Organisation	Code
FZK	MATTINA
IKE	IKEMIX (premix) MC3D 3.2 (task 2 only) IDEMO (explo)
IRSN-CEA	MC3D 3.3.06 (task 2 and 4) MC3D 3.4.02 (task 3)
JAERI	JASMINE-PRE 2.1 (task 2) JASMINE 3.x (task 3 & 4)
KAERI	TEXAS-V
KMU	TRACER-II
NUPEC	VESUVIUS
KINS	IFCI 6.0
UCSB	PM-ALPHA.L.3D (premix) ESPROSE (explo)
UW	TEXAS-V

Table 2: Organizations and codes used in the OECD program SERENA (Meignen, 2005)

The major characteristics and differences were established in a specific document, and summarized in (Meignen, 2005).Note that the VAPEX code was also analyzed although the developing organization EREC (Russia) did not finally participated to the program. Note also that some codes are dedicated to a phase of the FCI so that, in such a case, users are using pairs of codes: IKEMIX/IDEMO for IKE (U. Stuttgart, Germany), PM-ALPHA/ESPROME for UCSB (Santa Barbara, USA). MATTINA is a code based on the SIMMER-III description without specific explosion model. It may be noticed that, although several publications exist on the FCI calculations with SIMMER-III (Cheng et al., 2015; Morita et al., 1999; Tobita et al., 2006), the code did not participate in any international code comparing and benchmarking on FCI.

Regarding the premixing modelling, different approaches can be highlighted regarding the description of the melt:

- existence of a specific numerical field to describe the fragmented melt jet: MC3D (Picchi, 2017), IKEMIX (Bürger, 2006; Pohlner et al., 2006), JASMINE (Moriyama et al., 2008);
    - among these codes, only MC3D uses a real field for the fragmented melt: for the others, the jet is in fact described by an external model and is mainly used to "generate" (input) melt drops in the mixture; the MC3D description is then much more flexible;
- melt only described with a discrete fuel drop description: PM-ALPHA, TEXAS-V, VESUVIUS, VAPEX;
- Mixed description continuous/discrete: IFCI, MATTINA.

Figure 29 shows a conceptual picture, from (Meignen, 2005), highlighting the differences in description and the potential large impact regarding fragmentation. The "JET" description generally involves a Kelvin-Helmholtz based model (the fragmentation is induced by the tangential shear) while models in other codes were related to single drop fragmentation models, often based on Rayleigh-Taylor mechanisms (acceleration induced fragmentation).

An interesting feature is that a small half of codes used a Eulerian description for the melt drops: MC3D, IFCI, MATTINA, TRACER, whereas the majority involved a Lagrangian description: TEXAS, PM-ALPHA, VAPEX, IKEMIX and JASMINE.

Apart from TEXAS (one-dimensional), most of these codes are two-dimensional, whereas MC3D and PM-ALPHA can perform calculation in three-dimension. The program clearly highlighted the limitation of TEXAS and its one-dimensional description. Only PM-ALPHA provided 3d calculations.

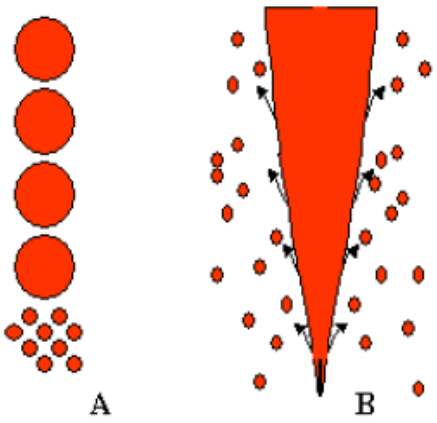

Figure 29: Conceptual picture depicting the two different jet break-up mechanisms: A : leading-edge break-up, B: continuous jet column fragmentation (Meignen, 2005)

Regarding the explosion codes, the model can be divided in two groups:

- the "Micro-Interaction" codes: ESPROSE, VAPEX, IDEMO;
- The "Non-Equilibrium" codes: MC3D, IFCI, JASMINE, TEXAS, TRACER, VESUVIUS.

The pressurization during the explosion is, with no doubt, due to the rapid heat up and phase change of the coolant. However, the detailed process of pressurization, i.e., the way the heat is transferred from fragments to the coolant, and the boiling processes itself is problematic issue for FCI modelling. If the role of fragmentation dynamics appeared quite rapidly, the local processes of heat and coolant mass transfers (and thus pressurization) have long been considered as "a mystery" , expression used by Corradini, in 1993 (Corradini and Hohmann, 1993).

Currently, there are two very different approaches of modelling that will be named here as Equilibrium Micro-interaction (MI) and Non-Equilibrium approaches (Berthoud, 2000b) (Meignen et al., 2012), (Meignen, 2005) sketched in Figure 30, and discussed in the following sections.

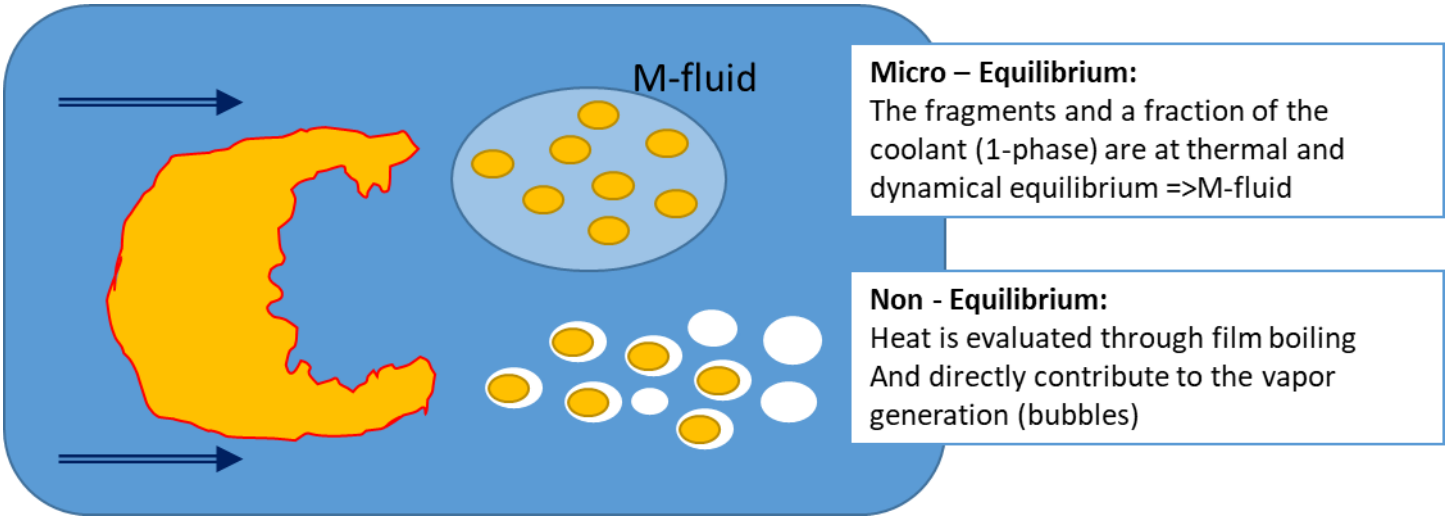

Figure 30: Equilibrium Micro-Interaction and Non-equilibrium approaches

A comparison of the behaviors of MC3D and IDEMO under simplified 1D initial and boundary conditions was undertaken by IRSN and IKE in the frame of the SARNET project and summarized in (Meignen, 2005).

2.4.2. The Micro-Interaction models

The original "Micro-Interaction" model already discussed above has then been translated to multidimensional codes, starting with ESPROSE, rapidly followed by IDEMO. At the time of SERENA program, the VAPEX modelling was very close to ESPROSE. For the present purpose, we may be more precise in the determination of the name of the model, calling it "Equilibrium Micro-Interaction". Indeed, it is based on the idea that only a part of the coolant participates in the interaction through the establishment of a very local melt-water-gas "mixture". This mixture, called m-fluid, is thermally homogenous (ESPROSE) or quasi-homogenous (IDEMO). Thus, basically, these models are merely extension of the thermal detonation model in a 2 or 3-dimensional description.

Originally (ESPROSE, (Chen et al., 1999, 1997).), the fragments are supposed to be quenched instantaneously and in thermal and hydrodynamic equilibrium with vapor and a given amount of the cold fluid. The heat transfer rate is then given by the fragmentation dynamics and the entrainment rate of cold water into the mixture. The entrained coolant and the gas are then considered as a single homogenous fluid. The pressurization is due to dilatation or vaporization of the entrained coolant in the mixture.

The IDEMO model has similar bases of modelling. However, a small thermal disequilibrium was introduced in a parametric way. Indeed, the imposed heat transfer coefficient of 5.10^5 W/m^2/K, with small fragments of imposed diameter of 50 µm leads to a very strong heat transfer, much higher (about 10 times) than it was measured in the TREPAM experiments (Berthoud and D'Aillon, 2009). So, in fact, a quasi-equilibrium occurs. Another difference is that the m-fluid transfers its heat to the surrounding, the not participating coolant (which is totally isolated in the original concept in ESPROSE). The impact of this difference is difficult to characterize as the details of the modelling have not been explained in open literature.

The characteristic behavior of an IDEMO is given in Figure 31 for a 1D calculation with initial conditions (1 % of corium melt, 30 % of void). The steady state[3] is reached after about 1 m and is characterized by the presence of four distinct pressure levels.

- the pressure peak: very sharp, around 40 MPa;
- a change of slope of the decreasing pressure (with small oscillations) at about 28 MPa;
- a very flat plateau at about 22 MPa: this is in fact the critical pressure of water;
- a final steady pressure, here at about 10 MPa.

The origin and reason of the plateau at the critical pressure have been discussed but could not be explained. In addition, it is found that its length is increasing, so that that pressure is not actually steady. This could be due to a numerical trick.

A case with a high void (70 %) is shown in Figure 32. Here also, the behavior is rather "strange", with an initial escalation and increase of the shock with a maximum and then a continuous decrease. This behavior could not be explained.

It may be emphasized that these behaviors are not observed from the validation calculations against experimental results which, in general, do not provide sufficient information for the analysis of the model behavior.

[3] The impression that the behavior is not exactly steady in Figure 31 comes from the space discretization and the fact that the sampling in time is not coincident with the traveling of the wave.

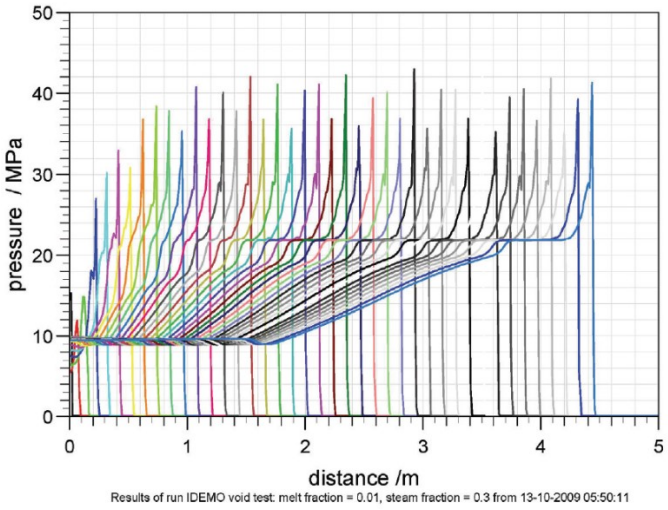

Figure 31: Typical behavior of IDEMO of a 1-D explosion development and propagation with initial conditions as given in the figure (Meignen et al., 2012)

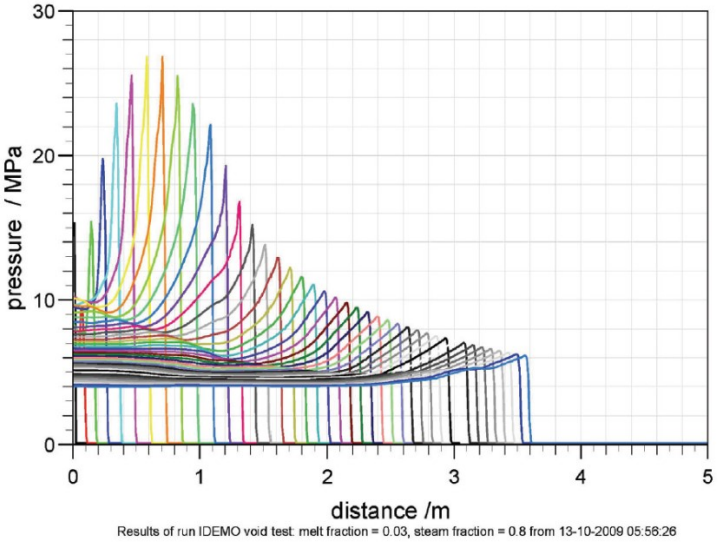

Figure 32: Behavior of IDEMO at high void. When the void is larger than 0.7, the pressure starts to increase along one or more meters and then decreases. No steady state is reached by the code. No explanation could be given about this behavior (Meignen et al., 2012).

2.4.3. Non-equilibrium modelling

Despite a lack of knowledge on the heat and mass transfer processes, several codes, in particular MC3D-EXPLO, have chosen to introduce a detailed modelling. The fragments are quenched with a finite heat transfer rate evaluated by specific laws. In fact, the non-equilibrium modelling can be interpreted in most cases as being quite similar to the MI model with the differences that the entrainment rate of water in the m-fluid (MI model) is related to the amount of vaporized water per amount of fragmented melt.

It may be highlighted that, up to a recent version, the MC3D model hypothesized a "transient" heat transfer process, which would originate from direct contact between water and the melt at the collapse of the vapor film No model was provided, and a constant heat transfer coefficient was adopted (5.10^4 W/m²/K). It is noticed that this value is 10 times smaller than the one used in the IDEMO model. However, quite recently, the TREPAM experiments conducted by CEA (financed by IPSN) (Berthoud and D'Aillon, 2009) tended to indicate that this transient situation does not hold and, finally, film boiling always occurs. It happens also that typical values for the film boiling heat transfer coefficient is of the order of the chosen value for the constant "transient" heat

transfer, so that this improvement in modelling (and understanding) did not yield finally important changes in the results.

Recent numerical simulations of heat transfers between corium drops and water with MC3D-MESO(Zambaux, 2016), a dedicated application built during the RSNR-ICE project (2014-2018), confirmed the presence of a vapor film-like behavior, i.e., sharp density variations at a pseudo interface delimitating the pseudo-film, even for very largely supercritical pressures (e.g., Figure 33), thus validating the general principle of MC3D. The simulations also indicated that the film was always evolving in a quasi-steady state even under sharp pressure variations. Also, the volume occupied by the film appears to be sufficient to produce the requested pressurization, at least when the water is saturated, which might be locally the case around the drops. The large melt temperature and, probably, the small scale of the fragments, tend to reduce the impact of instabilities of the vapor film.

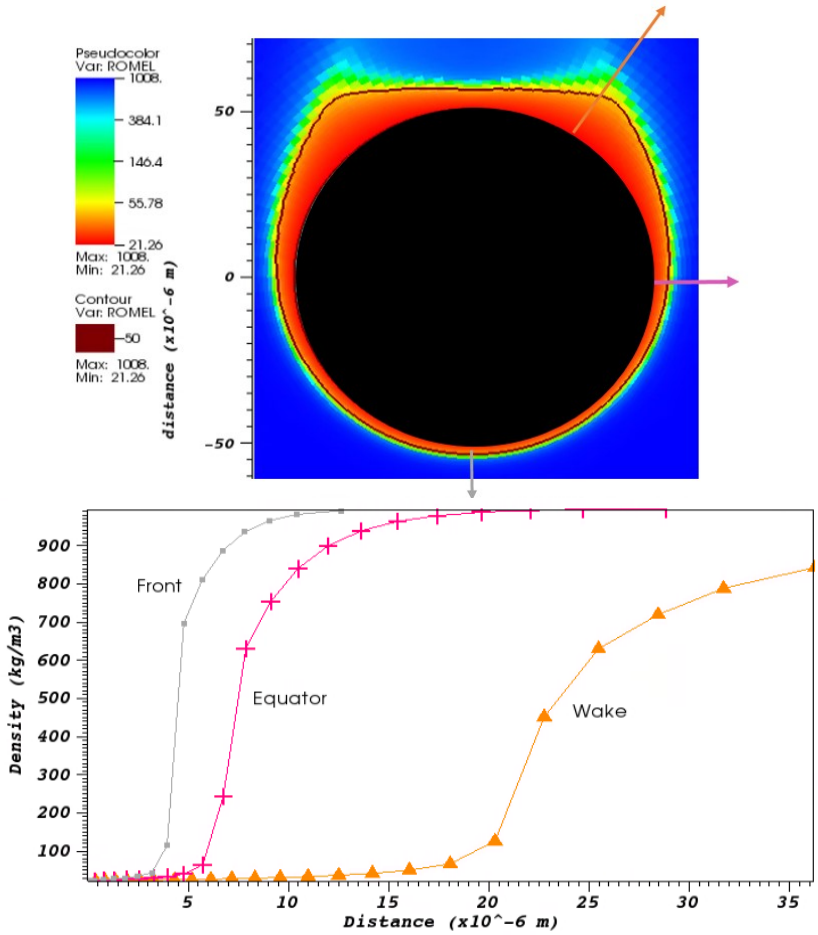

Figure 33: Simulation using the MESO application showing the development of the gas film around a small cylinder (2D simulation, P=24 MPa, d=100 µm, T_l=293 K, T_c=2500 K). Top graph: density map. Bottom graph: evolution of the density along the angles indicated by the arrows.

This heat from the fragments is supposed to directly contribute to vapor generation and vaporization is deduced by a heat flux balance at the coolant interface (Figure 34):

$$\Gamma_{lv}^{f} = \frac{\Phi_{flim} + \Phi_{ra,fi} - \Phi_{cv,fl}}{h_v - h_l}$$

Φ_{flim} is the film boiling heat flux leaving the fragment and arriving to the film interface, which is expected to have the same interfacial area as the fragment. $-\Phi_{cv,fl}$ is the convection heat flux in the liquid part. A first difficulty is to express properly this heat flux, particularly in the very transient situation of explosion. MC3D uses a standard convection correlation, and it appears that in general $\Phi_{flim} \gg \Phi_{cv,fl}$ so that the heat is essentially transformed into vapor. The radiation effect is accounted in $\Phi_{ra,fi}$, which is the fraction of radiation directly

absorbed at the interface and producing vapor. Evaluating this fraction is not an easy task, but this is not really problematic as it can be shown that, for small particles, even for the very high considered melt temperatures, the radiation heat flux is always much smaller than film boiling.

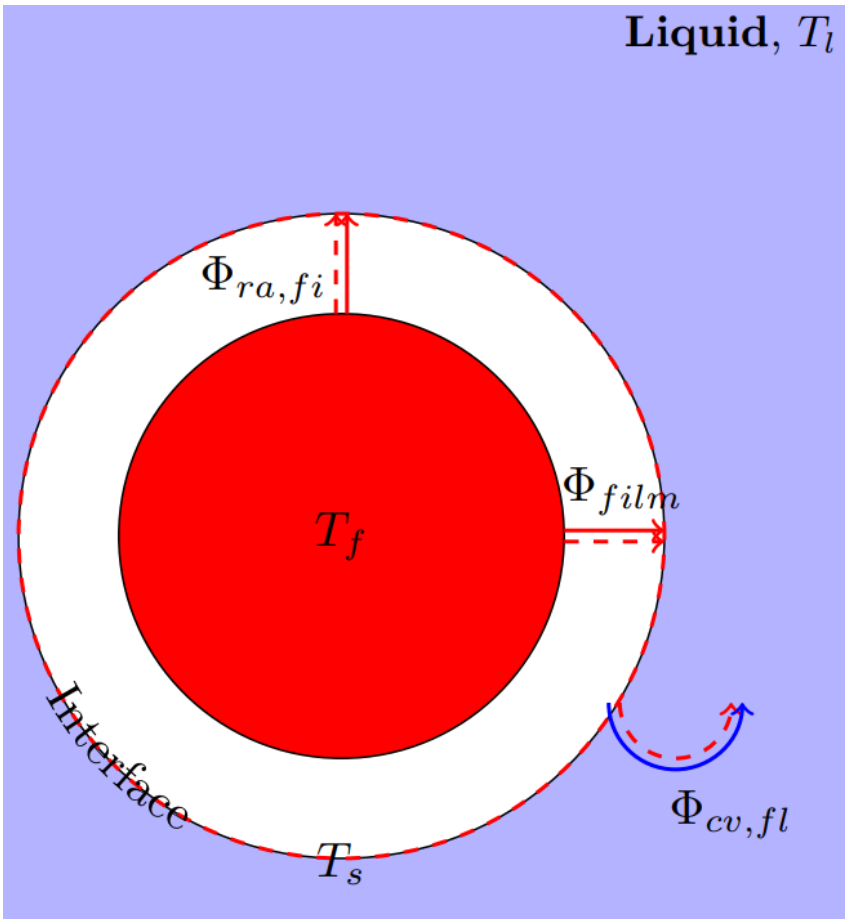

Figure 34: Sketch of heat transfers around fragments (and drops) in MC3D.

$h_v - h_l$ in the previous expression is the effective latent heat associated to the vaporization.

One can notice that measurements and models are available for the film boiling heat transfer: however, it concerns the heat leaving the fragment, whereas the balance needs the heat going to the ambient water from the interface ($\Phi_{cv,fl}$). In the current modelling, the convection term appears to be small and most of the film itself is not explicitly expressed and is accounted for though the use for h_v of the enthalpy at the mean film temperature. For stability reasons, the liquid enthalpy is expressed at the bulk liquid temperature.

In the MC3D-EXPLO model, the vapor generated around the fragment is expected to produce bubbles, which may in turn condense, so the global vaporization (and pressurization) is related to the balance between both effects. So, the behavior of the generated bubble is a crucial point.

The Figure 35 shows the typical behavior of MC3D (version 3.7, from (Meignen et al., 2012)), to be compared with Figure 31. Note the different representation compared to Figure 31 since the results are here pressure histories at different levels whereas IDEMO output is a pressure profile at different time; Both can be easily compared, however.

A first significant difference is the much longer time (distance) needed to obtain a steady state, never reached in this calculation. This may be due to the finite time scale of heat transfer from the created fragments.

A second difference is the behavior with no identified pressure plateau. The bottom pressure is slowly decreasing but this is due to the fact that the steady state is not reached. If no steady state is reached, it is however noticed the regularity of the pressure pulse with a width almost constant.

Overall, the behavior is quite similar to the one sketched by Board et al. in Figure 22. The peak is rather rounded, but this is due to a numerical dissipative treatment (artificial viscosity). There is first slow pressure decrease up to a point which might be interpreted as the Chapman-Jouguet point, from which the pressure decreases more rapidly.

When the void is large, the behavior shown by IDEMO, with a first increase and then decrease of pressure, does not appear in present MC3D computation where there is a continuous pressure decrease. This behavior seems then much more stable and less subject to ambiguity.

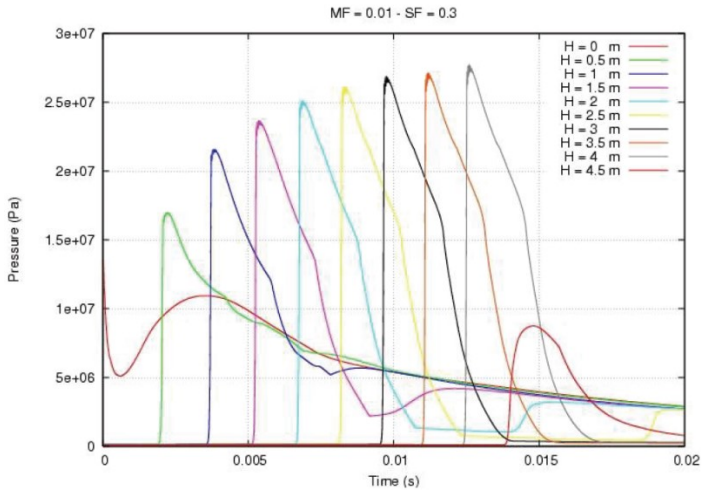

Figure 35: Typical behavior of MC3D (V3.7) of a 1-D explosion development and propagation with initial conditions as given in Figure 31 (Meignen et al., 2012).

This exercise of studying the behavior in 1D conditions has been undertaken again and extended in the present frame of work (version 3.10) and the results are summarized chapter 3.

Concluding, the non-equilibrium approach must face several important difficulties:

- evaluating the melt area production during the fragmentation;
- figuring the amount of heat used for the vapor production;
- behavior of the vapor produced and further condensation if any.

All this is intricated because it depends on the local flow configuration, and this is the reason for the choice of the simpler representation of the MI models. Even several numerical models are available in CFD code trying to capture the vaporization, the details of the local mechanical and thermal interactions are not well understood and need to be investigated in general, at least numerically due to the experimental difficulties encountered in this area of research. The research axis 1 and 3 of the French RSNR-ICE project (2014-2019) proposed the use of numerical simulations for both, but separately, the fragmentation and the heat and mass transfer. The results are discussed with more details later.

It is clear that a "coupled" approach taking into account the transient aspect of every phenomenon is necessary, but, up to now, neither experiments nor numerical work could provide valuable precise information.

2.4.4. On the fragmentation processes

The fine/secondary fragmentation of a hot molten liquid drop in another liquid coolant may occur by two different processes (Meignen, 2005):

- the “thermal” fragmentation;

- the hydrodynamic fragmentation.

2.4.4.1. Thermal fragmentation

Thermal fragmentation is a very specific phenomenon where a drop of melt can undergo a very fine fragmentation under the effect of a small perturbation (see e.g.(Nelson and Duda, 1985)). The process occurs in a cyclic manner and is due to the instability of the vapor film covering the drops. Under some process not yet fully clarified, water and melt can be in close quasi-contact (a real contact being thermodynamically impossible) which yields local pressurizations that will destabilize the drop itself. Figure 36 provides a typical example of thermal explosion, from the pioneering studies of Nelson & Duda (Nelson and Duda, 1985). The figure shows the result submitting a liquid drop of iron oxide to small pressure perturbation, from 1 to 10 bars. In such conditions, the Weber number is small so that the drop should be stable by hydrodynamic fragmentation. Nevertheless, it is observed that the drop undergoes a spectacular complete explosion in very fine debris. The explosion occurs in fact through 2 to 3 cycles of compression-expansion of the vapor film and the « bubble » generated by the fragmentation.

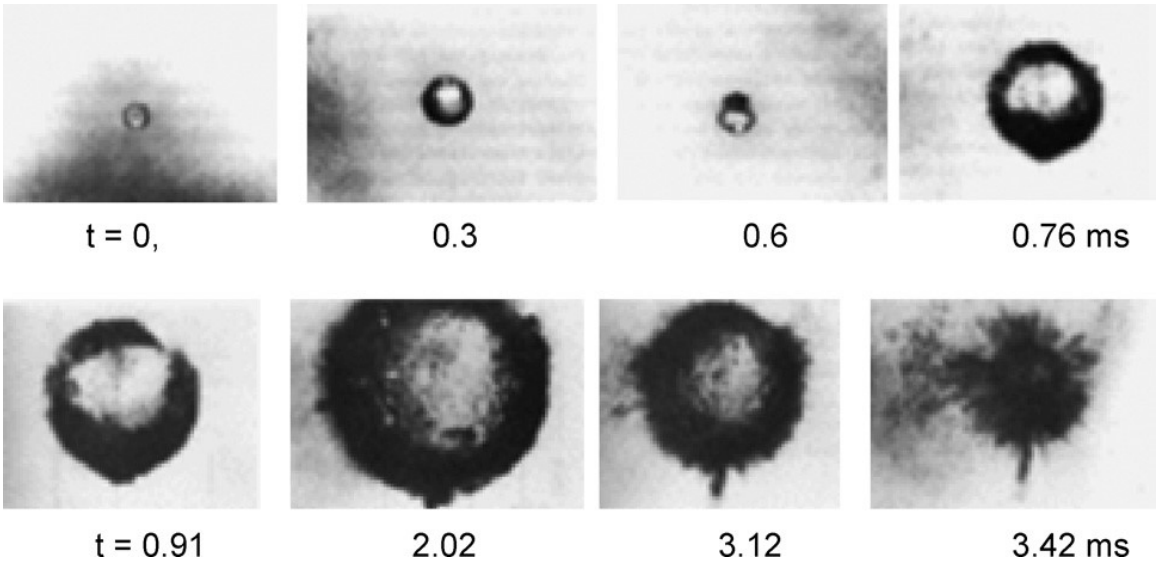

Figure 36: Example of evolution of a drop explosion by thermal fragmentation process, from(Nelson and Duda, 1985)

This phenomenon is expected to induce, in some specific situations, a triggering of more massive explosion. It has continued to receive some attention, in particular at KTH who recently demonstrated the particular ability of alumina to self-trigger an explosion by this mean (Zambaux et al., 2018).

2.4.4.2. Hydrodynamic fragmentation

Hydrodynamic fragmentation is a classical process due to the shear between the drop and ambient fluid (Figure 37).

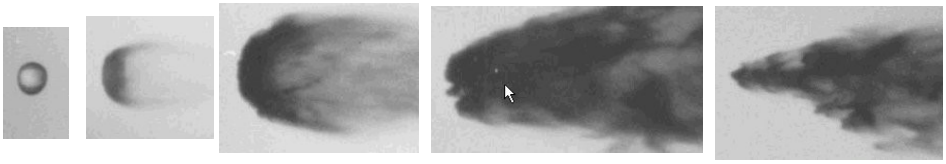

Figure 37: Hydrodynamic fragmentation of a water drop submitted to a Mach-2 shock wave (in air) (Joseph et al., 1999)

It is believed that thermal fragmentation can have an impact only at the beginning of the process and, very rapidly, the hydrodynamic process is overwhelming. It is not included in current version of MC3D and the fine hydrodynamic fragmentation is supposed to be the dominant process.

The fragmentation rate is deduced from the characteristic fragmentation time (Ranger & Nicholls (Ranger and Nicholls, 1972)):

$$\tau_{RN} = \frac{D_d}{\Delta V_{dc}} \cdot \sqrt{\frac{\rho_d}{\rho_c}}$$

At first order, a fragmentation rate can then be deduced considering that fragmentation occurs regularly in time, during a given number of characteristic dimensionless times $t_f^* = t_f/\tau_{RN}$:

$$\Gamma_f = -\frac{d\alpha_d}{dt} \approx \frac{\alpha_d}{t_f} = \frac{1}{t_f^*} \cdot \frac{\alpha_d \Delta V_{dc}}{D_d} \cdot \sqrt{\rho_d \rho_c} \equiv C_f \cdot \frac{\alpha_d \Delta V_{dc}}{D_d} \cdot \sqrt{\rho_d \rho_c}$$

t_f^* is the dimensional time for fragmentation, of the order of unity (the recommended value in EXPLO is 0.5). ($t_f^* = 1$ from (Carachalios et al., 1983)). There is a significant uncertainty on the fragmentation time due to qualitative determination in the experiments of when the fragmentation is effectively complete. In the following, the default MC3D uses $t_f^* = 1$. At that point, it must be recognized that the above fragmentation law is a rough approximation of the reality so that the modeling cannot capture the local details of the interaction. Any improvement should introduce a time dependence, needing thus the introduction of supplementary information, e.g., deformation.

Fragmentation in gas (L/G configuration) is the subject of numerous experimental investigations with increasing visualization capabilities and numerical works with an abundant literature. In the frame of steam explosion, we are however firstly interested in the fragmentation of drops in a liquid coolant (L/L), since, as discussed above, the initial void almost disappears for the most interesting cases. A more elaborate bibliographic review is proposed in chapter 4, but we can anticipate here that the knowledge is much less advanced in this situation. Experimentations can hardly provide details of the local mechanisms since optical methods are much less efficient.

However, the fragmentation characteristics can now be analyzed thanks to Direct Numerical Simulations, although only simplified situations without boiling nor solidification could be handled up to now.

Among the various results obtained, it appeared that fragmentation in water does not behave as in gas (see Figure 37 for a typical example at high Weber number). Recent analysis will be found in (Escobar, 2016) and new simulations using the Basilisk software are presented in chapter 4. Let us anticipates that it appears that fragmentation in water does not behave as in gas. In the latter case, the fragments are swept away from the parent drop, entrained by the carrier phase (Figure 37). In liquid environment, fragmentation and entrainment occur with similar time scales, with a weak dispersion of the fragments which seem to be "trapped" in the wake during the fragmentation. These simulations tend then to confirm somehow the assumption of a localized melt-water interaction, i.e., the micro-interaction hypothesized by Theofanous and co-workers (Chen et al., 1997). This is contrasting with what presupposes the current modelling of MC3D, where fragments are supposed to be swept away. The energy transfer processes between the fragments and their immediate surrounding environment are therefore probably affected.

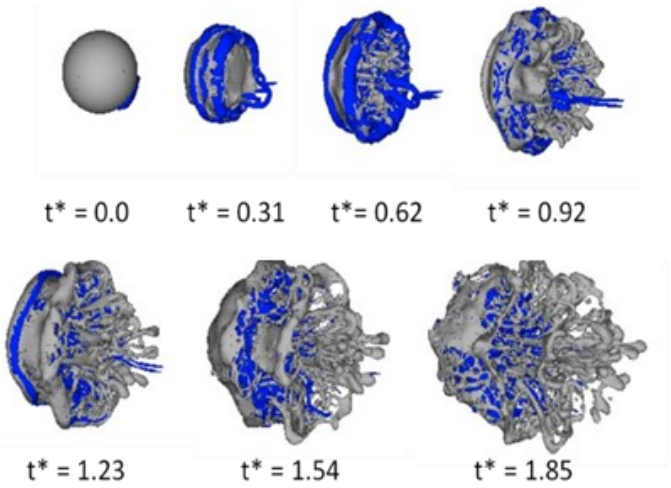

Figure 38: Simulation of liquid-liquid fragmentation using the GERRIS code (Popinet, 2003) at We=533.61: insight of "Micro-Interaction zone"(Escobar, 2016). The blue part is a visualization of the vortex

The DNS is able to reveal the details of the process at large Weber number, as shown in Figure 39. As the Weber number is increased to values characteristic of SE, the small-scale instabilities at the interface progressively take the lead and the fragmentation is initiated at the surface, close to the equator, before being trapped in the vortices behind the drop.

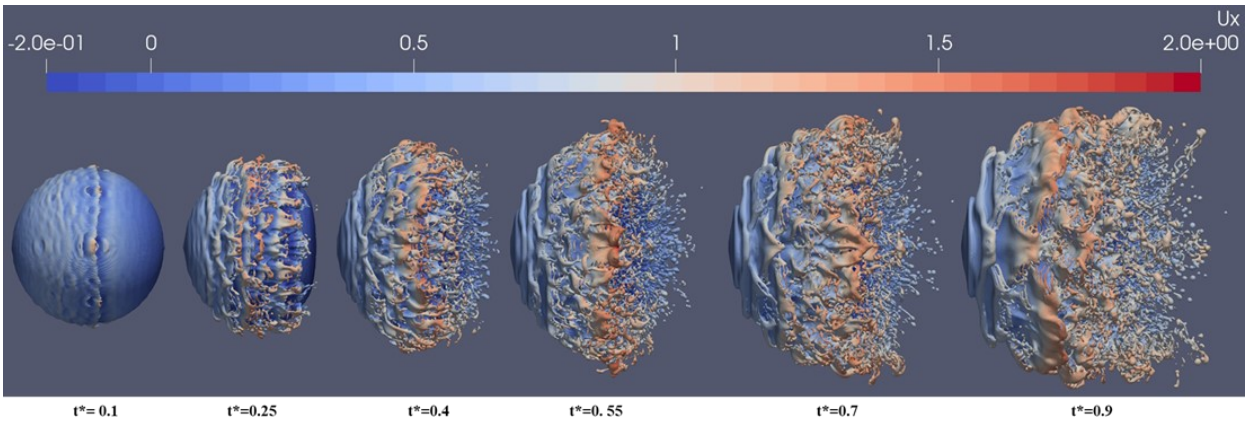

Figure 39: Simulation of liquid-liquid fragmentation using the Basilisk code at We=1280. The surface color is related to dimensionless velocity in the flow direction (see chapter 4 for more information).

Most of the SE models do not compute the size of the resulting fragments (not needed in the original MI model). For the models where a diameter is needed, as in MC3D, a constant size is generally considered, between 50 and 100 µm. Indeed, inspection of all KROTOS results indicates that, whatever the composition, (U-Zr)O_2 or Al_2O_3, the Mean Sauter Diameter of the fragments is always in the range 75-100 µm. This is difficult to understand. This analysis described later in chapter 4, indicates that this may be due to the solidification at the front of the parent drop.

In the MC3D's simplest model, the size of the fragments is a constant, 75 µm, adjustable by the user. Of course, the size should change according to the actual conditions. If the validation generally done in a global way, thus integrating heat and mass transfers, it is however desirable to go to a modelling as precise as possible and necessary. This is why, an additional model with a prediction of the fragment size based on a Weber criterion is available in MC3D code:

$$D_f = We_{ch}\frac{\sigma}{\rho_{fluid}\Delta V_{dc}^2}$$

- subscript c is for the ambient coolant phase (liquid or gas);

- $\Delta V_{dc}$is the difference of velocity between the drops and the ambient coolant phase, expected to be representative of the fragment-coolant velocity slip;
- We_{ch} is called the "characteristic" Weber number of fragmentation: it is the Weber number that each fragment has at its creation, considering that it has the same velocity as its parent drop. This Weber number should theoretically be smaller than the critical Weber number, and its value is about 3 in liquid/gas situation. However, this model hides the details of fragment creation, in particular the entrainment of the fragmenting melt with water, which is clearly seen in Figure 39.

This formulation can be easily related also to the Kelvin-Helmholtz model, which may imply that the fragmentation originates from tangential instabilities at the surface of the drop. In fact, for low Weber numbers, Rayleigh-Taylor instabilities may play a role, but the impact is minor for explosion situations. The model needs then two parameters (We_{ch} and $C_{frag} = 1/t_f^*$) **which are adjusted by fitting against fragmentation data** in liquid/liquid configuration. Only data in non-boiling conditions are available and we include for the analyses experimental data by Kim et al. (1983) and Achour (2021), and numerical works from Castrillon Escobar (2016), and new simulations discussed later.

The notion of fragmentation time is in fact very uncertain, since no precise definition can be used for experimental data. It should then be considered only as indication. Figure 40 shows the results for $We_{ch} = 30$ and $C_{frag} = 1$. Note at first that results from the DNS analyses are consistent with those from the experimental data. Overall, a noticeable scatter is obtained for both the experiments and simulations. However, the couple of parameters could also be adjusted with $We_{ch} = 20$ and $C_{frag} = 0.5$ with very similar results. In fact, this parameter setting is the one used in the MC3D validation report.

It is remarked that the characteristic Weber number We_{ch} is set to 30, much larger than the critical stability Weber number (12). This can be explained by the different speed of instabilities and entrainment of fragments compared to the drop (so that $\Delta U_{fc} < \Delta U_{dc}$, see Figure 39). We can admit that this choice cannot provide a good agreement for the low Weber numbers, which are however not the in the scope of the present work. A non-constant value according to the We experienced by the melt drop may be sought.

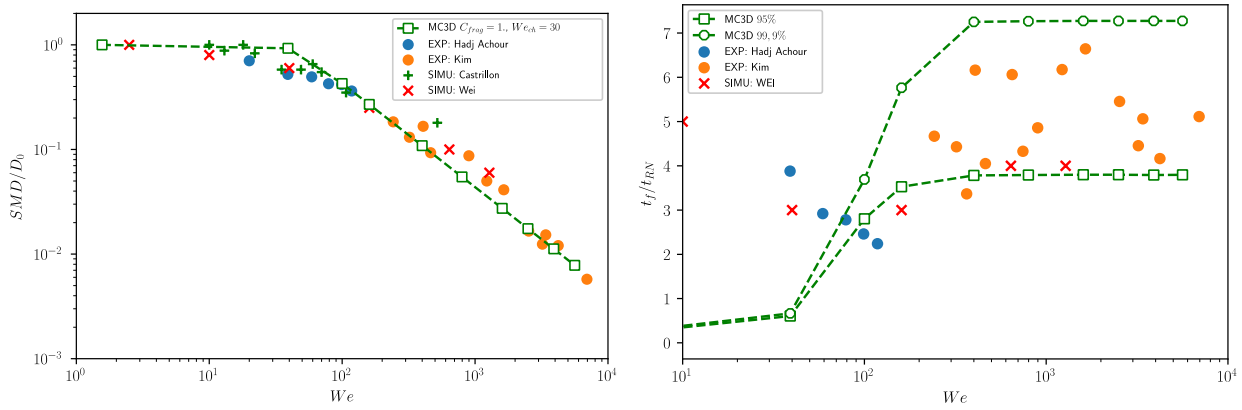

Figure 40: Sauter Mean Diameter (left) and fragmentation time (right): verification of MC3D-EXPLO drop fragmentation model in cold liquid/liquid configuration against available experimental data, from (Kim et al., 1983)(Kim et al., 1983) and (Achour, 2021)(Hadj-Achour et al., 2021), and numerical works from (Castrillon Escobar 2016)(Escobar, 2016), and new simulations. Results for the MC3D model of the fragmentation time is given with two criteria of the fragmentation grade.

2.4.4.3. Fragmentation of an impulsively accelerated hot liquid drop

The question is now to determine the impact of thermal effects on the fragmentation of impulsively accelerated hot liquid drops.

The theoretical work of Lamome (Lamome and Meignen, 2008) considered that thermal fragmentation was due to localized contacts, or quasi-contacts, of the water and the melt and the possibility of these contacts depends on the thermodynamical conditions and on the perturbation. By instability analysis, this work indicated that pressure perturbations beyond 15 bars would favor the hydrodynamic fragmentation in terms of time scale.

Burger et al. (Bürger et al., 1996) performed various series of experiments in an installation called DROPS at IKE. This installation was later modified at CEA-Grenoble by De Malmazet (De Malmazet, 2009) and sketched in Figure 41. In these experiments, the flow of water is horizontal and is obtained from a piston. The test section is terminated by a shutter to prevent reflection of the wave. However, the piston produces only a moderate pressure rise. In the experiments from De Malmazet, the pressure rise is at maximum about 2.5 bars, for a velocity jump of about 15 m/s, i.e., Weber numbers of the order of 2000. This will lead to a very moderate compression of the vapor film and thus it is not representative of the actual situation during a steam explosion. In addition to tests realized with cold gallium, discussed in chapter 4, IKE conducted experiments with hot gallium, at about 550 °C and tin, at about 1000 °C. Fragment sizes are not reported in the available literature. Bürger focused on the fragmentation time, but this was measured in fact as function of the projected area of the "cloud" produced by fragmentation (fragments and void, see fig.40 of (Bürger et al., 1996)). The experiments with hot gallium seem to show a transition to hydrodynamic fragmentation characteristics beyond We ~300. The case with tin is less clear, but the projected area variations are also linked with the hydrodynamic fragmentation time for Weber numbers beyond 300.

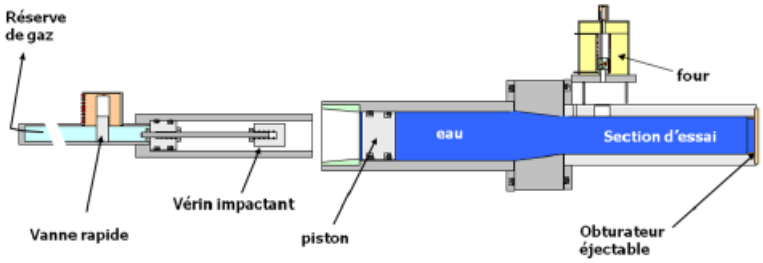

Figure 41: Schematic representation of the DROPSG installation, reproduced from (De Malmazet, 2009)

De Malmazet also studied the fragmentation of hot liquid tin drops, with improved visualization tools and could observe, in the situations of slowly increasing water velocity, the typical behavior of localized thermal fragmentation in addition to the hydrodynamic effect (Figure 42).

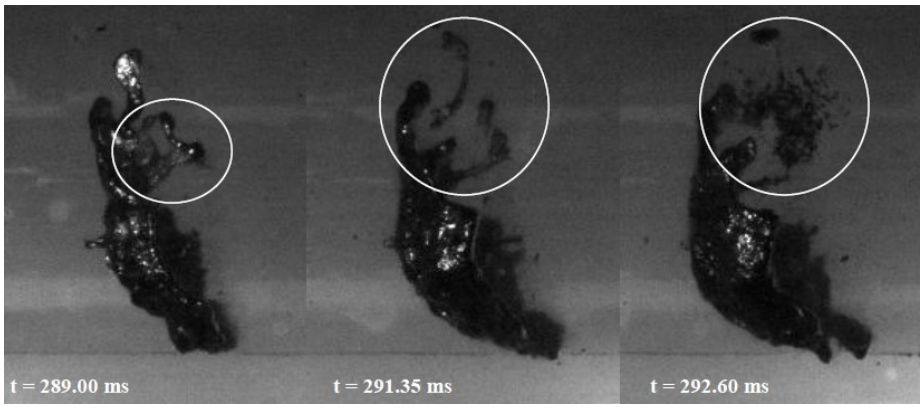

Figure 42: Evidence of local thermal fragmentation effects in a DROPSG test with slow velocity increase

A typical situation for tests with a faster velocity jump is shown in Figure 43. The fragmentation seems much closer to a hydrodynamic process than a thermal one.

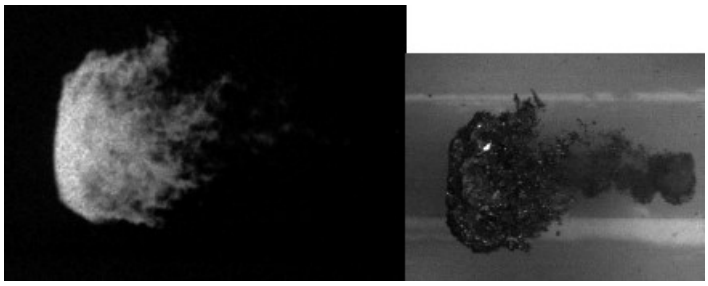

Figure 43: X-ray image and optical one for a typical test by De Malmazet, reproduced from (De Malmazet, 2009)

De Malmazet reported important thermal effects but could not characterize them precisely regarding actual contribution to total fragmentation. Unfortunately, he did not report the final fragment sizes.

Theofanous and co-workers (Chen et al., 1999) conducted the SIGMA experiments, involving steel drops (1650 °C) submitted to a 265 bar shock in a shock tube. However, visualizations do not give precise information of the fragmentation process. In addition, the drop is quickly exposed to reflection. Although this may happen in reality, it makes the analysis of controlling mechanism more difficult. Two of the six tests were performed with 6 % of void in the test section, which produces a much faster water flow. Although the debris size measurements are not very precise, it is clear that these two tests produced much finer fragments compared to the others.

Concluding, the hydrodynamic fragmentation process seems to be dominant in stream explosion conditions, but we clearly cannot rule out any thermal effects and their characterization remains an open question.

Another important effect with hot liquid melt is the fact that solidification can hardly be avoided and controlled. As previously highlighted, for some reasons to be clarified, it happens that the use of the fragmentation model presented in the previous section to real steam explosion cases (e.g., KROTOS tests, see Figure 153 appendix 1.1 appendix) leads to too small fragments. The likely reason, currently under investigation, is the impact of the cooling and solidification of the melt at the surface of the parent drop, during fragmentation. No dynamic model applicable to CFD codes has been produced to estimate the impact of co-current solidification on the drop size. (Haraldsson et al., 2001) evidenced the phenomenon with Pb-Bi mixtures and, using a model proposed by (Epstein, 1977) could suggest a criterion for a “freezing controlled regime” of fragmentation. However, the Epstein model assumes of a thin crust behaving elastically, which seems quite difficult considering the conditions in freezing situation. The model needs the Young's modulus, which is drastically decreasing to 0 as the temperature becomes close to the solidus. Thus, the applicability is unclear. However, the Li pioneering work (Haraldsson et al., 2001) is a good attend and needs further attention. Another fast solution for direct application is to use a parametric “effective” surface tension. As for FCI with UO_2/ZrO_2 melts, a value of 2 $J.m^{-2}$ provides reasonable results with MC3D (Picchi and Meignen, 2021). Nevertheless, since solids and liquids have in reality more or less same surface tensions, it cannot be the real physical mechanism into play.

2.4.5. Summary of MC3D-EXPLO modelling (V3.10)

MC3D is multi-phase CFD platform based on the Eulerian approach. Navier-Stokes equations are solved for all phases and the interactions/transfers are evaluated by different closure/constitutive laws. Regular staggered grids are assumed, with velocities expressed at the faces and the other variables expressed at the center of the cells. Only one pressure is assumed in the model, i.e., assuming fast equilibrium in bubbles and vapor films. This assumption will be discussed later. Mass and energy balances are based on a finite volume approach, whereas the momentum balances are expressed in non-conservative form with mixed finite differences / finite volume approach. An artificial viscosity model is introduced to deal with shock wave overshot problems.

Volume conservation : $\alpha_l + \alpha_g + \alpha_d + \alpha_f = 1$

Mass conservation: $\partial_t(\alpha_k \rho_k) + \mathrm{div}(\alpha_k \rho_k \boldsymbol{U_k}) = \Gamma_k$

Momentum conservation:

$$\alpha_k\rho_k\partial_t(\boldsymbol{U_k}) + \alpha_k\rho_k(\boldsymbol{U_k} * \nabla\boldsymbol{U_k}) = -\alpha_k\nabla P + \alpha_k\rho_k\boldsymbol{g} + \bar{\boldsymbol{U}}_{\boldsymbol{k}}\Gamma_k + \sum_{j\neq k} K_{kj}(\boldsymbol{U_j} - \boldsymbol{U_k}) + \mathrm{div}\overline{\overline{A_k}} - M_{ck}^{am} - M_{ck}^{l} - M_{ck}^{t}$$

Energy conservation:

$$\partial_t(\alpha_k\rho_k e_k) + \mathrm{div}(\alpha_k\rho_k e_k\boldsymbol{U_k}) = -P\partial_t\alpha_k - P\cdot\mathrm{div}(\alpha_k\boldsymbol{U_k}) - \Gamma_k H_k + \sum_{j\neq k} K_{kj}Q_{kj} + Q_{ki}$$

With c continuous phase (which can be liquid or gas); l liquid; g gas; d drop; f fragment;

- $\bar{\bar{A}}_k$: Diagonal tensor describing the artificial viscosity.
- Γ_k: Volumetric mass transfer rate;
- K_{kj}: Friction factor;
- Q_{kj}: Heat transfer with phase j;
- M_{ck}^{l}: lift term;
- M_{ck}^{t}: Turbulent diffusion term;
- M_{ck}^{am} : added mass term;
- Q_{ki}: Heat transfer with interface.

The PREMIX models consider, in addition, lift and turbulent diffusion terms, not relevant for explosion calculations.

2.4.5.1. Flow map

The flow map (Figure 44) is the same for PREMIX and EXPLO and is based on the assumption that the coolant is either with liquid continuous conditions (bubbly flow) or with gas continuous conditions (droplet flow), as a function of the relative void fraction $S = \frac{\alpha_g}{\alpha_g+\alpha_l}$. Between two thresholds S_B and S_G, a "transition" flow is described as a composition of bubbly and droplet flows (with void fraction equal respectively to S_B and 1-S_G).

Most of the constitutive laws are then written and the sum of the contributions in liquid and in gas weighted by the volume fractions F of each type of flow:

$$f = F_{bubbly}f_{liquid} + F_{droplet}f_{gas}$$

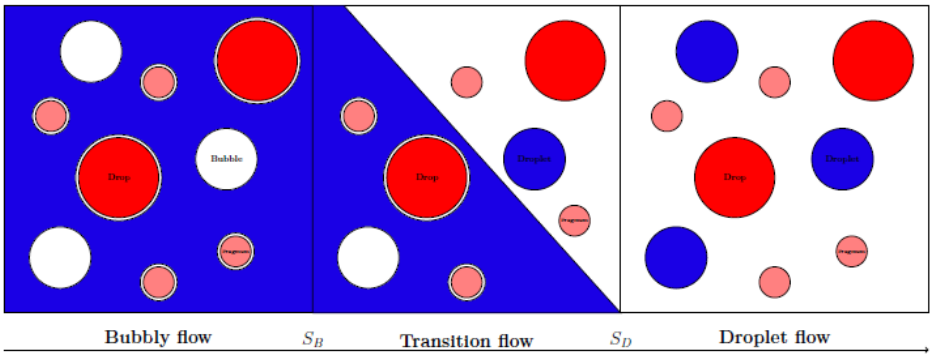

Figure 44: MC3D flow map (default values: $S_B = 0.3, S_D = 0.7$)

In the EXPLO application, the melt is under the form of discrete particles. The melt drops are the result of the fragmentation of jet during premixing. They are described thanks to a multiple size group (MUSIG) type approach with different classes according to their size. All classes share the same velocity field (homogeneous approach). Fragments are always assumed to be homogenously dispersed in a continuous phase which may be either the liquid or the gas depending on relative gas (vapor and incondensable gas) volume fraction $S = \frac{\alpha_g}{\alpha_g+\alpha_l}$ (shown in Figure 44).

In contrast with the PREMIX model, the melt cannot be in a continuous (un-fragmented) form. To account nevertheless to such local situations, the drops and fragments interfacial area are gradually decreasing beyond a local melt volume fraction of 60 %. This point is important because it may introduce a mesh size dependency in some situations. This issue will not be addressed in the present work.

In MC3D, a partition of the fragments is carried out and they are either in liquid, or in gas configuration (Figure 44). Each fragment reacts with the medium with which it is in contact.

$$\Gamma_{f,MC3D} = F_{bubbly} f(\rho_l, V_l - V_d) + F_{droplet} f(\rho_g, V_g - V_d)$$

F_{bubbly} is the volume fraction of the bubbly flow, i.e., with liquid as a continuous medium. $F_{droplet}$ is the volume fraction of the droplet flow, i.e., with gas as the continuous medium.

2.4.5.2. Artificial (or numerical) viscosity

For compressible fluid dynamic solver including MC3D, some numerical diffucities arise for shock involved simultion. In fact, the shock thickness decreases when shock amplitude increases. With a strong pressure, the shock thickness can become smaller than the mesh size. Such mesh can not capture the the shock behavoir (the steep varaition of physical properties), which will cause the numerical osscilations. Decreasing the mesh size to shock thickness scale is very costly and less realistic because the shock moves in space and the thickness is very small. In the another hand, the shock thickness increases with the dissipating viscosity term. A classical process proposed by (VonNeumann and Richtmyer, 1950) to reduce numerical oscillation is to increase numerically the dissipation at the shock point by adding pseudo-viscosity, also referred to as artificial viscosity. For 1-D single-phase shock, the artificial viscosity ν_a is:

$$\nu_a = \max\left(-(b_0 \Delta x)^2 \cdot \frac{dU}{dx}, 0\right)$$

This pseudo-viscosity only has an effect in the flow zones where $\frac{dU}{dx}$ is strongly negative, which corresponds to shock. In this equation, Δx corresponds to the width of the mesh and b_0 a dimensionless coefficient (5 by default) allowing shock depth to be adjusted with respect to 4~6 mesh width.

For a multidimensional calculation, artificial viscosity is not the same in all directions. Along the direction x_i , it is taken as equal to:

$$\nu_{ai} = \max\left(-(b_0 \Delta x_i)^2 \cdot \frac{dU_i}{dx_i}, 0\right)$$

This pseudo-viscosity is included in the momentum equation by adding on the right the term $\mathrm{div}\bar{\bar{A}}$ where $\bar{\bar{A}}$ is a diagonal coordinate tensor:

$$a_{ij} = \alpha \rho \nu_{ai} \frac{dU_i}{dx_i} \delta_{ij}$$

The pseudo-viscosity is a function of the velocity field. In a multiphase calculation, the number of artificial viscosities equals the number of velocity fields. If, for a mixture *k*, the diagonal tensor defined by the following equation is called $\bar{\bar{A}}_k$:

$$a_{kij} = \alpha_k \rho_k \nu_{aki} \frac{dU_{ki}}{dx_i} \delta_{ij}$$

With:

$$\nu_{aki} = \max\left(-(b_0 \Delta x_i)^2 \cdot \frac{dU_{ki}}{dx_i}, 0\right)$$

3. Analysis of the current MC3D-EXPLO (3.10) behavior

3.1. Objectives and simulation set up.

To understand the FCI phenomena and current physical models and behavior of the application EXPLO, a specific 1D case is built and analyzed (Figure 45). Here, we are interested in the propagation, amplification or decrease of a simple pressure impulse at the bottom (trigger). It is important to stress that the one-dimensional geometry is the effective one in the KROTOS experiments. Thus, this work should help understanding the behavior of these experiments, particularly those with corium, performed in the frame of the SERENA-2 and in the ICE projects. Of particular interest is the analysis of the impact of the amount of initial void in the mixture, of the size of the generated bubbles (see discussion in 2.4.3) and the size of the fragments (2.4.4).

Hence, several series of calculations are performed:

- series 1, monophasic simulation (water) for different trigger pressure; the objective is simply to have a reference for the propagation of the trigger perturbation;
- series 2, diphasic simulation (water + vapor) for different initial void fraction; the main objective here is to analyze the effect of void;
- series 3, tri-phasic/explosion simulation (water + vapor + corium); the main objective of this exercise is to analyze combined effect of void and melt amounts, effect of the main parameters of the fragmentation and heat transfer models; the focus is put on the understanding of the general behavior, of the rate of amplification (or damping) and of the final steady state, if any.

It must be highlighted that this work complements the validation work done for each of the code versions. The simulation geometry is very simple, consisting of a long pipe with a trigger at the bottom, similar to the one used in KROTOS experiments, i.e., pressurized gas capsule. In the KROTOS experiments, the trigger generates a shock wave of about 50 bars (tests in pure water). The velocity jump Δv associated with the pressure jump ΔP is estimated with the relation:

$$\Delta P = \rho_l . \Delta v . c$$

c being the speed of sound. Thus, for typical 3 mm drops of corium, the associated Weber number is roughly:

$$We_{\Delta P} = \frac{\rho_l \Delta v^2 d}{\sigma} = \frac{\Delta P^2 d}{\rho_l c^2 \sigma}$$

The graphs in Figure 46 show the velocity jump and the estimated Weber number as a function of the shock pressure. It is noticed that at least 20 bars are necessary to induce hydrodynamic fragmentation (We >12). Below this limit, thermal fragmentation (§2.4.4) occurs and it is recalled that it can be generated by very small perturbations, down to 1 bar, depending on the solidification level of the drop. It is reminded that thermal fragmentation is not taken into account in MC3D models.

The simulations consider a pipe sufficiently long to reach a quasi-steady state. In general, the explosion requires several meters (it is reminded that the KROTOS test section height is only 1m). At the bottom of the calculation domain, the "trigger" is composed by a pressurized non-condensable gas chamber, comparable to the KROTOS trigger capsule (with however different dimensions). The rest of the section is initialized homogeneously with a given mixture of melt, water, and vapor. The grid is regular with a homogenous cell size of 4 mm. Mesh convergence is discussed in the appendix 1.2. Let us nevertheless already notice that the explosion time scale is of the order of 1 ms, whereas a characteristic wave speed is 1000 m/s, depending on the initial void. Thus the “reaction” length is of the order of one meter, much larger than the mesh size. However, the shock wave “thickness”, i.e., time required for the pressure to escalate to its maximum, is much smaller, so the precise capture of the shock may need much smaller cell size. For practical applications, this is not affordable with the current codes, and models are necessary to smooth the behavior and suppress oscillatory unstable behavior (so-called artificial viscosity). There is a clear loss of precision, but the energetic of the explosion is generally preserved.

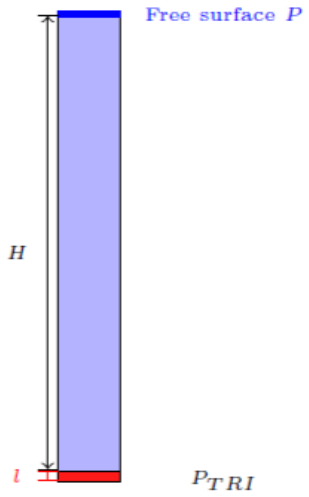

Figure 45: geometry of 1D simulation

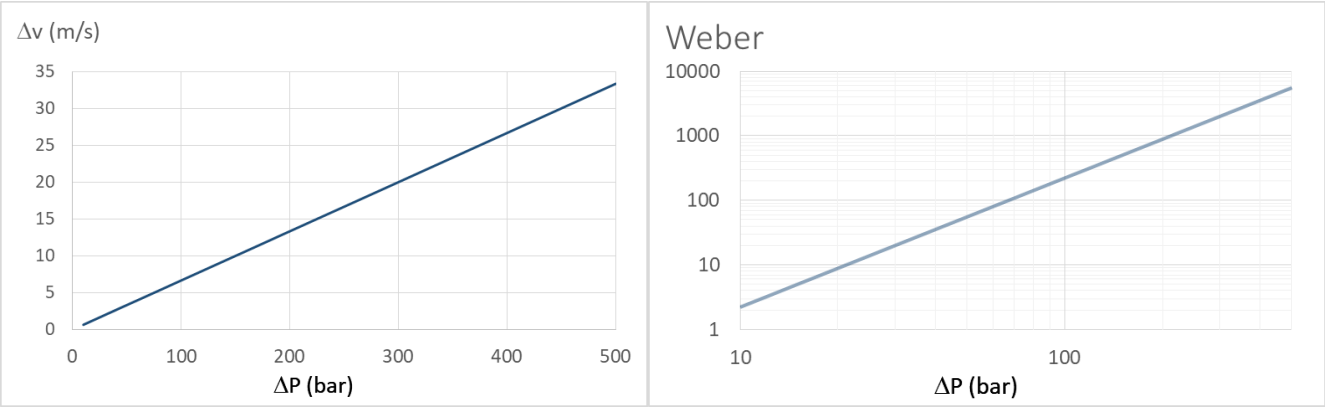

Figure 46: Associated velocity jump and Weber number for a shock wave in water

3.2. Trigger propagation in water/vapor mixture

This first series of tests aims at highlighting the role of the KROTOS trigger, a high-pressure expanding bubble, as an "evolutional boundary condition". To do so, one must fit appropriately the characteristics of the trigger. The propagation test in water allows to approximately fit the trigger characteristics to the KROTOS situation, based on the KT-4 test[4] (Figure 153 appendix 1.1). As for KROTOS, we employ a pressurized gas chamber, essentially with a non-condensable gas, argon. The internal pressure is fixed to 50 bars, which is the effective peak pressure propagating in the test section in the KT-4 test. The effective volume is set in a way to recover approximately the pressure decrease behind the peak.

We must, at first, emphasize some important points:

1. The geometry is different from the one used in more common analyses of shock propagation with infinite boundaries of both sides. Here, one of the boundaries is closed, with an expanding gas bubble. The validation manual reports such tests for verification of the behavior: this is not here our point of interest.
2. The exact geometry of KROTOS is different since the bottom of the test section is a cone terminated by a small gas capsule. The capsule pressure is about 130 bars, but, to the conical shape at the bottom, the pressure in the cylindrical part of the test section is about 50 bars.

[4] A more recent test was performed by CEA with the current installation and gave very similar results.

3. In many other experiments (TROI, FARO L-33), the trigger is a small amount of explosive, the behavior of which being hardly reproducible with precision in MC3D. In such cases, the trigger does not produce a shock but a thin pressure peak. Unfortunately, no specific attention has been put on the effect of such perturbation on the fragmentation.

Figure 47 shows the pressure evolution in time and space for the trigger pressure in pure water. For pure water, the trigger propagates with a constant speed with a good conservation of the pressure front magnitude. Behind the shock front, slow decreases in pressure magnitude are observed.

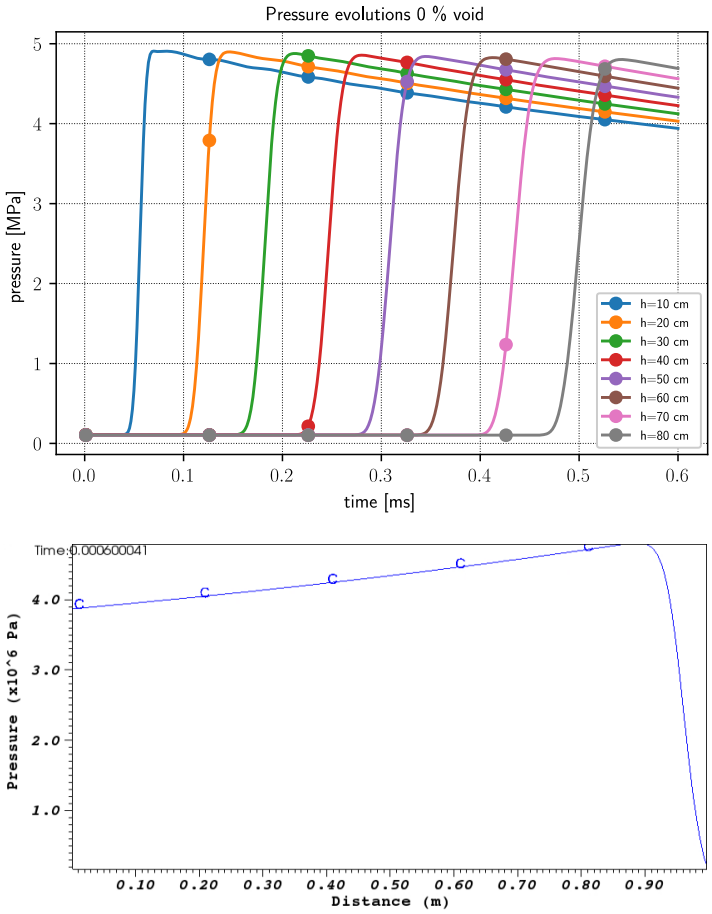

Figure 47: Pressure evolutions (top) and profile at t=6 ms (bottom) in pure water for Ptrigger = 5 MPa

It is of high importance to analyze the behavior of the trigger propagation in a two-phase water-vapor mixture flow in view of the analysis of the results of explosion tests and the role of the initial void is a key issue. Indeed, when the explosion is externally triggered, i.e., with a remote trigger, usually at the bottom of the test section, the front of the melt, which will experience at first the trigger shock, may be composed of solidified melt and bubbles[5]. As the solidified melt will not fragment, its presence should have a weak impact[6] so that the trigger should propagate first in a two-phase mixture. Even in "mono-dimensional" tests as in KROTOS, the vapor (and the melt) might not be uniformly distributed spatially, particularly when using a heavy melt such as standard $(UZr)O_2$ corium. Thus, some 2D effects should appear but the 2D MC3D validation calculations with KROTOS tests indicate a quasi-1D behavior with limited 2D effect (the propagation at the wall is slightly in advance compared to that in the center)(Picchi and Meignen, 2021).

[5] The melt at the front have exchanged more heat with water than the rest and, in the experiments, it is often observed that the first part of the flowing mixture has often rapidly the behavior of a solid, due to some inhomogeneity of the initial heat in the melt.

[6] The solidified parts will still exchange their heat and produce void.

Figure 48 shows the pressure propagation in a two-phase water-vapor mixture with 10 % and 30% of initial void. The characterization of a shock propagation in a bubbly flow is a complex issue that cannot be discussed in detail (see e.g., (Delale, 2012; Prosperetti, 2015)). One will notice oscillations of the pressure peak, when the void is limited, for example in the 10 % test (not visible for 0 and beyond 30 % of void). An oscillatory behavior is also observed in experiments (e.g., (Frolov et al., 2017)), due to the difference of compressibility and the oscillatory behavior of the bubble compression (Rayleigh-Plesset equation). In our simulations, with only one pressure for all the fluids, this cannot be precisely reproduced. Oscillations can be reduced or amplified by changing the bubbles heat transfers. Artificial viscosity also contributes to smooth the behavior. This is not very important in the present context.

The void strongly decreases the shock speed. Whereas it takes about 0.6 ms for the trigger to travel 0.9 m in the absence of void ($c{\sim}1500\ m/s$), it takes about 9 ms ($c{\sim}100\ m/s$) for the 10 % void case and about 11 ms in the 30 % void case ($c{\sim}80\ m/s$). A very strong attenuation of the pressure load is also observed. In the illustrated 10% void case, the pressure peak decreases with a factor of 2 every 12 cm approximately. Figure 49 reports the characteristic distance of attenuation (50 %) of the shock amplitude with the initial void. **A major conclusion is that the trigger shock amplitude may be reducing considerably while traveling through the front of a voided mixture within some few centimeters. There may then be an inherent difficulty to trigger an explosion with a distant trigger device positioned at the bottom**.

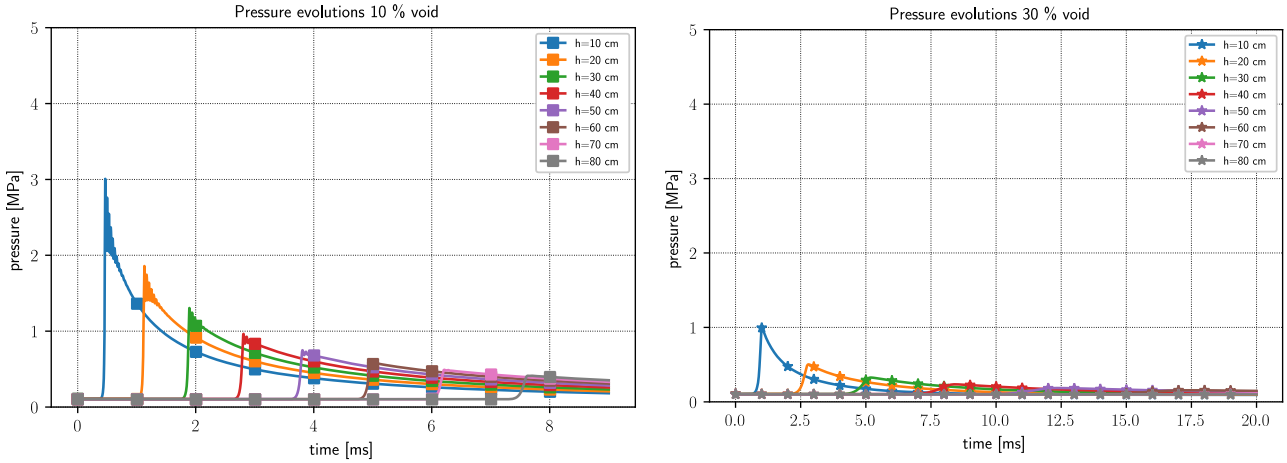

Figure 48: Pressure propagation in 2-phase mixture for $P_{trigger}$ = 5 MPa, with 10 % (left) and 30 % (right) of initial void in the mixture.

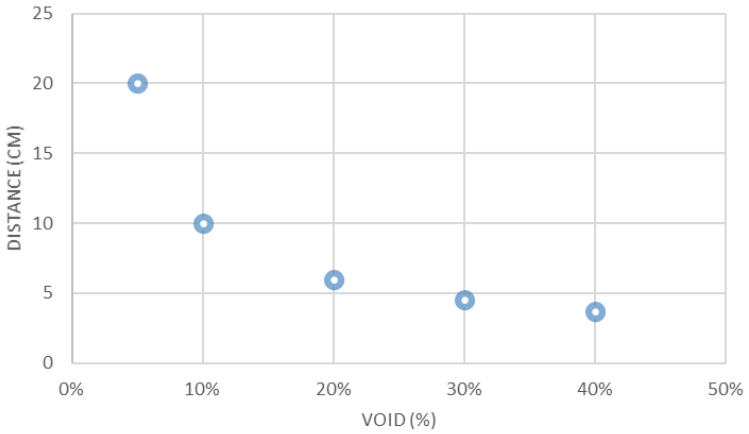

Figure 49: Characteristic distance of attenuation (50 %) of the shock amplitude with the initial void of the mixture.

Generally, the vapor temperature can increase greatly during the passage of shock (Figure 51). If a small bubble diameter is used (which depends on the model parameter), the condensation can be significant, and a large part

of vapor will be condensed and unable to recover (expand) to its original state when the shock leaves. Another consequence is that the mixture becomes quasi-liquid with a very small amount of vapor after the shock has passed. For very low compressibility mixtures, even a small amount of condensation of the vapor (or pressurization of the liquid) will result in a decrease (or an increase) in pressure. To conclude, the low compressibility of mixture and the heat exchange between this small amount of vapor and liquid will cause this oscillation.

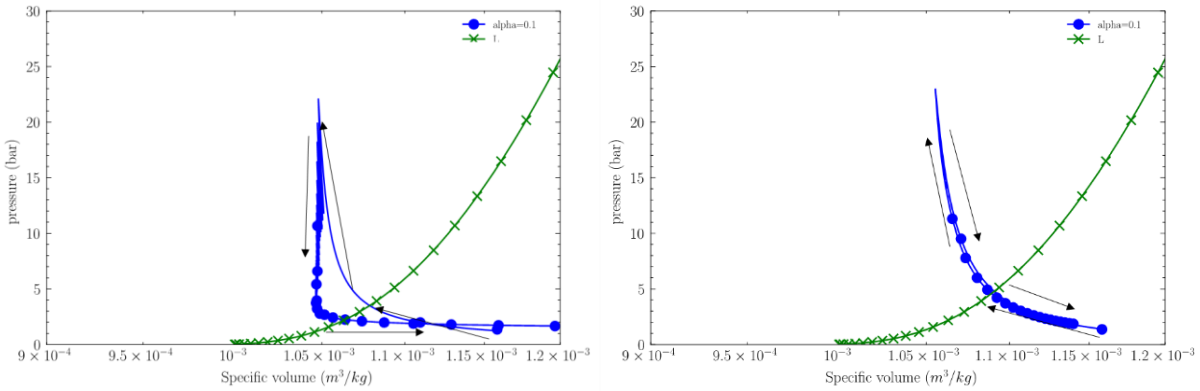

Figure 50: Plot of pressure and specific volume of mixture (blue curve) at a fixed height h=0.2m, for two cases with same initial void 10% and different bubble size (0.5mm and 5mm), left: bubbles with smaller size 0.5mm, considerable condensations occur when the shock arrives, and unable to recover (expand) to its original state when the shock leaves. The green curve is curve of saturated water. The black arrow indicates the direction followed by the mixture during shock passage.

Figure 51 illustrates the gas temperature and void histories at h=0.10 m for all the calculated cases. When the pressure wave arrives, two important phenomena may have considerable influence: the water becomes immediately strongly subcooled, and the bubble diameter shrinks. Condensation plays in fact a minor role in the process. Indeed, with an adiabatic behavior, upon the passage of the shock the void should decrease as:

$$\frac{\alpha}{\alpha_0} = \left(\frac{P}{P_0}\right)^{-1/\gamma}$$

This gives a volume reduction down to about 5 % of the original value for a shock of 50 bars. However, as the shock propagates, the pressure attenuation leads to a smaller void reduction. Nevertheless, one can notice that if the shock amplitude is larger than, say, 50 bars, the propagation in 1D steam explosions leads to a mostly complete disappearance of the void just behind the shock (for initial void <50%).

In contrast, the gas bubbles experience a very strong increase in temperature due to the strong compression and the limited heat loss during the passage of shock. In fact, the temperature may increase very rapidly beyond the limits of the known steam properties. Indeed, beyond about 3000 K (depending on the pressure), the vapor starts decomposing so that the properties used in the code are no more accurate. Let us remind that this effect is very well-known and evidenced in sono-luminescence experiments (Mitropetros et al., 2006). However, due to the very small amount of vapor in most cases just behind the shock, this should not have a major impact. In MC3D, a limit (~3500 K) is introduced for the steam temperature and beyond which the properties are supposed to be constant.

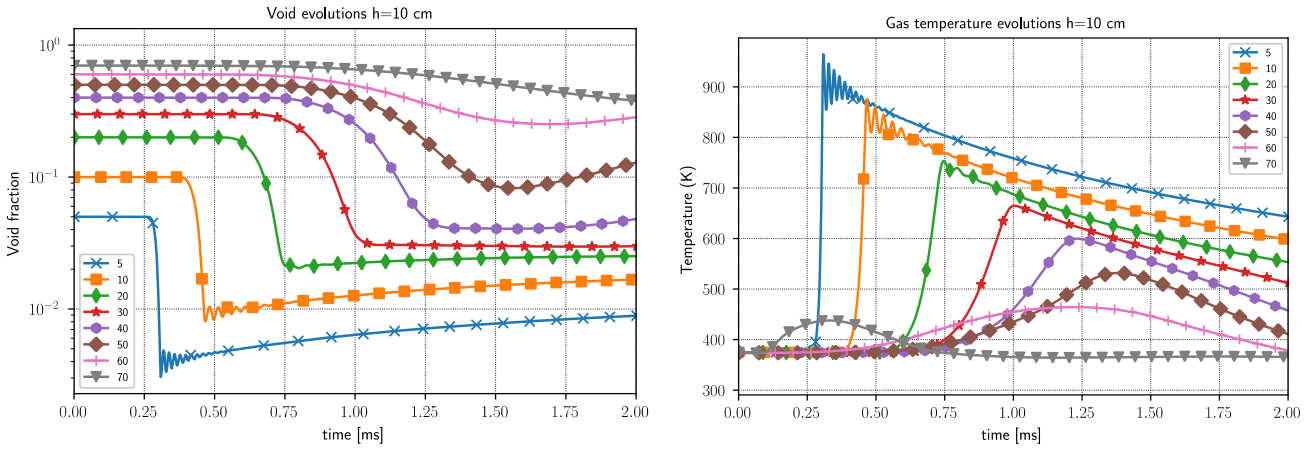

Figure 51: Void and gas temperature profiles at at h=0.1 m in diphasic medium for Ptrigger = 5 MPa.

Let us finally comment that the behavior of a bubble submitted to a shock wave cannot be precisely represented in the code. The collapse of a bubble is a problem studied for a long time and a well-known solution with imposed spherical symmetry has been given by Rayleigh (Landau and Lifshitz, 2013). The collapse should occur in a very short time of the order of micro-seconds. It is also known that the collapse is stable (Rayleigh-Taylor instability may occur only when the pressure inside the bubble is larger than in the surrounding). In fact, experiments and theory show in general the occurrence of asymmetric deformation with formation of liquid jets (e.g. (Mitropetros et al., 2006; Plesset and Chapman, 1971) for cavitation bubbles collapse). In any case, it is believed that these details have a low impact, if any, on the development of the explosion.

3.3. Explosion simulation: pressure escalation and pressurization propagation

The objective of this series of simulation is to characterize the pressure loads in function of the fuel and void fractions (and other important parameters of model) and identify the situation in which the explosion can reach and sustain a steady propagation. The initial and boundary conditions for explosion calculation are summarized in Table 3. The whole domain is still represented by a cuboid, but the length is extended to 9m with the same mesh size. The initial drop size is 3 mm in all calculations (the sensitivity to this parameter is weak). Corium premixing experiments give a mean Sauter diameter in the range 2-3 mm, whereas it is in the range 5-10 mm for the few KROTOS premixing experiments with alumina.

It must be noticed that the initial conditions may evolve during the calculation since they do not correspond to an equilibrium state and the shock may propagate in slightly different local conditions before its arrival. To minimize this effect, the coolant thermodynamical state is set to local equilibrium, with the temperature equal to the saturation one. However, the variations reported are not considered to have a real impact on the explosion.

The exact melt thermo-physical properties do not have an important impact for our analysis. For the full 3-phase problem we have chosen, as a reference, a "classical" uranium-zirconium oxide $(UZr)O_2$ (80 w% UO_2, 20 w% ZrO_2), with an initial temperature of 3000 K, i.e., superheat relatively to the liquidus of about 80 K. Clearly, in a real case, the melt drops should have experienced cooling during the premixing process and the melt may not be fully liquid. This is not accounted for in this exercise. The sensitivity related to the material properties will however be checked, using alumina, the reference material of KROTOS test. The initial content of energy is almost the same (13% more for alumina). However, the much smaller density should affect the entrainment and thus the fragmentation rate.

Table 3: Initial and boundary conditions for the explosion calculation, the volume fraction of drop, vapor, and liquid change for different cases

Gas chamber	$P_{TRIGGER}$	50 bars
	l	0.1 m
	$T_{TRIGGER}$	537.2 K
	composition	100% argon gas
Mixture zone	P	1 bar
	H	8.9 m
	T_L & T_V	373. K
	T_D	3000. K
	d_D	3. *mm*
	d_V	3. *mm*
	α_V	0.3
	α_L	0.69
	α_D	0.01
Top surface	P_{Out}	1 bar

Table 4: Properties of corium and alumina melt used in simulations

Quantity\material	COR8020 (80 w% UO_2, 20 w% ZrO_2)	(AL2O3)
Emissivity (-)	0,75	0,795
T solidus (K)	2870	2314
T liquidus (K)	2920	2334
Latent heat (J/kg) (=E_{liq}-E_{sol})	3.17 10^5	1.17 10^6
Cp liquid (J/kg/K)	510	1420
Cp solid (J/kg/K)	450	1370
Surface tension (N/m)	0.6	0,69
density (kg/m3)	7500	2600
Total available energy (J/m3)	1.11 10^{10}	1.25 10^{10}

Unless otherwise stated, the parameters are those given in Table 5, the initial drop size is 3 mm, a representative value for corium premixing cases. The variation of this parameter does bring interesting new features. The fragment size is computed from the model given in §2.4.4.2, with a characteristic Weber number of 30, and fragmentation rate coefficient of 1. However, the minimum size (threshold) is specified as 75 µm. As discussed above, the bubble size evaluation is a critical point in the model. Here bubbles as mostly generated from the boiling in the interaction process and they are expected to be in the size of the fragmenting drops, as sketched in

Figure 52. Another possible minimum value would be the order of the size of the fragments. The volume fraction of melt drop is some few percent, as in the KROTOS tests.

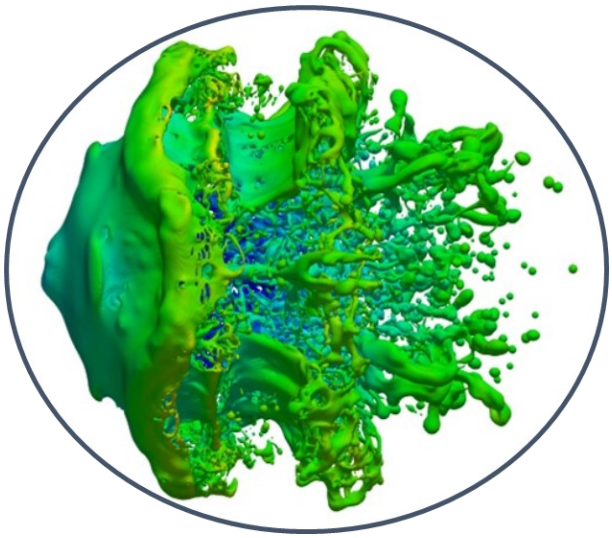

Figure 52: Sketch of the assumed local interaction, the size of bubbles is supposed to be that of fragmenting drop.

Table 5: Main parameters/models for the evaluations. Values in parenthesis will be used for the parameter influence analysis.

Parameters / model	**Value**
Melt volume fraction	1% (2-3 %)
Drop size	3 mm
Fragment size	Model, Df_{min}=75 µm (Df_{min}=10 µm)
Characteristic Weber (We_{ch})	30. (20.)
Fragmentation rate coefficient (C_{frag}).	1. (0.5)
Minimum bubble diameter	5 mm (0.1 mm)
Artificial viscosity coefficient	5 (1-10)
Mesh size	4 mm (1 cm)
Characteristic Weber number We_{ch}	30
Coefficient of fragmentation	1

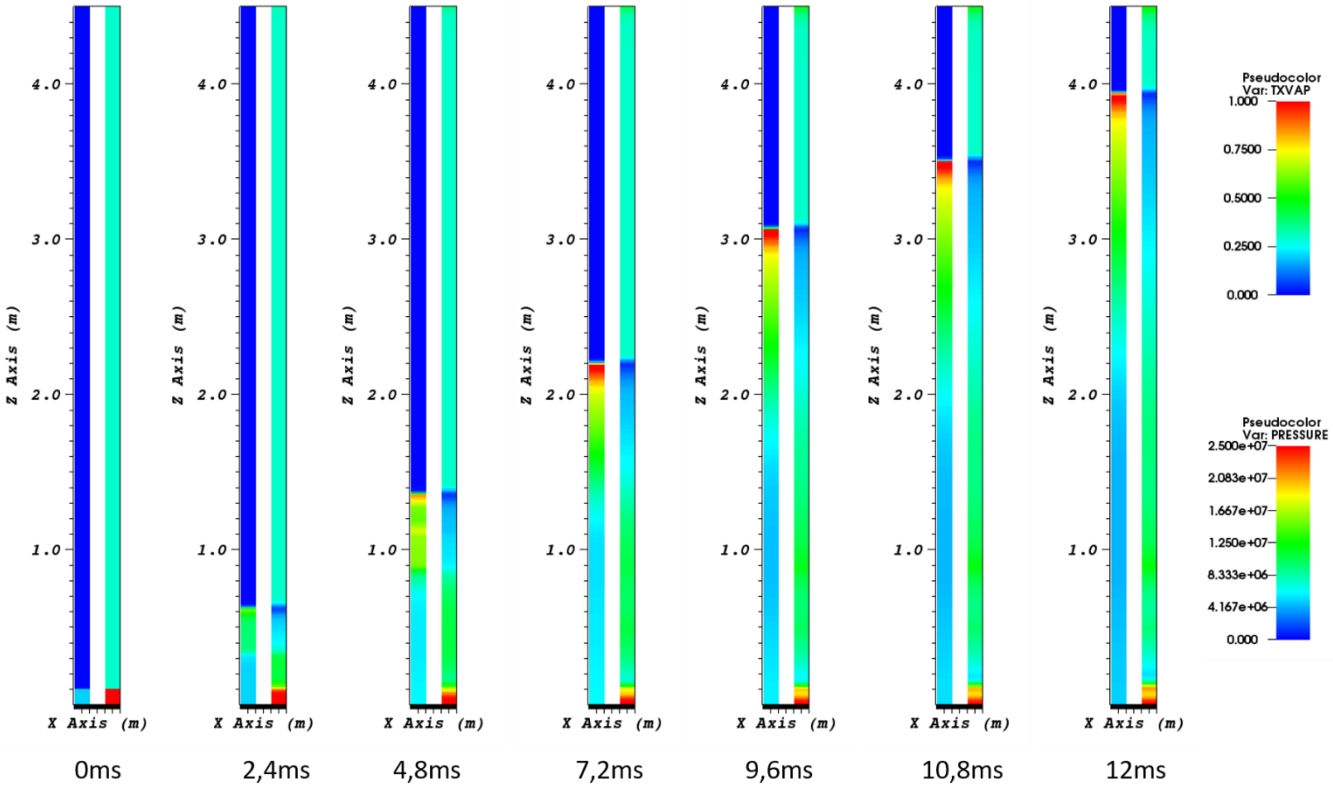

Figure 53: Pressure escalation and propagation for typical explosion calculation. Each series of graph is for a different time. The plot on the left shows the pressure, the plot on the right shows the void fraction (zoom for the first 4.5m)

3.3.1. General behavior, impact of the initial void

We start by showing the features of explosion for the case with 30 % void through a visualization of the explosion propagation in Figure 53. The propagation of a real shock i.e., detonation-like behavior is observed. Indeed, the shock propagates at about 500 m/s, much faster than the speed of sound in bubbly conditions (before the shock). After the passage of the shock, a collapse of the initial void is found, consistently with the previous results. The velocity slip between the corium and water behind the shock induces fine fragmentation and thus large heat transfers. There is then a competition between the effects of void generation due to the heat transfer, and the large pressure damping effects due to the initial void.

The pressure histories at distinct heights are provided in Figure 54 for the cases with 10, 30 and 40 % of initial void. Note that the time scales are different, due to the different shock propagation speeds. The time scales are limited either to the calculation time, 20ms, for the large void cases, to the moment when the shock reaches the top of the domain. The general trends are similar:

- the pressure amplitude increases with time and space up to a quasi-steady situation;
    - comparing different cases, the pressure peak decreases with the initial void;
    - comparing different cases, the speed decreases with the initial void;
- a first sharp pressure peak is observed, followed by a quasi-stationary pressure plateau;
    - comparing different cases, the plateau duration increases (slowly) with the initial void;
    - for one single case, this duration also slightly decreases with time and space; this unsteady behavior is due to the increasing distance with the evolutive “boundary condition” at the bottom, i.e., the bubble evolution at the trigger;
- then a strong pressure damping is obtained.

It is also important to note that the distance to reach the steady state, i.e., the maximum pressure loads, in these quite representative conditions, is about 2 m, so much longer than test sections on the available experiments and may reach even larger values at low void; this will be rediscussed. Thus, the observed explosion strengths in experiments are not at their possible maximum.

However, the detailed examination of the curves shows some noticeable differences regarding the stability of the behavior. The case with 40 % of void is remarkably stable whereas the two other cases are somewhat erratic at first view. In fact, there is some “low frequency” modulation of the pressure peak with a repeating pattern of some milliseconds (depending on the case). This behavior is believed to be due to the modeling, although the exact reason could not be evidenced. This is likely due to the combined fragmentation and heat transfer mechanisms in conjunction with the strong flow changes during the short interaction time. This behavior can be smoothed numerically, but this is not interesting for our purpose. In any case, the variations are limited, and the global behavior remains largely predictable.

Upon the passage of the shock, the void nearly collapses (Figure 55), at least for the case with void lower than 30%. Thus, as already anticipated, for these cases, the drop fragmentation should occur in a nearly fully liquid environment. For the other cases, the void remains but with a much higher density due to the large pressure. Then, a high density “vapor” should take place locally along the drop surface. Nevertheless, it is quite clear that the behavior should be very different in the high void cases, that cannot be examined yet (using simulations like those presented in the next chapter). **Thus, the cases with large initial void remain quite uncertain as for the fragmentation characteristics**.

Pressure and void evolve almost inversely. However, it can be noticed that, at the considered distance (4 m), the void after peak remains for a short time with a lower value than initial void (Figure 55), whereas the pressurization is due to the void production. We would expect that the void exceeds the initial value. This is because the temperature (hence the density) of vapor has a sudden increase due to compression by the shock, but a simple depressurization (the shock leaves) cannot lead to a sudden decrease of vapor temperature (hence the density). With a higher density, even though more vapors are generated during vaporization, they do not occupy more volume.

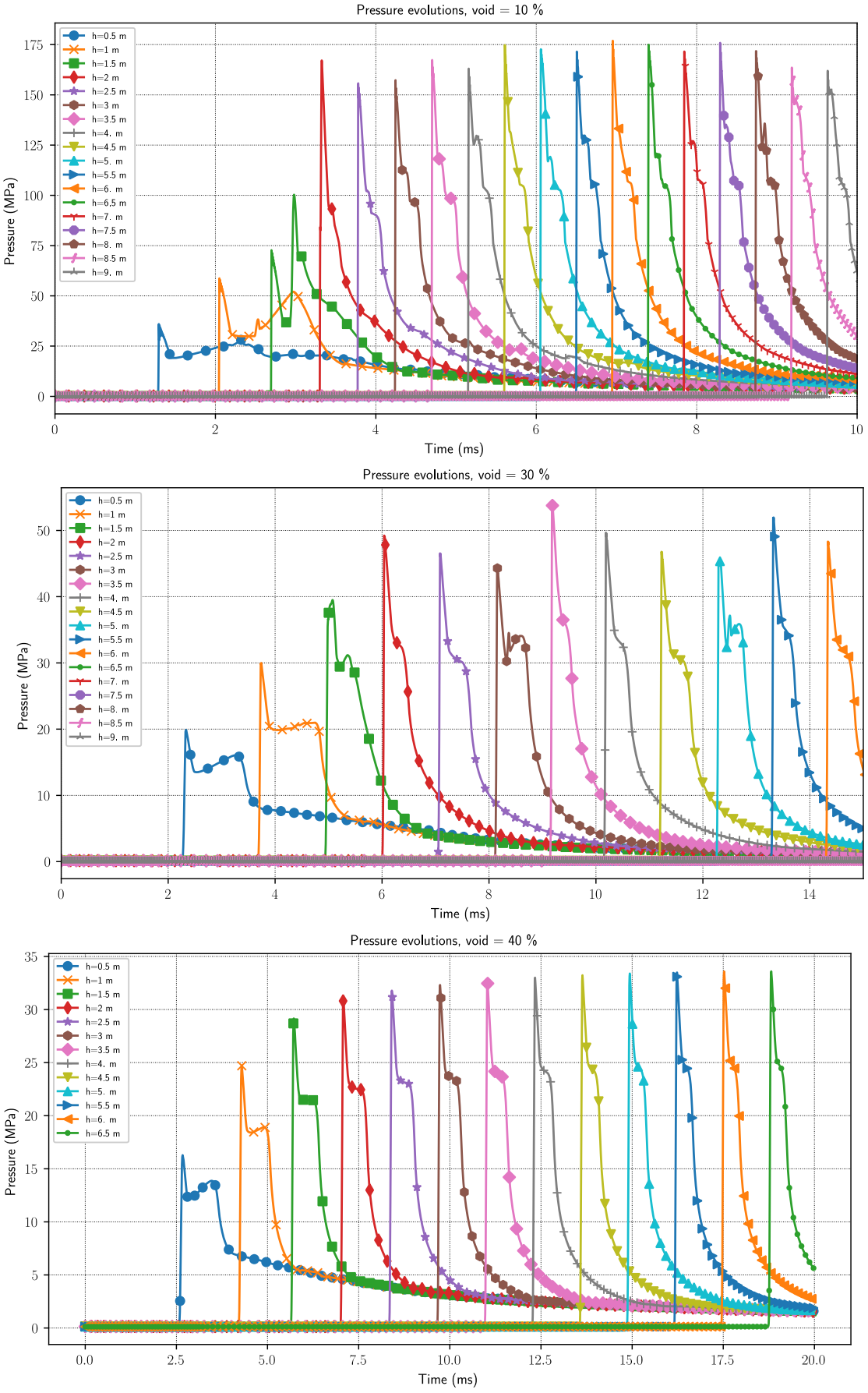

Figure 54: Pressure profiles varying with time at different height for respectively 10 % (top), 30 % (middle) and 40 % (bottom) of initial void fraction (different time scales are different)

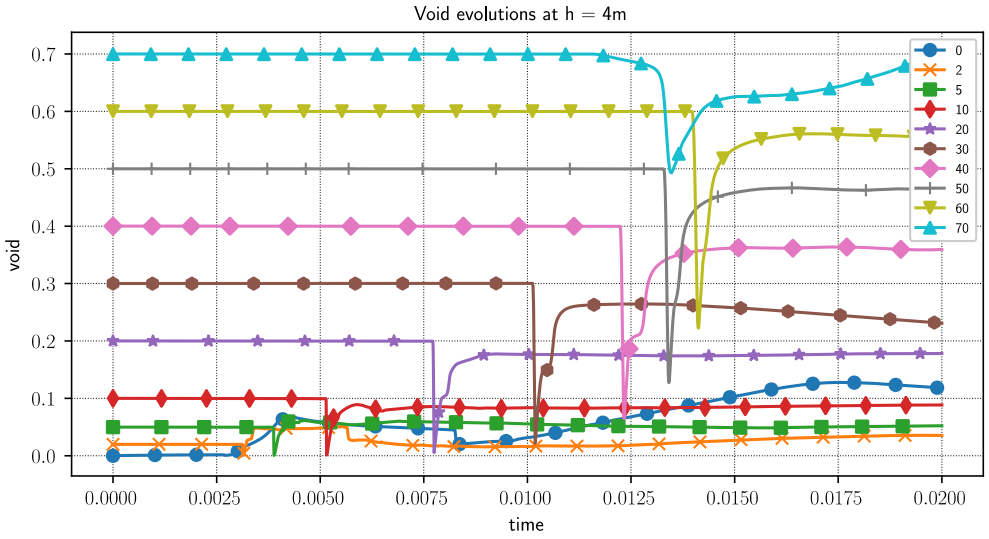

Figure 55: Void evolution along time at h=4 m for all calculated cases

The first pressure peak is corresponding to the travel along the Hugoniot adiabatic curve (Figure 56). Then the pressure reaches rapidly the quasi plateau of short duration, during which the specific volume of the coolant remains also almost constant. The detailed analysis shows that the end of this period corresponds approximately the end of the fragmentation and heat transfer, corresponding thus to the CJ point. Nevertheless, the process is much more complex than expected from the standard detonation theory sketched out in Figure 22 and Figure 23. In practice, the "reaction rate" is strongly varying during the process as the drops and fragments are entrained and deliver energy at varying rate, according to the local details of the multiphase flow. The "reaction" then continues in different ways with different time scales. Indeed, strong thermal disequilibria are likely to occur between the liquid and the produced vapor (this is the core of the MC3D model but also underlies the MI model where the equilibrium is very local). After the "reaction zone", the pressure then rapidly decreases and goes slowly to a thermodynamical state that is quite close to the initial one. This is because the amount of vaporized water is limited, and the initial and final thermodynamic states are not so different. The calculation only investigates the propagation phase whereas in the experiments, the shock reaches the water level and then reflects as a rarefaction wave while the pressure is still large in the test section. The unconstrainted conditions lead to an expulsion of the water at high velocity. This cannot happen in the present simulations.

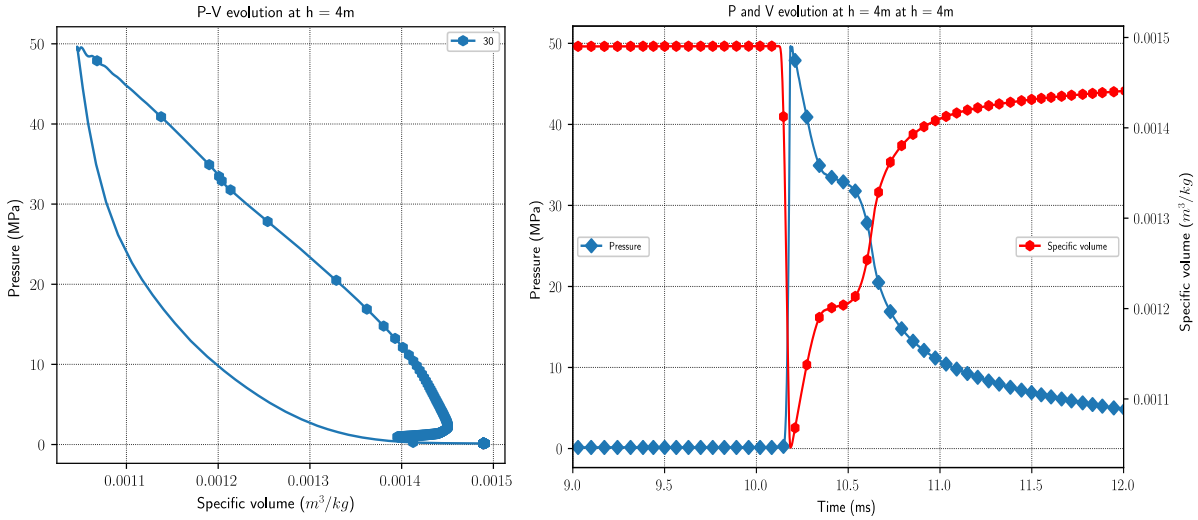

Figure 56: Evolution in the P-v plane (left) and evolutions of P and the specific volume v (of the coolant mixture) with time (right) at h=4 m for the 30 % void case. The dots and crosses on the graphs are corresponding to the same times

The steady state should be reached when the fragmentation process has maximized the vaporization. However, the conditions to reach this situation are not obvious. It is believed that fragments of smaller size would be obtained when the local pressure increase. On the other hand, it is also believed that the final explosion strength should increase when the fragments size decrease. These two arguments lead to indefinite increase of explosion strength once it starts, which does not sound realistic. The explosion strength, as a function of final fragment diameter, must have an extremum, more properly speaking a maximum, as can be verified by sensitivity calculations of fragment size. However, in our simulations, the fragment size is limited to a pre-defined value, 75 µm, which provides a limitation to the process. The situation where this limitation is not used will be rediscussed later, but it can be anticipated that the model reaches an intrinsic limitation and cannot properly describe the cases with finer fragments as there is only one single filed for fragments. Figure 57 provides the time evolution of the mean fragment diameter (SMD) and the mean size for all the melt, including drops and fragments. One can notice, at first, that the cases with low void (0 and 5 %) do not reach this lower pre-defined limit (75 µm), due to the lower ambient liquid velocity at the passage of the shock. The case at 0 % of void even show a fine fragmentation only quite lately, so that this (non-realistic) case takes a very long time to start a noticeable explosion behavior (Figure 58). All the other cases reach rapidly this limiting fragment size (75 µm). Nevertheless, the evolution of overall SMD can also give indications on the fragmentation grade and it shows that the complete melt fragmentation (when the SMD reaches 75 µm) takes a long time and a long distance in general.

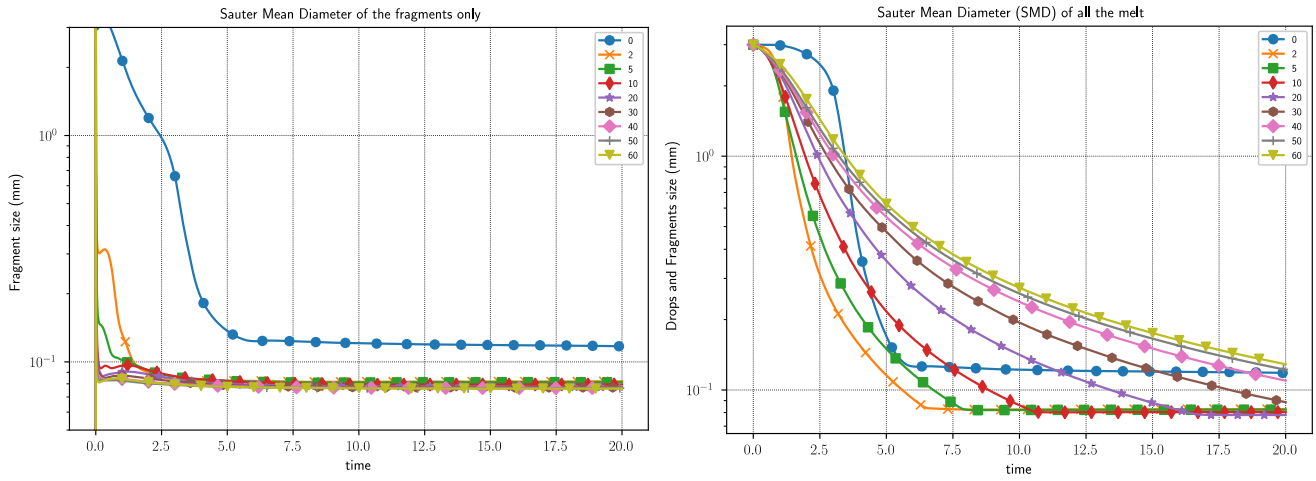

Figure 57: Sauter Mean Diameter of the fragments (left) and drops + fragments (right) averaged over time.

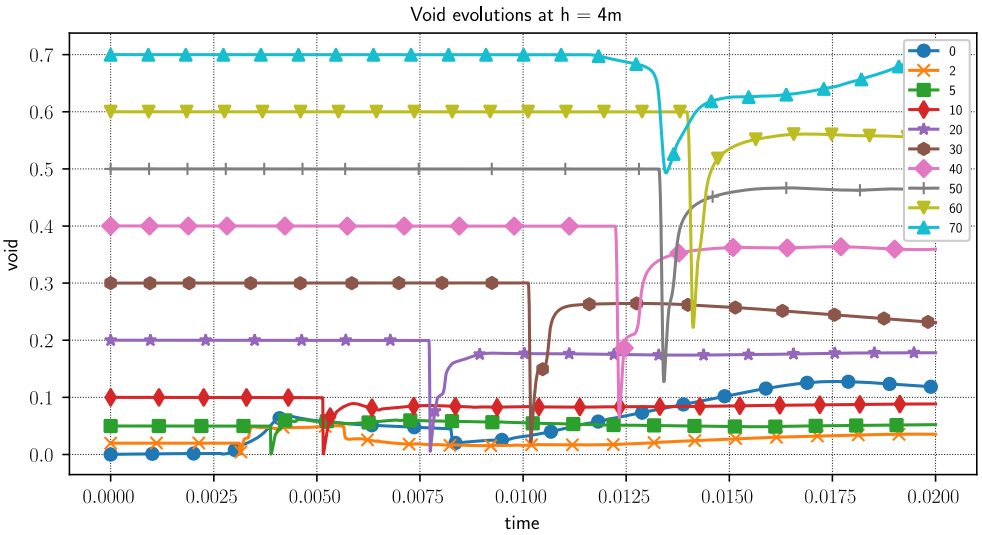

Figure 58: Vapor volume fraction varying with time at h=4m for case of different initial void

More details are given in Figure 59 to Figure 61. Figure 59 compares the fragmentation grade (dashed lines, more properly the drop volume fraction) and pressure for cases with 10 to 40 % void, at a fixed height 4 m, where the quasi-steady situation is reached. For the 10 % of void, the fragmentation is almost instantaneous (but incomplete). The fragmentation time noticeably increases with the void, due to lower pressure, but remains very fast compared to the duration of pressure peak. The two other graphs compare the mean fragment temperature (i.e., the temperature of the fragment field) with the fragmentation and with the pressure. It is clear that the behavior is dominated by the heat transfer, which takes much more time than the fragmentation. The end of the quasi-plateau of pressure corresponds in fact to the moment when the fragment temperature goes below the minimum temperature to maintain the film boiling, taken to be the saturation temperature + 100 K in the model. At that point, it is necessary to return to the already commented effect of the very small fragments. When they are below the limit of 50-75 µm (depending on the conditions and model parameters, the heat transfer is so fast that the mean fragment temperature (of new fragmented ones and pre-existent ones) may drop below the film boiling conditions whereas fragmentation may continue. There is then an intrinsic model limitation and, in any case, the code user may always consider a minimum fragments size of the order of 75 µm to be sure that this numerical effect does not come into play.

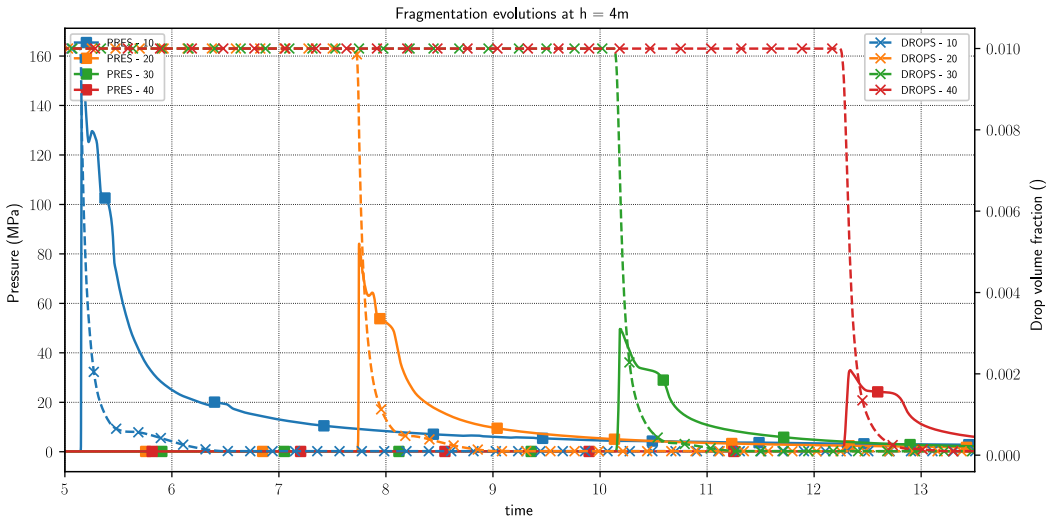

Figure 59: Fragmentation and pressure versus time for 4 cases with void from 10 to 40 % at the height h=4 m.

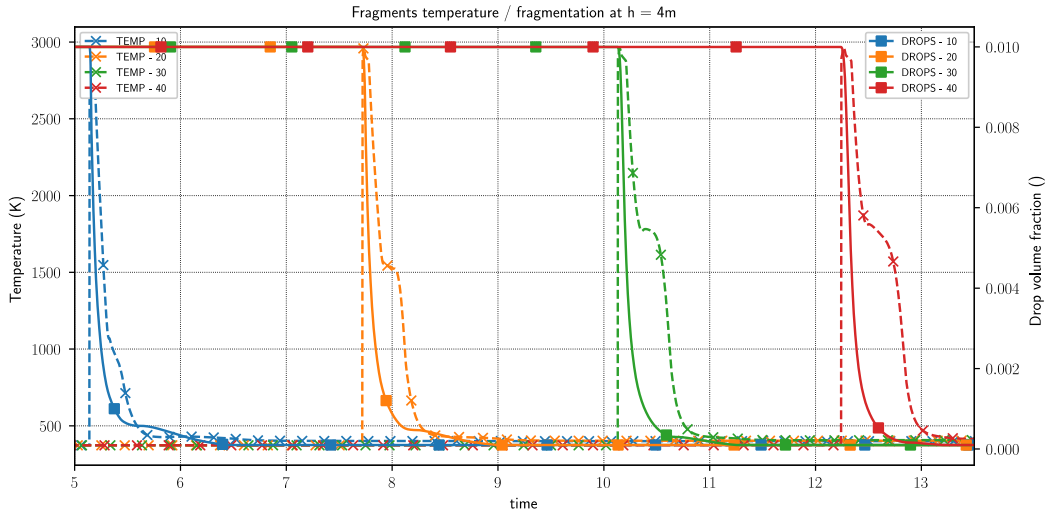

Figure 60: Fragmentation and fragments temperature versus time for 4 cases with void from 10 to 40 % at height h=4 m.

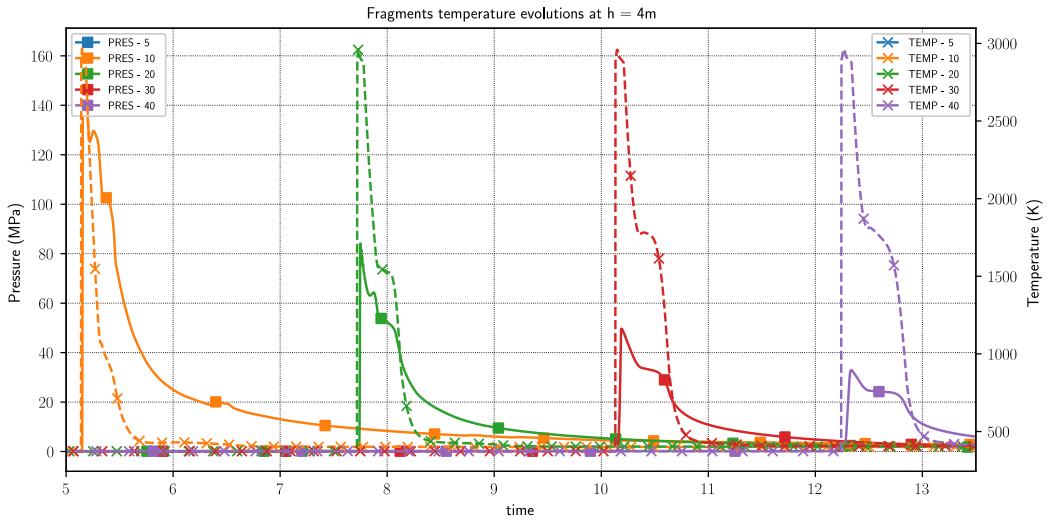

Figure 61: Pressure and fragments temperature versus time for 4 cases with void from 10 to 40 % at height h=4 m.

3.3.2. Combined effect of melt and void fraction.

Providing indicators of the explosion strength is not an easy task. Obviously, the maximum pressure (after filtering possible numerical very fine peaks) gives a first easy idea of the violence of the explosion, for a given geometry. However, the mechanical effect of the pressure load on structures is not only a matter of the maximum pressure. It is often claimed that the best indicator is the so-called “impulse”, defined as the integral of pressure along time at a given position. Although it is also an instructive result, previous studies made at IRSN indicated that none of the impulse or maximum pressure alone can provide a precise indicator of the energetic and of the effect on the structures. Depending on their material, e.g., metal, or reinforced concrete, the effect of strong high pressure or inversely moderate but long-lasting explosion, with the same impulse, will be very different. The kinetic energy of the mixture is also largely used to evaluate the “efficiency” of the explosion, i.e., the ratio of mechanical energy due to the explosion to the initial thermal energy. This last indicator is easy to evaluate in calculations and likely the most accurate. However, it cannot be easily used in the present calculation since it is necessary to wait for the complete depressurization of the test section.

The impulse, as defined above, is also an indicator which is difficult to establish, particularly in the present case with a one-dimensional analysis, as it depends on the duration of integration. In a real steam explosion, the explosion time scale is linked to the time for the pressure wave to reach the water upper level and to come back as a rarefaction wave. But, in the present case, due to the fixed test section length, the behaviors of the different calculations are very different, and it is difficult to establish rules to compare the impulses. **In fact, in most of the calculations, except the case with void lower or equal to 10 %, the pressure wave does not reach the top level (but reached the quasi-steady behavior).** We have chosen however by evaluate the impulse at the bottom over a fixed calculation time, 20ms. Thus, the impulses provided in this section must be considered as qualitative and meanly give orders of magnitude.

The maximum pressure indicated in this chapter generally corresponds to the steady state value, but not necessarily to the value at a fixed position. The results are presented together with the maximum pressure for the case with 1% of melt in Figure 62. Both have more or less the same trends, with a strong decrease when the void increases up to 20-30 %. Beyond these values of void, it is seen that the impulse tends to slowly increase whereas the maximum pressure slowly decreases. This is due to the increase of the thickness (duration) of the pressure pulse when the void increases.

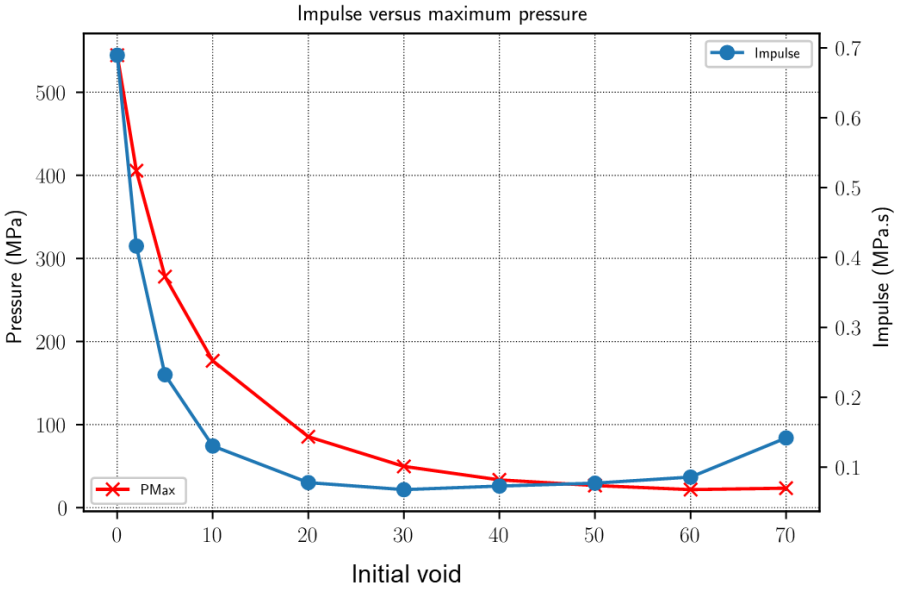

Figure 62: Comparison of the effect of void on the maximum pressure and the impulse for the cases with 1% of melt

Figure 63 gives the combined effect of void and melt volume fraction for these two indicators separately. Some of the computations crashed before ending due to a too strong pressure, the limit of which being apparently of

the order of 600 MPa, which should however be largely sufficient for realistic calculations in real situations. These calculations are distinguished in the figures with empty symbols.

The increase of the melt fraction leads to a strong increase of the pressure loads (maximum pressure and impulse). Of course, in a real case, the increase of the melt fraction would lead to an increase of the void. However, it is seen that the loads may be very strong even with large void. Also, it is important to notice that the behaviors at very small or very large void shows trends which are not comparable with the other calculations, due to the very long time taken to develop the explosion.

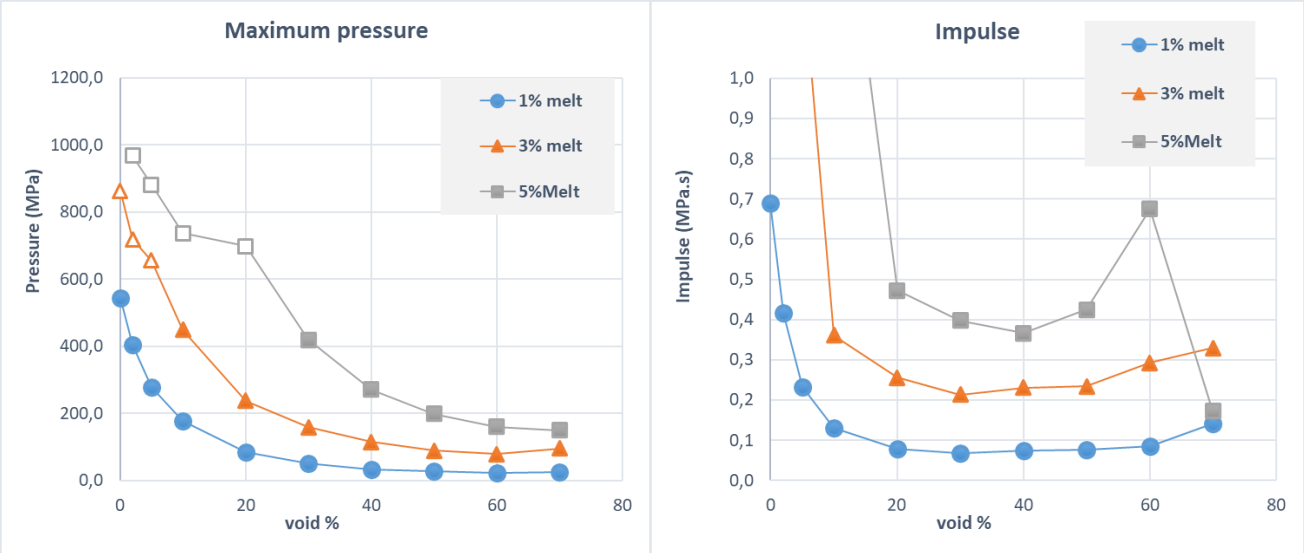

Figure 63: Maximum pressure (MPa) reached in the domain and impulse (MPa.S) at a fixed position h=3 m for all calculations performed. Empty symbols denote incomplete(crashed) calculations

Two other interesting indicators are given in Figure 64: the approximate distance to reach a quasi-steady behavior and the "pressure gradient", which is the maximum pressure divided by the distance. These two indicators are particularly interesting for comparisons with experiments. The 3 series of calculations behave similarly, with very long distances (some could be evaluated) at low void. Interestingly, the distance at moderate void is similar, about 2 m, whatever the melt content. In contrast, the pressure gradient strongly increases with the melt content.

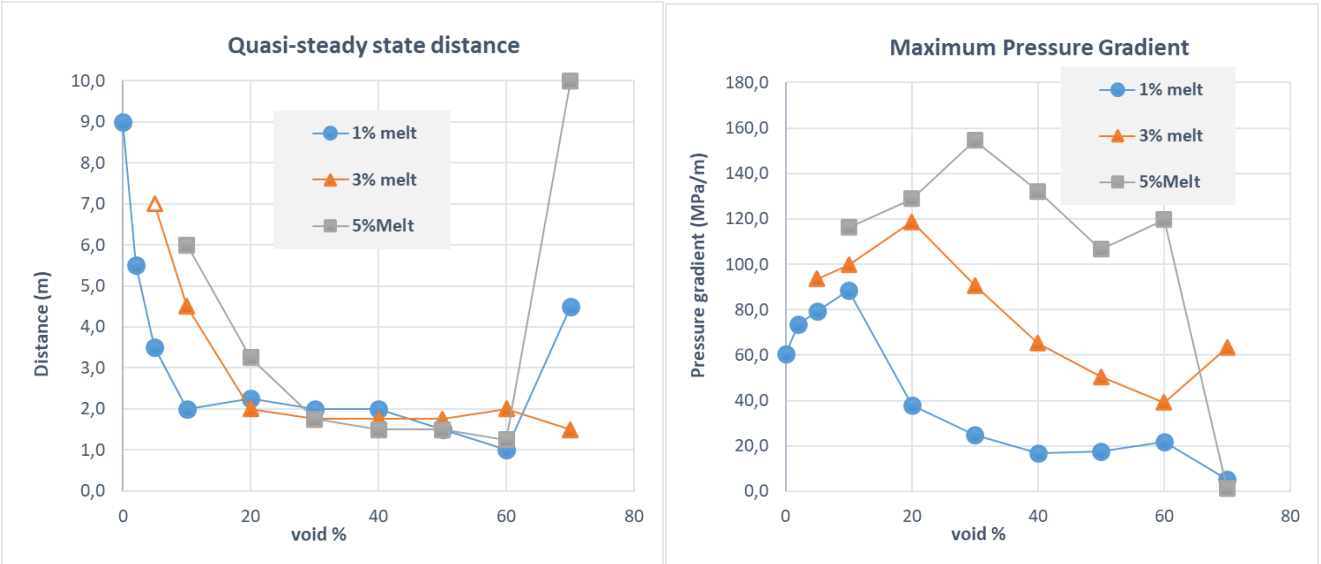

Figure 64: Approximate distance to reach quasi-steady behavior and "pressure gradient" in the developing phase

3.3.3. Impact of fragmentation model parameters

We have indicated previously that the confrontation of the fragmentation model with available data does not permit to fixe precisely the parameters and there are several possibilities of variations:

- We_{ch}: the characteristic Weber number of the fragments,
- C_f: the inverse of the dimensionless time for fragmentation.

It is important to check the sensitivity of these parameters. The previous calculations were performed with We_{ch}=30, C_f = 1. The sensitivity study will consider the case We_{ch}=20, C_f = 0.5, as an alternative.

The results are synthetized in Figure 65. Although some differences can be noted, these are largely acceptable and the sensitivity is, as expected from the fragmentation analysis, quite minor in the context of the steam explosion.

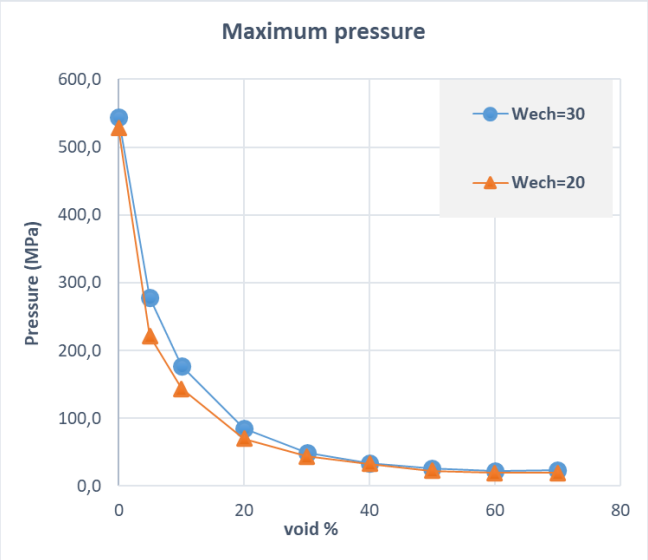

Figure 65: Comparison of the maximum pressures for the two series of calculations varying the fragmentation parameters (see the text)

3.3.4. Material effect

The study of material effect will be limited to comparing the most commonly used materials in KROTOS tests, namely alumina, which led to strong instantaneous explosions, and (U-Zr)O_2 corium, which led to much lower loads. It is reminded also that the alumina tests involved very low void (due to good mixing with water), whereas corium tests involved always voids in the range 10-30 %, for the same melt volume fractions. The series of calculations using alumina were made with a drop diameter of 5 mm, representative of experimental results in KROTOS premixing (unexploded) cases. Results are shown in Figure 66. The results with 0 % of void show very different trends but may be neglected due to non-physical initial conditions. One will notice, except for this case, that the trends are very similar, particularly for the explosion. Note, however, that the distance for the establishment of this maximum pressure is noticeably longer with alumina. In fact, the thermal energy per unit volume is very close for both materials (*cf.* Table 4). In contrast, the much lower density (similar surface tension) leads to different behavior for the entrainment (much faster with alumina) and fragmentation rate (smaller). Both effects lead to a global decrease of the fragmentation rate, which may be accommodated with a longer distance to reach steady state.

Now, the MC3D results at low void, which are representative for alumina cases, indicate that the explosion strength recorded in the experiment could be much higher (up to a factor of 4) when increasing the test section length. There should however be a limit as the premixing is a cooling phase and solidification will increase when the water depth is increased.

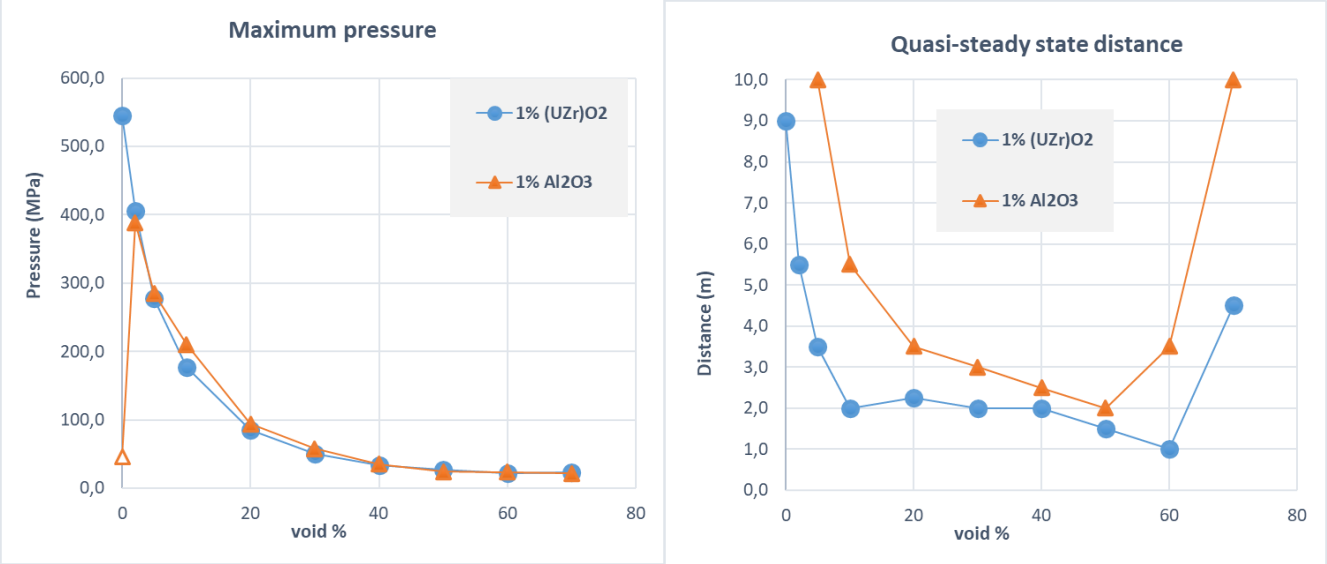

Figure 66: Alumina versus corium: maximum pressure and distance to reach quasi-steady behavior.

3.3.5. Condensation effects – bubble size

Another important conclusion of this study is related to strong impact of bubbles on the explosion strength. In the above calculations, the bubbles were given a large diameter, of the order of the drop size, similarly to micro-interaction models. Thus, condensation effect is rather limited (let us recall that some models do not even consider any thermal effects between the MI mixture and the ambient coolant).

The description of the geometrical characteristics of the void, e.g., bubble size, is a very intricate problem that will be rediscussed in the last chapter. The question here is not related to the behavior of the existing bubbles before the shock, but to those produced by the strong heat transfer due to the fragmentation. An Interfacial Area Transport model is available in MC3D but its use for the explosion calculation has been judged rather dubious since:

- the physics of generation and evolution of the void is very particular and unclear;
- it is not clear that one single field for the gas is sufficient since, as can be seen in the presented results, the original void does not really disappear and should evolve differently than the vapor produced by vaporization which is caused by the fine fragmentation.

However, one can also use the simpler model, which take into accounts effects linked to the mass transfer (boiling, condensation) and variation of pressure. A minimum bubble diameter is introduced, which could be seen also as an “initial bubble size” in the vaporization process. Then, opposite to the previous calculations, another possible initial (minimum) size for bubbles at their creation may be the size of fragments. With an order of magnitude of 100 µm, it is then easy to imagine that strong condensation effect might appear.

The present study confirms that this minimum value, in certain situations, could have considerable effect on explosion. Figure 67 gives the pressure evolutions for 30 % of void, to be compared to the results in Figure 54. The behavior is much more erratic likely due to the co-existence of strong boiling process at the fragments surface and strong condensation effect in the created bubbles. The behavior is still that of an explosion, but condensation predominance is clear since the explosion yields very low loads. In contrast, the case with very low initial void is almost not sensible. The results are synthetized in Figure 68. The difference in behavior observed at low initial void is difficult to analyze but it may indicate that the pre-existing void may behave differently and may have to be modeled in a different way compared to the produced void. **This may then indicate the necessity for a precise modeling to separate the pre-existing and produced void (in the MI models, the void is always included in the single MI mixture, whatever its origin).**

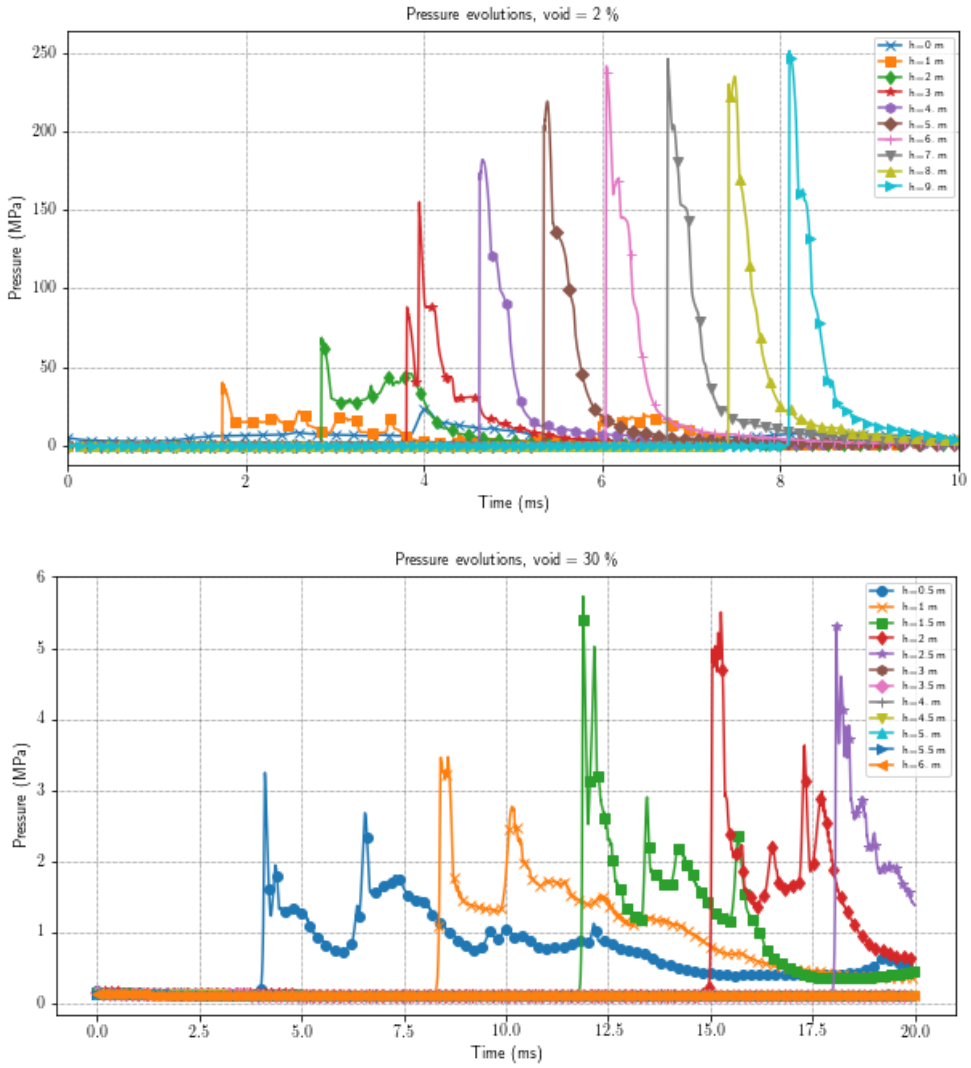

Figure 67: Pressure evolutions with a minimum bubble size of 100 µm for 2 cases of 2% and 30 % of initial void

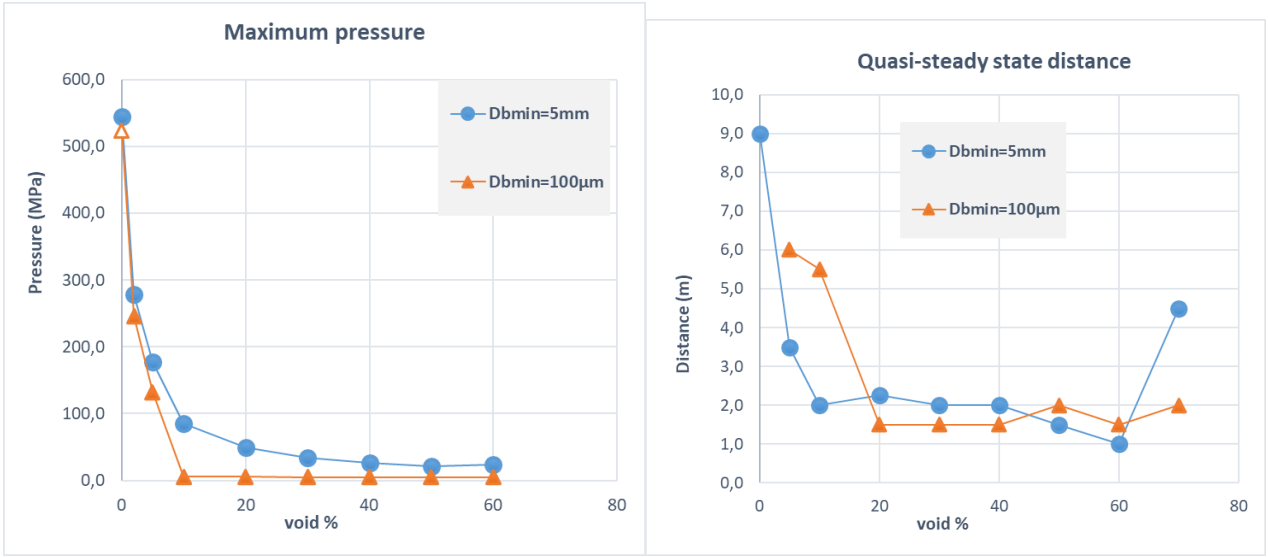

Figure 68: Impact of the initial bubble size for the maximum pressure and distance to reach a steady behavior

3.4. Conclusions

The sensitivity calculations led to the following most important conclusions:

- The void in the initial condition has a considerable importance on the propagation of the shock wave. The shock can hardly propagate in a bubbly coolant, and this may have a crucial impact for externally triggered explosions if the front of the melt is solidified.
- The explosion develops as a detonation wave, following the assumptions made in the first “thermal detonation” models by the mid 70’s. The results are consistent with those obtained in the KROTOS installation with alumina as melt material. Nevertheless, the detailed characteristics of the phenomena occurring in the “reaction zone” remains to be clarified, particularly the generation of void though the film boiling mechanism. Thus, the pressurization is evaluated with a level of uncertainty that can be reduced with improvements of the models.
- The distance to achieve a quasi-steady state, i.e., maximum load, is at least two meters in this one-dimensional geometry and may be much larger at small void.

Two paths for model improvement are highlighted:

- The unicity of the fragment field poses numerical problem due to the averaging process for the temperature between the “old” cooled fragments and the “new” hot ones.
- The unicity of the gas phase also leads to strong limits in the modeling of the behavior during the interaction. The pre-existing gas and the one created from the vaporization may be separated. This is however a quite intricate task from the numerical point of view.

These improvements are foreseen for next evolutions of the model, together with an improved fragmentation model considering the delays related to the deformation prior to the appearance of the first fragments.

4. Analysis of combined fragmentation and heat transfer

As presented in the introduction section, one of the most important questions to be answered for explosion modeling is, on a small scale, what happens when a liquid molten drop with a very high temperature is fragmentating in water, under the action of a shock wave?

Strong fragmentation of drops and violent vaporization of the coolant are expected. But the corresponding process and mechanisms are still unclear. Considering the extreme conditions involved during the steam explosion, experiment studies are facing high complexity and strong various difficulties already discussed in chapter 2. First, the fragmentation and associated heat transfers are highly transient processes which occur in a very small time (some milliseconds) and space scales (some millimeters), which make it very difficult to get detailed information during the interaction. Second, the explosion happens generally in extreme physical conditions (very high pressure and temperature). Conducting experiments that reproduce such conditions poses both technological and safety challenges. Measuring detailed and accurate characteristics in such conditions may be considered as simply impossible nowadays. On the other hand, with the continuous increase of computing power for high performance computer and the development of numerical techniques for two phase flow Computational Fluid Dynamic (VOF, adaptive mesh refinement, etc.), the high-fidelity simulations become possible for some simple academic studies. In this part, we investigate the drop fragmentation and associated heat transfer using Direct Numerical Simulation (DNS) tools. The objective is to better understand the fragmentation process of corium drop and the associated heat transfer, to raise and describe the most important phenomena involved in interactions and further to model such processes in the MC3D code.

Here, we firstly frame the physical process that we want to study. Numerical simulations are carried out for a hot and initially quiescent corium drop submerged in continuously flowing water. We consider that the drop has a diameter of 4 mm and is subjected to a flow of water at different speeds (without gravity) which may correspond to the coolant velocity immediately following a pressure shock wave. The initial aerodynamic Weber number (based on the ambient flowing water, Figure 46) varies between 1 and 2560. Steam explosion may involve higher Weber number conditions, but it is expected that the covered range of Weber numbers is sufficient to cover the involved phenomenology.

Before going to the numerical description, we first discuss the representativity of our simulations. It is noticed, at first, that the drop is initially spherical whereas the real shape may be much more complicated. Starting from a simple geometry allows to better highlight the main characteristics without loss of generality. Second, only two phases (liquid water and corium drop) are considered in the current study, without boiling. It should however be representative of the real interaction process, at least for the beginning of the process, for the following reasons:

- The drop fragmentation is initiated by the velocity slip (induced by the shock wave) between drop and environmental fluid. As shown in the previous chapter, the shock wave will strongly compress vapor into a very low void, and thus the vapor film surrounding the melt will become very thin. The previous study indicated that fragmentation should mostly occur during the period of high pressure. In such conditions, at least for this period of very high pressure, the vapor film is so fine that it should not have an important impact on the hydrodynamic fragmentation which should then be due to the interaction between liquid water and drop.
- Secondly, steam explosion involves in general high pressure and temperature. When the pressure is larger than the critical pressure (which is the most interesting cases for steam explosion studies), the vapor and liquid cannot be distinguished and separated by an interface. Although the first part of the ICE project helped demonstrating that film boiling phenomenology can still be considered as representative, the large vapor density and suppressed surface tension between water and its vapor re-enforced the hypothesis of negligible impact of the film.

It must be noticed that the process of thermal fragmentation described in section 2.4.4.1 cannot be not captured by the current DNS, since boiling is not considered. De Malmazet observed the thermal effects in their experiments, but the contribution of thermal fragmentation (through local contacts between melt and water) to the total fragmentation cannot be quantified. As indicated previously, the thermal effects are expected to decrease with the increase of Weber number. In addition, the thermal effects on fragmentation for a "reactor"

case is still quite uncertain since the existent experimental tests that evidenced the thermal fragmentation did not use prototypical corium. On the other hand, the theoretical work of Lamome and Meignen (Lamome and Meignen, 2008) showed that, beyond perturbations of about 15 bars, the hydrodynamic processes become rapidly dominant. As a result, the conclusion based on simulations of hydrodynamics fragmentation can be extrapolated to real conditions, at least, for high Weber cases (explosion).

Of course, the real heat transfers are affected by the current simplification, but the aim here is not to describe the heat transfer itself, but the impact of fragmentation for a given type of heat exchange. Radiation is not considered, but it can be easily shown that, under real steam explosion conditions, this type of exchange is not preponderant (although not totally negligible).

The present study also imposes additional simplifications of real situation, due to the high numerical and modeling complexity. The heat transfer is resolved by the advection and diffusion of passive scalar (the temperature) with a fixed Prandtl number (set to 1 for the coolant). It is then not fully representative of the actual heat exchanges in steam explosion conditions, particularly when the pressure decreases. However, it is expected that the results can still be used to improve the MC3D general model of fragmentation-heat transfer interaction.

Another strong limitation regarding the real Steam Explosion (SE) phenomenology is the lack of consideration of the melt solidification and its effect on fragmentation. As discussed in the previous chapters, it is believed that solidification should first limit the size of the fragments though the apparition of a thin crust on the surface, the characteristics of which being very unclear. Modeling solidification is a huge task since this implies very complex phenomena at the scales of the atoms with very unclear mechanical characteristics. This problem is often tentatively overcome by increasing artificially the surface tension. However, solidification is not a surface phenomenon (surface tension is almost the same in solid and liquid states), so that it may be more representative to consider that solidification acts as an increase of the viscosity. We could not follow this path in the present work.

Problem description:

An initially quiescent and hot spherical drop of temperature T_0 and diameter D_0 is suddenly immersed into another cold fluid with a temperature T_{inf} and a uniform velocity V_0. The two fluids are separated by an interface with surface tension σ. Both fluids have their own physical properties, including density (ρ_D and ρ_C), dynamic viscosity (μ_D and μ_C), thermal conductivity (λ_D and λ_C), and specific heat capacity (C_{pD} and C_{pC}). For this exploratory study of the link between fragmentation and heat transfer, all physical properties are constant.

Before presenting our simulation details and results, we will first give a quick literature review about previous studies.

4.1. Literature review on secondary fragmentation

Over the past decades, investigations have mostly focused on drop fragmentation in Liquid-Gas configuration for atomization applications (Faeth et al., 1995; Gelfand, 1996; Guildenbecher et al., 2009; Pilch and Erdman, 1987; Theofanous, 2011). In contrast, very few experimental studies have been performed in the Liquid-Liquid configuration. In our case, the density ratio between fuel and coolant is relatively small (**Liquid-Liquid configuration**) comparing to the Liquid-Gas configuration (Pilch and Erdman, 1987). In this bibliography, we will also include some important conclusions for LG configuration since the instabilities, breakup mechanism can have some similarity.

4.1.1. Characterizing the hydrodynamic fragmentation

The associated very small length and time scales, along with the highly transient aspect of the process, makes the drop fragmentation a very complex problem. To describe, characterize further develop models for such process, the first step is to identify the physical properties of interest and relative characteristic quantities (generally, the dimensionless number) which these properties depend on.

The scope of study for hydrodynamic fragmentations includes but is not limited to onset of fragmentation (e.g., the critical Weber number and the maximum stable drop size), the mechanism (different instabilities), classification of breakup modes, the size distribution of daughter fragments (eventually the Sauter Mean Diameter), the drag coefficient and breakup time etc.

To make the conclusions applicable for general cases and find the dominant factors, most investigations and analysis are conducted using dimensionless groups. Some have already been introduced in the chapter 2 but, for the sake of readability, they will be redefined here.

For a system containing two immiscible fluids, the main dimensionless parameters[7] are listed as follow,

- Ratio of density between drop and environmental fluid $\rho_R = \frac{\rho_D}{\rho_C}$,
- Ratio of viscosity between drop and environmental fluid $\mu_R = \frac{\mu_D}{\mu_C}$,
- Weber number $We = We_C = \frac{\rho_c \Delta U_{D-C}^2 d_0}{\sigma}$, which represents the ratio of disruptive hydrodynamic forces to the stabilizing surface tension force,
- Reynolds number $Re = Re_C = \frac{\rho_c \Delta U_{D-C} d_0}{\mu_C}$, the ratio of inertial forces to viscous forces for surrounding flow,
- Ohnesorge number $Oh = Oh_D = \frac{\mu_D}{\sqrt{\rho_D \sigma d_0}}$, a dimensionless number that relates the viscous forces to inertial and surface tension forces for the drop, which is an important number to represent the viscous effects on drop breakup.

Complementarily, the Ranger & Nicholls (RN) time (Ranger and Nicholls, 1972) t_{RN} is generally used as a characteristic time scale for fragmentation. From experimental observations, in any situation, fragmentation occurs in some few t_{RN}.

(1) $$t_{RN} = \sqrt{\frac{\rho_D}{\rho_L}} \frac{d_0}{U_0}$$

Among extensive investigations (Pilch and Erdman, 1987; Krzeczkowski, 1980), the initial Weber[8] number based on surrounding flow and Ohnesorge number based on the physical properties of drop are found to be the independent parameters to characterize the breakup behavior.

4.1.2. Fragmentation mode

Pilch and Erdman (Pilch and Erdman, 1987) compiled data and studied the breakup of isolated liquid drops suddenly exposed to a high-velocity flow and flow inlet velocity is assumed constant on the time scale of drop breakup. Based on the experimental observation in gas flow fields, they propose five distinct modes of drop breakup as determined by the initial Weber number (Figure 69), and they argue that liquid-liquid systems have almost similar breakup modes. As the Weber number increases, the breakup modes are successively:

- Vibrational breakup only occurs for small Weber number. In this mode, larger Weber number leads to larger oscillation amplitude, which can cause the drop decomposition into a few large fragments. When the breakup occurs, the overall breakup time is long compared to the other breakup mode.

[7] Depending on the situation, the Bond number and Capillarity number can also get involved.

- With presence of gravity, the Bond number (Bo) also called the Eötvös number (Eo), $Bo = \frac{(\rho_D - \rho_c) g d_0^2}{\sigma}$, measures the importance of gravitational forces compared to surface tension forces.
- Capillary number (Ca) $Ca = \frac{\mu_D \Delta U_{D-C}}{\sigma}$ represent the relative effect of viscous drag forces versus surface tension forces acting across an interface, which can be important for low weber number cases ($We < 1$).

In the present study, we focus on hydrodynamic fragmentation induced by velocity slip (generally big weber number) without gravity, so they are not considered here.

[8] the weber number can be instantaneously varying, and the initial weber is most used to characterize the breakup behavior. In the following part, weber number refer to its initial value unless otherwise stated.

- Bag breakup is characterized by the formation of a more massive toroidal rim and an attached thin hollow bag blown downstream. The bag bursts firstly, forming a large number of small fragments, the rim then disintegrates a short time later, producing a small number of large fragments.
- Bag-and-stamen (also called multi-mode) breakup is similar to bag breakup, but with the addition of a column of liquid (stamen) oriented along the drop axis parallel to the approaching flow. The bag, the rim and the stamen successively disintegrate into fragments of multiple sizes.
- Sheet stripping is characterized by the continuous stretching of a thin sheet from the periphery layer of the deforming drop. The sheet then disintegrates into small fragments.
- Catastrophic breakup is initialized by the wave crest stripping, which is described as the formation of large-amplitude, small-wavelength waves on the windward surface of the drop, and the continuous eroding of the wave crests by the action of the inlet flow. Then the large-amplitude, long-wavelength waves ultimately penetrate the drop, creating several large fragments before wave crest stripping can significantly reduce the drop mass. Drop penetration by large-amplitude surface waves is referred to as "catastrophic breakup".

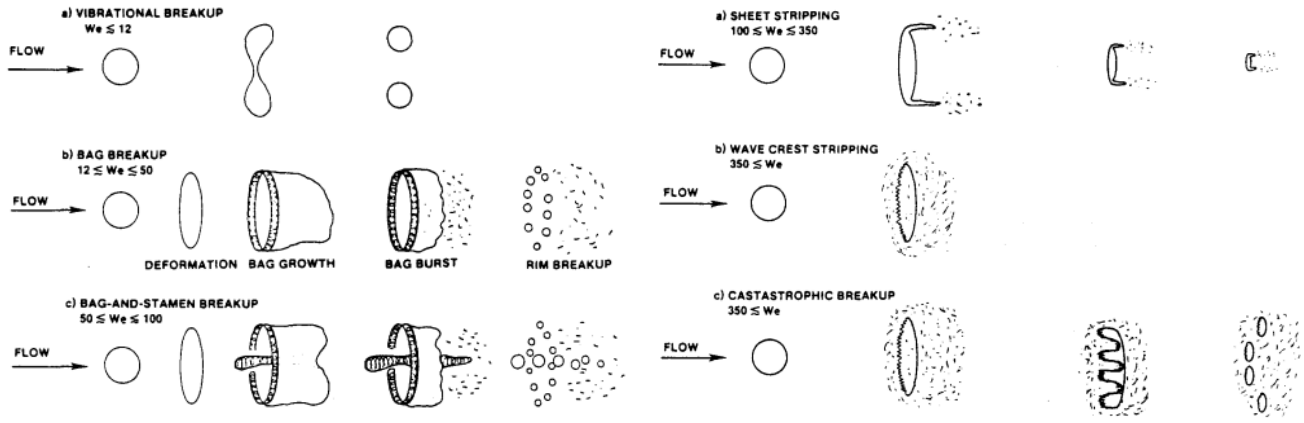

Figure 69: Five breakup modes as function of the initial Weber number proposed by Pilch and Erdman, from (Pilch and Erdman, 1987)

The literature is very abundant regarding bag breakup, with detailed pictures allowing the precise identification of the phenomena. It is noticed that a sudden change of the underlaying major mechanism seems to occur by We = 100. In fact, the phenomena beyond this Weber number are increasingly unclear. Pilch and Erdman propose a cascading phenomenon for the “catastrophic” breakup which has not been clearly identified. However, Theofanous clearly doubted about the observation sketched in Figure 69 for this regime and attributed it to visualization artifacts(Theofanous, 2011).

As already said, very few clear experimental data are available in liquid-liquid configuration. In fact, several experiments were proposed in the frame of FCI studies, where solidification and high temperature are involved, and the effective mechanisms could not be precisely observed (Haraldsson et al., 2001; Kim et al., 1983).

(Kim et al., 1983) made such experiments and studied the fragmentation of a gallium drop of a few millimeters in a flow of water with the DROPS installation already discussed. Based on the observations (e.g., Figure 70), they proposed three fragmentation regimes (cf., Figure 71) according to the initial Weber number. For a Weber number ranging from 30 to 500, the regime is characterized by a first draw-off of still intact gallium skins and then a subsequent breakup of these skins. In the so-called transition range (Weber number between 500 and 1300), with the increase of Weber number, the appearance of clouds of fragments was also observed, which is explained by direct stripping of crest of waves by the author. For a much higher Weber number (13000~3600), the regime was characterized by direct stripping mechanism. Due to the low resolution of images (see, Figure

70), t is difficult to obtain precise information about the scale of the various instabilities and the precise fragmentation mechanisms using the reported interface contours.

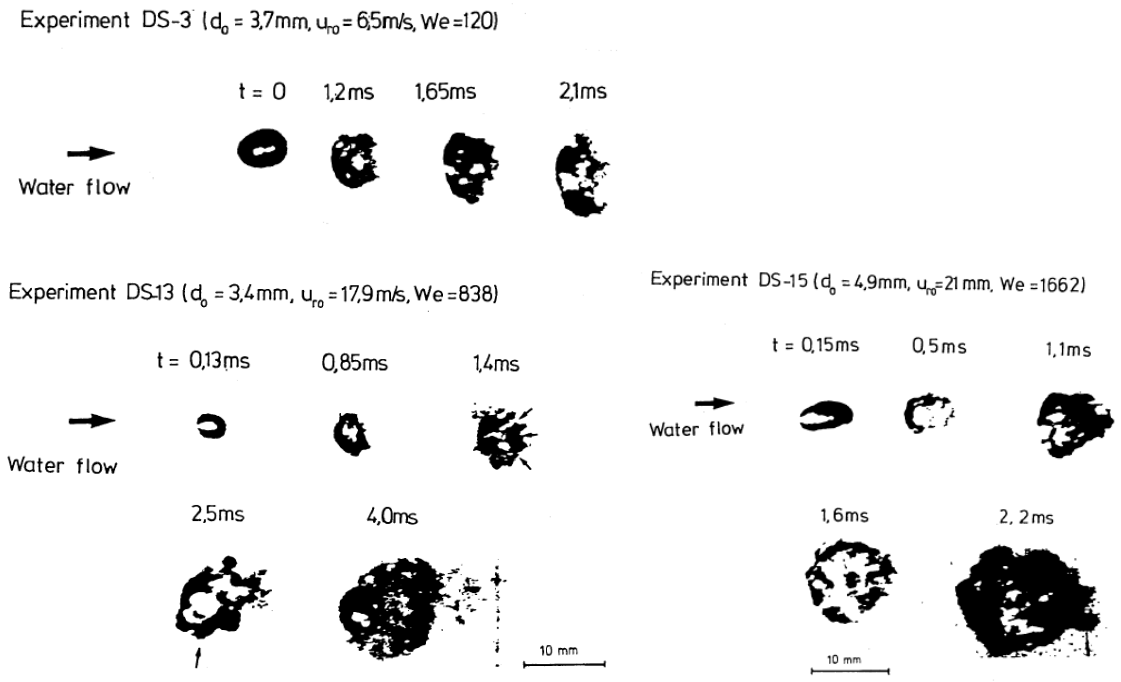

Figure 70 : Deformation of a gallium drop placed in a water flow for different Weber numbers, from (Manfred Burger et al., 1998)

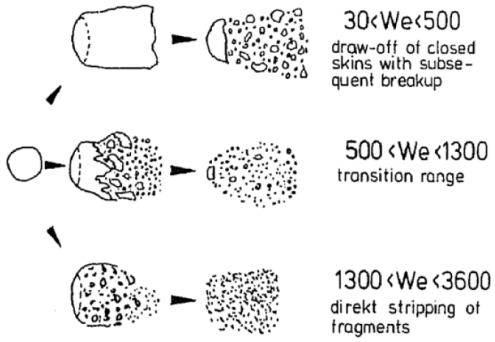

Figure 71: Schematic representation of the different fragmentation regimes observed in the liquid-liquid case, according to (Kim et al., 1983)

(Khare et al., 2012) performed 3D simulations to investigate the deformation and fragmentation of an impulsively accelerated liquid drop (of low-density ratio, 8.29) using VOF and adaptive mesh (Gerris, (Popinet, 2003)). Their simulations covered a wide range of We numbers, and they identified the oscillatory, bag, multimode and shear breakup regimes. It should be noticed that the orientation of bag in their simulation is different from the classical one in the LG configuration. Their work mainly focused on the breakup phenomenology and hasn't used the

Ranger Nicholls as time scale to analyze their results. Their simulations for higher Weber number cases represent only the early phase of fragmentation.

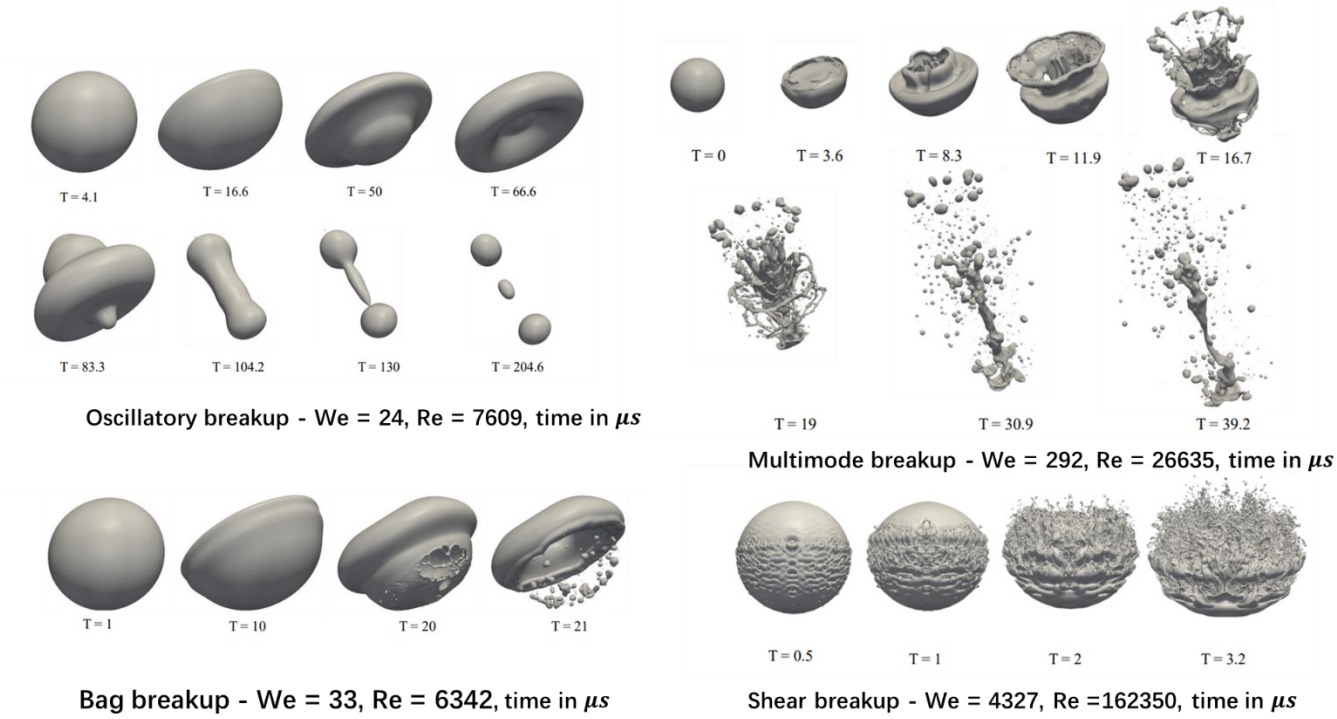

Figure 72: Observation of oscillatory, bag, multimode and shear breakup (Khare et al., 2012) of an impulsively accelerated liquid drop (of low-density ratio, 8.29) based on DNS simulation

Recently, Castrillon Escobar (Escobar, 2016) made 3D numerical simulations with the Gerris solver of Weber numbers in the range 0.6~534. He could propose a new classification of the droplet breakup specific to the liquid-liquid configuration, reproduced in Figure 73. Due to a lower density ratio (the inertia in the surrounding fluid will be more important in the liquid-liquid case), the first difference observed is the confirmation of a forward bag breakup in LL configuration, rather than the classical backward bag breakup in LG configuration, for small Weber number (12~18). With the increase of the Weber number, the breakup regimes in LL configuration proposed by (Escobar, 2016) are successively the elongation, forward-bag, wake-vortex interaction, and the catastrophic breakup. (Escobar, 2016) explained the breakup behaviors by interaction of the vortex rings with the interface. From the DNS results, he first observed that a wake vortex ring is created during the oblate part of the droplet deformation when flow separation occurs.

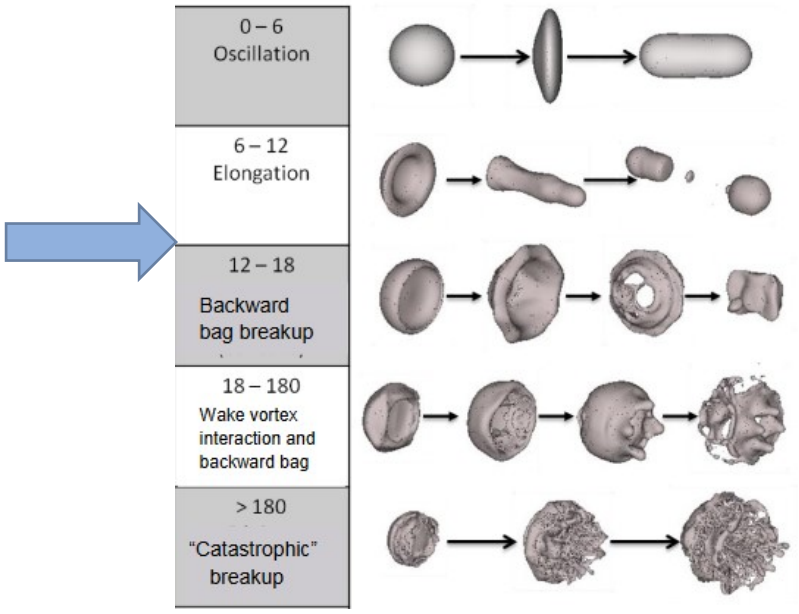

Figure 73: Classification for liquid/liquid configuration proposed by (Escobar, 2016) based on DNS simulation (ambient liquid flow from left to right).

Meanwhile, (Hadj-Achour et al., 2021) made fragmentation experiments of drops of low melting point metal alloy (62◦C for Field's metal) falling into water under the effect of gravity. By varying the water temperature, he could adjust the solidification and could somehow "freeze" the melt at some state of deformation. Combined with visualizations of the falling drops, he could confirm the absence of classic bag breakup of the LG configuration (backwards bag) and observe a rather gradual phenomenology without sudden topological changes beyond the elongation configuration.

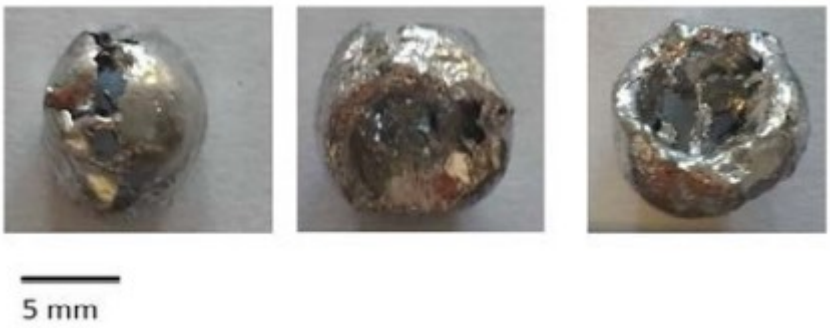

Figure 74: Solidified drop during the formation of forward bag , initial drop of 85 ◦C and ambient water of 20◦C, We = 40 (Achour, 2017)

Our first objective in this work is to extend the study of Castrillon Escobar with more precise simulations, larger Weber numbers and include heat transfer.

4.1.3. Kelvin-Helmholtz and Rayleigh-Taylor Instabilities

Although different breakup modes are qualitatively identified from experimental observation, the precise and fundamental mechanisms governing fragmentation are still subject to discussion, not to mention models/correlations to quantitively predict drop dynamics.

Many researchers try to analyze the characteristic scales of breakup (time, size) using instability theories. Here, we present two basic and widely discussed type of instabilities in breakup studies, the Kelvin-Helmholtz (KHI) and Rayleigh-Taylor Instabilities (RTI).

To highlight the mechanism, we talk about the stability of the interface in a simple one-dimensional situation, i.e., interface between two parallel layers of fluids having different properties and velocities (depicted in Figure 75). The two fluids are subject to different tangential velocities and the interface is subject to acceleration (more precisely subject to a differential pressure leading to a perpendicular displacement and acceleration of the interface), including gravity. To simplify, the effects of viscosity are not considered.

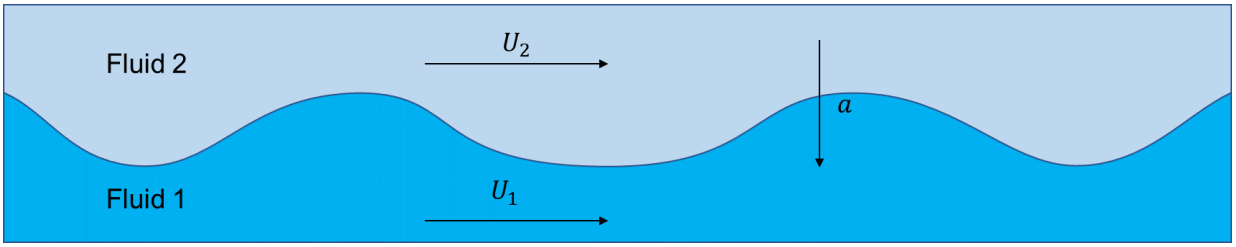

Figure 75 Stability of the interface between two layers of fluids

The derivation of different scales is based on the linearized analyses by examining the growth of a small-amplitude perturbation (wave) of the interface under the influence of the various forces acting on it (velocity lag, acceleration like gravity). By considering potential flow of two incompressible fluids, the analysis leads to the following growth factor (Yih, 1980):

$$kc_i = \left[\frac{\rho_1\rho_2(U_1-U_2)^2}{(\rho_1+\rho_2)^2}k^2 - \frac{\sigma k^3 - a(\rho_1-\rho_2)k}{(\rho_1+\rho_2)}\right]^{\frac{1}{2}}$$

where k is the wave number, $k = \frac{2\pi}{\lambda}$, λ is the wavelength of the perturbation and c_i the wave celerity. Regarding the stability of the perturbed interface, if kc_i is positive, the perturbations will grow, while any perturbation will be damped for kc_i negative.

- When the instabilities are only driven by the acceleration perpendicular to the interface, i.e., $U_1 - U_2 = 0$ & $a \neq 0$, we are talking about the RTI, the growth factor then becomes:

$$kc_i = \left[-\frac{\sigma k^3 - a(\rho_1-\rho_2)k}{(\rho_1+\rho_2)}\right]^{\frac{1}{2}}$$

  $kc_i = 0$ gives the limit wavelength for RTI stabilities:

$$\lambda_{RT} = \frac{2\pi}{k_{RT}} = 2\pi\sqrt{\frac{\sigma}{a(\rho_1-\rho_2)}}$$

  In this case, the system is stable for disturbances of wavelengths shorter than λ_{RT}, and the stabilizing effect of the surface tension overcomes the destabilizing effect of acceleration. Physically speaking, the acceleration tends to accentuate any existing perturbation, while the surface tension "stretches" the surface and tries to restore it back to its original plane shape.

  By searching the maximum of the growth factor kc_i, the most dangerous wavelength $\lambda_{RT,m}$ can be obtained:

$$\lambda_{RT,m} = 2\pi\sqrt{\frac{3\sigma}{a(\rho_1-\rho_2)}} = \sqrt{3}\lambda_{RT}$$

- When the instabilities are only driven by the velocity difference parallel to the interface, i.e., $U_1 - U_2 \neq 0$ & $a = 0$, we are talking about the KHI, the growth factor then become:

$$kc_i = \left[\frac{\rho_1\rho_2(U_1 - U_2)^2}{(\rho_1 + \rho_2)^2}k^2 - \frac{\sigma k^3}{(\rho_1 + \rho_2)}\right]^{\frac{1}{2}}$$

$kc_i = 0$ gives the wavelength for KHI stabilities:

$$\lambda_{KH} = \frac{2\pi}{k_{KH}} = 2\pi\frac{(\rho_1 + \rho_2)\sigma}{\rho_1\rho_2(U_1 - U_2)^2}$$

Now, we can qualitatively explain some observed mechanisms for the drop breakup with the drawing below.

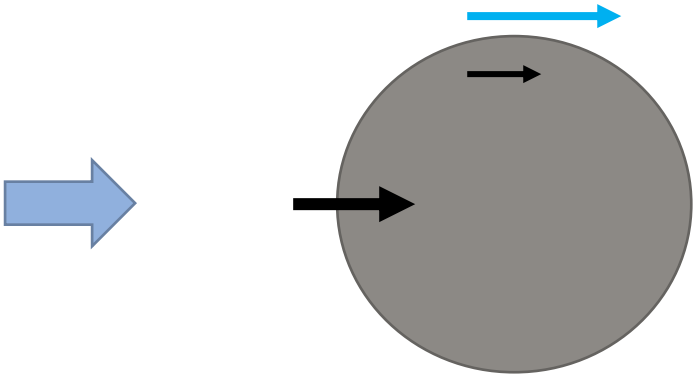

At the front of the drop, a perpendicular force is exerted on the drop interface, which produces RT instabilities. At the equator, there is a differential velocity, which produces KH types of instabilities. Both mechanisms are always present, and one will be dominant as a function of the flow and material properties. In particular, we can qualitatively explain the bag breakup of the LG configuration as the first mode of RTI. Bag and stamen would be the second mode. Stripping is obviously dominated by KH mechanisms. The catastrophic breakup at large We, as presented by Pilch & Erdmann seems largely influenced also by RT mechanisms. The fact that RT would be dominant at small and large Weber numbers, while KH would be at intermediate Weber numbers seems quite dubious.

Of course, capillary effects will also play a role, at the end of the process in general, during the burst of the bag for example, or for the fragmentation of the ligaments that are generally formed in a transient way (see e.g., Figure 76).

To explain the jet fragmentation, based on their experiments on LG system, (Marmottant and Villermaux, 2004) argue the mechanism is due to two successive instabilities. First, a Kelvin-Helmholtz type instability triggers axisymmetric modulations on the interface by shear between the two fluids. Then, these axisymmetric waves undergo transverse azimuthal modulations (caused by RTI) when the gas velocity goes beyond a critical velocity, which appear and grow until destabilization with the formation of ligaments, Figure 76. That is to say, the transverse azimuthal wave crests (caused by RTI), more or less strong, will always exist accompanying a Kelvin-Helmholtz type instability. Similar mechanism is expected for the stripping fragmentation of the drops

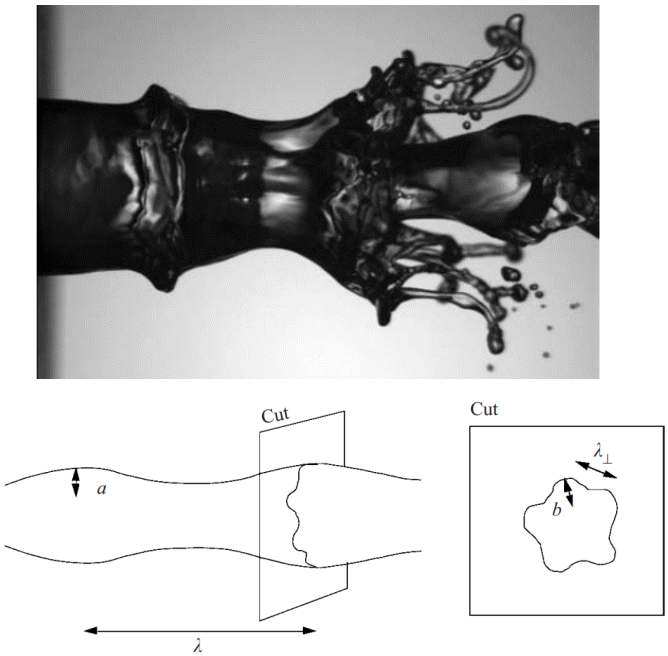

Figure 76: Breakup regimes, surface instabilities, and development of instability proposed by (Marmottant and Villermaux, 2004)

4.2. Numerical simulation: open issues/remarks for fragmentation simulations

In addition to the experimental investigation mentioned above, there are also many numerical simulations studying the drop breakup induced by velocity slip.

Using a front tracking scheme, (Han and Tryggvason, 2001) performed 2D axisymmetric simulations to study the breakup of diesel drop of low-density ratios. They found that the Weber number separating different breakup regimes decreases as the Reynolds number increases. (Quan and Schmidt, 2006) performed simulations of an impulsively accelerated liquid drop in gas flow using interface tracking scheme and mesh adaption techniques and found a larger drag coefficient for deformed drop than that of typical steady state drag coefficients of solid spheres and they explained this increase by the large recirculation region behind the deformed drop. (Khare et al., 2012; Khare and Yang, 2013) performed 3D simulation to investigate the deformation and fragmentation of an impulsively accelerated liquid drop (of low-density ratio, 10) using VOF and adaptive mesh (Gerris). Their simulations covered several breakup regimes and study the drag coefficient and found that it initially increases due to droplet deformation and then decreases at the onset of breakup, while the time-average value decreases with increasing We number. Using the same solver Gerris, (Jalaal and Mehravaran, 2014) conducted 2D and 3D simulations in shear breakup regime to study the transient growth of drop instabilities. They observed different modes of instabilities occurring during drop breakup, including Kelvin–Helmholtz instability (2D and 3D simulations), and the transverse azimuthal modulation or the Rayleigh–Taylor instability (3D simulations). (Jain et al., 2015) studied experimentally and numerically (still using the Gerris solver) the breakup of small water drop of high-density contrast (1000) for We numbers in the range 20– 120 and observed several breakup modes, bag, bag-stamen, multi-bag and shear breakup. They also found a transition regime between bag and shear breakup at We = 80 with formation of multiple lobes.

4.2.1. 2D or 3D simulation

We give priority to the 3D simulations rather the 2D ones due to the inherent three-dimensional nature of the breakup process:

- 2D simulations, either in plane or axisymmetric coordinates, are criticized because they cannot capture the turbulence behavior. As a result, the results of 2D simulation are only representative for low Reynolds.
- The formation of transverse azimuthal wave crests observed in experiments and simulations (Khare et al., 2012; Castrillon-Escobar et al., 2015; Jalaal and Mehravaran, 2014) at high Weber number cases could not be describe by 2D simulations.
- The previous work by Castrillon Escobar (Escobar, 2016) shows that, even for low Weber number ($We = 2.96$), three-dimensional cases generate lower frequencies of oscillation than the 2D-symmetry case.

4.2.2. The (quasi) DNS and mesh sizes

The goal of a so-called direct numerical simulation (DNS) is to resolve all necessary time and space scales and thus do not need to model the effect of unresolved scales. For the computation of dynamic aspects of the single-phase and multiphase flows, the Kolmogorov length scale is considered as the smallest scale to be resolved. Viscous boundary layers must also be described with a sufficient number of meshes. For multiphase flows, additional difficulties come from the existence of interfaces with sharp physical properties transition. In practice, the DNS simulation of the interface characteristics are not possible in the current context and thus a sub-mesh model of the interface is necessary, with the addition of the surface tension effect, obtained from the Laplace law,

$$\Delta P = \sigma\left(\frac{1}{R_1} + \frac{1}{R_2}\right) \quad (2)$$

where R_1 and R_2 are the main radius of curvature of the interface. Thus, the simulations should be designed more properly as “quasi”-DNS. The Laplace effect has received various numerical description but most of the models are considering it as a volume effect (Brackbill et al., 1992). The strong physical property changes at the interface also poses a serious difficulty. Most of the model, including the one used in this study, considers in fact only one phase with variable properties. At the interface, the various properties (viscosity, conductivity…etc.) are interpolated from the volume fraction of each phase. Clearly, this is a rough approximation, the role of which is diminishing when the mesh size is decreasing.

The position of the interface (within a cell) may be obtained in various ways (Tryggvason et al., 2011):

- Tracking the interface: this one is represented by a collection of points, the position of which being tracked with a specific method. A major drawback is the non-preservation of the volumes and needs for very precise numerical schemes.
- Guess of the interface position: the Volume-of-Fluid (VOF) method is reconstructing the interface at each time step as a function of the gradients of the tracked volume. Among them, the VOF-PLIC method is considering the interface as a locally plane surface. This is the method employed in the Basilisk tool used in the present study.

For VOF method (used in study), topology changes, such as those occurring during reconnection or breakup, are implicit during the reconstruction process (Tryggvason et al., 2011). From a geometric perspective, drops with less than 2 cells per diameter cannot be represented with VOF methods. Topology change is initiated automatically once two interface segments enter the same computational grid cell. VOF thus contains an inherent breakup length scale of the order of the local grid size, making the topology-change process grid dependent. As a result, the exact moment of topology change might not be predicted accurately (which we will also see from our simulations).

Moreover, the numerical error of VOF-PLIC representation will probably be significant for drops with less than 8 cells per diameter. From a practical point of view, we need that drops preserve their physical behavior during processes such as deformation, fragmentation, and translation (Pairetti et al., 2020).

However, the error in volume of the broken-off liquid structure is only of the order of the volume of the local grid cell, thus should not significantly affecting drop sizes larger than several local grid-cell volumes. Still, owing to the inherent grid dependency, it is incumbent to an interface-capturing DNS user to demonstrate grid independence (Gorokhovski and Herrmann, 2008) of his results.

Knowing the different length scales to be resolved, we can now conclude that DNS for high Reynolds number and high Weber number cases is still in its infancy due to high computational cost. When the mesh size could not resolve all the length scales, we are neglecting the sub grid terms. As such, we better call it quasi-DNS, or under-resolved DNS. Despite that quasi-DNS neglects the sub-grid terms, it can still yield valuable insight into the breakup process and the resulting drop-size distribution if it can be shown that the small-scale non-resolved phase-interface dynamics does not influence the larger-scale resolved phase-interface dynamics.

A measure for this prerequisite is the grid convergence of the resolved-scale drop-size distribution: Refining the grid should not alter the resulting resolved-scale drop-size distribution.

The previous works on this issue were mainly done for jet atomization simulations. (de Villiers et al., 2004) performed relatively coarse simulations of the Diesel jet breakup under typical operating conditions. They performed a one-level grid-convergence study and found that these distributions were significantly different, even for larger size fragments. This indicates that for their employed grid resolution, the quasi-DNS assumption is questionable. (Kim et al., 2006) performed a limited grid-convergence study, observing indications for grid-converged drop-size distributions for drops that were resolved by at least two grid points. (Pairetti et al., 2020) found that the mesh resolution affects not only the capability of generating small droplets but also the frequency of ligament detachment. They also find that, a simulation with coarser mesh will have fewer small drops, more large liquid structures, and probably a higher atomized volume.

4.2.3. Important quantities for breakup analysis and modelling

4.2.3.1. Deformation length characterization

At the beginning of interaction, the spherical drop will firstly undergo deformation. To characterize such behavior, the projected length of deformed drop in different direction is defined. The maximum projected length in the stream-wise direction (along with the flow direction) and in the cross-stream direction are called the D_{wise} and D_{cross}.

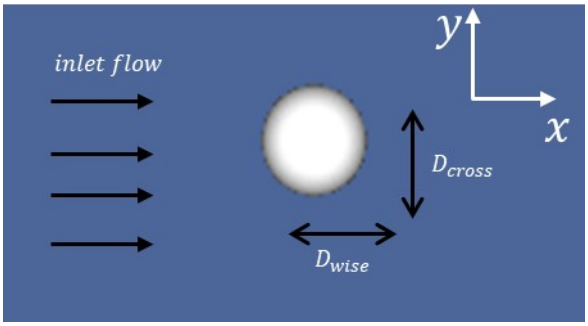

Figure 77: Definition of deformation parameter for drop in x-y plan when inlet flow is along the x-direction

4.2.3.2. Forces acting on the drop

Gravity is not accounted for in our simulations since it has a negligible effect. There are two forces exerted on the drop when it moves through an environmental fluid, the drag force F_Γ and the surface tension force F_σ. The surface tension force F_σ is given by

$$F_\sigma = \int_{\delta\Gamma} \boldsymbol{\sigma k n}\, \delta\Gamma$$

The drag force can be written as

$$F_\Gamma = -\int_{\delta\Gamma} (-p\boldsymbol{I} + 2\mu\boldsymbol{D}) \cdot \boldsymbol{n}\ d\delta\Gamma$$

The drag force can be further decomposed into a pressure drag F_p and a viscous drag F_μ:

$$F_\mathrm{p} = \int_{\delta\Gamma} p\boldsymbol{I} \cdot \boldsymbol{n}\ d\delta\Gamma$$

$$F_\mu = -\int_{\delta\Gamma} 2\mu\boldsymbol{D} \cdot \boldsymbol{n}\ d\delta\Gamma$$

Here Γ is the interface of drop, physical quantities defined towards outside the interface, i.e., all properties defined and evaluated in the surrounding fluid side.

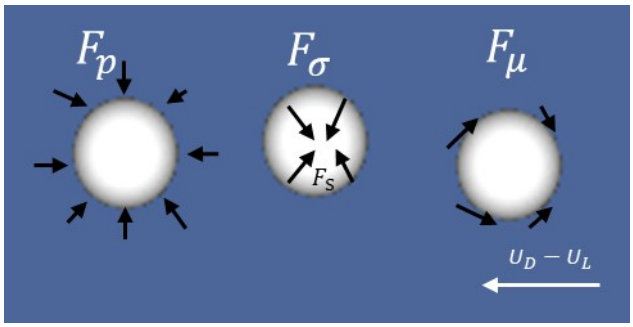

Figure 78: Force that the drop can undergo in another liquid

These forces act on the drop and accelerate it in the direction of flow. However, the contribution of surface tension to the overall acceleration of the drop is negligible. First, since Weber number is the ratio of the destabilizing aerodynamic force to the stabilizing surface tension force, surface tension is only important for low Weber number cases. However, for low Weber number cases, the drop has no large deformation and undergoes quasi-periodic oscillation, which cannot effectively contribute to the overall acceleration of the drop. Therefore, the drag force is considered as the effective force accelerating the drop.

On the anther hand, the drag force can be correlated by $F_\Gamma = -0.5C_d\rho_L(dU)^2A_{front}$ where C_d the drag coefficient, dU the velocity difference between inlet flow (U_{inlet}) and drop mass centroid (U_{drop}), and A_{front} the drop frontal area.

According to the Newton's second law, we have, $m_{drop}\frac{dU_{drop}}{dt} = 0.5C_d\rho_L(dU)^2A_{front}$.

After simplification, the drag coefficient in our simulation can be computed as:

$$(3)\quad C_d = \frac{4}{3}\frac{\rho_{drop}}{\rho_L}\frac{1}{\left(U_{drop}-U_{inlet}\right)^2}\frac{D_0^3}{D_{front}^2}\frac{dU_{drop}}{dt}$$

4.2.3.3. Sauter mean diameter (SMD)

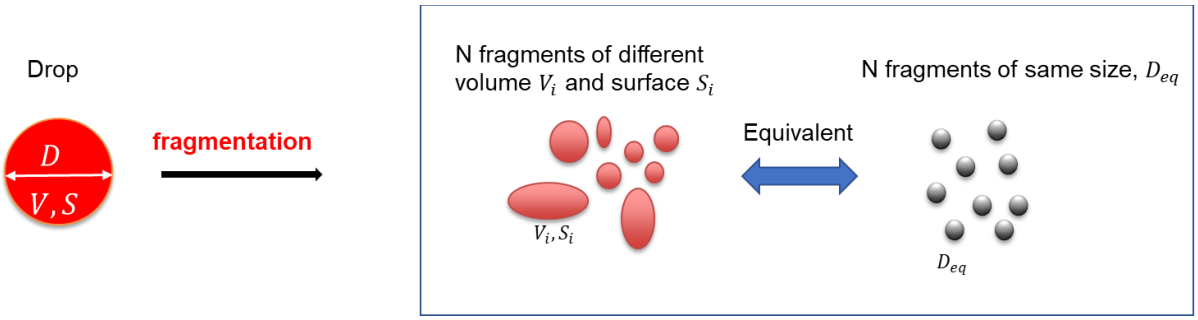

Figure 79: Illustration of fragmentation process and the corresponding equivalent fragments for modeling

After fragmentation, the spherical drop breaks up into several fragments (may be in spherical or irregular form) of different volume and surface. For the sake of the analysis and comparison with results of CFD codes like MC3D, we are led to introduce convenient ways for the characterization.

A first straightforward way is to define size average. There are many ways to do this.

To define an equivalent diameter using total surface area, the $D_{2,0}$ can be defined by equation, $\sum_N S_i = N(\pi D_{2,0}^2)$.

To define an equivalent diameter using total volume, the $D_{3,0}$ can be defined by equation, $\sum_N V_i = N\frac{\pi D_{3,0}^3}{6}$.

To define an equivalent diameter using the ratio of volume to surface area, the $D_{3,2}$ (called also Sauter Mean Diameter/SMD or D_s) can be defined by equation, $\frac{(\pi\frac{D_S^3}{6})}{(\pi D_S^2)} = \frac{\sum_N V_i}{\sum_N S_i} = \frac{D_{3,0}^3/6}{D_{2,0}^2} = \frac{V_{tot}}{A_{tot}}$, which yields, $D_S = \frac{D_{3,0}^3}{D_{2,0}^2} = \frac{6V_{tot}}{A_{tot}}$.

As the total volume of drop conserves during fragmentation, $V_{tot} = cst$, thus the SMD reflects the change in total interfacial area during the fragmentation, and its value is inversely proportional to the surface area. SMD is thus the diameter of the equivalent drop that will preserve both the total volume and the total surface.

The SMD is the representative size for our study. Here, we try to give a simple explanation. The idea is to take all the fragments as an object of study and to model the overall heat transfer behavior. The total surface area and volume of all fragments are $(\sum_i A_i)$ and $(\sum_i V_i)$. We supposed that all fragments together have an average temperature T and average heat transfer coefficient $\overline{h}$, the evolution of temperature should follow the equation:

$$\rho C_p \left(\sum_i V_i\right)\frac{dT}{dt} = \overline{h}(\sum_i A_i)(T - T_{bulk})$$

which yields

$$\rho C_p D_s \frac{dT}{dt} = \overline{h}(T - T_{bulk})$$

This simple analysis allows to show the importance of SMD for the heat transfer modeling, which is widely used in the CMFD-type software. However, it is not so simple:

- **$\overline{h}$ represents the mean heat transfer coefficient as it also depends on the diameter, so it's difficult to conclude from the classical correlation.**
- **The smallest fragments will be cooled before the largest ones. Therefore, during the cooling process, the SMD will progressively loose its representativeness, given priority to cold fragments.**

The SMD is then to be considered with caution as an indicator. Then, in thermal-hydraulic problems, in particular FCI, the use of only one single size is not sufficient to describe the behavior of melt, and MC3D uses multiple size group (MUSIG) type approach to describe drops of different size.

4.3. Numerical and simulation setup

4.3.1. Basilisk solver

The Basilisk solver used in our application is dedicated to the incompressible flow of two immiscible liquids (Popinet, 2021). In fact, the model involves only one single fluid with two "phases" with an indicator of the volume fraction of one phase. The interface is handled by the Volume of Fluid method. In this study, the physical properties (heat conductivity, viscosity, density, etc.) do not depend on the temperature and are simple functions of the phase indicator. A supplementary module is used to solve the equation of heat advection-conduction (equation (4), $\mathfrak{D} = \frac{\lambda}{\rho C_p}$). The total equation set is:

$$\nabla \cdot \boldsymbol{U} = 0 \tag{1}$$

$$\boldsymbol{\rho}\frac{\boldsymbol{\partial U}}{\boldsymbol{\partial t}} + (\boldsymbol{\rho U}\cdot\boldsymbol{\nabla})\boldsymbol{U} = -\boldsymbol{\nabla P} + \boldsymbol{f} + \boldsymbol{\nabla}\cdot\boldsymbol{\mu}[\boldsymbol{\nabla U} + (\boldsymbol{\nabla U})^T] + \boldsymbol{f_\sigma \delta_s} \tag{2}$$

$$\frac{\boldsymbol{\partial C}}{\boldsymbol{\partial t}} + \boldsymbol{\nabla}\cdot(\boldsymbol{CU}) = \boldsymbol{0} \tag{3}$$

$$\frac{\boldsymbol{\partial T}}{\boldsymbol{\partial t}} + \boldsymbol{U}\cdot\boldsymbol{\nabla T} = \boldsymbol{\nabla}\cdot(\boldsymbol{\mathfrak{D}\nabla T}) \tag{4}$$

Physical quantities such as density and viscosity are established as average values from linear interpolation using phase volume fractions, while the diffusivity coefficient is a harmonic average weighted by volume of fluid to maintain a sharp interface for temperature diffusion.

One of the advantages of Basilisk is the optimization of the mesh by adaptive mesh refinement (AMR) with a wavelet-based strategy based on the estimation of numerical errors in the representation of spatially discretized fields (the velocity, volume fraction and temperature in our case). An example of meshes used in our simulations is shown in Figure 80 A detailed illustration of wavelet based error estimation can be found by (van Hooft et al., 2018).

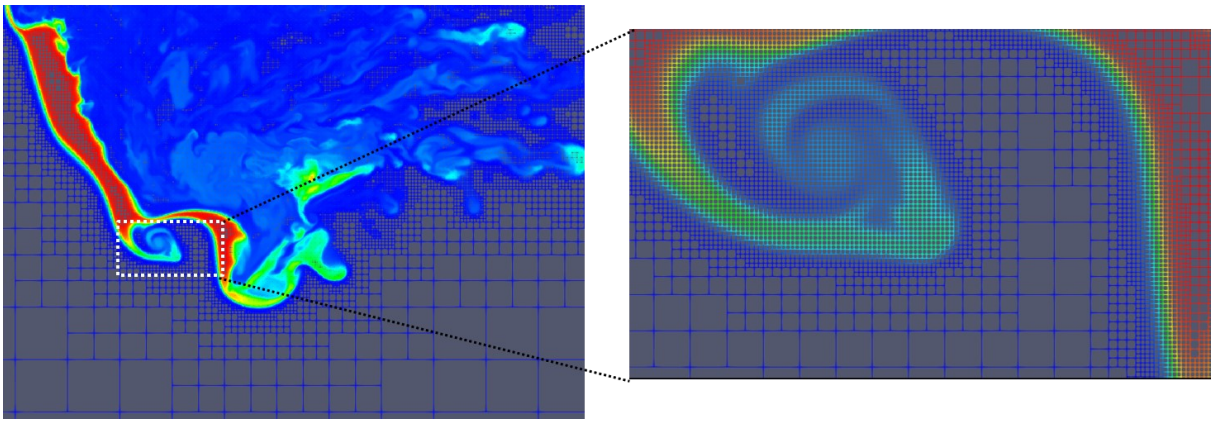

Figure 80: A example of meshes used in our simulations (case We=640 defined in Table 10). Meshes are automatically refined at the interface and the zone with high turbulence (inside the wake) and large temperature gradient

4.3.2. Characteristic length scale and mesh size

On the one hand, the accuracy of a numerical simulation with interface and fragmentation depends greatly on ratio of the size between the smallest mesh and the smallest structure that we want to capture. It shows the necessity to use a mesh as fine as possible to capture the flow characteristics. On the other hand, not all the

structures of flow can be solved because that would involve, sometime, an overwhelming computing time. It means that a reasonable compromise in the mesh size should be made. Thus, it is important to figure out the length scale, and then based on this length scale, we can estimate a suitable mesh size for our study to both capture the flow characteristic and optimize the use of computation resource.

In fact, for our application, three main phenomena which should be considered and captured are the fragmenta tion, the dynamical and thermal boundary layers, which will give three length scales.

As for fragmentation, the characteristic length scale should be in the same order of magnitude as the instabilities which can develop at the interface of the drop. For our application, the velocity shear is the main reason to cause the drop hydrodynamic fragmentation, thus, the wavelength of Kelvin-Helmholtz instabilities can provide a first estimation of the characteristic size of the particles (Zhdanov, 1995),

$$\lambda_{KH} = 2\pi \frac{(\rho_D + \rho_C)\sigma}{\rho_D \rho_C \Delta U_{D-C}^2} = 2\pi \frac{\left(1 + \frac{\rho_C}{\rho_D}\right)\sigma}{\rho_c \Delta U_{D-C}^2} \tag{5}$$

Here, λ_{KH} represents the minimal size beyond which the instability will start to grow and develop, it can be regarded as the smallest size of structure needed to be captured. Defining the characteristic Weber number as $We_{Ch} = 2\pi\left(1 + \frac{\rho_C}{\rho_D}\right)$, the scale of drops that are produced during fragmentation is given by:

$$\lambda_{KH} = \frac{We_{Ch}\sigma}{\rho_c \Delta U_{D-C}^2} = \frac{\boldsymbol{We_{Ch}}}{We} D_0 \tag{6}$$

which means the smallest mesh size should inversely depend on the Weber number of drops of diameter D_0 in the fluid ($We = \frac{\rho_c \Delta U_{D-C}^2 D_0}{\sigma}$).

As for the dynamics, minimum length scales are considered using the principle discussed in (Pairetti et al., 2020). The Kolmogorov scale η defines the length for resolving all the turbulent structures.

$$\eta = \frac{D_0}{Re_T^{\frac{3}{4}}}, \qquad Re_T = \frac{\rho_L u_t D_0}{\mu_L} \tag{7}$$

where u_t is the typical velocity fluctuation. (Pope, 2000) suggests the resolution of all scales by DNS is only possible when the mesh size is smaller than 2 times the Kolmogorov scale, which means the smallest mesh also depends on the turbulent Reynolds number Re_T. Typically, the turbulent Reynolds number Re_T is 10% to 20% of Reynolds number Re evaluated from the inlet velocity (Tiselj et al., 2020). In our simulation, we assume that $Re_T = 0.2Re$.

As the heat transfer is highly influenced by the flow advection, the thickness of thermal boundary layer, i.e. the length scale for the heat transfer, is related to the dynamic boundary layer by the Prandtl number (Kalman and Letan, 1985), the smallest mesh thus depends on the Prandtl number Pr. It's supposed that this thermal length depends linearly on the length scale of turbulence and the thickness ratio of dynamic and thermal boundary layer.

$$\frac{l_{thermal}}{l_{dynamic}} = 1, \qquad Pr = 1. \tag{8}$$

$$\frac{l_{thermal}}{l_{dynamic}} = Pr^{-\frac{1}{3}}, \quad 2 < \mathrm{Pr} < 10 \tag{9}$$

However, as the flow is not necessarily dominated by viscous forces, an accurate capture of the heat transfer may need a thinner mesh. Indeed, our sensitivity study indicates that convergence on heat transfer is more difficult than that of the dynamic aspects, even at Prandtl = 1.

Therefore, depending on the Weber number, Reynolds number and Prandtl number, the smallest mesh, thus the level of refinement could be determined. In Basilisk, the level of refinement l corresponds to 2^l meshes per direction. Limited by the actual computation resource, the maximum level of refinement was 13 (AMR allows at maximum 2^{13} meshes per direction).

Considering the whole calculation domain is 22.5 times the initial drop diameter, the smallest mesh (for level 13) in the simulation is given by:

$$\Delta x = \frac{22.5 D_0}{2^{13}} = 2.7\ 10^{-3} D_0 \tag{10}$$

Moreover, to avoid having high intensity artificial currents or losing the mass of the liquid due to low spatial resolution, it should be ensured that the smallest drops are resolved by at least 10 mesh points on the diameter, which factor 10 is taken into accounting in equation (6).

To guarantee that a fragment of size $d \sim \lambda_{KH}$ can be well resolved, the following condition should be fulfilled:

$$\Delta x * 10 < \lambda_{KH} \tag{11}$$

which is equivalent to:

$$\frac{22.5 D_0}{2^{13}} * 10 < \frac{2\pi \left(1 + \frac{\rho_C}{\rho_D}\right)}{We} D_0 \tag{12}$$

Strictly speaking, the maximum Weber number allowed by equation (12) is only 257.

Using the same principle, to guarantee the dynamical and thermal length scale estimated in equation (6) can be well resolved, the following condition should be filled:

$$\Delta x < 2\eta * Pr^{-\frac{1}{3}} \tag{13}$$

which is equivalent to:

$$\frac{22.5 D_0}{2^{13}} < 2 \frac{D_0}{(0.2Re)^{\frac{3}{4}}} Pr^{-\frac{1}{3}} \tag{14}$$

and the maximum Reynolds number allowed by equation (14) is 32755 for Pr=1 (gases or saturated water) or 13793 for Pr=7 (cold water).

Limited by the current computational capabilities, these three smallest length scales discussed above may not be captured for all simulated cases. However, as discussed in chapiter 4.2.2, even if not all the length scales are captured for higher Reynolds number cases, these simulations can still yield valuable insight into the breakup mechanisms if it can be shown that the small-scale non-resolved phase-interface dynamics does not influence the larger-scale resolved phase-interface dynamics. A sensitivity analysis related to the mesh dependency is provided in chapter 4.4.2.

4.3.3. Test Case

4.3.3.1. VOF advection of 2d circle in reversed single vortex flow

To assess the VOF advection algorithms of Basilisk and study the influence of refinement criterion, the classical test, simulation of stretching and recovering process of an initially circular interface, was made.

A circle of radius 0.2 is initially positioned at point (-0.2, -0.236338) in a unit square domain. All other boundaries are periodic, and the velocity field is computed by the stream function:

$$\boldsymbol{\psi = -\frac{1,5}{\pi} sin(\frac{2\pi t}{T}) sin(\pi(x + 0,5))\ sin(\pi(y + 0,5))}$$

.

In this test, the period of the stretching cycle is set to 15. The interface reaches a maximum deformation at time $\boldsymbol{t = \frac{T}{2}}$, while at time $\boldsymbol{t = T}$ it returns to the initial position because the temporal component is periodic. The difference between the initial and final shapes is a good indication of the accuracy because it measures the

accumulated errors during VOF advection.

$$E = \frac{\sum_i \left\| f_i^{ini} - f_i^{fin} \right\| V_i}{\sum_i V_i}$$

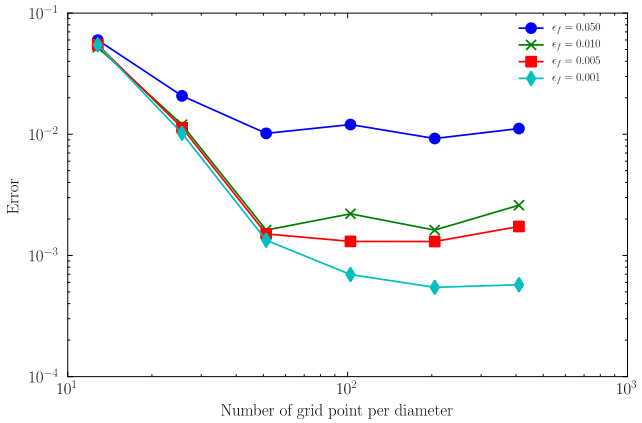

Figure 81: Errors in function of mesh size for the single vortex test, different curves corresponding different threshold for mesh refinement

$\boldsymbol{\varepsilon_f}$ is the error threshold used in automatic mesh refinement. Basilisk will perform a wavelet analysis to find the zones to be refined, and indeed, zones with an error greater than $\boldsymbol{\varepsilon_f}$ will be automatically refined, up to the maximum level. Mesh refinement can be performed based on any user-defined variable. In this test case, it is done based on VOF.

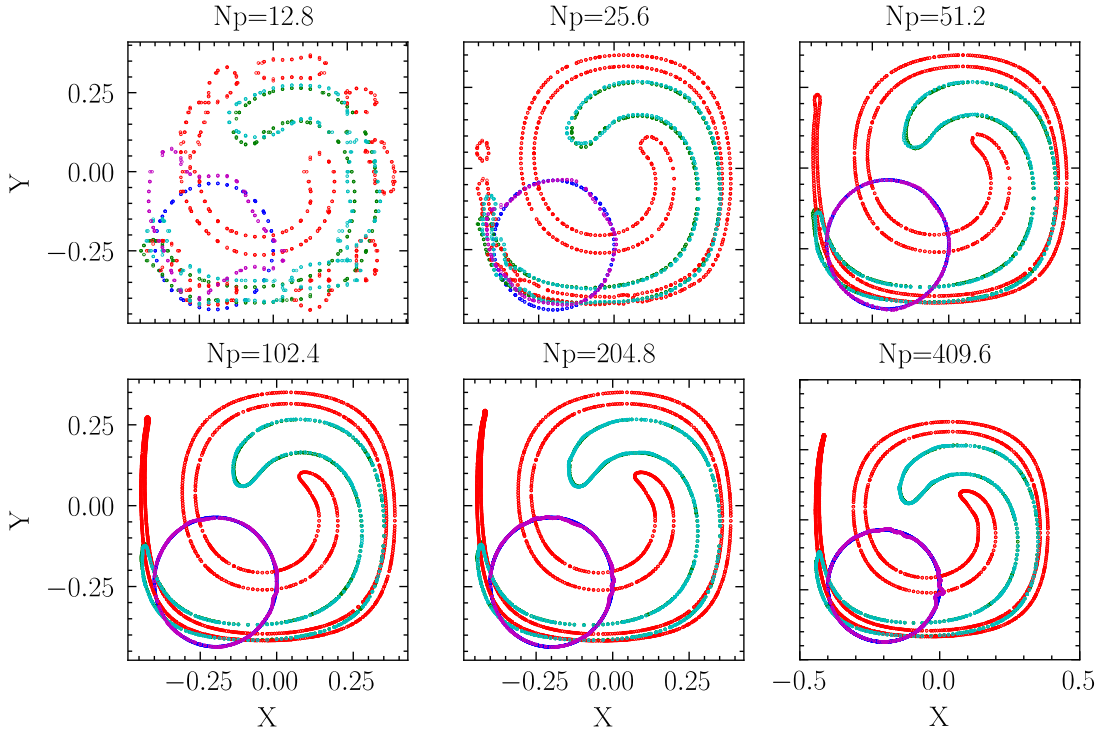

Figure 82: Interface at 0, T/4, T/2, 3T/4 and T for $\boldsymbol{\varepsilon_f = 0.005}$, different sub-figures represent different grid size (number of grids per diameter)

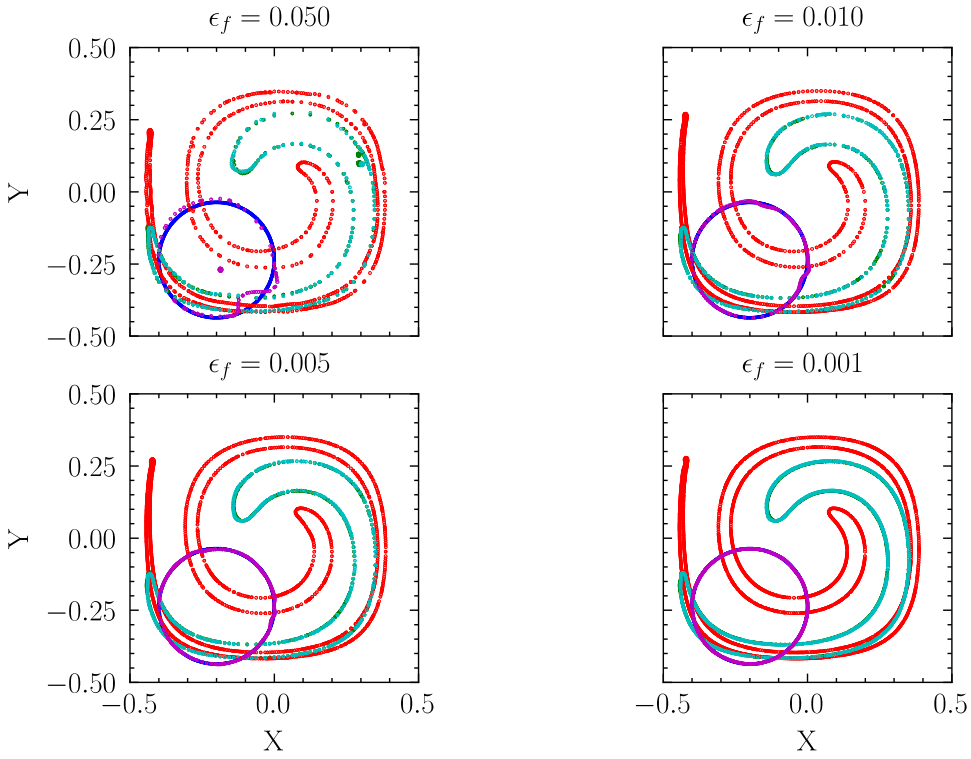

Figure 83: Interface at 0, T/4, T/2, 3T/4 and T for $\boldsymbol{Np = 102.4}$ ***(number of grid points per diameter)****, different sub-figures represent different threshold for mesh refinement*

This test shows the following behavior of the solver:

- To have satisfactory results, it's necessary to use a small threshold for mesh refinement. When this threshold is too big, the accuracy of results cannot further improve by level increase because this threshold does not allow an effective detection of a potential need for mesh refinement to the maximum level.
- When the threshold for mesh refinement is smaller enough (<0.01), the finer mesh gives generally more accurate results.

In our simulations, the threshold for mesh refinement is set to be 0.005.

4.3.3.2. VOF advection of sphere in reversed single vortex flow

As all our simulations are performed in in three dimensions, which involves much complex topological structures, here, we do also the 3D-testcase for the VOF advection of sphere in a non-linear time reversing solenoidal flow using the same configuration as (Enright et al., 2002).

A sphere of radius 0.15 is initially positioned at point (0.35, 0.35, 0.35) in a unit cube domain. All other boundaries are periodic, and the velocity field is computed using stream function, yielding:

$$\boldsymbol{u = 2sin^2(\pi x)\, sin(2\pi y)\, sin(2\pi z)\cos\left(\frac{\pi t}{T}\right)}$$

$$\boldsymbol{v = -sin(2\pi x)\, sin^2(\pi y)\, sin(2\pi z)\cos\left(\frac{\pi t}{T}\right)}$$

$$\boldsymbol{w = -sin(2\pi x)\, sin(2\pi y)\, sin^2(\pi z)\cos\left(\frac{\pi t}{T}\right)}$$

Under the effect of this reversing velocity, the initial spherical interface will be stretched to form thin sheets at $\boldsymbol{t = \frac{T}{2}}$, and come back to its original spherical shape at $\boldsymbol{t = T}$. In this test, the period is set to be 3.

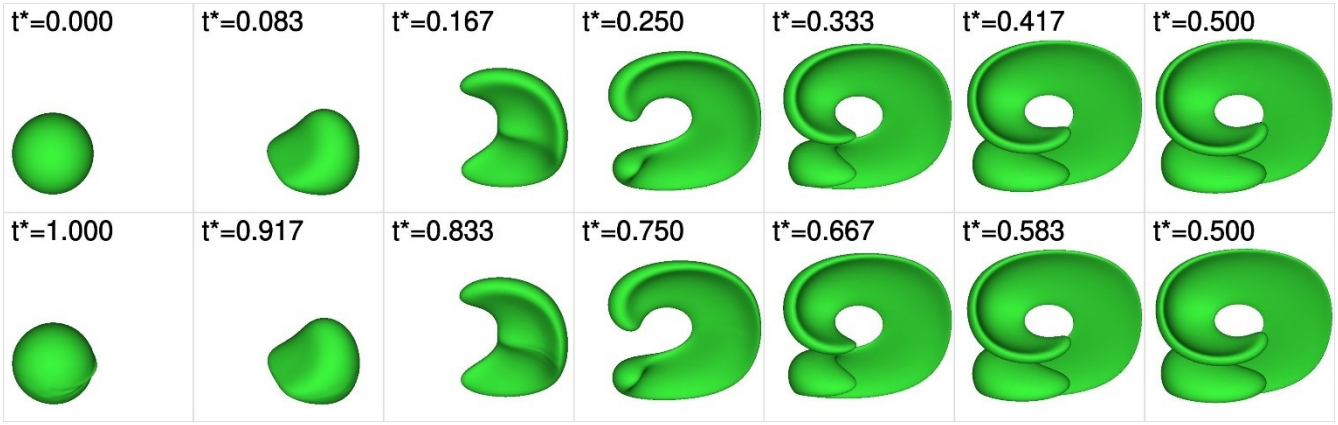

Figure 84: Interface at different instant for every T/12, and for $\boldsymbol{\varepsilon_f = 0.005}$*, level=9 (maximum 153.6 grids per diameter)*

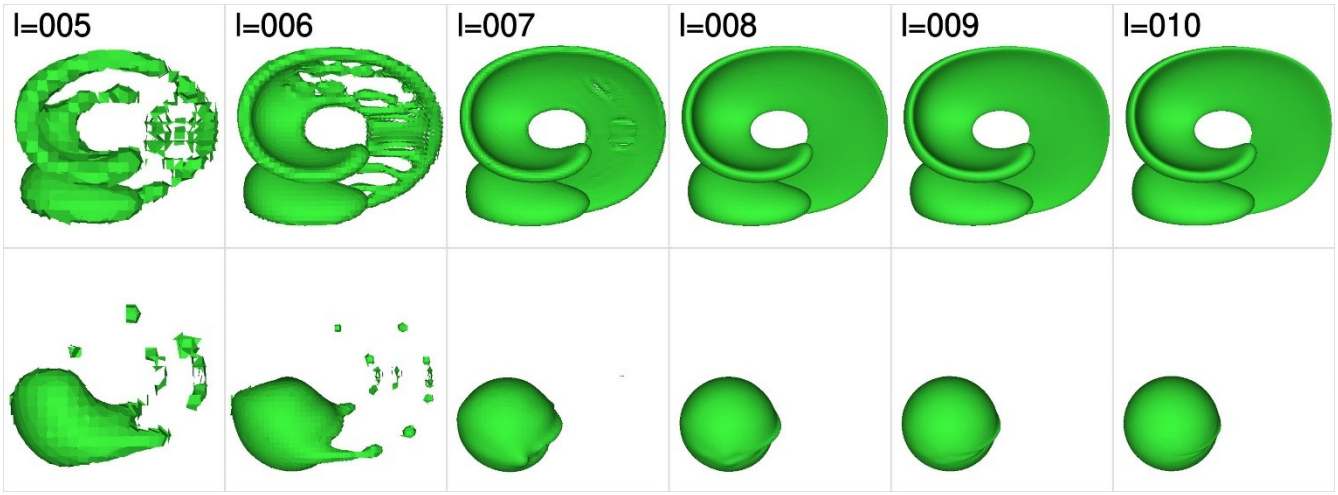

Figure 85: Interface at T/2 (maximum stretching) and T (should come back to initial position), and for $\boldsymbol{\varepsilon_f = 0.005}$*, level=5 to 9 (maximum 9.6 to 153.6 grid per direction)*

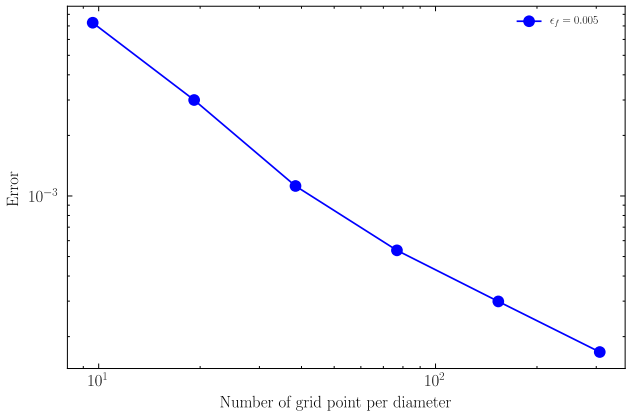

Figure 86 errors in function of mesh size for $\boldsymbol{\varepsilon_f = 0.005}$

This test shows the following behavior of the solver:

- When the mesh is too coarse, the numerical effect is so strong that it cannot capture all the deformation behavior. But such effect can be check by a mesh independence study. If the behavior is purely a numerical effect, it can be reduced when using a finer mesh.

- For simulation involved highly drop deformations, 100 grid per diameter seems to give reasonable results with small error.

4.3.3.3. 1D transient conduction (thermal diffusion)

The objective of this first test is to validate the transient diffusion solver in term of accuracy and efficiency when the AMR is used. The test case is about a solid flat wall which is quenched from a high temperature we try to find the one-dimensional temperature distribution inside the slab. Supposing that the initial temperature, the thickness, and thermal diffusivity of slab are all equal to be unity, and the boundary temperature is fixed to be 0, the analytical solution can be obtained by solving the heat diffusion equation by separation of variables,

$$\boldsymbol{T(x,t) = \frac{4}{\pi}\sum_{n=0}^{\infty}\frac{1}{2n+1}\sin\big((2n+1)\pi x\big)\exp\big(-(2n+1)^2\pi^2 t\big)}$$

Considering our application and the order of magnitude of time step (in μs), the computation is performed for $4\ ms$. The results of computation are in good agreement with the analytical one indicated in the Figure 87.

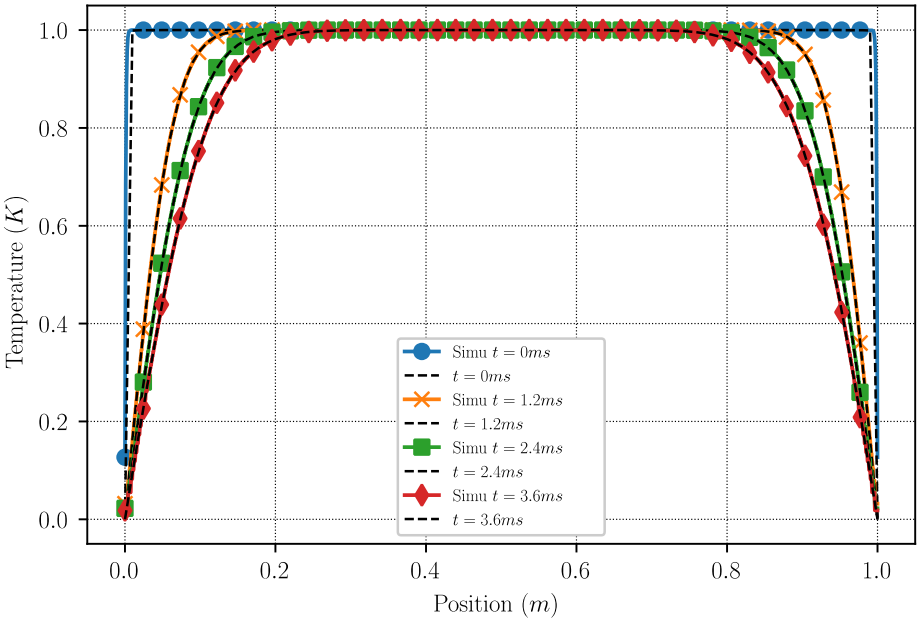

Figure 87: Comparison of temperature profiles between simulation and analytical solution at different time steps

Test for contact of two materials

In the second test-case, the heat conduction between two semi-infinite solids of different physical properties and initial temperature are considered and it is supposed that they have a perfect conduct with no thermal resistance. The boundary condition is supposed to be constant. This hypothesis is only valid for the onset (the very beginning) of heat conduction for solids of finite length, which is the situation in our test-case.

Equation of heat conduction in dimensionless form:

$$\boldsymbol{\frac{\partial T^*}{\partial t^*} = \nabla\cdot(\nabla\mathfrak{D}^*\,T^*)\frac{\partial T^*}{\partial t^*}}$$

$$\rho_i^* = \frac{\rho_i}{\rho_0},\ Cp_i^* = \frac{Cp_i}{Cp_0},\ \boldsymbol{\lambda_i^*} = \frac{\lambda_i}{\lambda_0},\ \mathfrak{D}_i = \frac{\lambda_i}{\rho_i Cp_i}\mathfrak{D}_i^* = \mathfrak{D}_i/\mathfrak{D}_0$$

$$T^* = \frac{T_i - T_{0,int}}{T_{1,int} - T_{0,int}} \; t^* = \frac{t}{(l^2/\alpha_o)} \text{ and } \mathrm{x}^* = \frac{\mathrm{x}}{l}$$

The left side has a high initial temperature with the physical properties of corium. The right side has a low initial temperature with the physical properties of water. All physical properties are rendered dimensionless using the properties of water as a reference. The analytical solutions are in the following form:

$$T_s^* = \frac{\sqrt{\lambda_1 \rho_1 Cp_1}}{\sqrt{\lambda_1 \rho_1 Cp_1} + \sqrt{\lambda_0 \rho_0 Cp_0}} = \frac{\sqrt{\lambda_1^* \rho_1^* Cp_1^*}}{\sqrt{\lambda_1^* \rho_1^* Cp_1^*} + 1}$$

$$T^* = \begin{cases} T_s^* \left(\mathrm{erfc}\left(\frac{\mathrm{x}^*}{2\,\mathrm{sqrt}(\mathfrak{D}_0^*\, \mathrm{t}^*)} \right) \right) & \text{if } \mathrm{x} > 0 \\ T_s^* + (1 - T_s^*) \left(\mathrm{erf}\left(-\frac{\mathrm{x}^*}{2\,\mathrm{sqrt}(\mathfrak{D}_1^*\, \mathrm{t}^*)} \right) \right) & \text{if } \mathrm{x} < 0 \end{cases}$$

The results from our simulation and analytical solution are shown in the Figure 88,which shows good agreement.

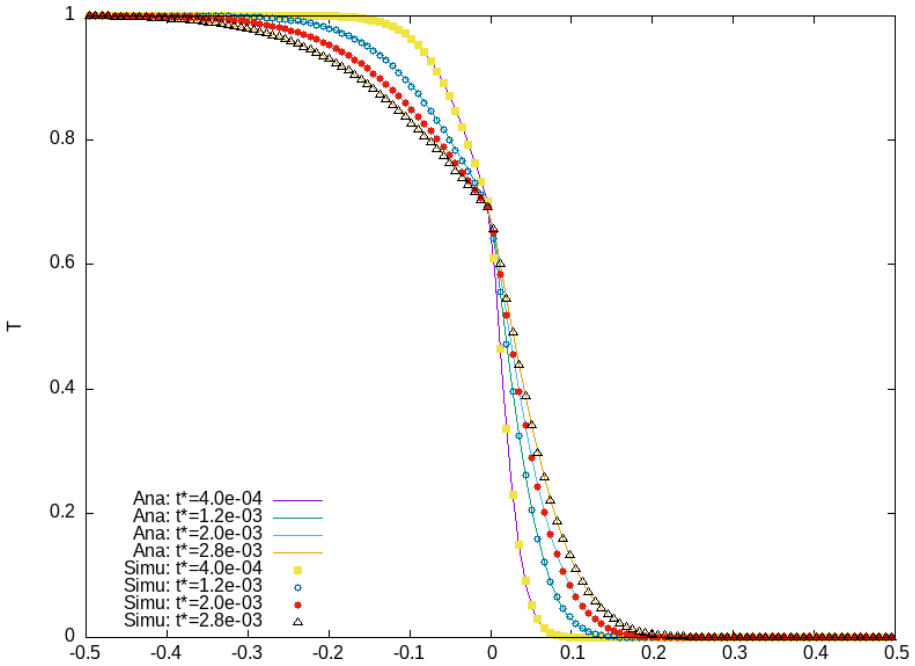

Figure 88 Comparison of temperature profiles between simulation and analytical solution at different time steps

4.3.3.4. Convective heat transfer in single phase

The objective of this validation test is to make sure that the convection and diffusion of temperature field as well as the thermal boundary are well predicted in the simulation. Calculations of a monophasic flow around a heated cylinder is performed. The Nusselt number from simulation is compared to the one from the classical correlations. Table 6 presents the expression of the correlation as well as their domain of application. Different Reynolds number varying between 20 and 280 are tested.

This study uses similar conditions used in the previous studies (see (Zambaux, 2016)). We consider a cylinder (or a sphere in 3D) of diameter D=300 µm, at constant temperature T_D and the inlet liquid T_f circulates around this cylinder with a constant inlet velocity U. In this part, all the calculations have been carried out with the constant physical properties (the effect of temperature on physical properties is not considered) and the properties for cylinder and liquid are set to be the same. The calculation is performed in the dimensionless form by varying the viscosity and thermal diffusivity of fluid.

Table 6: Classical correlations of heat transfer around a cylinder/sphere with a fixed wall temperature (Whitaker, 1972)

Name of correlation	Numerical expression	Range of application
Whitaker (cylinder)	$Nu_{Whit} = \left(0{,}4Re_D^{0,5} + 0{,}06Re_D^{\frac{2}{3}}\right) Pr^{0,4} \left(\frac{\mu}{\mu_W}\right)$	$1 < Re_D < 10^5$; $0{,}67 < Pr < 300$
Whitaker (sphere)	$Nu_{Whit} = \left(0{,}4Re_D^{0,5} + 0{,}06Re_D^{\frac{2}{3}}\right) Pr^{0,4} \left(\frac{\mu}{\mu_W}\right) + 2$	$1 < Re_D < 10^5$; $0{,}67 < Pr < 300$

The dimension of the calculation domain is set as 7 times the cylinder diameter. In term of initialization, the VOF of cylinder and liquid zone equal respectively to 1 and 0. The cylinder is initial in still while the liquid is initially move in velocity U.

Table 7: Physical properties and parameters used in the validation test

Parameters	Values
Diameter of cylinder D	1.
Inlet velocity U	1.
Temperature of cylinder T_D	1.
Temperature of inlet liquid of T_f	0.
Density of the fluid ρ	1.
Reynolds number Re	From 20. to 280.
Prandtl number Pr	1 (corresponding the equal thickness of thermal and dynamic boundary)
Viscosity μ	$\frac{1}{Re}$
Diffusivity $\mathfrak{D}$	$\frac{1}{RePr}$

As for boundary conditions: at the left, the liquid enters the domain with a fixed velocity and temperature; at the right, the liquid leaves the domain freely (the pressure outlet condition) and the temperature in this boundary is supposed to be adiabatic. For the other sides, they are sliding and adiabatic wall.

As the Navier-stoker and energy equations are solved in the whole domain, including the zone of cylinder, the temperature and shape of the cylinder are reset manually after each iteration, i.e., the interface between the cylinder and fluid is reconstructed, the velocity and the temperature of cylinder is reinitialized.

To calculation the final Nusselt number from the simulation, we calculate the transient heat flux through the interface, then the transient Nusselt number and the average Nusselt number when the flow goes into the permanent state (Figure 90).

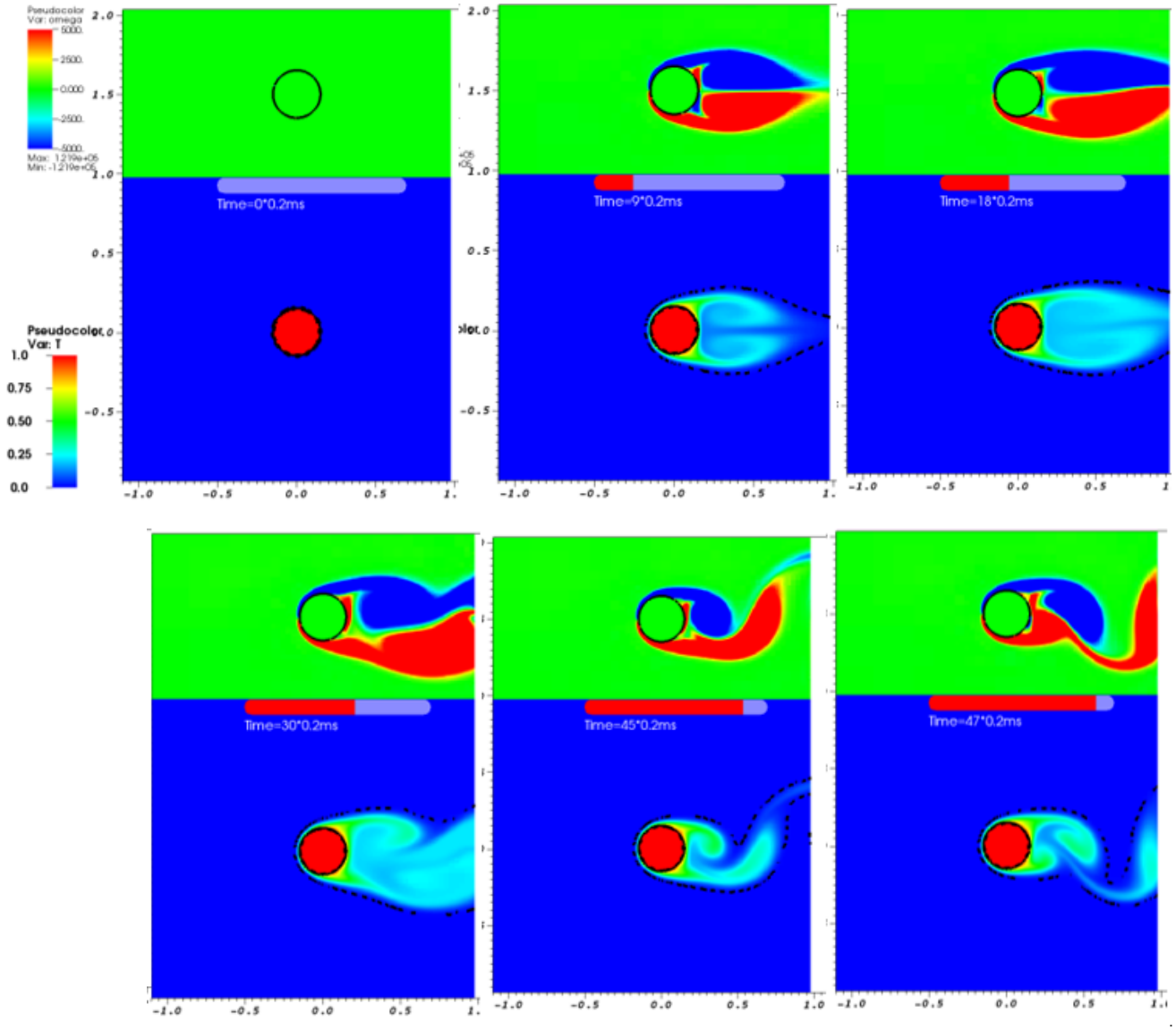

Figure 89: Example of simulation: temperature and vorticity field for Re=280 at different time step. The time is respectively 0ms, 1.8ms, 3.6ms, 6ms, 9ms and 9.4ms

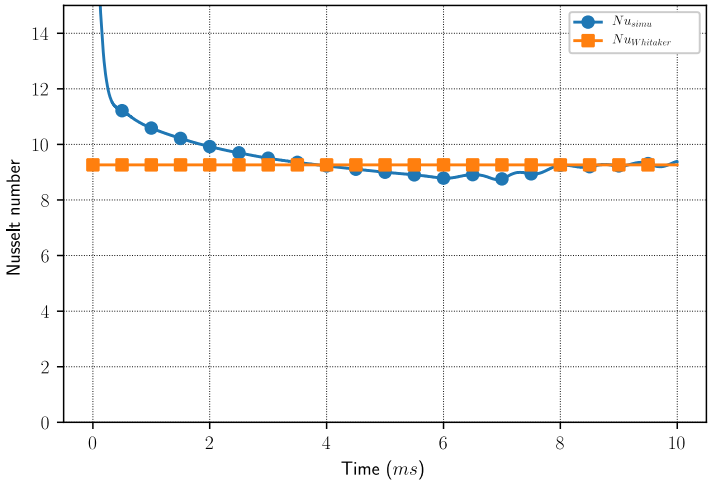

Figure 90: Transient Nusselt number in the example case, Re=280. The permanent Nusselt number is average from t=8ms to t=10ms

Figure 91 presents the resulting Nusselt numbers obtained for all the Reynolds numbers considered. Solid lines show the results given by the correlations presented in Table 6. It clearly shows that the numerical calculations with actual model give results in agreement with the different correlations. Considering that the uncertainty of the correlation can be from 10% to 30%, we can consider that, for a single-phase flow, the numerical model is validated, which makes it possible to continue the analysis.

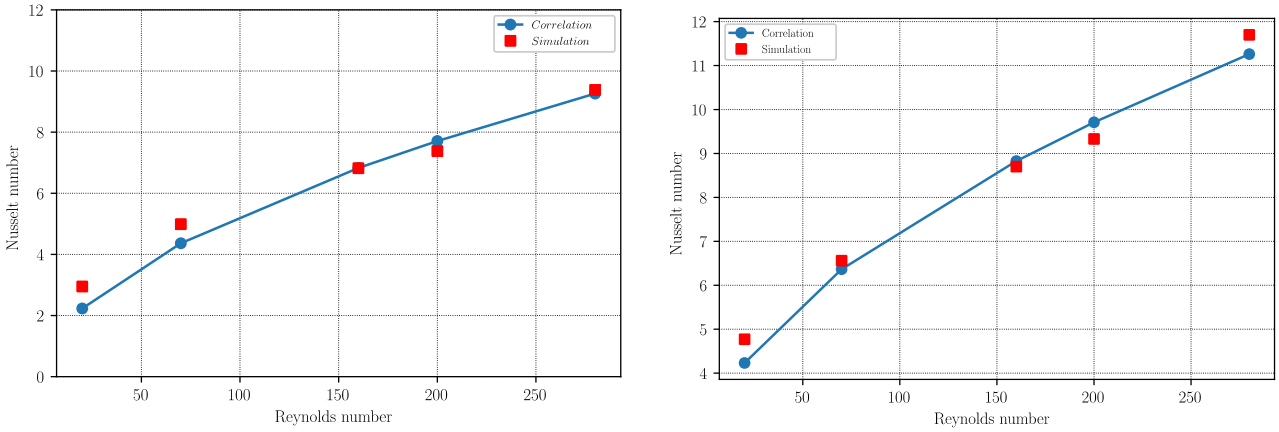

Figure 91: Comparison of the heat transfer calculated from the numerical simulations and classical correlation, left 2D cylinder, right 3D sphere

4.3.4. Simulation set up

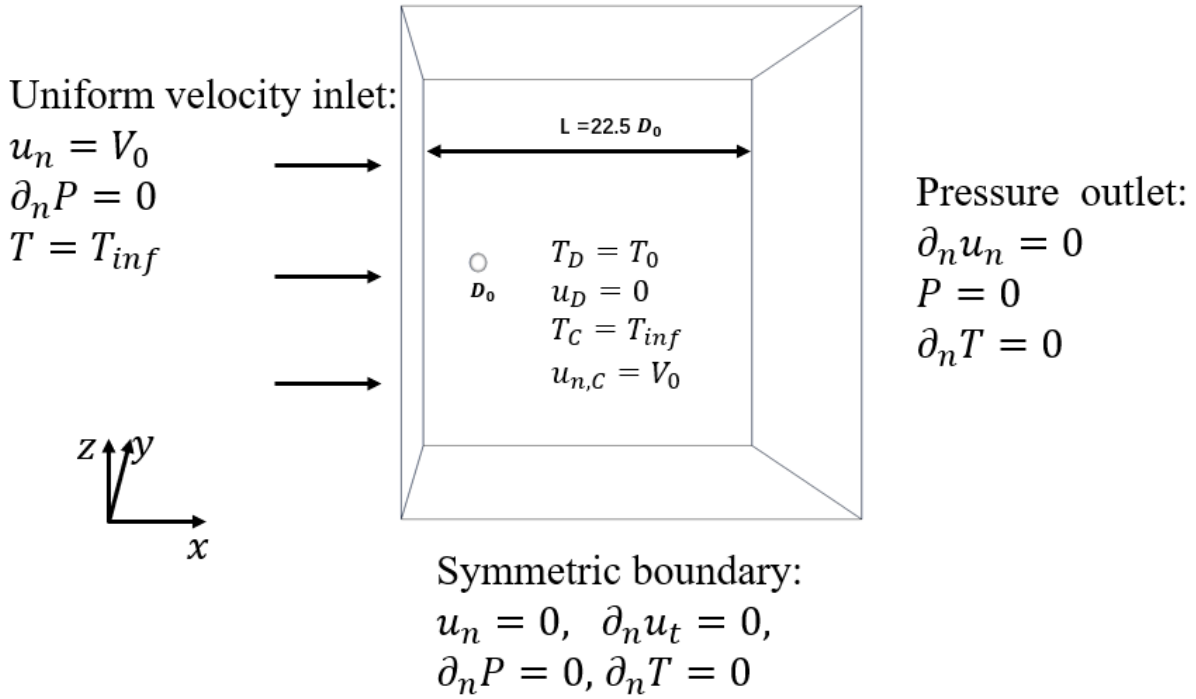

Figure 92: Computational domain (3D) for the drop fragmentation. Initially, the spherical drop is in repose and under the action of an ambient flow of uniform velocity.

The general description of calculation domain is illustrated in Figure 92. We are using a cubic domain of size $22.5D_0$ and initial the drop is positioned at $3.75D_0$ from the left boundary, which ensure a low impact of the boundary conditions on the flow and on the drop.

Boundary conditions: For the left boundary, the cold water entre the domain with a uniform velocity. For the right boundary, the flow can leave freely. For the other boundaries (top, bottom, front and back), they are set to sliding and adiabatic walls (symmetric boundary).

Initial conditions: The droplet is quiescent with a homogenous high temperature and the ambient fluid with homogenous low temperature is moving with uniform velocity identical to the inlet flow. Even though such initial condition is largely used in fragmentation involved simulations (incompressible flow solver). It is problematic because there are discontinuities for temperature and velocity at drop and liquid interface. The justification for such choice is based on the solver incompressibility. Knowing that the wave (any information in the calculation domain) propagates with an infinite speed, the flow inside the domain will adapt itself to be compatible with the inflow boundary conditions by satisfying the divergence free condition just after the first timestep, which means, the influence of initial condition is small. Another consequence of such behavior is that the dop suddenly gets a no-zero centroid velocity without any deformation after this first timestep. (Hadj-Achour et al., 2021) suggest that such increase of centroid velocity depends on the density ratio between drop and ambient fluid by using unsteady Bernoulli analysis. And the smaller density ration results in big centroid velocity increase. (In our case, for density ratio equals 8, we observe a velocity increase about 7%). [73] also points out that this sudden increase of centroid velocity is not a numerical artefact but based on the momentum conservation equations. Even the meaningful velocity slip is that between the drop centroid and the inlet flow, and the corresponding corrected Reynolds number and Weber number can be defined based on such velocity slip, we will not use the corrected ones to keep the same convention with previous studies of secondary atomization.

Physical property: The physical properties of the fluids are summarized in Table 8. For the melt drop, typical physical property of corium and water were used for meld drop and the ambient fluid respectively. It is noticed that the difference between corium and metals (e.g., the Fields metal and Wood's metal, used in experiments in the GaLaD , JaLaD or JeDi, performed by LEMTA in the frame of the RSNR-ICE project) is essentially in the conductivity, which is much more important.

Table 8: Physical proprieties used in simulation

Material	**Drop**	**Water**
Density $(\boldsymbol{kg/m^3})$	8000	1000
Viscosity $(\boldsymbol{Pa \cdot s})$	8 e^{-3}	1.e^{-3}
Conductivity $(\boldsymbol{W/m/K})$	2.88	0.6
Specific heat capacity $(\boldsymbol{J/kg/K})$	520	4179
Surface tension $(\boldsymbol{N/m})$	0.4	

In order to make the conclusions applicable to more general cases, the simulations are performed in dimensionless form. The dimensionless variables used in our simulation are presented Table 9, where:

- D_o: initial diameter of drop;
- U_{inlet} : the velocity of inlet fluid;
- T_{inlet} : temperature of inlet water;
- $T_{D,int}$: initial temperature of drop;
- σ_o: surface tension between drop and inlet fluid;
- ρ_0 and μ_0: the density and viscosity of inlet fluid.

Table 9 Main variable in dimensionless form used in our simulation

Physical quantities	**Real parameter**	**Scale**	**Dimensionless parameter**
Coordinate	x	$x = D_o \cdot x^*$	x^*
Velocity	U	$U = U_{inlet}U^*$	U^*
Time	t	$t = \frac{D_0}{U_{inlet}}t^*$	t^*
Density	ρ	$\rho = \rho_0\rho^*$	ρ^*
Viscosity	μ	$\mu = \mu_0\mu^*$	μ^*
Surface tension	σ	$\sigma = \sigma_0\sigma^*$	σ^*
Pressure	P	$P = \rho_0 U_{inlet}^2 P^*$	P^*
Temperature	T	$T = (T_{D,int} - T_{inlet})T^* + T_{inlet}$	T^*

The dimensional equation set then becomes:

$$\nabla^* \cdot \boldsymbol{U}^* = 0 \tag{17}$$

$$\boldsymbol{\rho}^*[\frac{\partial \boldsymbol{U}^*}{\partial \boldsymbol{t}^*} + (\boldsymbol{U}^* \cdot \boldsymbol{\nabla}^*)\boldsymbol{U}^*] = -\boldsymbol{\nabla}^* \boldsymbol{P}^* + \boldsymbol{\nabla}^* \cdot \frac{\boldsymbol{\mu}^*}{\boldsymbol{Re_0}}[\boldsymbol{\nabla}^* \boldsymbol{U}^* + (\boldsymbol{\nabla}^* \boldsymbol{U}^*)^T] + \frac{\boldsymbol{\sigma}^*}{\boldsymbol{We_0}} \boldsymbol{k}^* (\boldsymbol{\delta_s} \boldsymbol{n}^*) \tag{18}$$

$$\frac{\partial \boldsymbol{C}}{\partial \boldsymbol{t}^*} + \boldsymbol{\nabla}^* \cdot (\boldsymbol{C}\boldsymbol{U}^*) = \boldsymbol{0} \tag{19}$$

$$\boldsymbol{\rho}^* \boldsymbol{Cp}^* (\frac{\partial \boldsymbol{T}^*}{\partial \boldsymbol{t}^*} + \boldsymbol{U}^* \cdot \boldsymbol{\nabla}^* \boldsymbol{T}^*) = \boldsymbol{\nabla}^* \cdot \left(\frac{\boldsymbol{\lambda}^*}{\boldsymbol{Re_0 Pr_0}} \boldsymbol{\nabla}^* \boldsymbol{T}^* \right) \tag{20}$$

The Reynolds number, Prandtl number and Weber number In the above equations are based on the properties of inlet flow, with $Re_0 = \frac{\rho_0 U_{inlet} D_0}{\mu_0}$ $Pr_0 = \frac{\mu_0 Cp_0}{\lambda_0}$ and $We_0 = \frac{\rho_0 U_{inlet}^2 D_0}{\sigma_0}$.

Characteristic numbers

The drop has an initial diameter of 4mm. Depending the inlet velocity, the corresponding Reynolds and Weber number are estimated for each case. The simulated cases are summarized in Table 10.

Table 10: Inlet velocity and corresponding Weber and Reynolds number for each case

Case#	Inlet velocity (m/s)	We	Re
1	0,5	2,5	2000
2	1	10	4000
3	2	40	8000
4	4	160	16000
5	8	640	32000
6	11.31	1280	45254
7	16	2560	64000

4.4. Results and Discussion

4.4.1. Mass conservation of VOF

The VOF method implanted in Basilisk have a very good performance for mass conservation for the case investigated in the current study, which is not an easy task for other solvers, especially for high Weber number cases.

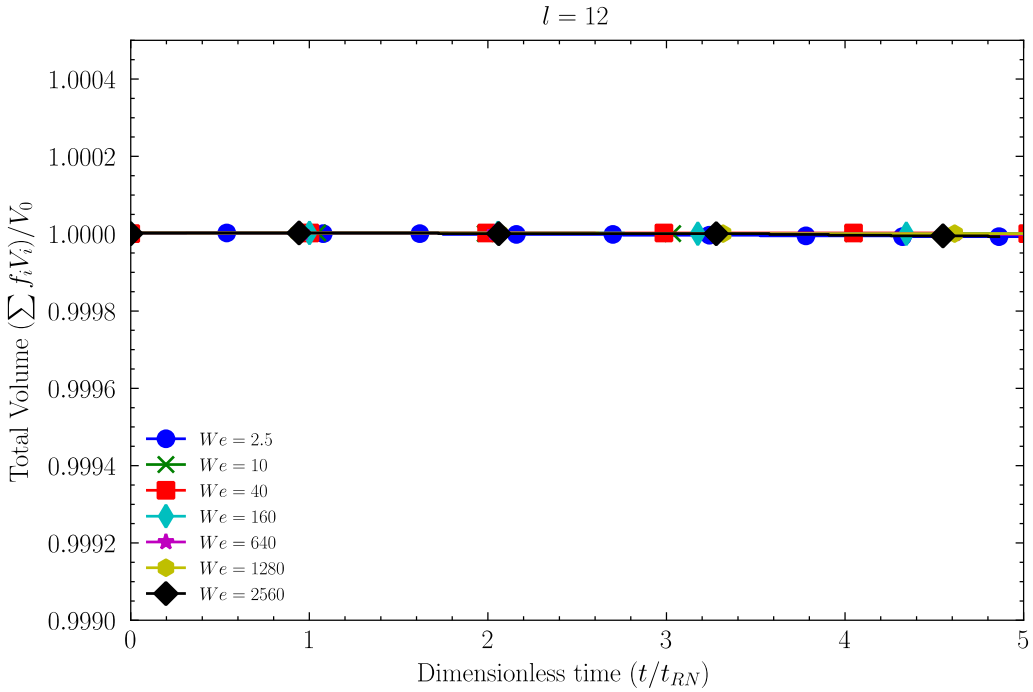

Figure 93: Total volume of drop $(\sum_i f_i V_i)/V_0$ during simulation (level of refinement 12)

4.4.2. Mesh independence

Before going to detailed analysis and discussion for simulation results, the mesh dependence is checked for each case.

The mass centroid velocity of the melt (all parts of melt, including small fragments and "residual drop") is important because it gives an estimation of global mechanic interaction between the melt and the surrounding fluid. Moreover, the mass centroid velocity is used to estimate the transient drag coefficient. The mass centroid velocity is calculated by $\frac{\sum_i f_i V_i U_i}{\sum_i f_i V_i}$ where f_i, V_i and U_i are respectively the volume fraction, the volume, and velocity in X-direction of cells i, the summation is looped on the whole computational domain. Figure 94 gives the dimensionless mass centroid velocity in X-direction as function of time. Compared with level of refinement 12, the level of refinement to 13 does not cause much difference on the mass centroid velocity, which shows an acceptable mesh convergence for the studied cases. One will notice that the entrainment characteristics are rapidly changing from the low Weber numbers, without any fragmentation, to We = 40. Beyond this Weber number, the entrainment seems to convergence and be independent of Weber number. This means that the effective drag also converges, and one may already conclude that the deformation processes, responsible at first for the change in drag, are similar.

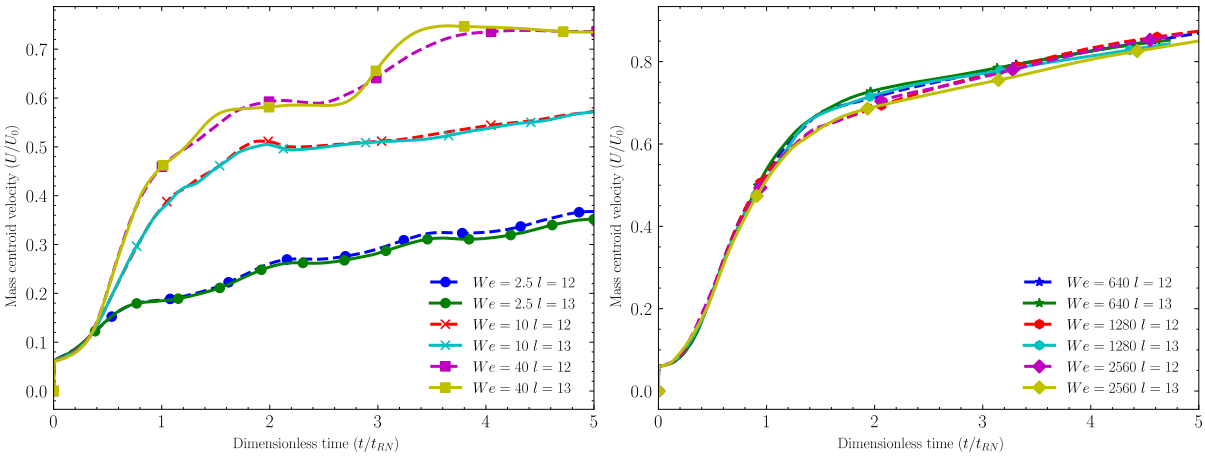

Figure 94: Mass centroid velocity for level 12 and level 13 for investigated cases

The interfacial area[9] gives a global characterization of the geometrical topology change of melt in the process of fragmentation. It's important for our study because it represent the real heat transfer area between melt and liquid. The dimensionless interfacial area is calculated by $(\sum_i A_i)/\mathrm{A}_0$ where A_i is the interfacial area of cells i after VOF interface reconstruction and A_0 is the initial surface area of drop, and the summation is looped on all cells contains interface (color function between 0 and 1). Figure 95 gives the dimensionless interfacial area as function of time. For low Weber number cases, the interfacial area seems to be converged while it's not the case for high Weber number cases, which means that a fine mesh is necessary for high Weber number cases. The level of refinement 12 cannot give as much detail as level 13 where larger and thinner waves exist (Figure 96). The difference between levels 12 and level 13 gives us an order of magnitude of the uncertainty of the results. Considering the final state, once fragmentation is completed, the difference of interfacial area between the two levels 12 and 13 if roughly 10 to 20 %. It should be noted that the present study is not intended to conduct a pure NDS search with high accuracy, but to find a model for the explosion. The uncertainties seem very reasonable for our application compared to the general uncertainties of the explosion, especially the boiling mechanism.

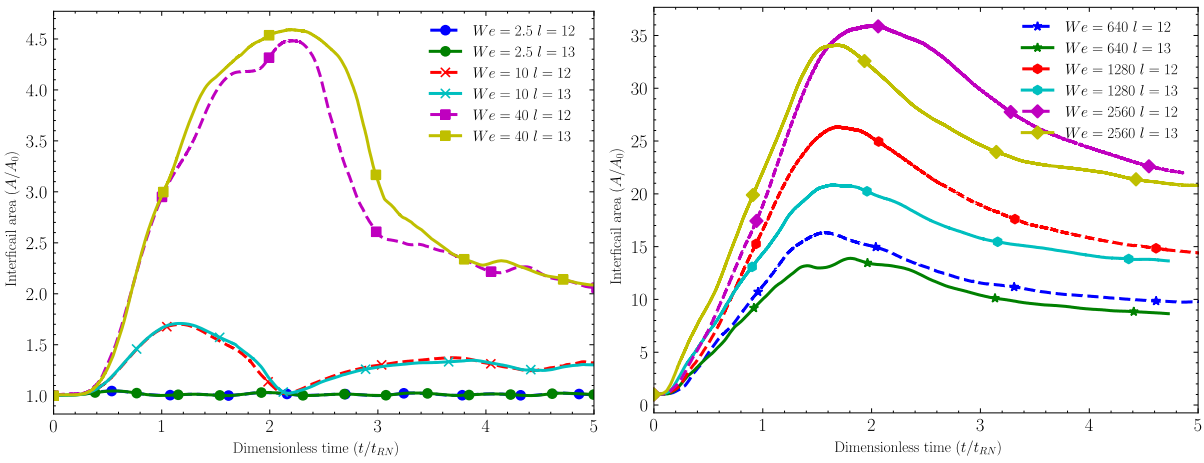

Figure 95: Dimensionless interfacial area for level 12 and level 13 for investigated cases

[9] In this chapiter, interfacial area means **the surface area of the interface** between the melt and coolant, in dimension [$\boldsymbol{m^2}$]

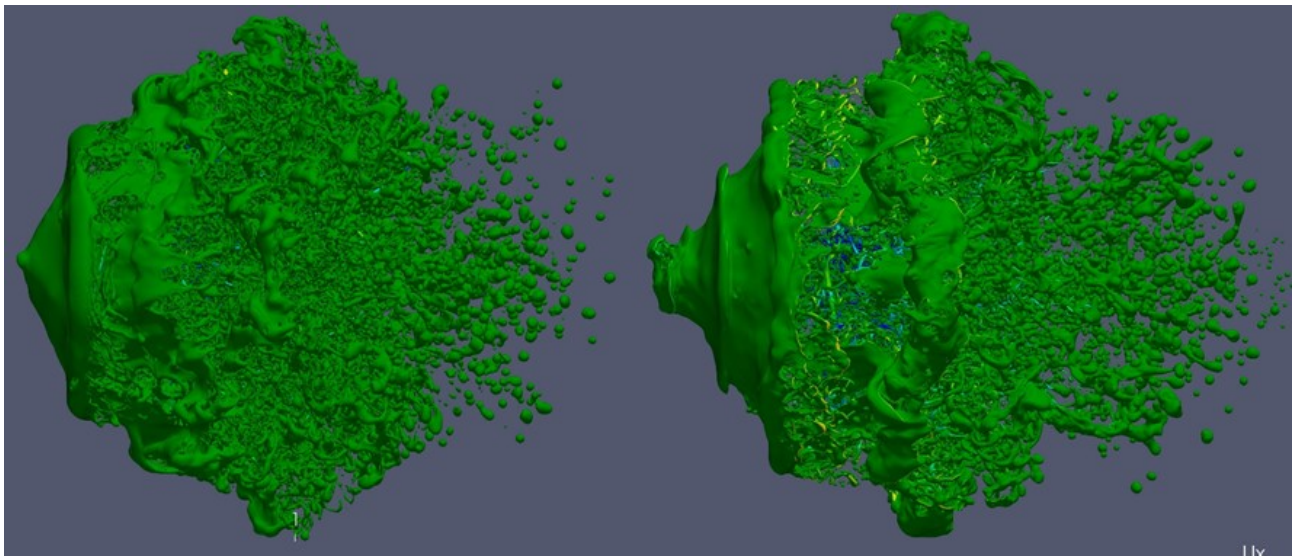

Figure 96: Interface (colored in green), side view projected in XZ plan; comparison between level 12 (left) and level 13 (right) for the same Weber number 1280 at same time $1.6T_{RN}$

The average temperature of melt gives a good estimation of global thermal interaction between melt and environment fluid. In addition, this average temperature is used to calculate the transient heat transfer coefficient. The dimensionless melt temperature is calculated by $(\sum_i f_i V_i T_i)/(\sum_i f_i V_i)$ where f_i, V_i and T_i are respectively the volume fraction, the volume, and dimensionless temperature of cells i, the summation is looped on the whole computational domain. As the heat transfer is highly influenced by the interfacial area, it's not surprised to find that the interfacial area seems to be converged for low weber number cases while big incertitude remains for high Weber number cases. Still, such uncertainties seem reasonable to propose a new model for explosion.

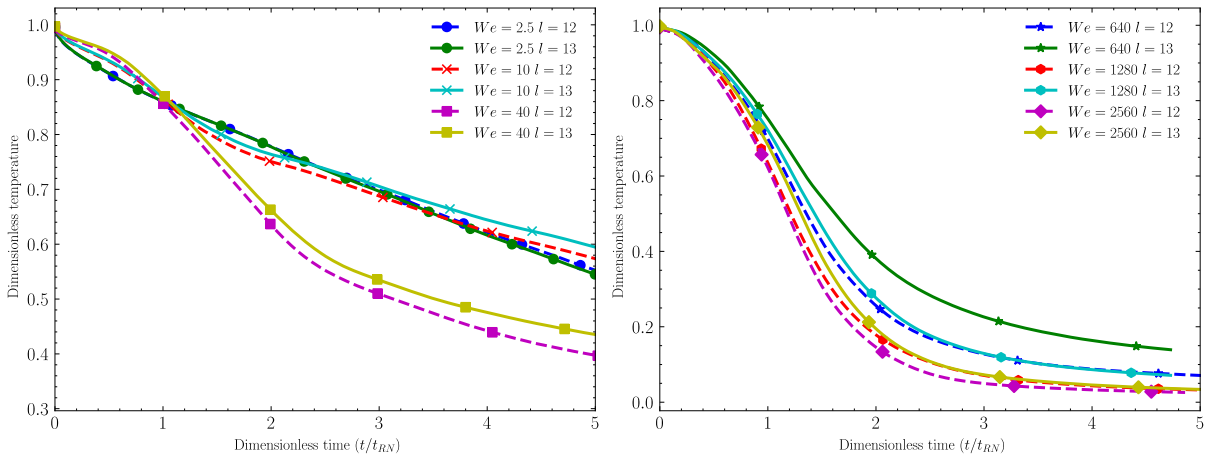

Figure 97: Dimensionless melt temperature for level 12 and level 13 for investigated cases

4.4.3. Fragmentation regimes

Different Weber numbers have been studied leading to the identification of different breakup regimes for liquid/liquid system.

4.4.3.1. Oscillation

As the Weber number represents the ratio of disruptive hydrodynamic forces to the stabilizing surface tension force, a small Weber means the surface tension dominate the drop behavior. As expected, low Weber

number (~2.5) leads to simple drop oscillation with a specific frequency without any breakup (Figure 98). Figure 99 displays the maximum projected length D_{cross} in z direction, which indicate the degree of drop deformation.

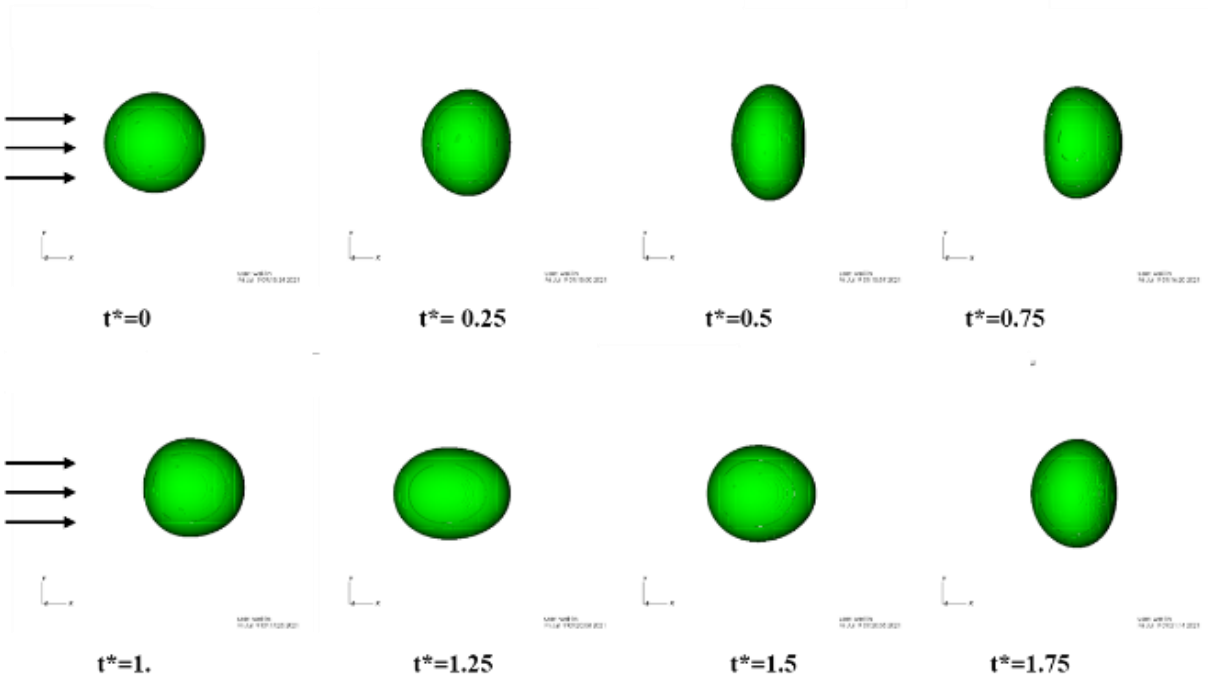

Figure 98: Interface evolution for case we=2.5, Re=2000, the interface is projected onto XZ-plan

It is not easy to characterize and compare such oscillation frequency with theoretical studies due to its transient nature. The Weber number we give here 2.5 is the initial value. As discussed in $4.2.3.2, the drop exerts surface tension, pressure drag and viscous drag forces. Firstly, the surface tension has no effective influence on drop's overall acceleration because the oscillation is quasi-periodic.

Similar to the pressure distribution over a fixed solid sphere, when the ambient flow passes through the initial quiescent drop, the flows at the front and the tail of the drop are both in stagnation (respect to the drop), thus they have higher static pressure than that at other position. The corresponding non-uniform pressure distribution induces non-equal forces on the surface of drop. The pressure in the upstream side of drop is bigger than that of downstream side, the pressure drag force accelerates the drop. The viscous drag also increases the drop velocity until the drop gets the same velocity with the ambient fluid. As a result, during the interaction, the drop is continuously entrained and accelerated by the ambient fluid, and its velocity progressively increases. Therefore, the real Weber number is always decreasing. However, the most theoretical studies predict with fixed velocity slip between drop and ambient fluid, which means the constant Weber number.

After $2\boldsymbol{t_{RN}}$, the drop has only minor acceleration (Figure 94). An average Weber number and oscillation period can be estimated. The period of oscillation can be estimated as $1.4\boldsymbol{t_{RN}}$ averaging the last two oscillations. The average Weber number during this same time is about 1.56. The dimensionless frequency f predicted by the model proposed by (Rimbert et al., 2020) follows the equation $\frac{f}{f_{RN}} = \sqrt{\frac{0.81}{We} - 0.06}$ where f_{RN} is a reference frequency defined by $f_{RN} = \frac{1}{t_{RN}}$. For the present Weber number (1.56), this analytical model predicts a period of $1.47\boldsymbol{t_{RN}}$, which is comparable with the present study.

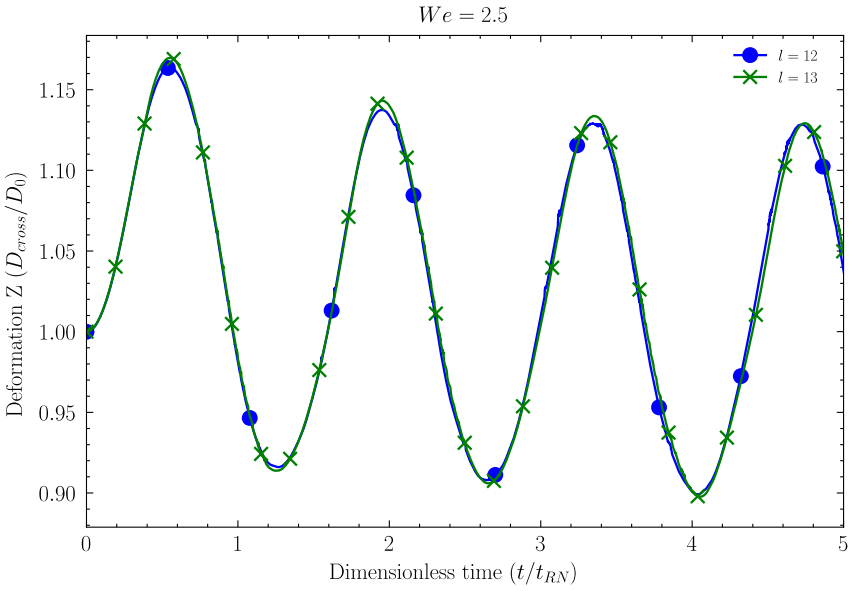

Figure 99: Deformation along Z-axis for case we=2.5, Re=2000

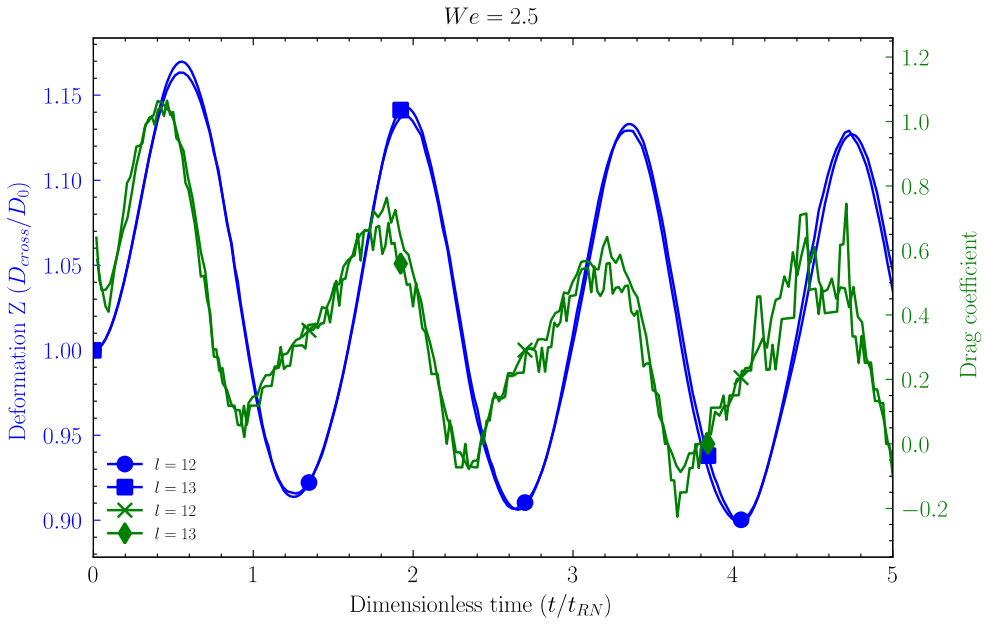

Figure 100: Transient drag coefficient (green curves) and deformation along Z-axis (blue curves), different legends indicate different level of refinement of grid

The transient drag coefficient eq. (3) and deformation along Z-axis are illustrated in Figure 100. With the oscillation of drop, the drag coefficient also oscillates with the same frequency. However, a phase shift between the drop deformation and drag coefficient is observed. In fact, the periodic variation of drag coefficient is directed related to the attachment and detachment of vortex rings in the wake of drop (shown in Figure 101). The drag coefficient is minimum when the vortex ring touches the drop and the drag coefficient begin to increase with the detachment of vortex ring. The attachment of vortex ring represents large velocity gradient at interface because the flow inside and outside the interface are in opposite direction (shown in Figure 102), which leads to a shear force in the opposite direction of drop acceleration at the tail of drop and reduce the overall drag force applied on the drop. In another hand, when the drop touches the vortex ring, the drop interface at its tail still has a positive velocity in X direction, which further lengthens the drop in the streamwise direction, reducing the drop length in the cross-stream direction to its minimum. As a results, there is a phase shift between the variation of

drag coefficient and oscillation, which can be considered as a delay in the deformation response to the vortex ring.

The static pressure difference inside and outside the interface suggests the intensity of the surface tension. We also find that for this low Weber (Reynolds) number case, the static pressure inside the drop is always big, which means, the surface tension is strong and resists the drop to have bigger deformation. As the viscous drag is much smaller than the pressure drags, the deformation is highly pressure controlled.

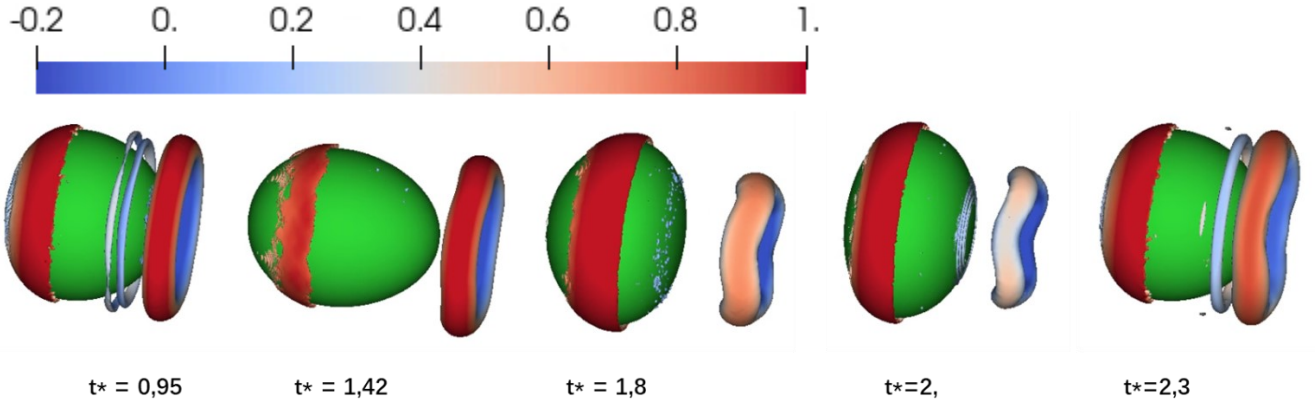

Figure 101: drop interface (with fixed color in green) and vortex ring (colored by X component of velocity) detected with lambda2 criterion (see Appendix 1.3 for more information about lambda2 criterion).

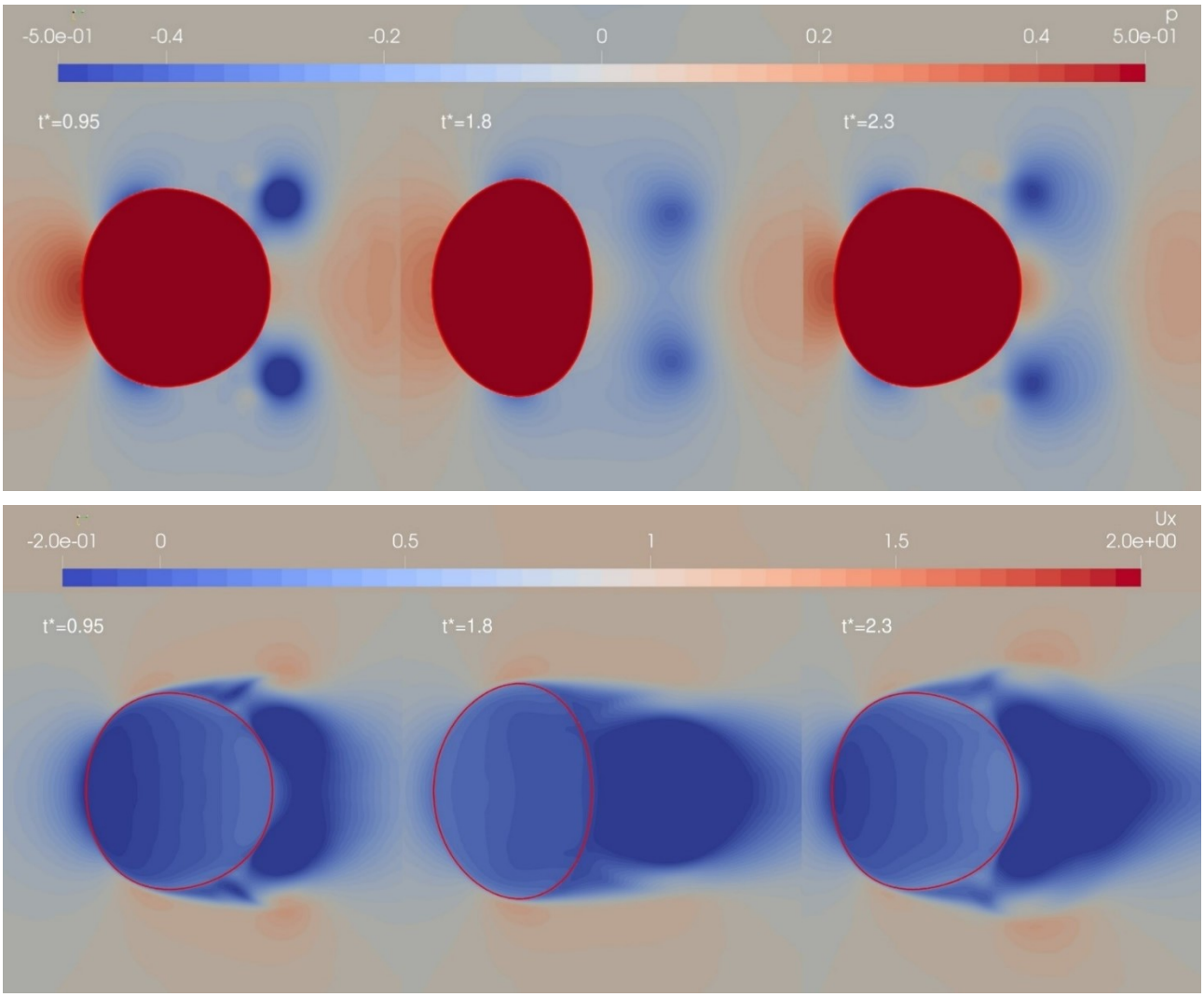

Figure 102: Dimensionless pressure ($\frac{P-P_{outlet}}{\rho U_0^2}$) distribution and velocity component in x direction at three special time, t=0.95 and 2.3 are corresponding to the attachment of vortex ring to the drop interface while t*=1.8 is corresponding to the vortex ring being far from the interface, interface in solid line, XZ-plan cut*

4.4.3.2. Elongation breakup

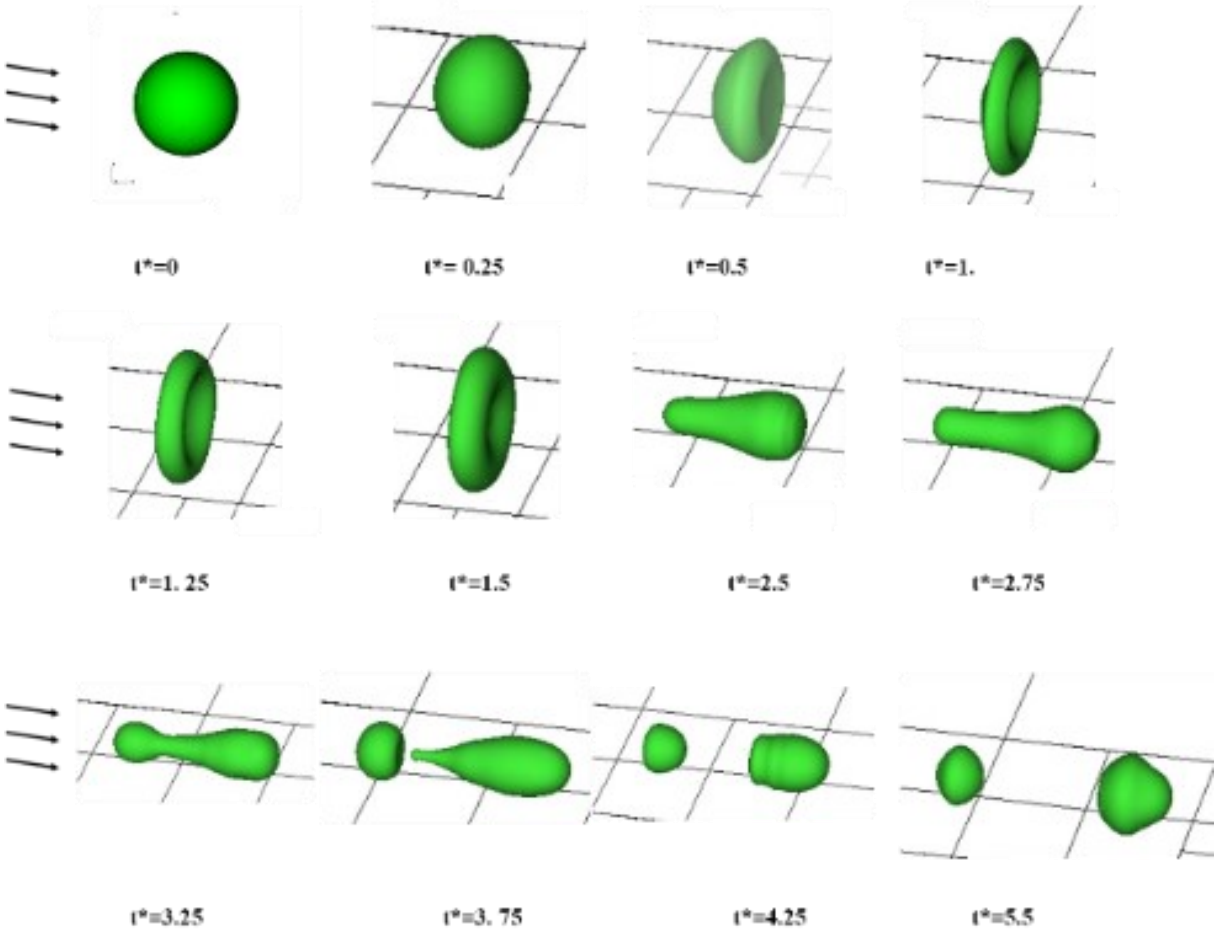

Figure 103: Interface evolution for case with We=10, Re=4000

Different from liquid/gas system, increasing the Weber number (~10) does not lead to a pulverization through the bag breakup but to a breakup into two daughters drops by elongation (as illustrated in Figure 103).

Analysis for early deformation, which highly depends on the pressure distribution, follows the same principle as we discussed in the case of Weber number 2.5. The difference between Weber number 10 and Weber number 2.5 is that with a higher Weber number (Reynolds number), the lower static pressure at the poles of the droplet now has a stronger effect on the interior of the drop, so that the pressure in the central part of the drop is the lower (cf. Figure 104). The pressure gradient inside the drop is then bigger than previous case Weber number 2.5. By consequence, the interior flow and the deformation is affected.

For the case Weber number 10 (Reynolds number 4000), the flow separation around the drop occurs after the pole and the velocity is maximal at the drop pole. Therefore, the pressure in the pole side is smallest (shown in Figure 104), the drop firstly relaxes and expands in the cross-stream direction. Along with this deformation, viscous boundary layer in the wake begin to develop, which greatly reduces the static pressure at the wake of drop. As the static pressure in the frontal part of drop is still big, the overall drag coefficient increases. At the same time, a vortex ring is formed at the wake of the drop, and it represents a shrink of local pressure and negative velocity in X direction. It interacts with drop and deform its interface, forming a concave in the tail of drop from $t = 0.8t_{RN}$. As a result, the drop forms a “dome” in the opposed orientation of inlet flow. The concave curvature makes the pressure outside interface bigger than that inside the interface because of surface tension. The pressure difference between the frontal and back part of drop interface decreases and the overall drag coefficient decreases until $t = 1.25t_{RN}$.

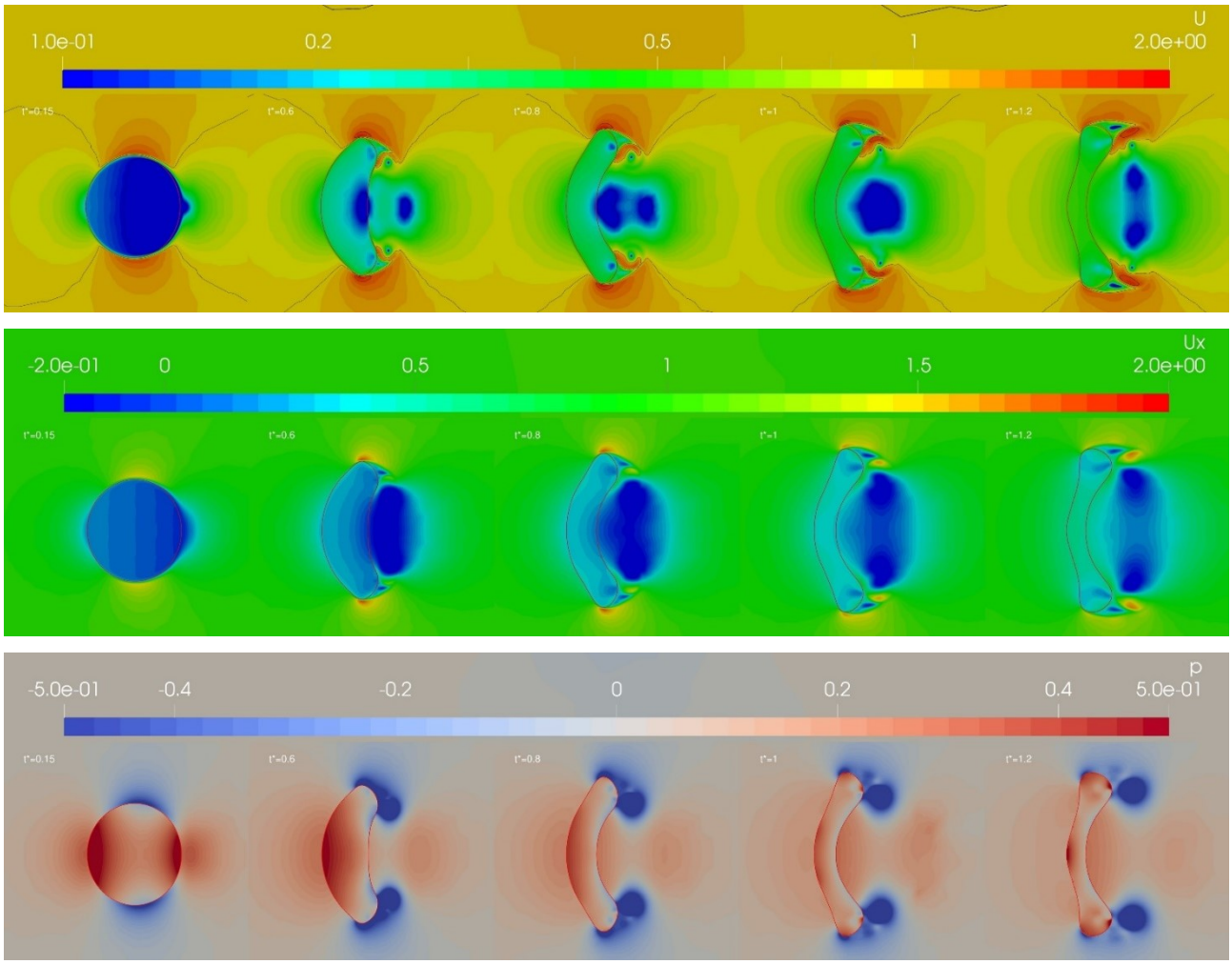

Figure 104: Dimensionless velocity magnitude, velocity x-component, and dimensionless pressure ($\frac{P-P_{outlet}}{\rho U_0^2}$) distribution at different time, interface in solid line, XZ-plan cut, We=10, Re=4000

From $t = 1.25t_{RN}$, even the frontal part of the drop starts to be deformed in to concave form, leading to a bigger ambient static pressure around the frontal interface. And the overall drag drop increases. However, the deformation of interface is so strong that the interface break through, creating a hole at the central line at $t = 1.7t$ (confirmed in Figure 105). The projected area in the cross-stream direction decreases and the overall drag force reduces. The formation of this hole is considered physically possible and not a numerical effect, because simulations for higher levels of refinement (level 13 and 14) always show the existence of a hole.

However, the hole will eventually close because the surface velocity around the hole has a positive velocity component towards the center of the drop. This reconnection can be seen as a group of axisymmetric fluid of opposite momentum collides, the velocity component in radial direction cancels each other out while the velocity component in X direction adds up. As a results, the drop contracts in cross section and start to extend in X direction (shown in Figure 107). Finally, the mother drop breaks up into two daughter drops by pinch-off mechanism. As illustrated in Figure 103 at $t = 3.25t_{RN}$, the surfaces tension on both sides of the bridge retracts the interface to the opposite direction, causing the interface to recede and finally break up. During this period, the drag coefficient has no big variation.

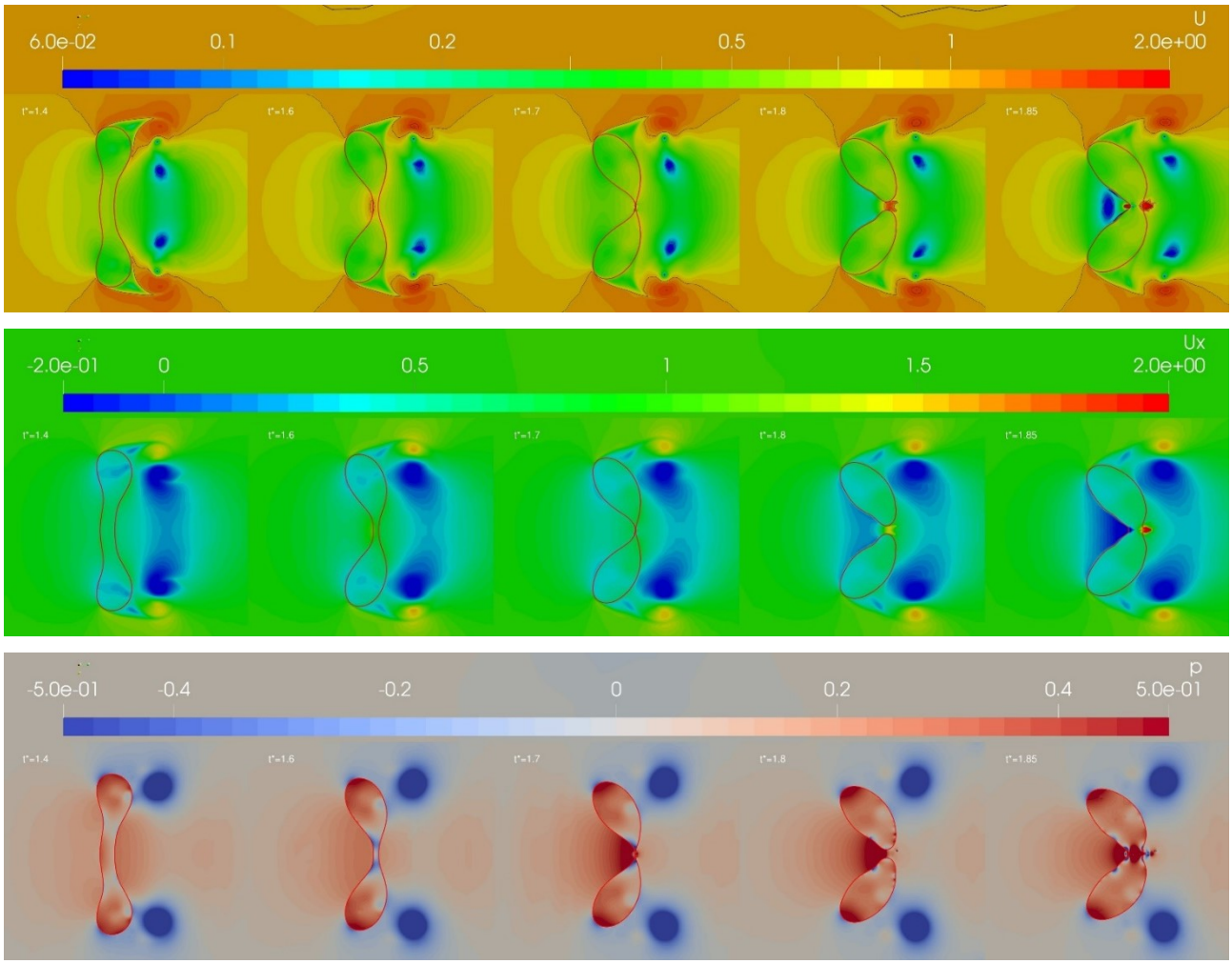

Figure 105: Velocity magnitude, velocity in x direction, and dimensionless pressure ($\frac{P-P_{outlet}}{\rho U_0^2}$) distribution and at three special time, t=0.95 and 2.3 corresponding the attachment of vortex ring to drop interface while t*=1.8 corresponding the vortex ring is far from the interface, interface in solid line, XZ-plan cut*

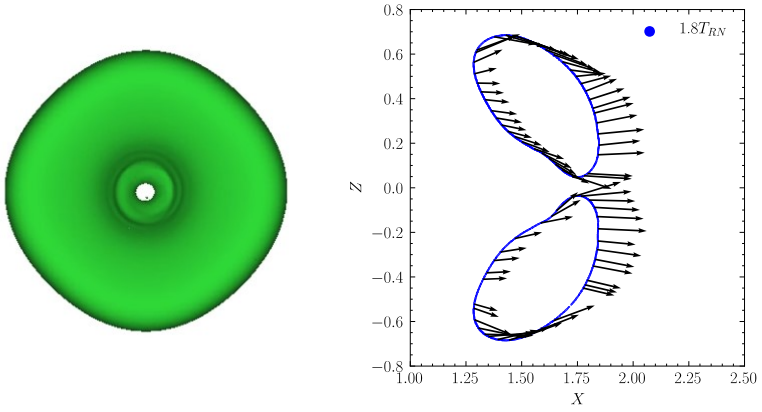

Figure 106 : 3D-view of interface in YZ-plan, 2D interface and surface velocity in XZ plan cut at T* =1.8

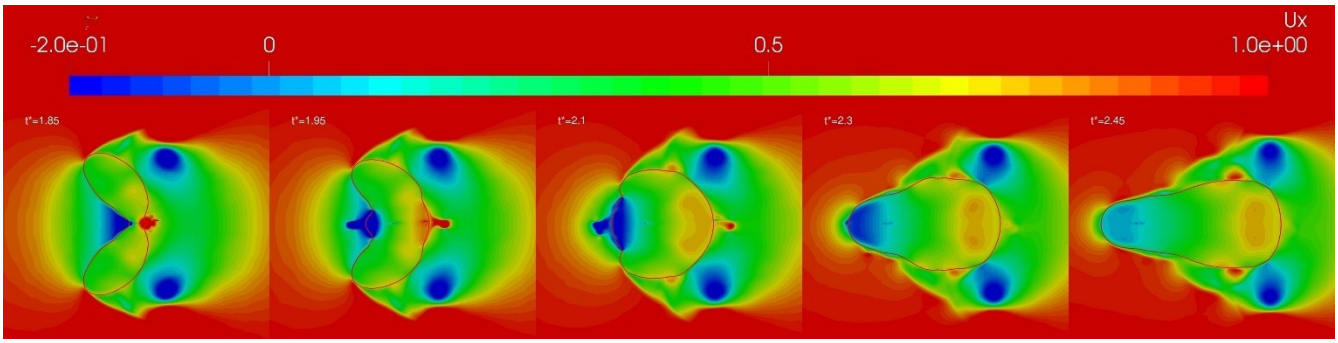

Figure 107: Velocity in X direction, interface in solid line, XZ-plan cut

To conclude, the variation of drag coefficient is not a simple consequence of increase of projected area in cross-stream direction but depends highly on the dynamic distribution of pressure around the drop, at least for these low Weber (Reynolds number case).

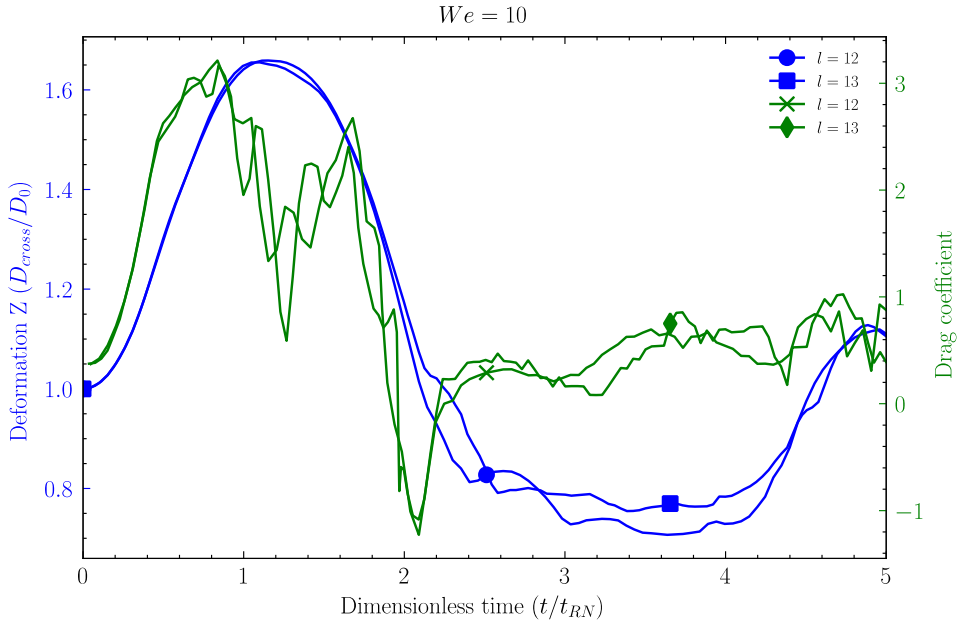

Figure 108: Transient drag coefficient (green curves) and deformation along Z-axis (blue curves), legend indicates different levels of refinement

4.4.3.3. Forward bag breakup

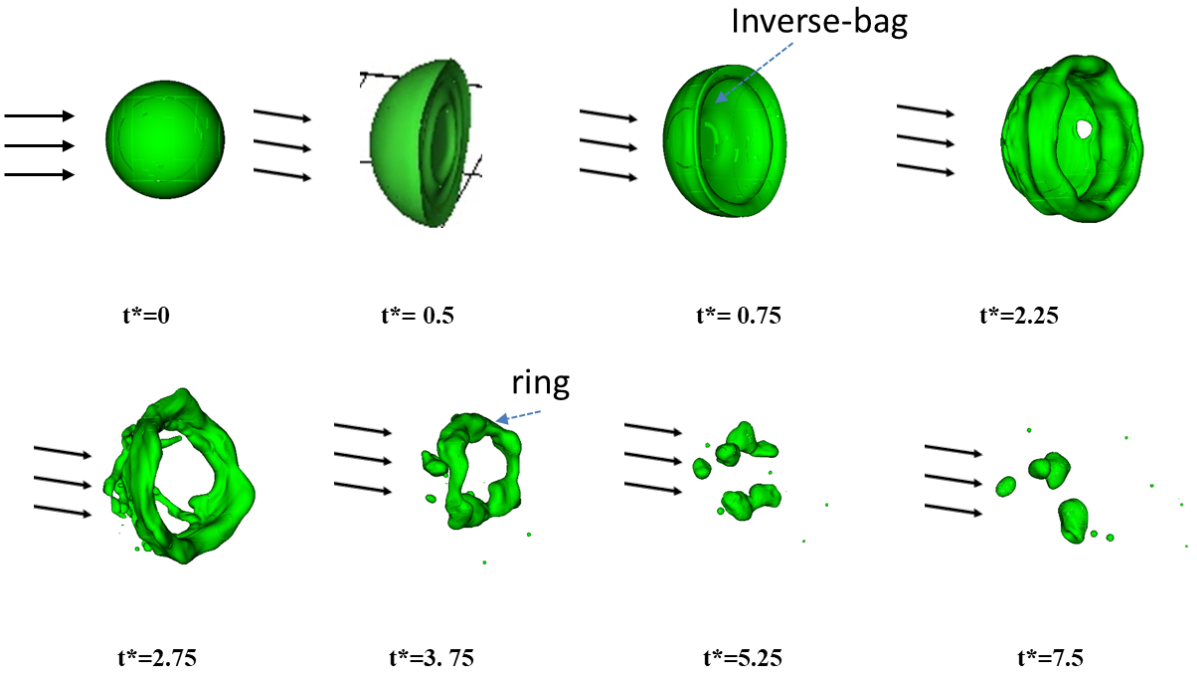

Figure 109: Interface evolution for case we=40, Re=8000

If the Weber number increases further (~40, Figure 109), different from those observed in liquid-gas (LG) configuration, i.e. the so called bag or bag-and-stamen breakup (e.g. (Qian et al., 2021)), an "inverse-bag" deformation (a thin hollow bag in the opposite orientation of inlet flow due to the shear at drop edges by surrounding water and flow recirculation/vortex ring in the wake of drop). Precisely, the orientation of the "bag" formed in liquid-liquid (LL) configuration is opposite to that in the LG configuration even if a “bag” is formed in both configurations. This is due to the important entrainment of the surrounding coolant in LL case, whereas the LG situation is dominated by Rayleigh-Taylor instabilities. This entrainment leads to a temporary configuration where the coolant is "entrapped" in this “inverse-bag”. However, this bag just takes a small portion of total mass, and most of the mass is accumulated at a toroidal ring perpendicular to the inlet flow. The toroidal ring disintegrates into a smaller number of fragments of the same size as the ring thickness, thus due to capillary effects, after the bag breakup.

The initial deformation stage is similar with that for Weber 10. However, the entrainment in the wake is stronger for Weber number 40 and we see clearly the interaction between vortex ring and the drop interface (shown in Figure 111, Figure 112, Figure 113). The bigger Weber (Reynolds) number means stronger recirculation and vortex ring in the wake of drop. Different from the case of Weber number 10 where the vortex ring is at rest with respect to the drop, as the shear force is stronger, the drop lateral boundary moves faster than the vortex ring, the vortex rings is entrapped in a concave bag (shown in Figure 110 Figure 113). This vortex ring, which represent a big velocity gradient, will continuously be stripping and thinning the bag interface until the bag breakup. It’s interesting to noticed that the drop firstly breaks up around the position of the vortex ring (t*=2.75 Figure 112, Figure 113).

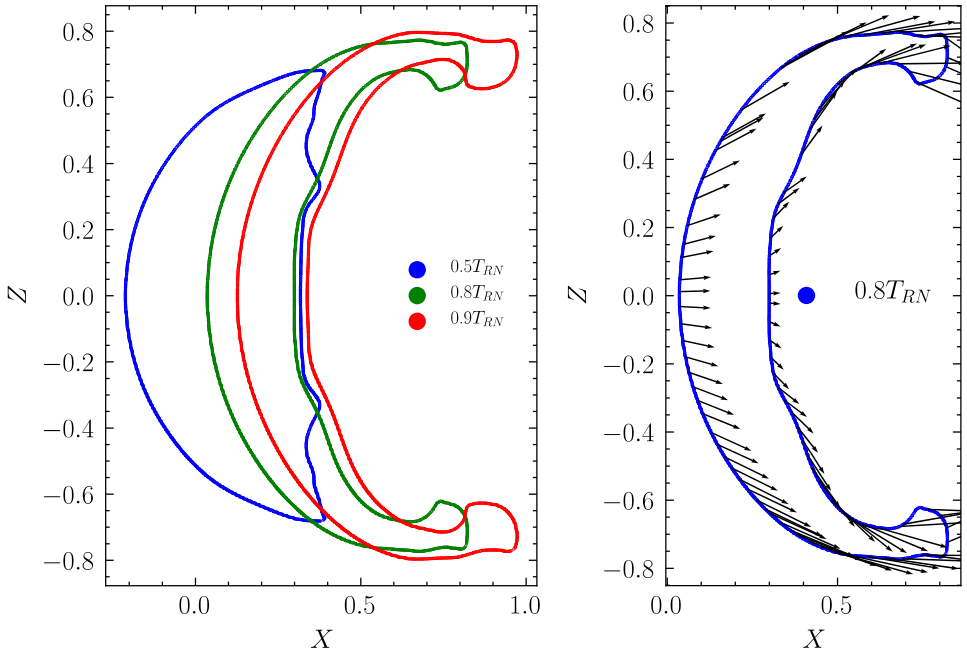

Figure 110: Interface and surface velocity at interface for Weber number 40 at T =0.5, 0.8, 0.9, XZ plan cut. From this figure, we see clearly that the boundray layer of the drop is continueously stripped by the surrounding flow around the vortex ring in the wake, while the tail part of drop is rather in repose.*

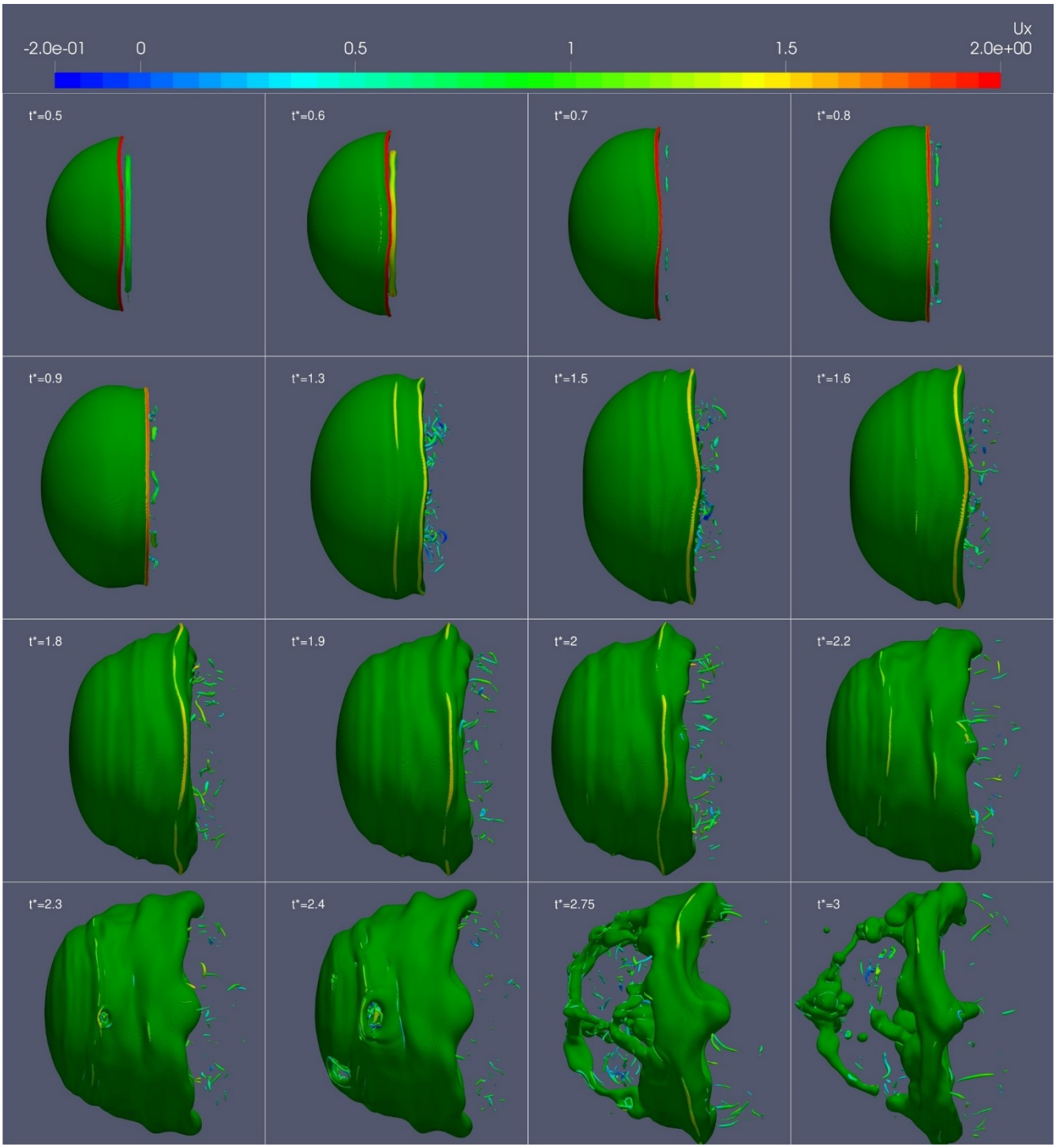

Figure 111: Interface (colored in green) and vortex structure (colored by velocity in X direction) detected with lamda2 criterion, side view projected in XZ plan

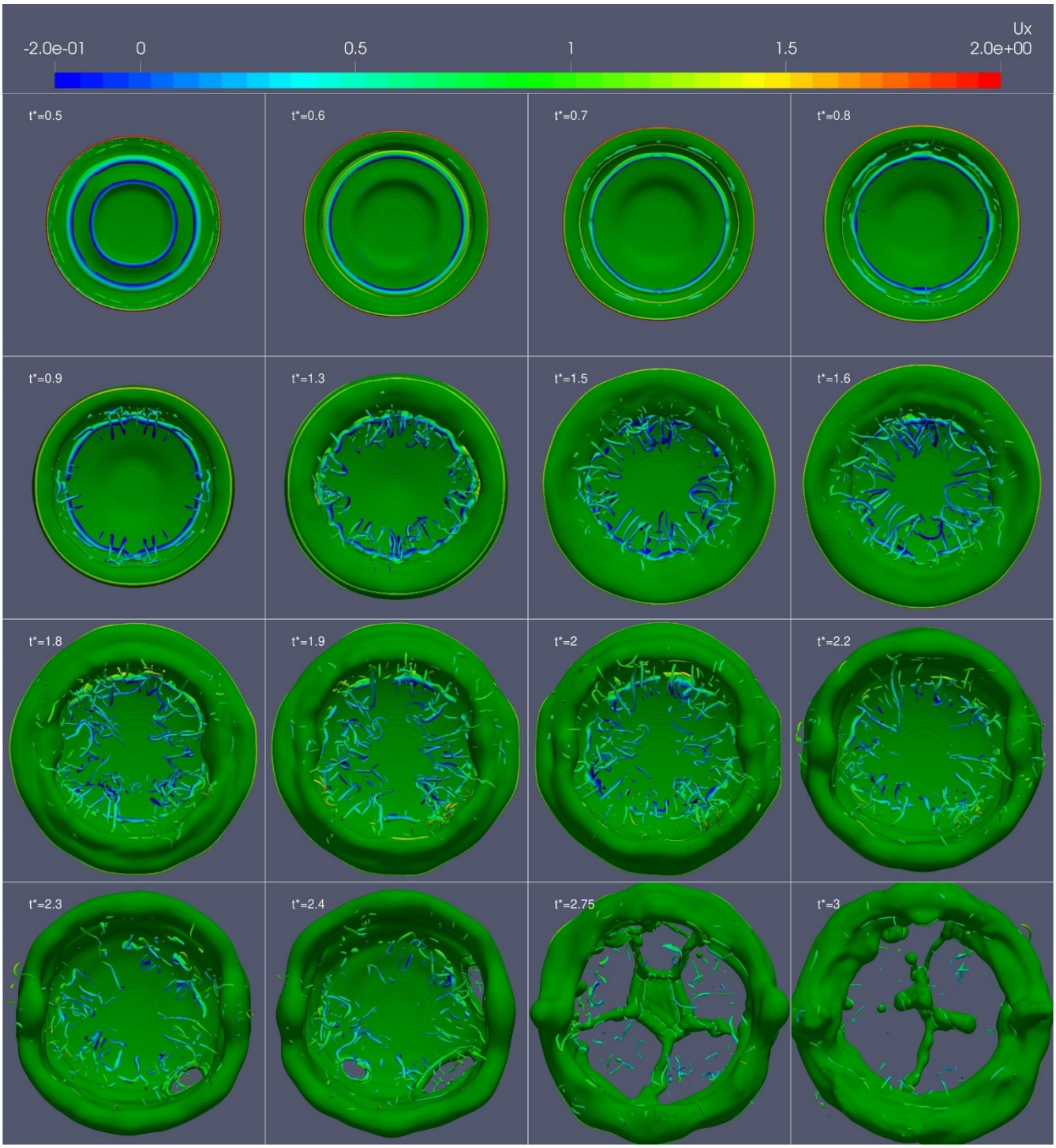

Figure 112: Interface (colored in green) and vortex structure (colored by velocity in X direction) detected with lamda2 criterion, right view projected in YZ plan

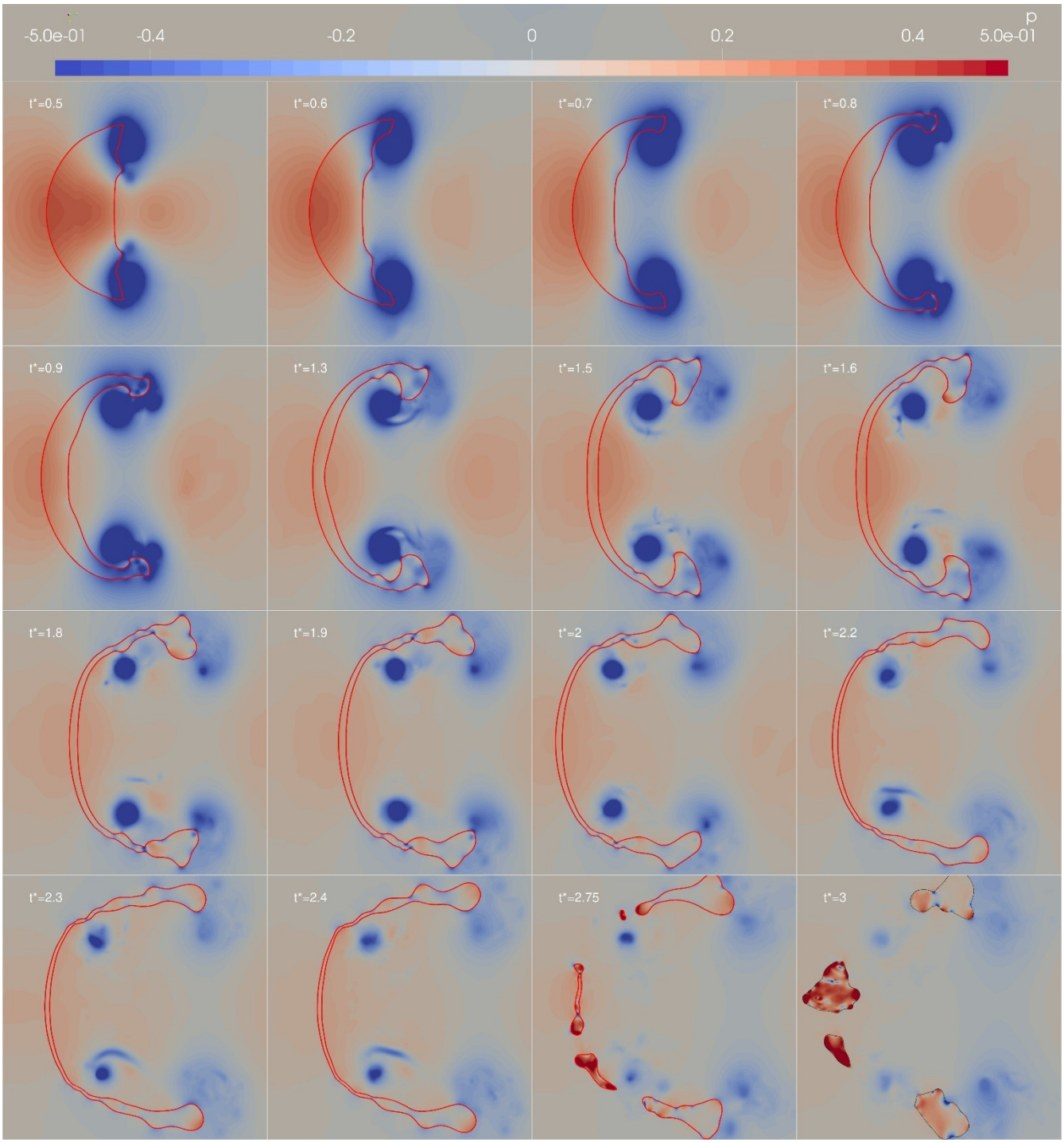

Figure 113: Dimensionless pressure ($\frac{P-P_{outlet}}{\rho U_0^2}$) distribution and at different time, interface in solid line, XZ-plan cut

4.4.3.4. Forward-bag-ligament breakup:

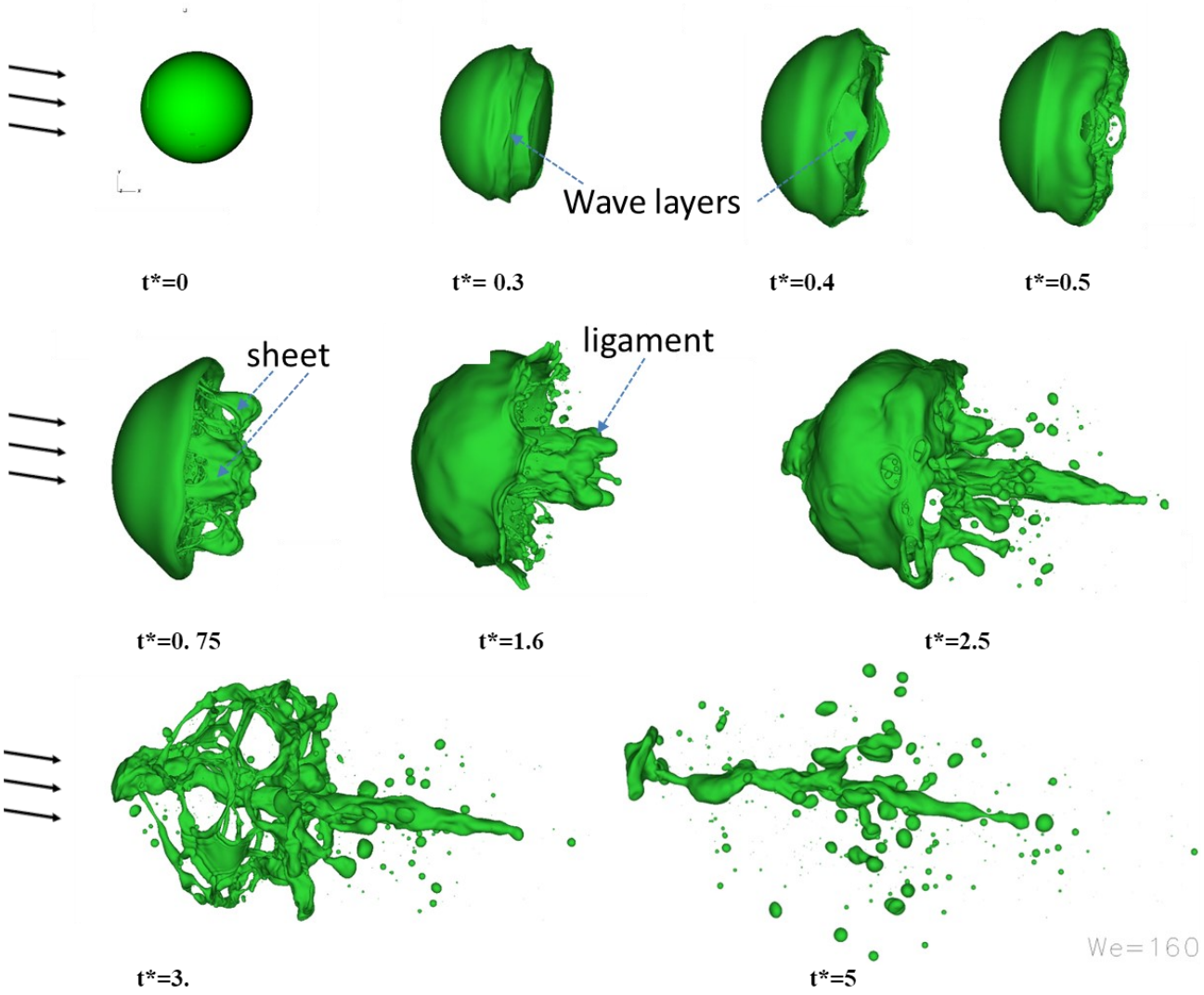

Figure 114: Interface evolution for case we=160, Re=16000

For higher Weber number cases (~160, Figure 114), large tangential instabilities due to the shear force at the interface (so of the Kelvin-Helmholtz type) are developing. A very thin 2D wave form layers are firstly formed at the edge of the drop. These layers quickly cover the drop, forming a forward bag. Several smaller fragments are observed (t*=0.5) at the drop tail and these fragments are entrained into the wake. Some transverse azimuthal modulations of the 2D wave were also observed (t*=0.3 and 0.4), forming some thin "sheets" (t*=0.75). Due to stretching of the interface corrugation crests, these sheets develop into ligaments (t*=1.6) which are entrained into the bag. Finally, the remaining bag breaks up into fragments of different sizes. We call this regime “forward-bag-ligament” breakup.

It is clear that, in contrast with LG cases where the melt entrainment is weak, the fragmentation in LL configuration leads to the formation of a local mixture (t*=0.4~2.5) which may support the "micro-interaction" concept developed by Theofanous and co-workers (Yuen and Theofanous, 1999).

The initial deformation stage is the similar with that for Weber number 40 (Figure 118), deforming into a concave bag. However, with a higher Reynolds (Weber) number, the viscous boundary layer is much thinner and the stretching viscous stress is much strong at interface (Figure 115 comparing to Figure 110), stripping the drop peripheric and forming thin layers (rather than a thick “rim” for Weber number 10) (shown in Figure 116 Figure 117 Figure 118). These thin layers are entrained by the strong recirculation in the wake of the drop, and further

detached from mother drop, forming “sheets” (t*=0.6 in Figure 117). These sheets break through, generating small ligaments and fragments (t*=0.75 in Figure 117). These fragments are transported by the flow in the wake, finally attach to the interior interface of the bag and cause some instability. (t*=0.9, 0.11 in Figure 118). At the same time, with the detachments of groups of axisymmetric multi-sheets with opposite momentum from the drop periphery, they collide in the central lines, forming big ligament (t*=1.3~2.75 in Figure 117 and Figure 118). As the velocity component in radial direction cancels each other out while the velocity component in X direction adds up during the collision. The ligament stays in the central line and moves in X direction, which eventually hit and break the bag interior interface (t*=2.2~2.75 in Figure 116).

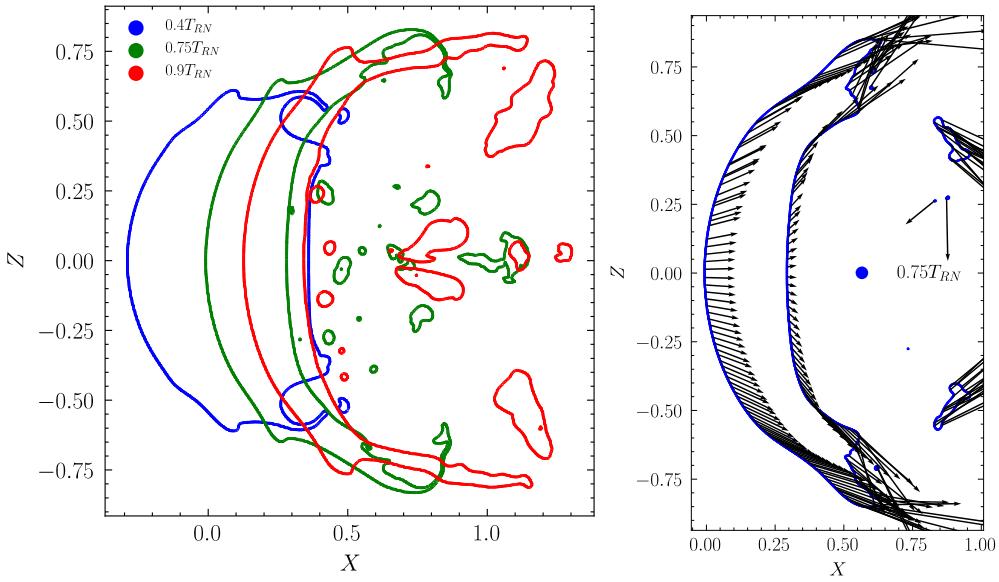

Figure 115 : Interface and surface velocity at interface for different Weber cases at T =0.45, 0.75, 0.9, XZ plan cut*

To conclude, the phenomenon concerened in this regime are:

- Formation of several thin layers in the form of waves on the surface of the drop (t*=0.3 and 0.4 Figure 116)
- The continuous stretching of these successive layers (one layer after the other) in the wake of drop (t*=0.6,0.75 and 1.4 Figure 116)
- Detachment of the layer from the mother drop, generating sheets, which turn into a ligament at the central line, and some small fragments are generated during these processes.
- Rupture of bag, forming small fragments

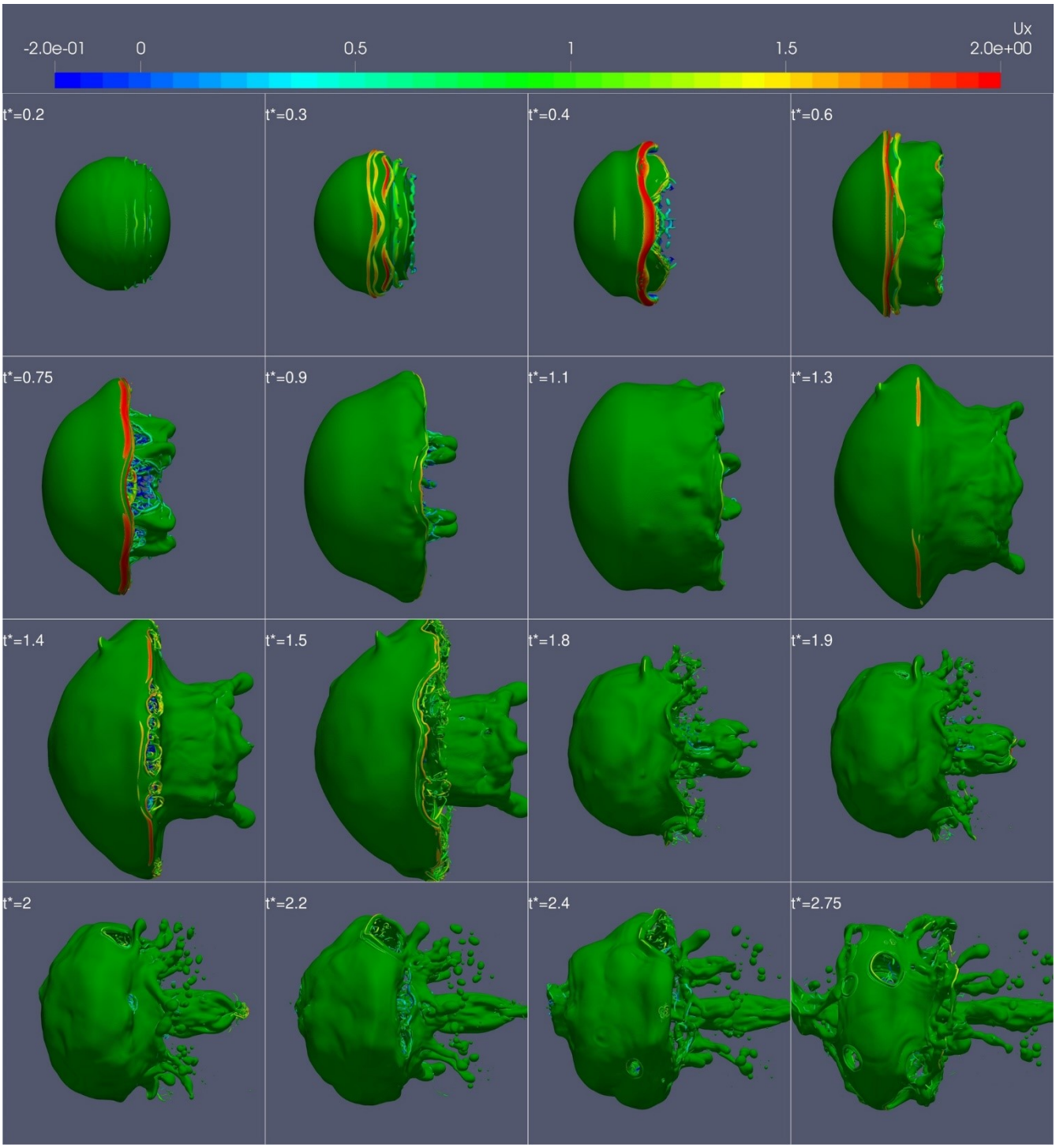

Figure 116: Interface (colored in green) and vortex structures (colored by velocity in X direction) detected with lamda2 criterion, side view projected in XZ plan, a, formation of vortex ring at t=0.3 and 0.6; b, stretching of interface around this vortex ring t*=0.3~1,3 (observation by combining with Figure 117 and Figure 118); c, formation of thin sheets at peripheric at t*=0.75, 1.1, 1.5 (Figure 117). d, entrainment of sheets from peripheric to central lines at t*=0.6~0.75, e, collision of sheets at central line and formation of ligaments at t*=1.1~2.4.*

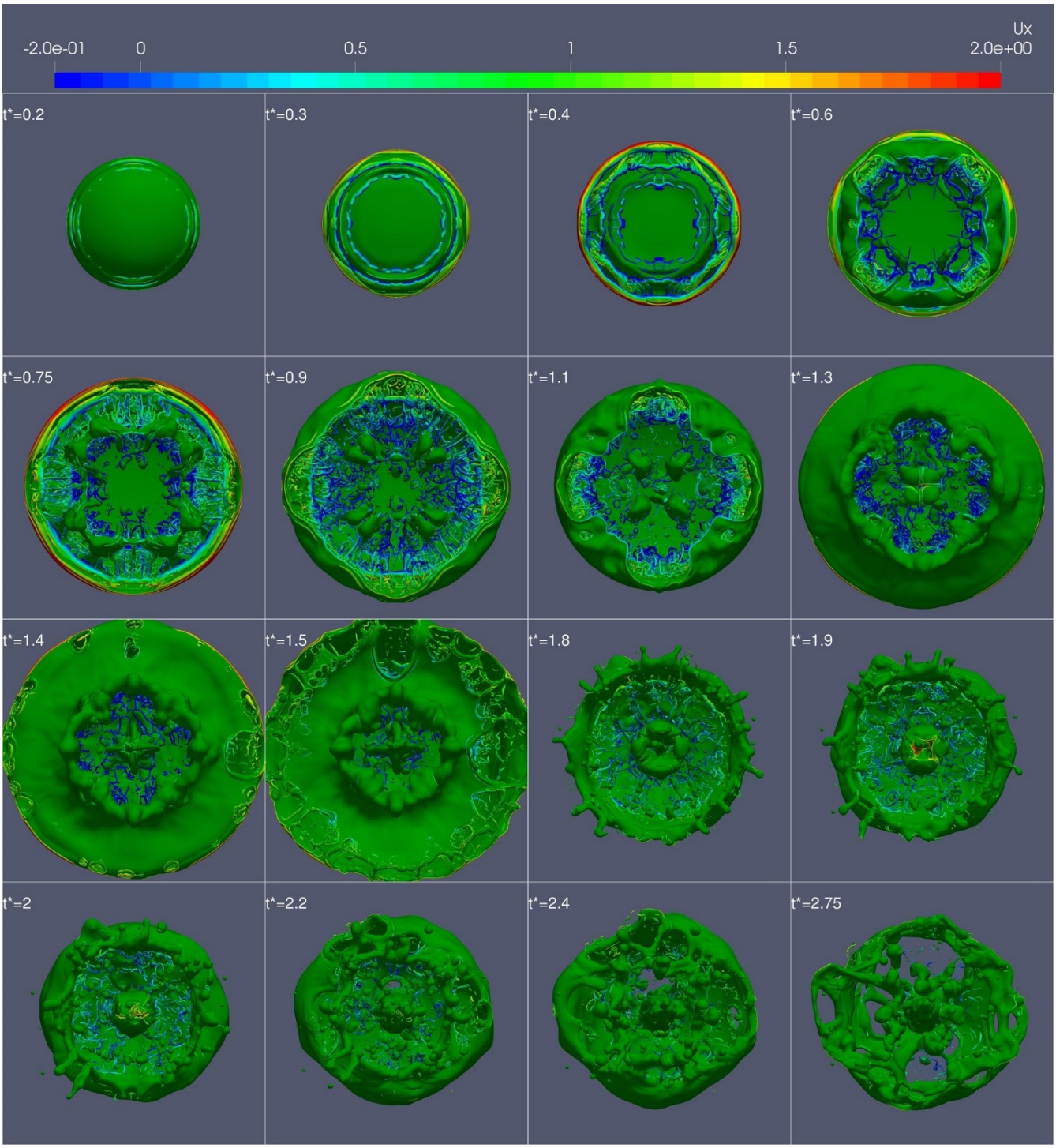

Figure 117: Interface (colored in green) and vortex structure (colored by velocity in X direction) detected with lamda2 criterion, right view projected in YZ plan a, formation of vortex ring at t=0.3 and 0.6; b, stretching of interface around this vortex ring t*=0.3~1,3 (observation by combining with Figure 118); c, formation of thin sheets at peripheric at t*=0.75, 1.1, 1.5 d, entrainment of sheets from peripheric to central lines at t*=0.6~0.75, e, collision of sheets at central line and formation of ligaments at t*=1.1~2.4.*

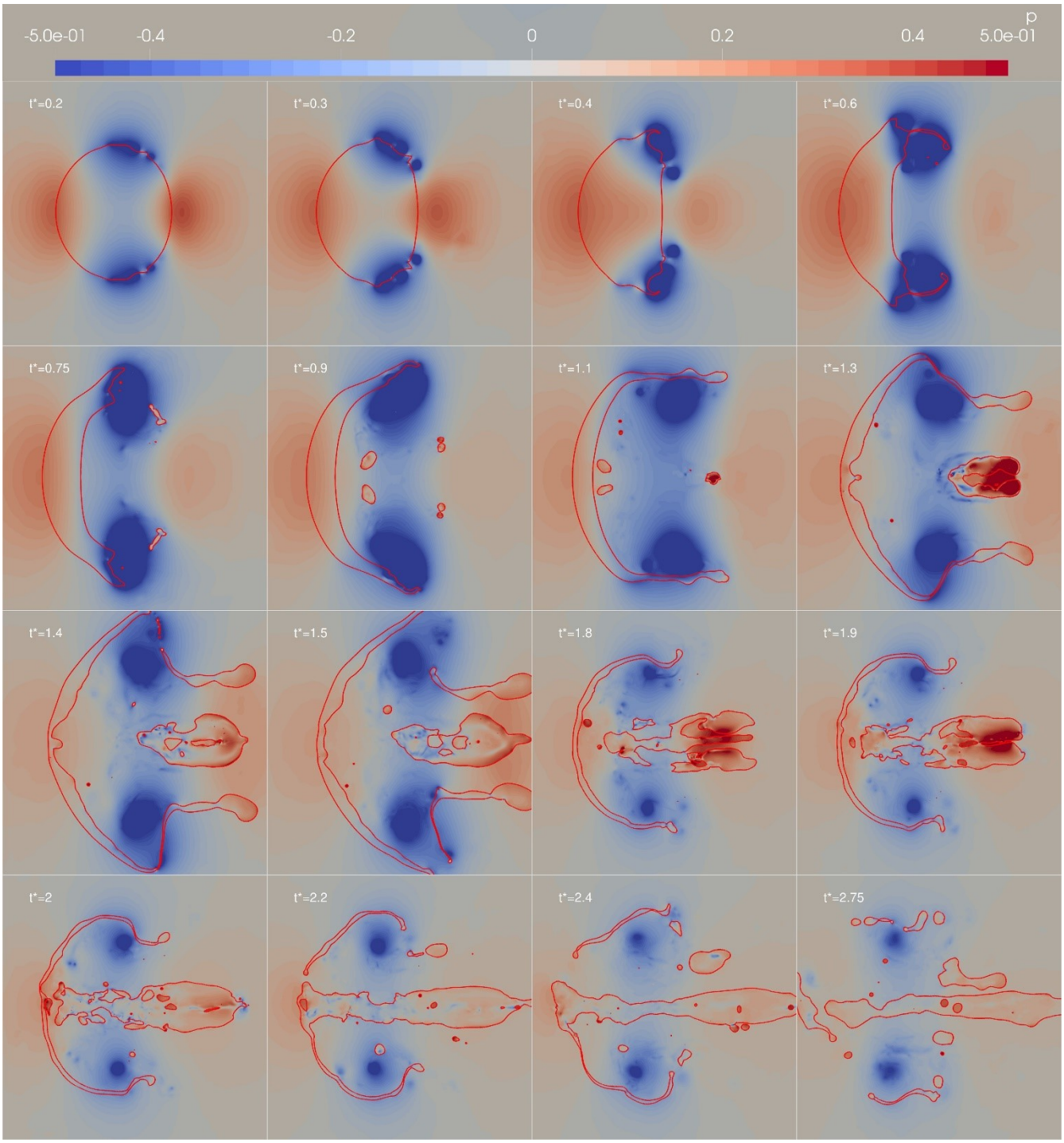

Figure 118: Dimensionless pressure ($\frac{P-P_{outlet}}{\rho U_0^2}$) distribution and at different time, interface in solid line, XZ-plan cut, a, formation of vortex ring at t=0.3 and 0.6; b, stretching of interface around this vortex ring t*=0.3~1,3 (observation by combining with Figure 117); c, formation of thin sheets at peripheric at t*=0.75, 1.1, 1.5 (Figure 117). d, entrainment of sheets from peripheric to central lines at t*=0.6~0.75, e, collision of sheets at central line and formation of ligaments at t*=1.1~2.4.*

4.4.3.5. Sheet-thinning

For high Weber number (640~2560), e.g., Figure 119, the typical sheet-thinning mechanism is confirmed. The drop is rapidly destabilized and deformed firstly as 2D layers of short wavelength and then develops to 3D patterns. Multiple parallel thin layers are formed perpendicular to the inlet flow, then these waveform layers develop into small sheets and detached from drop. The formation of small sheets is due to the combined effect of the shear and likely local Rayleigh-Taylor effects. These sheets are entrained and stretched into the wake of drop. When the sheets further disintegrate, the fragments are directly formed at the front and entrained into the center. At the same time, the drop itself gradually deforms into a hollow bag, furtherly breaking up into multiple sheets, then into fragments. As the fragments are mostly created by the thin sheet breakup, their size and SMD are relatively small.

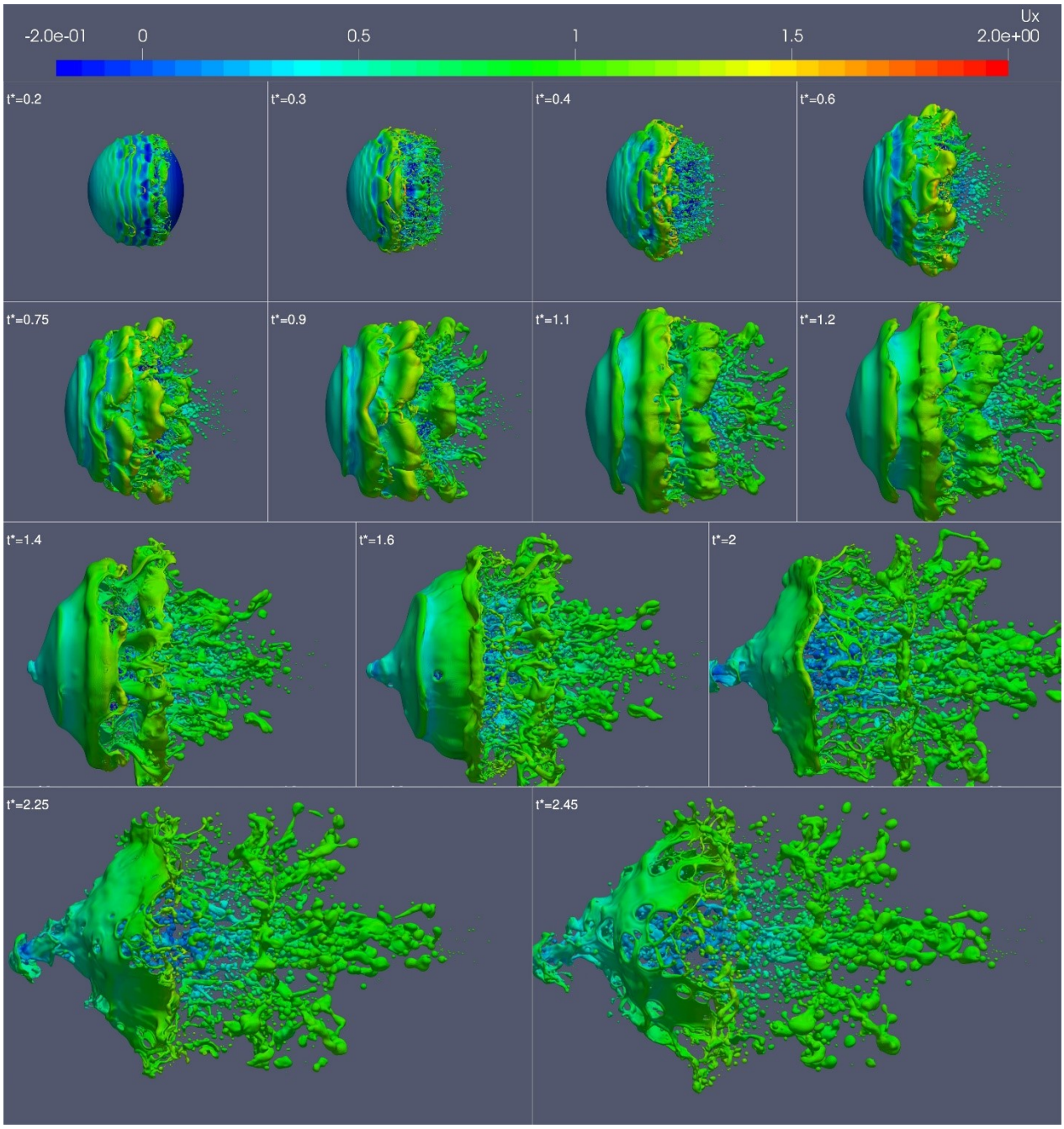

Figure 119: Interface in 3D view for the case We=640, Re=32000, (interface colored by velocity in X direction)

Another big difference is the observation of the appearance and development of Rayleigh Taylor instabilities in axisymmetric layers, which is called transverse azimuthal modulations by (Marmottant and Villermaux, 2004). Based on their experimental observation in Liquid-Gas jet system, they observe that it happens only when the ambient velocity goes beyond a critical velocity.

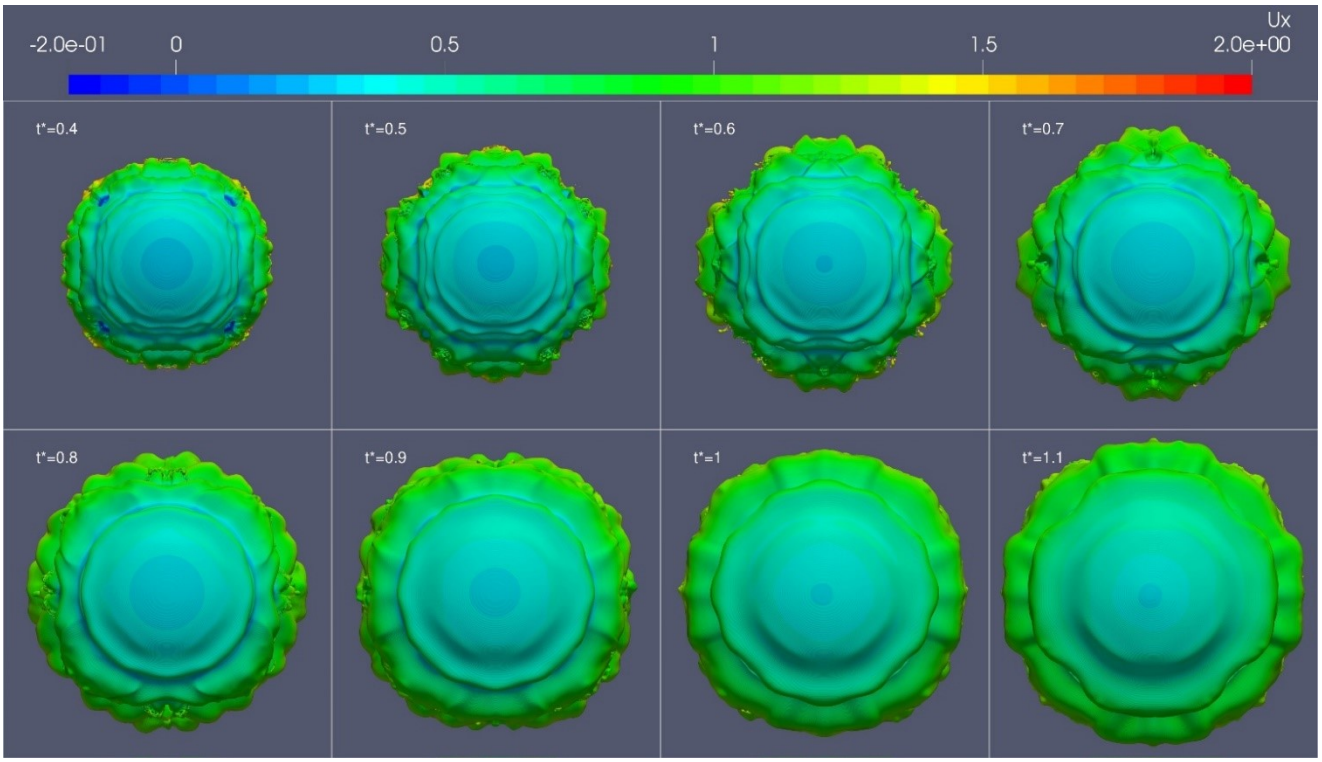

Figure 120: Interface (colored by velocity in X direction) form left view projected in YZ plan, observation of instability of Rayleigh Taylor.

For these high Weber number cases (640~2560), accompanying the deformation of drop in a concave bag, multiple wavy thin layers are observed at the drop periphery, likely due to the combined effect of axisymmetric and transverse azimuthal modulations proposed by (Marmottant and Villermaux, 2004). Instead of being entrained into the central line and forming ligament, the sheets (for high Weber number in the range 640~2560) directly detached from the mother drop and breakup into fragments (Figure 121).

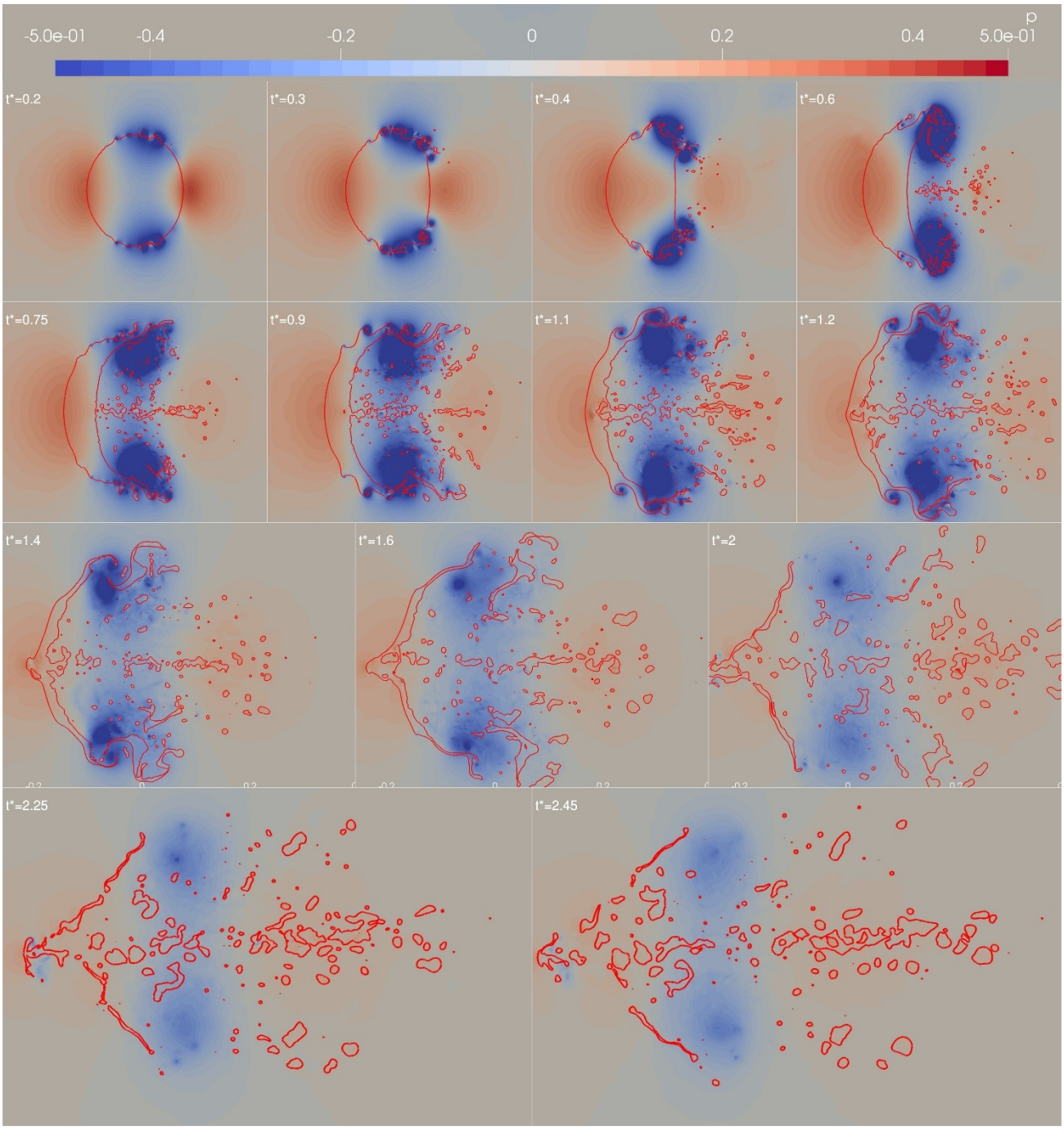

Figure 121: Dimensionless pressure ($\frac{P-P_{outlet}}{\rho U_0^2}$) distribution and at different time, interface in solid line, XZ-plan cut. a, observation of multiple local minimum pressures at t=0.3, 0.4, 1.1 and 1.3, corresponding to the maximum local velocity (or vortex ring formation) and strong interface stretching (generation of waveform layers structure); b, formation of sheets and their detachment from the mother drop at t*=1.1, 1.2, 1.4 and 1.6; c, sheets breakup into small fragments at t*=1.2, 1.4, 1.6 and 2*

4.4.4. Fragmentation characteristics

The contour of the drop in the early deformation phase (from beginning to $0.7T_{RN}$, shown in Figure 122) for all cases of different Weber numbers follows the same path, i.e., the drop vertical periphery elongates in the cross-stream direction and the rear of drop recoils, which is a direct consequence of uneven distribution of static pressure. The pressure dominates this early (deformation) phase. Nevertheless, with the increase of Weber number, the aerodynamic force overshadows the surface tension force, and some local deformation/instabilities and deformation of drop into forward bag are observed.

This local deformation can be seen as the development of Kelvin-Helmholtz instabilities caused by the strong velocity slip between drop and ambient fluid. Compared with the case We=10 (Re=4000), the case We=40 (Re=8000), the ambient flow separation is more important, and stronger recirculation (which causes bigger velocity gradient around interface) after the separation point interacts and deforms the local interface. This flow recirculation has a “cascade” effect, i.e., it represents some form of a transient and developing vortex and flow pattern after this separation point will be influenced if it’s strong enough. It’s also why multiple local deformation can be observed, for high Weber (Reynolds) number cases. Bigger Weber number (Reynolds) number represent smaller flow separation angle and stronger recirculation effect. Therefore, there are no KH instabilities or few KH instabilities in the rear of drop for low Weber cases while such instabilities can be even seen in the frontal surface of drop interface for high Weber (Reynolds) cases.

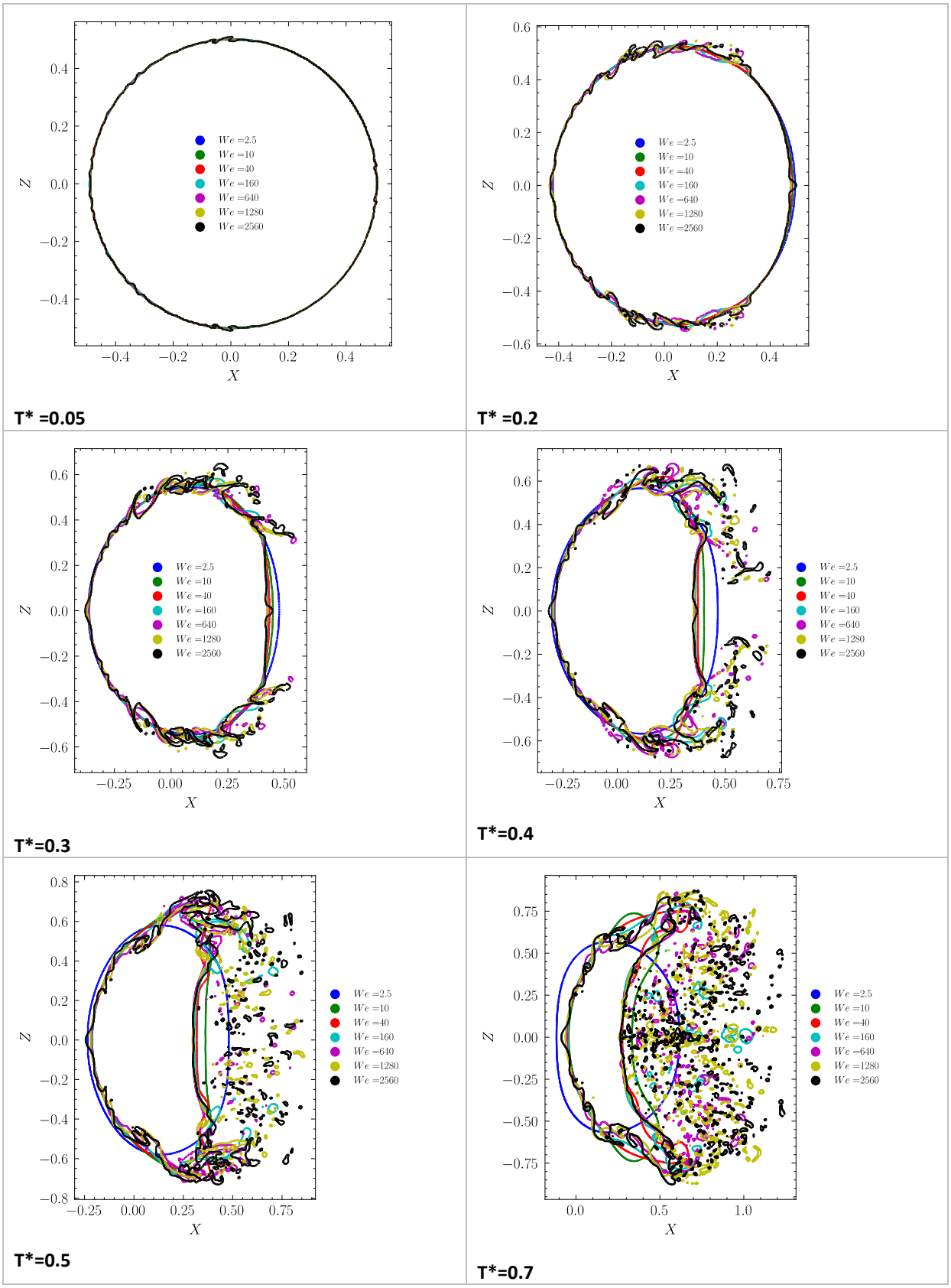

Figure 122: Interface contour for different Weber cases deformation phase, from beginning to $0.7T_{RN}$, XZ plan cut

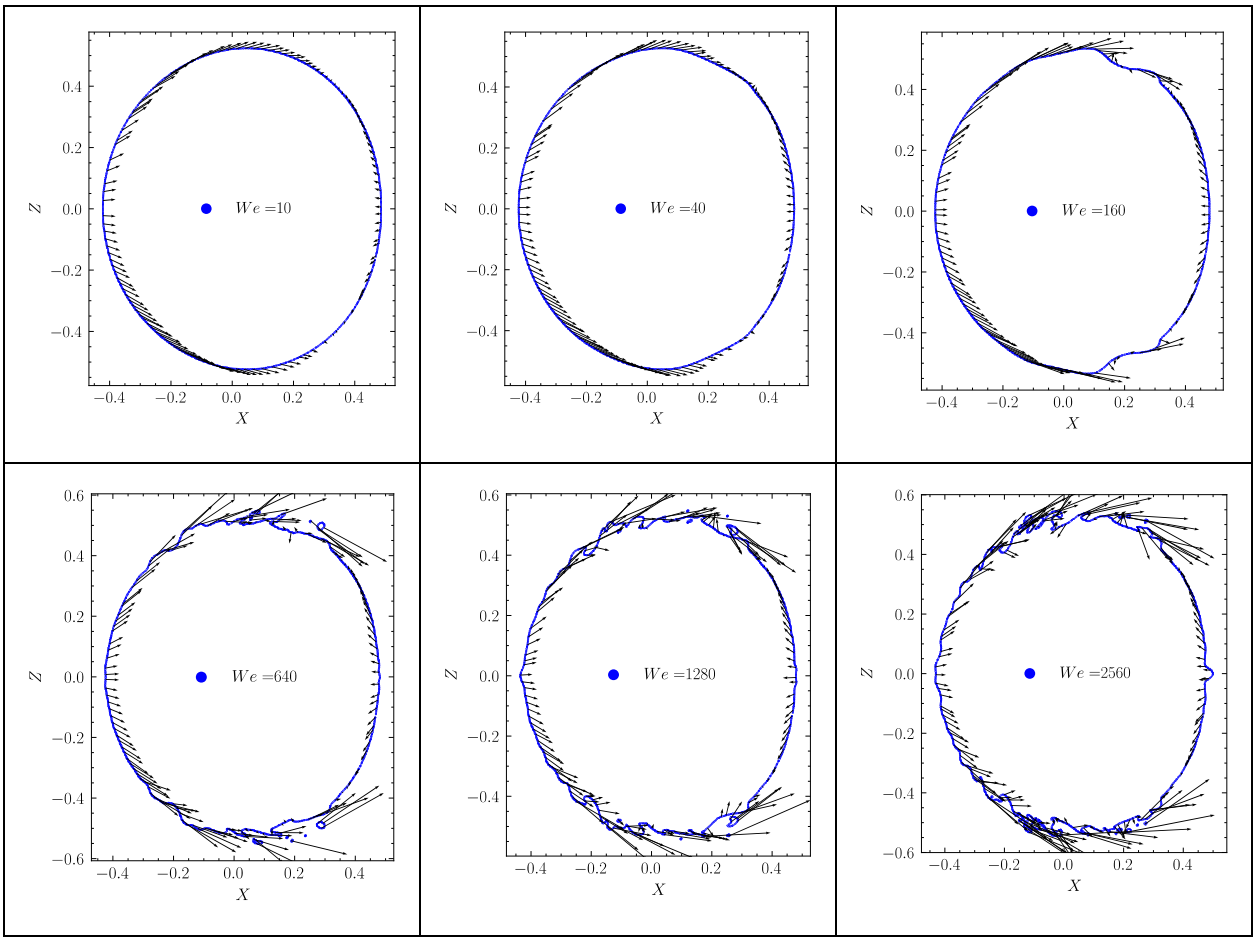

Figure 123: Interface and surface velocity at interface for different Weber cases at T =0.2T_{RN}, XZ plan cut

Another effect of high Weber conditions is the deformation of the contour into “inversed bag” because of stronger shear forces at the cross-stream edges. For high Weber number cases, the internal drop layer is continuously stretched backwards and outwards with a rather big moving velocity. As consequence, high Weber number cases have stronger deformation and occupy more space in cross-stream direction. Besides, the thickness of this internal layer decrease with Weber (Reynolds) number, thin sheets are generated in the viscous boundary layer of ambient fluid once this internal layer disintegrates from the drop. These sheets are entrained into the wake zone. What’s more, the stronger stretching also entraps some recirculation ambient fluid of inverse velocity in wake zone, which deform the rear of drop and finally into forward bag.

4.4.5. Probability Density Function

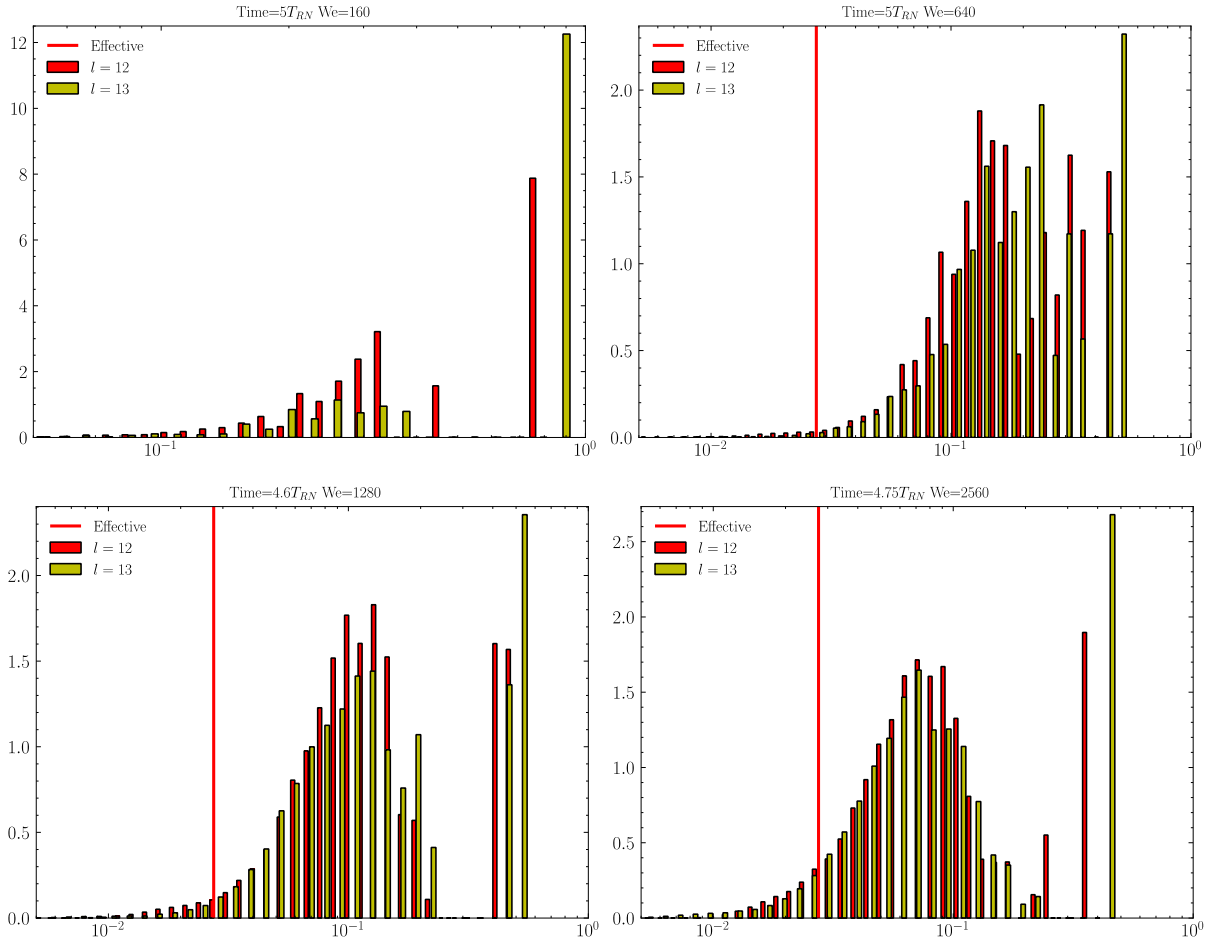

Figure 124: Mass weighted PDF, Y axis gives the probability density (probability per unit length) for different size of fragments, X: log(d30/D0), the vertical line "effective" indicates the position where the size is equal to 10 meshes for level 13 (5 meshes for level 12)

The mass-weighted probability density function (PDF) in shown in Figure 124, the vertical red line with the caption "effective" indicates the position where the fragment size is equal to 10 meshes for level 13 (5 meshes for level 12). When the size of the fragment is greater than this value, this fragment is resolved by at least ten meshes for refinement level 13 (five meshes for refinement level 12), which in turn justifies the choice of the mesh size. A higher Weber number leads to a smaller fragment size, which coincides with the previous discussion that a higher Weber (Reynolds) number generates thinner sheets and thus smaller fragments. The mass-weighted PDF seems to converge for small fragments (size between 0.001 and 0.15) while some differences are observed for larger structures (size between 0.2 and 0.4). Meshing of a higher level of refinement can keep the fine structures connected longer and the breakup of these structures will occur later. However, the influence of this effect on the final Mean Sauter Diameter should be minor with proper meshing (in our case, the convergence of small size fragment is observed).

4.4.6. Drag coefficient

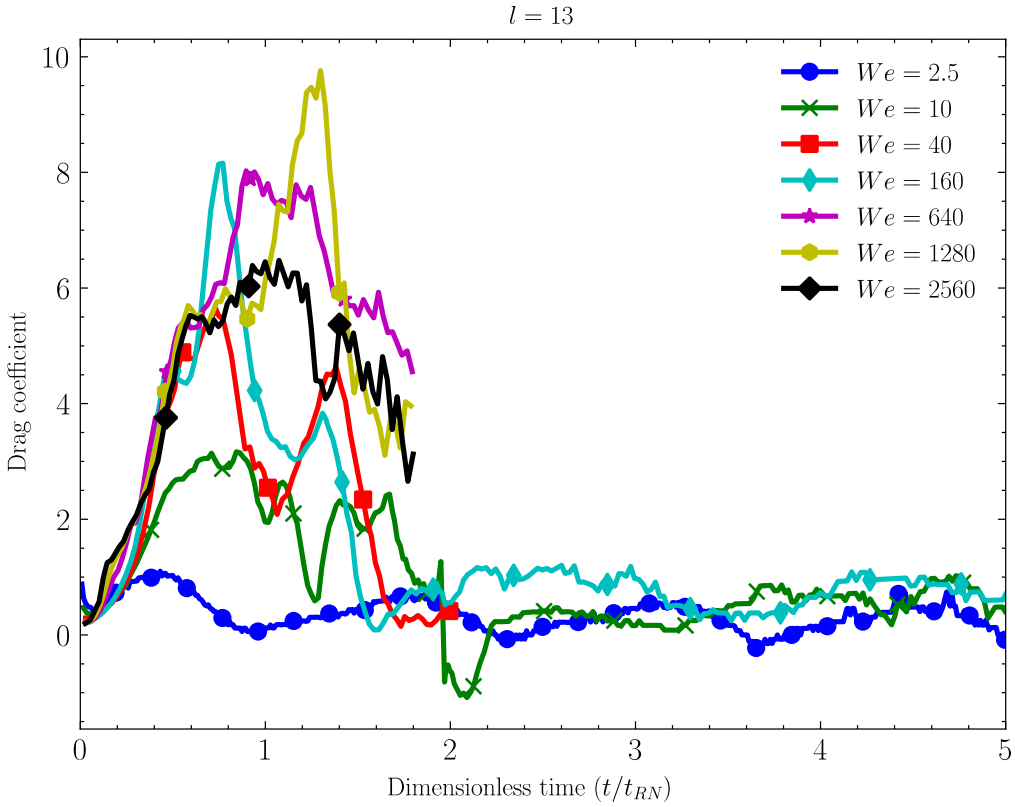

Figure 125: Drag coefficient for different weber cases (level of refinement 13)

The drag coefficient, *cf* eq. (3), of the deformable and fragmenting drop is a very important parameter to model the particles-flow dynamic interaction for MC3D. During such a transient process, the unsteady drag coefficient of the drop can change significantly. It's interesting to point out that the initial drag coefficient is almost the same for all the case, close to 0.45, which corresponds to a non-deformable sphere. Also, for the smallest Weber number, i.e., oscillating drop, it is seen that the drag coefficient oscillates around this value in the beginning. The variation of drag coefficient (for Weber number 160~2560) follows the same path in the initial phase (from 0 to 0.6 t_{RN}), which rapidly increases to a high value, corresponding the deformation of drop into bag. The fact that the drag follows the same path also demonstrates the dominant effect of pressure drag in this very beginning phase unless the drag coefficient should be much bigger for high Weber (Reynolds) number cases. The formation of bag and expansion of bag in perpendicular plane increase the projected interfacial area between the melt and fluid. Besides, the bag-form interface makes a low-pressure zone at the wake of drop and increases the pressure difference between the front and tail of drop. In addition, as discussed in the breakup regimes, the fluid entrained inside the drop-fluid local zone, of low velocity, can also increase the inertia. Both will increase the drag coefficient. When the bag finally breaks through, the drag coefficient decreases.

4.5. Thermal analysis

Even in simple situations, the literature related to concurrent fragmentation-heat transfer process is not really abundant. There exists an important activity related to the impact of deformation on evaporating droplets, in the context of combustion engineering, see e.g.(Sazhin, 2017) for a recent review. The present work aims to investigate the existence of MI zone and the impact of such configuration on the heat transfer using the Basilisk software.

Before giving the thermal analysis, we firstly recall that the temperature is made dimensionless using the formula in Table 9. All parameters used for the calculations (initial temperatures and physical properties in Table 8) are based on the corium. Therefore, the conclusions in this section are only valid for the specific case, i.e., a corium drop initially at 3000 K.

4.5.1. Temperature map from an axial cut

We are firstly interested in the mechanisms of heat diffusion inside the drop under the influence of oscillations. Indeed, in most of the cases, with the presence of boiling or not, solidification is expected to have a significant impact, and it will largely depend on the heat diffusion inside the drop. Several "crust" models have been built for the FCI models, including MC3D (Uršič et al., 2015). These are based on the assumption of weak heat diffusion, i.e., solely based on conduction. Nevertheless, this assumption has not been precisely evaluated yet.

Figure 126 shows the temperature map from an axial cut for Weber number 2.5. In this slowly oscillating case (with a period close to the Ranger & Nicholls time), the superficial internal boundary layer is entrained from the front of the drop, and then inside it. The thermal boundary layer at the front does not really grow with time, whereas there is an accumulation of colder liquid behind the equator. This accumulation progressively grows and occupies the whole volume after t*=6. This is important since the heat transfer occurs mostly at the front, meaning it should not be too much affected by the cooling, up to t*=6. The heat transfer seems almost stopped at t*=6: this is due to the entrainment of the drop in the coolant liquid, Figure 94

Therefore, in a solidifying material, any external homogenous crust may form only under specific conditions. In the situation depicted here, which is related to cases with low boiling, solidification is likely to start at the tail of the drop rather than at the front. In any case, the mixing inside the drop leads to a quite homogenous melt temperature.

Note that the surface temperature is dictated by the ratio of thermal diffusivities which are here of similar order. As a results, the surface temperature should drop immediately around the average of the coolant and drop temperature. This is not the case when film boiling is active and thus the thermal gradient at the interface in this case should be much less important (as well as the entrainment of the superficial liquid). So, any conclusion on solidification cannot be directly extrapolated.

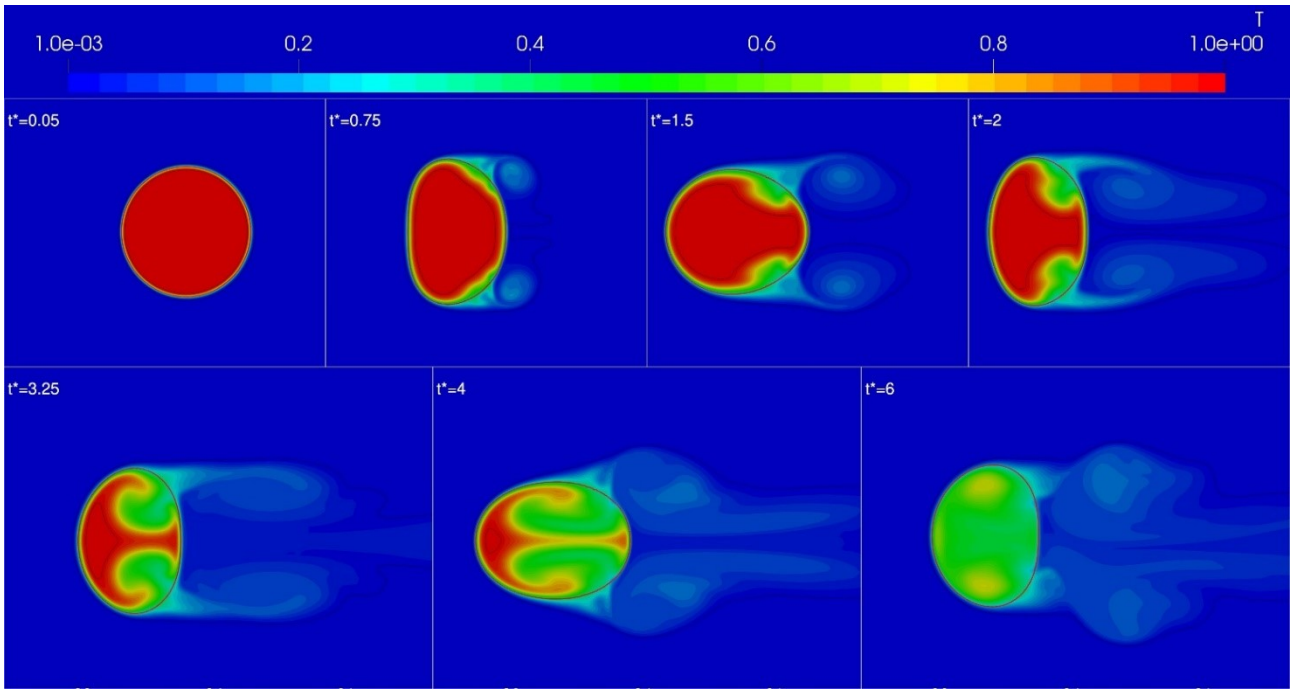

Figure 126: Temperature field (axial cut) at different time step for the case We = 2.5. The red solid line represents the drop-liquid interface. The black solid line inside (outside) the drop represents the iso-temperature contour 99% (1%) of the initial drop overheat.

Figure 127 shows the temperature map from an axial cut for Weber number 10. In this higher Weber (Reynolds) number case, cooling will be rapid where vortex rings are present (e.g., vortex at 1.5 and 2 t_{RN}), which means that the mixing effect is much more effective than diffusion itself. The main features for the previous case are still effective, with much important intensity. A strong mixing is already observed at t*=2, despite strong local and internal gradients. Furthermore, this mixing effect within the drop causes the temperature to tend to rapidly be quite homogeneous instead of maintaining a temperature gradient in the radial direction. Finally, the temperature is uniform inside the two drops (e.g., vortex at 1.5 and 2 t_{RN}). As these two “fragments” are rather large, they still have a hot temperature after 6 t_{RN}. Again, these drops have almost reached the coolant velocity, and thus the cooling rate decreases strongly.

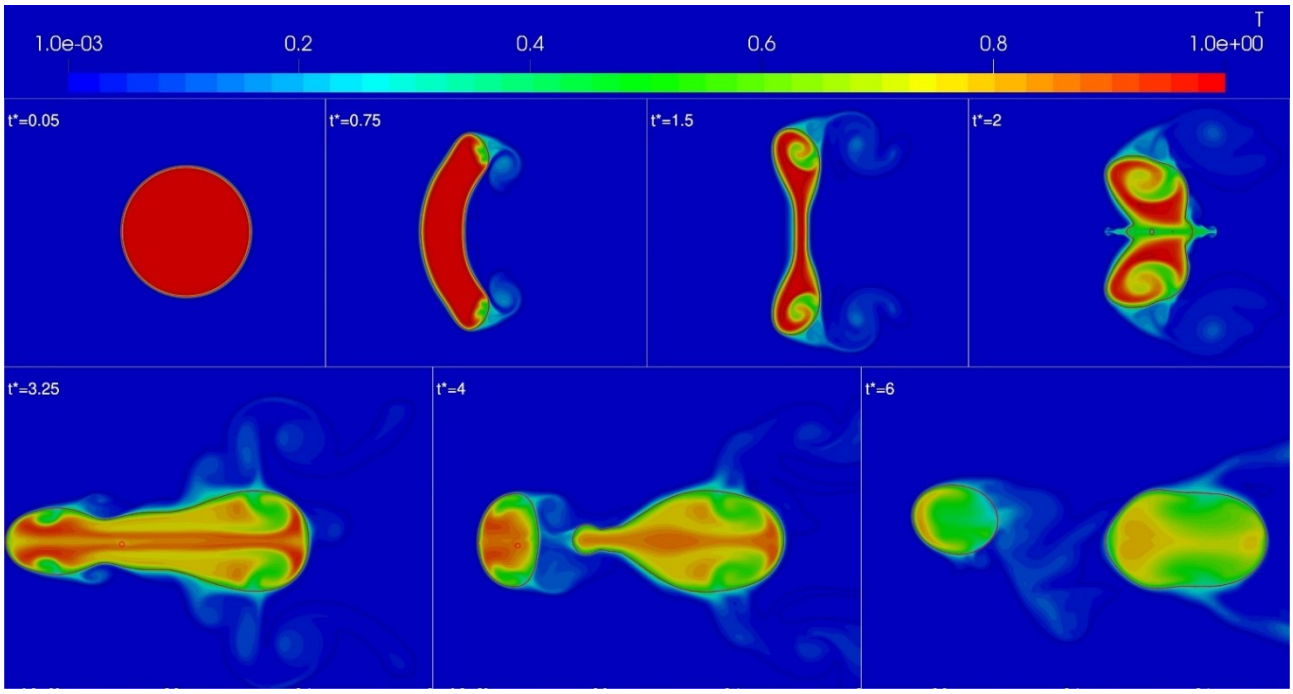

Figure 127: Temperature field (axial cut) at different time step for the case We = 10. The red solid line represents the drop-liquid interface. The black solid line inside (outside) the drop represents the iso-temperature contour 99% (1%) of the initial drop overheat.

Figure 128 shows the temperature evolution for the case We=40, for which a forward bag formation is observed. The mechanism previously described are intensified, with still a displacement of the cooled fluid towards the ring of the bag. The close-up in Figure 129 shows that the gradients at the interface do not grow significantly while the bag is thinner, up to t*~1.6, when the thickness is equal to 2 times the gradient. Note also that the cooling seems equally intense inside the bag, due to the coolant vortex inside it.

It is reminded that a solidification of the bag surface is possible and such a phenomenon was observed in the experiment by (Achour, 2017)(see Figure 74). Note however that this experiment was influenced by gravity which maintains a velocity differential. In contrast with the previous cases, the bag is not influenced par thermal mixing which remains located in the ring. But, since piercing of the bag has also started in the Achour test, the bag thickness was very small. Thus, it is not so clear if the solidification could be the result of a crust at the surface, or due to the merging of the two gradients.

It is also seen that the fragmentation induces a melt-coolant mixing within, for a transient period, a virtual sphere (dashed yellow line) with a volume equals approximately to 15 times the initial drop one. This may estimate at first order the volume of water interacting with the melt whereas the existing micro-interaction model use typical values from 5 to 12. It is however clear that, in this case, the entrained water temperature is far from being homogenous. The volume occupied by the water within the solid black line represents the dimensionless temperature greater than 0.01, which may represent a characteristic average temperature for entrained and mixed water. In addition, cooling is much faster for the small fragments (Figure 129, $3.25t_{RN}$, $4t_{RN}$ and $3.25t_{RN}$) that originate from the bag rupture. The large fragment from the rim breakup still shows high temperatures after 6 t_{RN}.

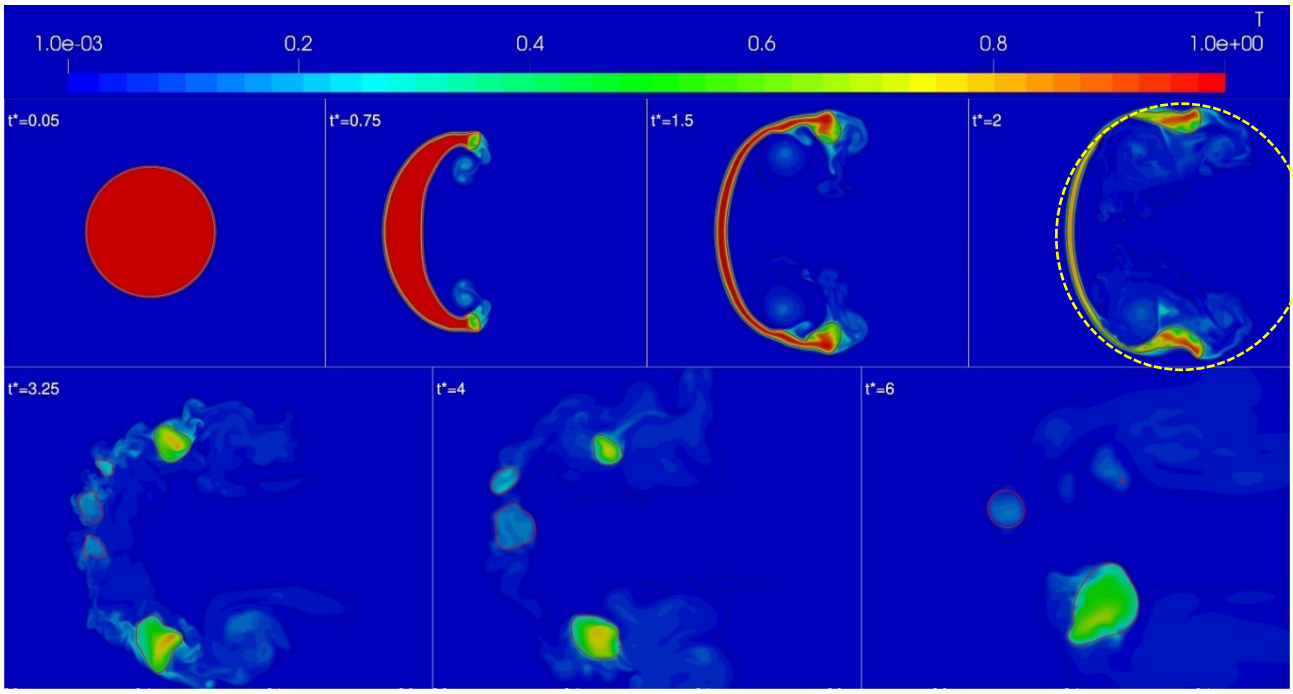

Figure 128: Temperature field (axial cut) at different time step for the case We = 40. The red solid line represents the drop-liquid interface. The black solid line inside (outside) the drop represents the iso-temperature contour 99% (1%) of the initial drop overheat.

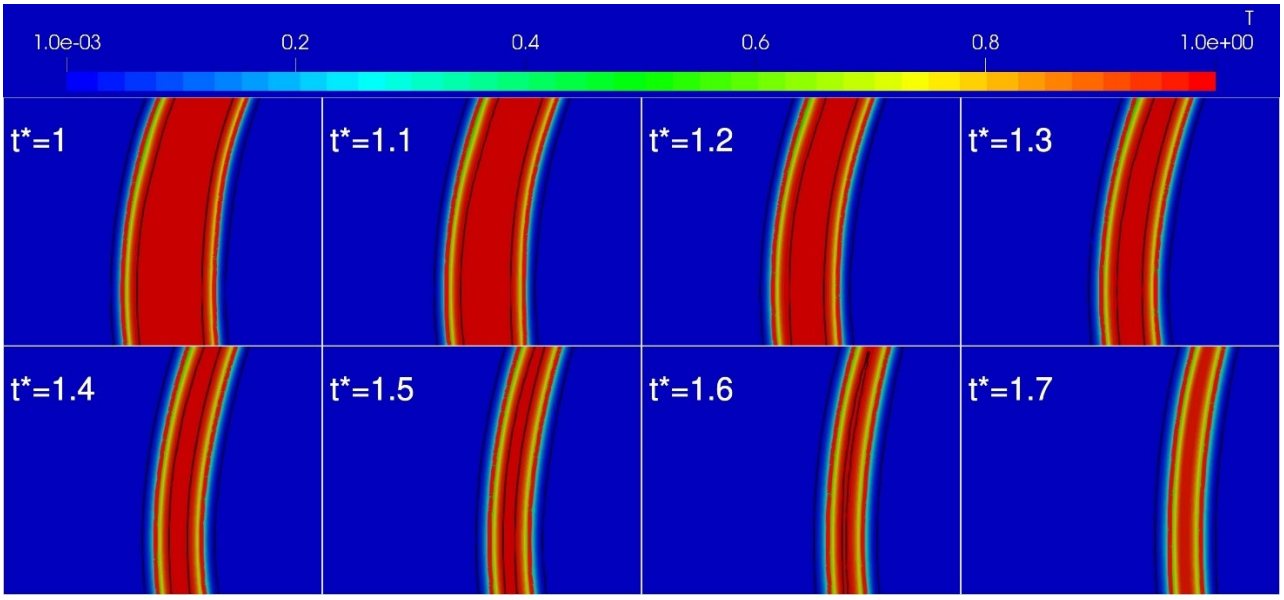

Figure 129: Zoom of temperature field (axial cut) at different time step for the case We = 40. The red solid line represents the drop-liquid interface. The black solid line inside (outside) the drop represents the iso-temperature contour 99% (1%) of the initial drop overheat.

The temperature maps for We = 160 are given in Figure 130. For the beginning stage (0~0.4t_{RN}), the cooling is most effective at the location of the vortex (rings). As a result, the cooling of the back surface is faster than that of the front surface. As the drop deforms into the shape of a bag, thin layers are formed at the periphery of the drop and are quickly cooled due to its large surface area (0.6~0.75t_{RN}). At the same time, these sheets are stretched into the wake of drop, the breakthrough of the sheet (Figure 131, 0.6t_{RN}) generate small ligaments and further fragments (Figure 131, 0.75t_{RN}), and they are fast cooled to a low temperature. These fragments are entrained into the bag and strike the bag interieur surface (Figure 130, 1.1t_{RN}), making the bag thinner at the

central line (Figure 130, 1.4t_{RN}). The cooling of the bag in the central line is more rapid (Figure 130, 1.9t_{RN}). As the leaves detach from the mother drop, coalesce, and accumulate in the central line, a large low temperature ligament forms (Figure 130, 1.5~2.4t_{RN}). Because the melt entrainment is greater, the volume of heated water is greater, occupying almost the entire volume inside the bag (Figure 130, 2.4 and 2.75t_{RN}), which make the existence of a local micro-interaction seems plausible. When the bag breakup into fragment of small size, they are faster cooled (Figure 130 and Figure 131, 5t_{RN}).

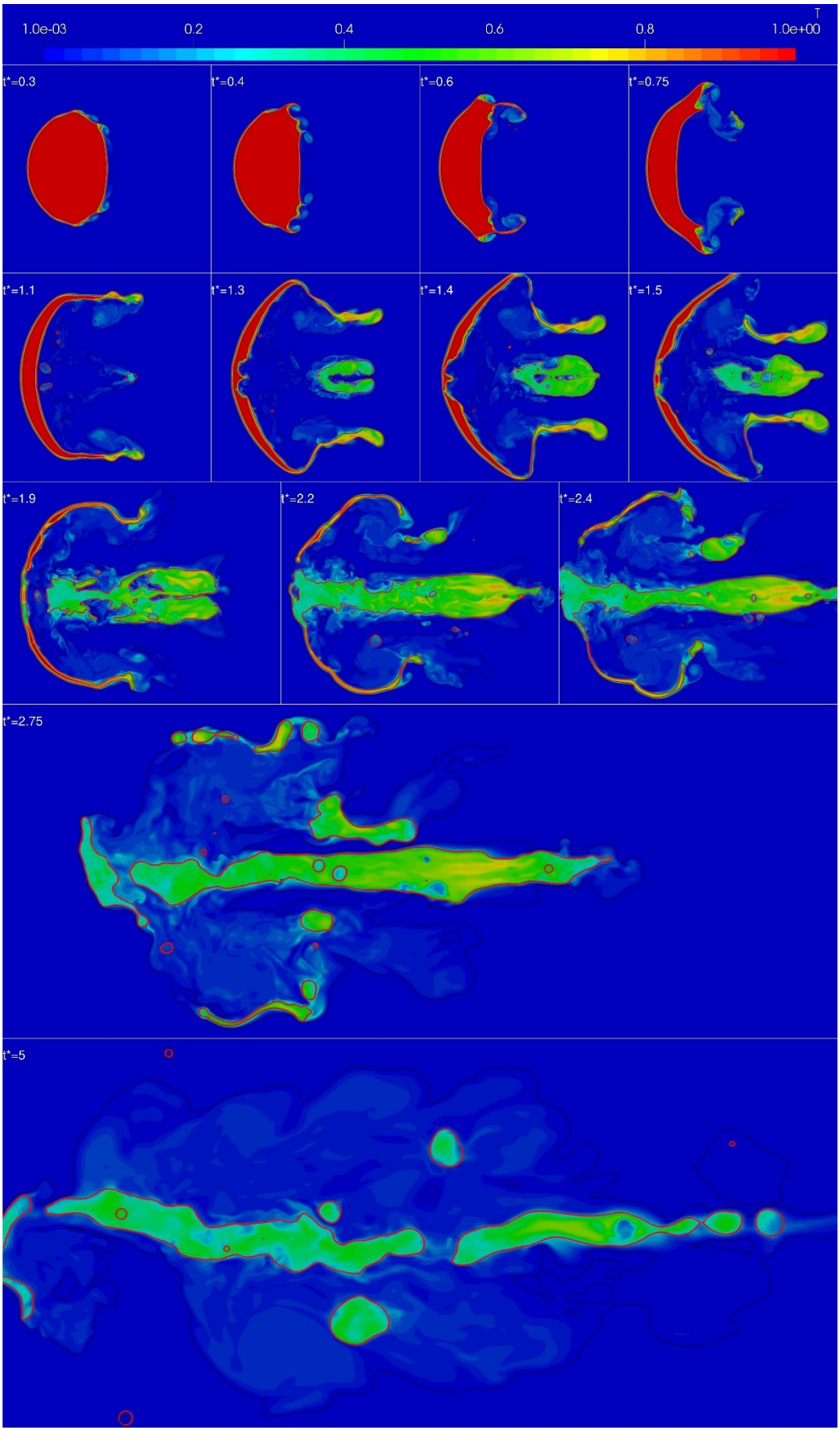

Figure 130: Temperature field (axial cut) at different time step for the case We = 160. The red solid line represents the drop-liquid interface. The black solid line inside (outside) the drop represents the iso-temperature contour 99% (1%) of the initial drop overheat

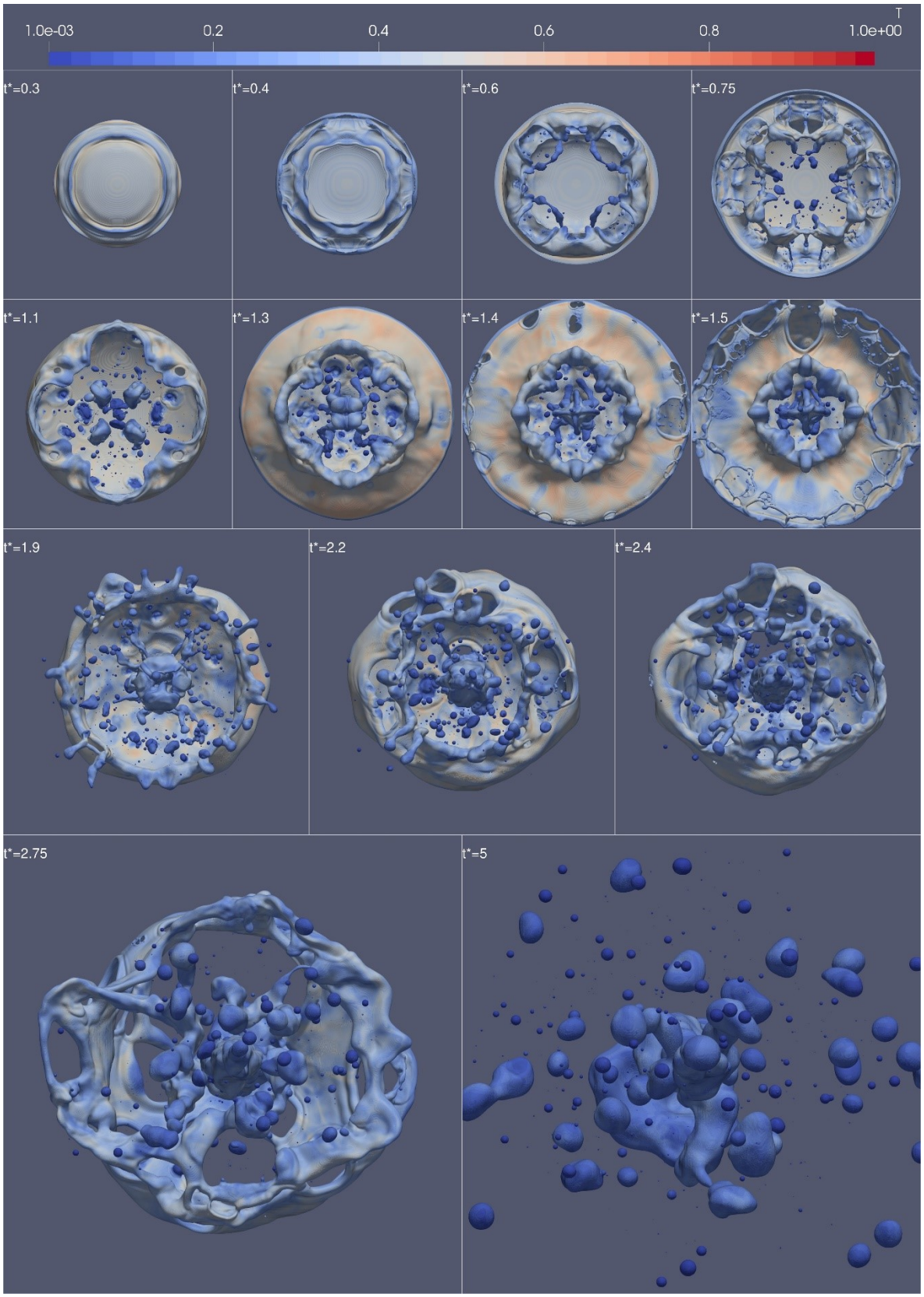

Figure 131: Temperature field at the drop interface for the case We = 160, view on YZ plan

The temperature maps for We = 640 are given in Figure 131. . For these higher Weber number cases, cooling is also more efficient at the edges, where the wave layer forms. These layers are stretched in the wake and become thinner, breaking directly into small fragments.

As for the previous cases, including the oscillating one, the fundamental mechanism is that the heat transfer is more intense at the front and the cooled layers are transported along the interface to accumulate at the tip of the waves. The ligaments and then, the fragments, are generated already relatively cooled.

Because of the increase of the exchange area, the entrainment of the thin heated coolant layers and small fragments in the wake is more important, almost all water inside the bag is heated. However, it is clear that the two phases remain for a large time with an important difference of temperature, so that the equilibrium hypothesis does not seem legitimate, on a phenomenological point of view. More, since the drops are arriving already quite cooled, the thermal role in the MI zone is, in the present context without boiling, rather limited. Nevertheless, in the context of steam explosion, the rounded shape of the smallest fragments show that they are formed still liquid, thus with a quite high temperature[10].

Due to large velocity difference and interfacial area, almost the entire melt is cooled to a very low temperature after $4.5t_{RN}$ (Figure 133). Then, in any case, the heat exchange of the fragments in the wake/MI zone may be limited, especially considering the velocity differences within this zone should be also limited (internal fluctuations).

[10] The notion of "liquid" state refers here to the mechanical properties. In real cases of steam explosion, it is also suspected that thermodynamic equilibrium is not achieved due to the intensity of the heat transfer, so that the melt may be subcooled with still liquid behavior at fragmentation.

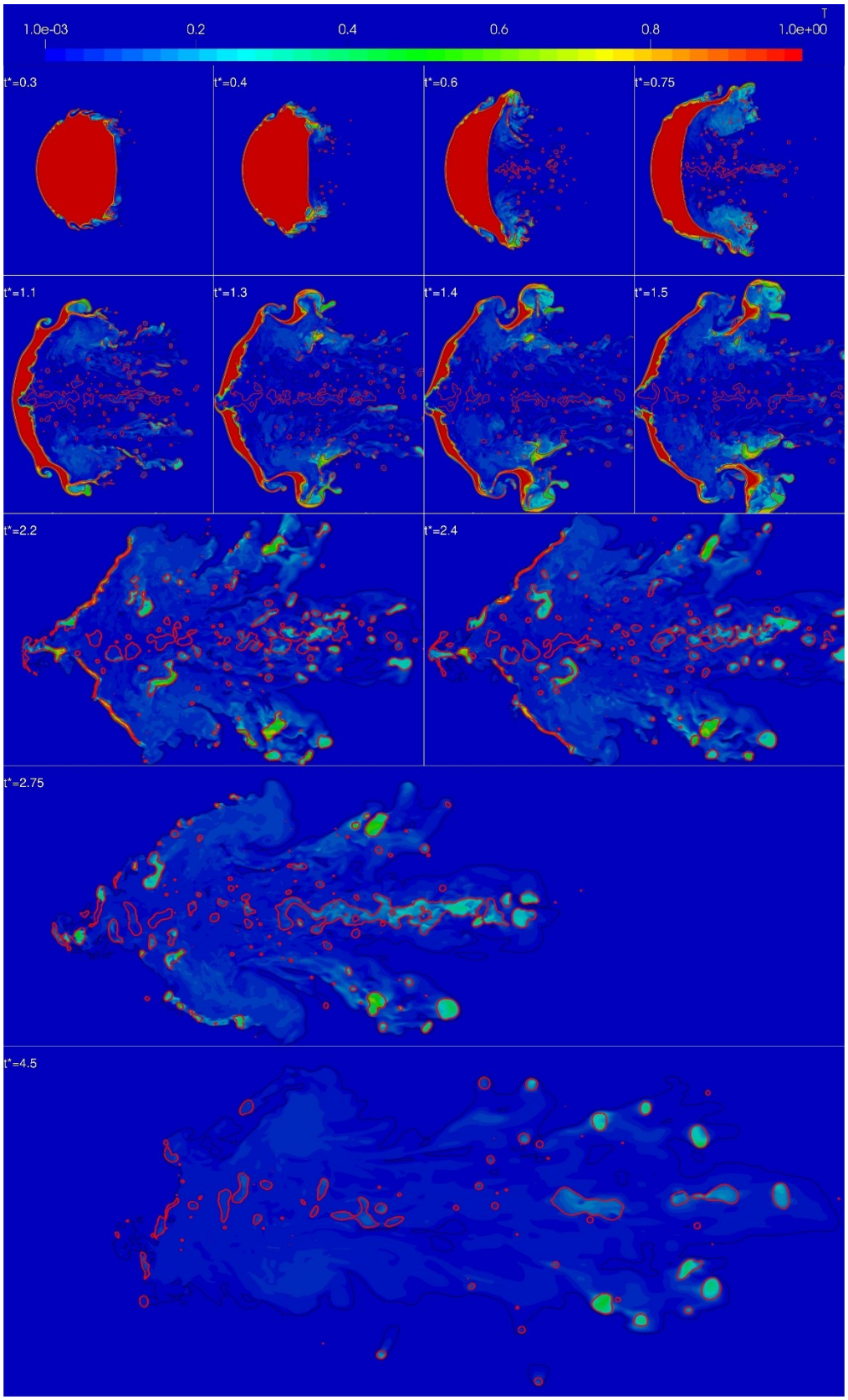

Figure 132: Temperature field (axial cut) at different time step for the case We = 640.

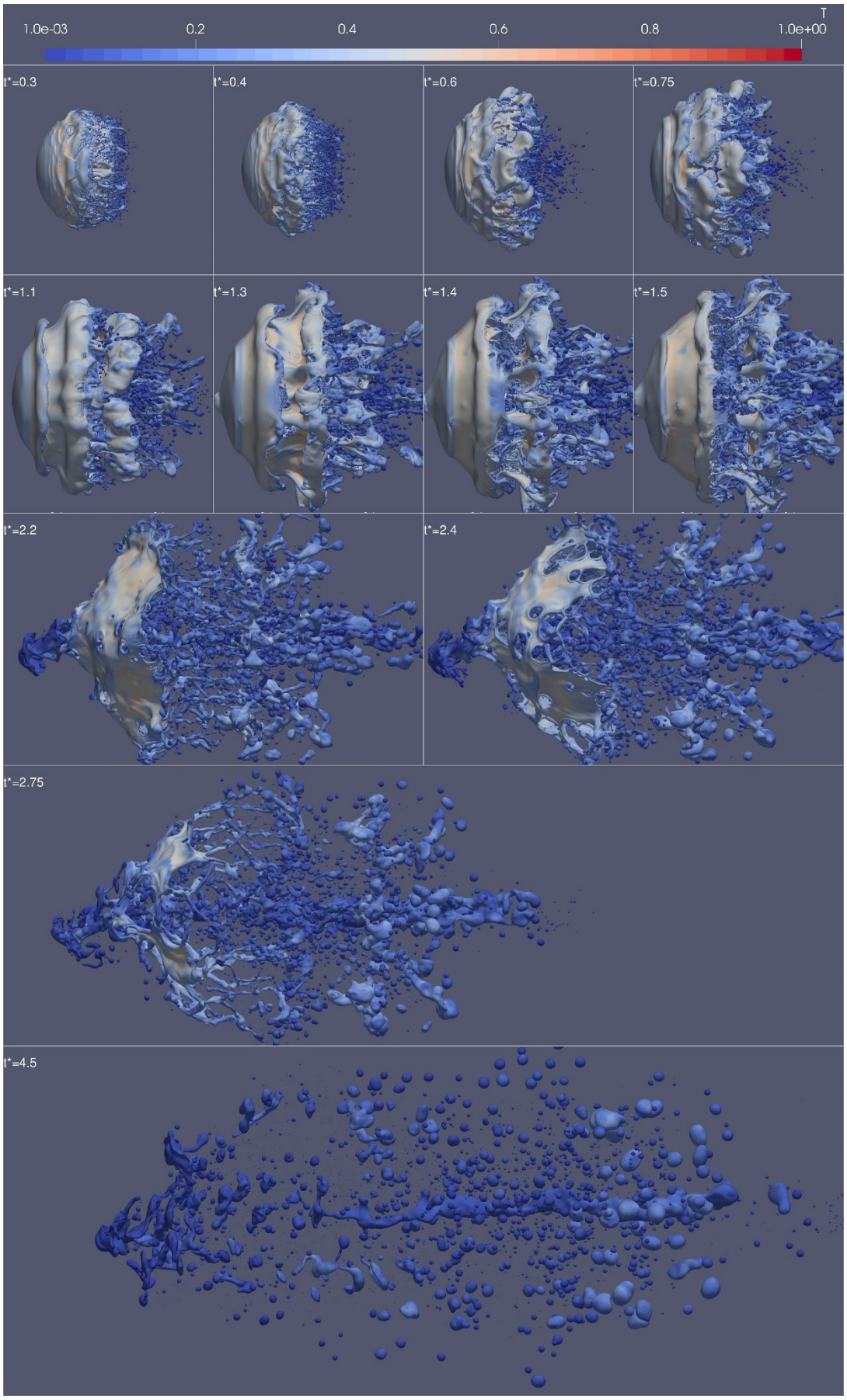

Figure 133 Temperature field at the drop interface for the case We = 640

4.5.2. Average temperature

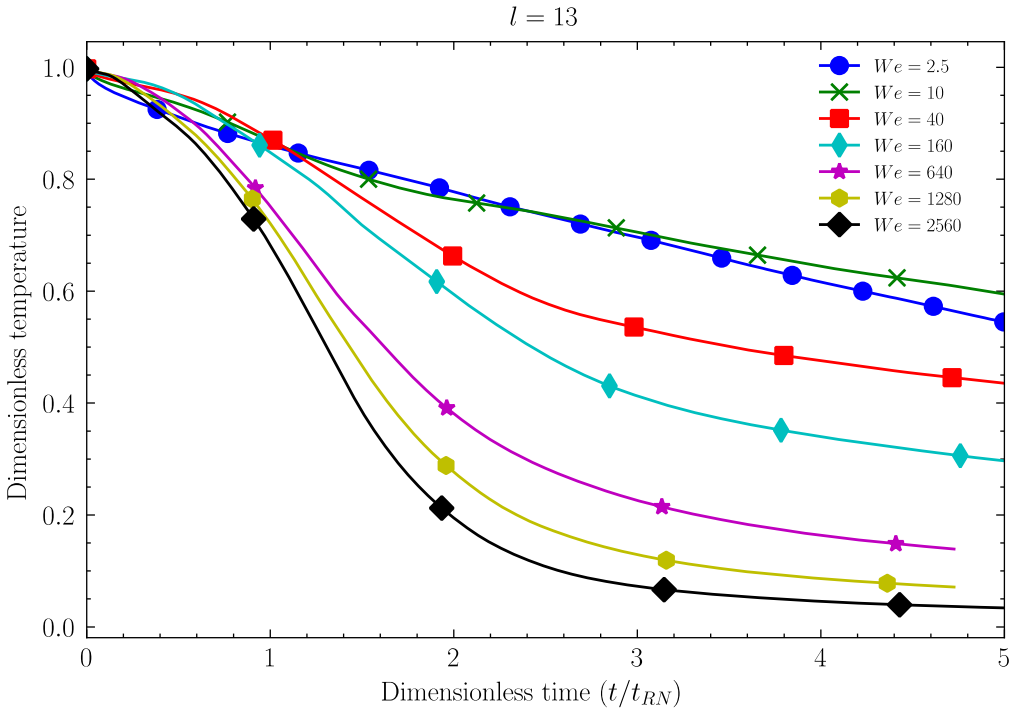

Figure 134: Variation of the mean drop temperature (dimensionless) for all investigated cases, as a function of the dimensionless time.

Figure 134 provides the mean temperature evolutions for all investigated cases, as a function of the RN time. It is clear, that the temperature does not scale precisely with the fragmentation time. For the fragmenting case (We > 10), we observe, after a short period of slow decline, a strong decrease in the temperature due to the drop deformation and fragmentation. The strong cooling effect at this period is due to the increase of interfacial area and agitation of the flow. Once fragmentation has occurred, after about $3t_{RN}$, the cooling rate becomes slower, likely due to the entrainment of melt, i.e., the end of the "micro-interaction" process. It is then noticed that, at the end of the fragmentation, the melt is generally strongly entrained by the ambient fluid and the thermal exchange is minimized. At that moment, the cooling grade is very dependent on the initial Weber number. From the present data, which might differ from the real case with film boiling, we may conclude that the explosion process (fragmentation + heat transfer) is efficient only Weber numbers higher than about 1000. The absence of scaling with the RN time confirms that, at least for the investigated cases, the cooling does not solely depend on the entrained water in the mixing zone, in the sense of the classical micro-interaction model. A preliminary important conclusion can be added that with the increase of Weber number, the cooling become much faster than the fragmentation.

We may also qualitatively conclude that, in case of solidification, this one will be more and more effective for inhibiting or limiting fragmentation with the increase of the Weber number. In this sense, there should exist an optimal Weber number for the explosion strength, in contrast with the common intuition that the explosion load should always increase with the Weber number. Meanwhile, the solidification will impact the size of the instabilities and resulting fragments. This should explain why the resulting fragments in steam explosion experiments are larger than expected when comparing with fragmentation laws without solidification effects.

4.5.3. Nusselt number

A transient heat flux can be evaluated by making the energy balance inside and outside of the drop.

From the drop side: we have the average temperature $\overline{T}$=$\frac{\sum_i V_i f_i T_i}{V_{tot}}$ and total energy of drop $E = \rho_D C_p V_{tot} \overline{T}$ with f_i, V_i and T_i volume fraction, volume and temperature in i-th grid, and $V_{tot} = \sum_i V_i f_i$. A heat flux Φ through interface can be estimated considering the energy loss of melt: $\Phi = \frac{dE}{dt}$.

From the fluid side: the average heat transfer coefficient h is defined as: $h = \frac{\Phi}{\boldsymbol{S}\cdot(\overline{T}-T_{inlet})}$ with $\boldsymbol{S}$ the interfacial area between melt and fragment and T_{inlet} the inlet velocity of water.

Finally, the average Nusselt number is computed using Sauter Mean diameter (SMD) $\boldsymbol{D_s}$ as hydraulic diameter $Nu = \frac{h\boldsymbol{D_s}}{\lambda_L}$.

The Nusselt number for all investigated cases is shown in Figure 135. At the very beginning phase (t*=0~0.05), Nusselt number firstly decreases, which corresponds to the establishment of the thermal boundary layer around the drop interface. However, this stage lasts only a short time, and the temperature of the drop does not show much difference. From t*=0.05 to 0.25, the drop undergoes only minor deformation, and the case with high Weber (Reynolds) number exhibits strong heat transfer and larger Nusselt numbers. From t*=0.4 to 2, the deformation of drop becomes significant, and the cooling of the melt occurs mainly at this stage, especially for high Weber cases. Even though the heat transfer is stronger, the Nusselt number based on the fragment size (SMD) is however lower because it already takes into account the increase of the interfacial surface, and important entrainment, during this stage, decreases the velocity difference (hence the Reynolds number). It highlights the dominant effect of interface increase on the cooling of melt. After 2 t_{RN}, both velocity slip between the melt and environment liquid and the interfacial area do not have big change, the velocity slip and interfacial area between the melt and the surrounding liquid do not change much, the heat transfer and Nusser number do not change much and the melt cools slowly.

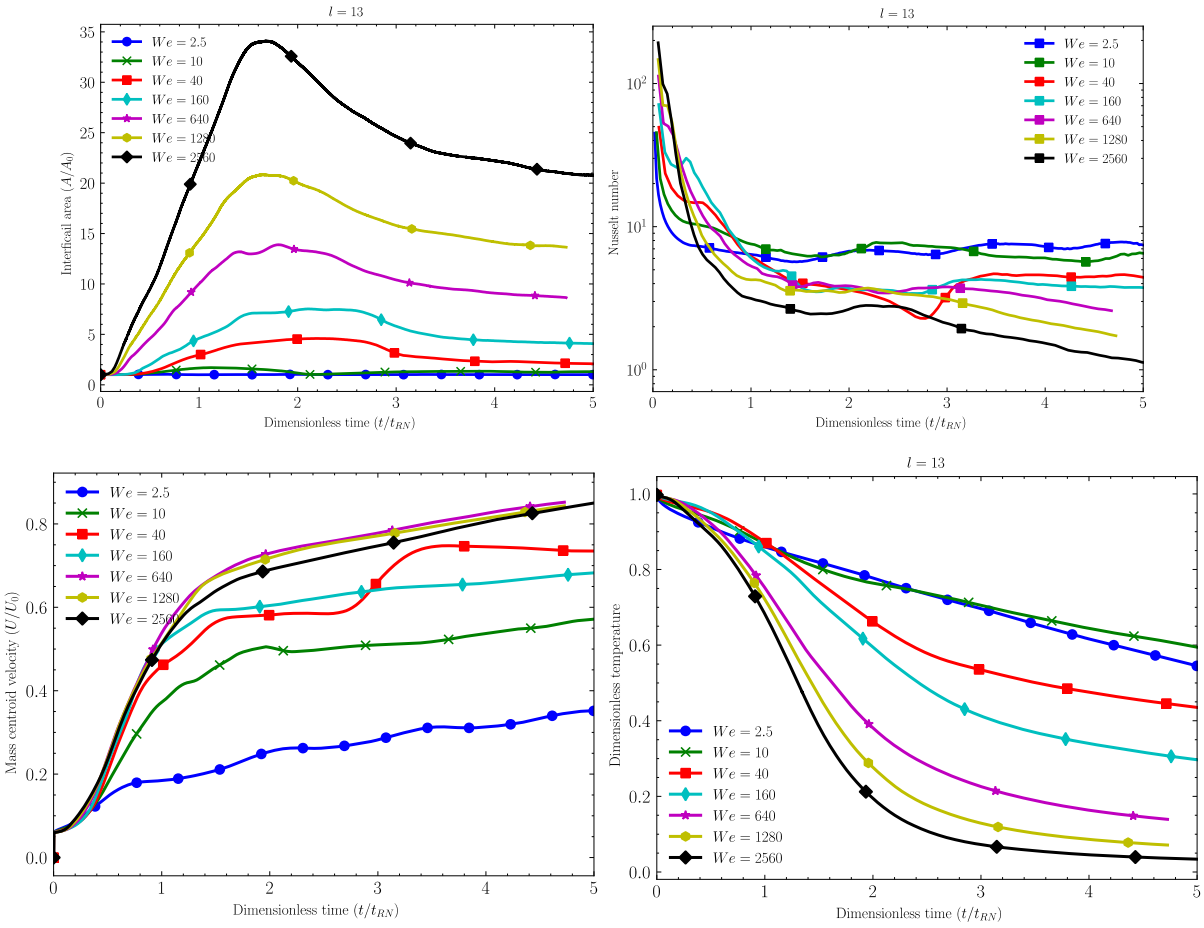

Figure 135: Interfacial area, Nusselt number, mass centroid velocity and temperature for all investigated cases

Figure 136 gives the volume of water whose temperature is higher than 1% of initial temperature difference between drop and water. Considering the large temperature difference between the hot corium drop and the coolant in the real situation, the final thermal equilibrium temperature of mixture should be quite low, thus, heating the coolant by 3% of the initial drop overheat could be representative of the final equilibrium temperature. This volume can give a first estimate of volume of the "entrained" water. The simulation shows this volume could grow up to about 15 times the initial drop volume for high Weber cases. This volume depends on Weber number, and a high Weber number leads to a larger amount of entrained water.

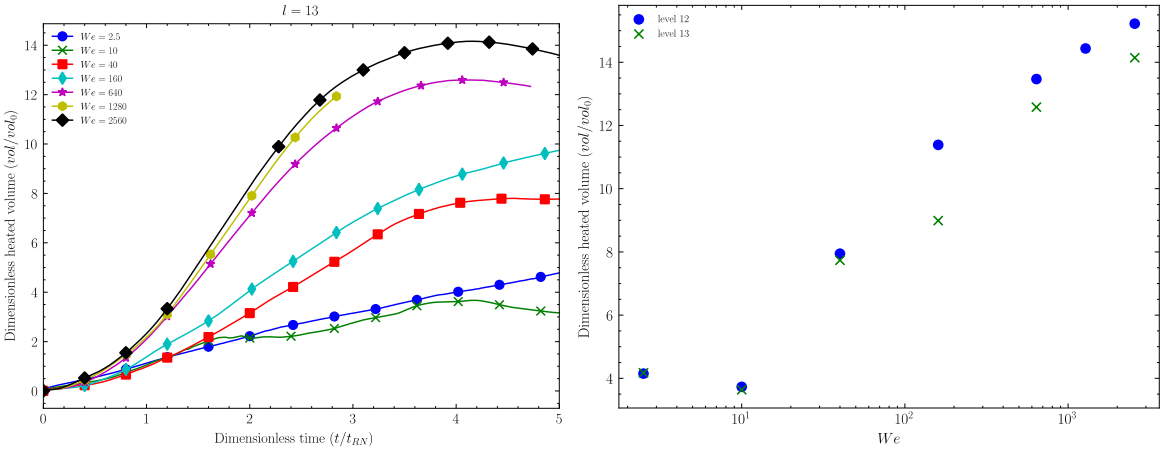

Figure 136: Volume of water whose temperature is higher than 3% of initial temperature difference between drop and water. The volume is dimensionless by the initial volume of drop. Left: volume as a function of time; Right: the heated volume at t=4.25 for different Weber cases*

5. Proposal for improvements of MC3D-EXPLO modeling

5.1. Synthesis of findings and needs

The analyses in previous chapters have led to complementary findings and needs for improvements.

From its first release, by 1995, the MC3D modeling has received numerous improvements but the overall basic image of the phenomenon was that of fragmentation leading to a fast dispersion of the fragments in the bulk liquid, as it would be if the fragmentation occurred in gas. From the work described in the previous chapter, it is estimated that this view should be revised and that, for a given time, the fragments would be trapped in the wake of the fragmenting drops, together with a given amount of water. This is the situation that was sketched by Theofanous, with the so-called Micro-Interaction concept. In contrast, it is also rather clear that Micro-Interaction models, where the three phases are in thermodynamical equilibrium, cannot hold. We are then led to consider a more general “Non Equibrium Micro Interaction” (NEMI) model, depicted in Figure 137.

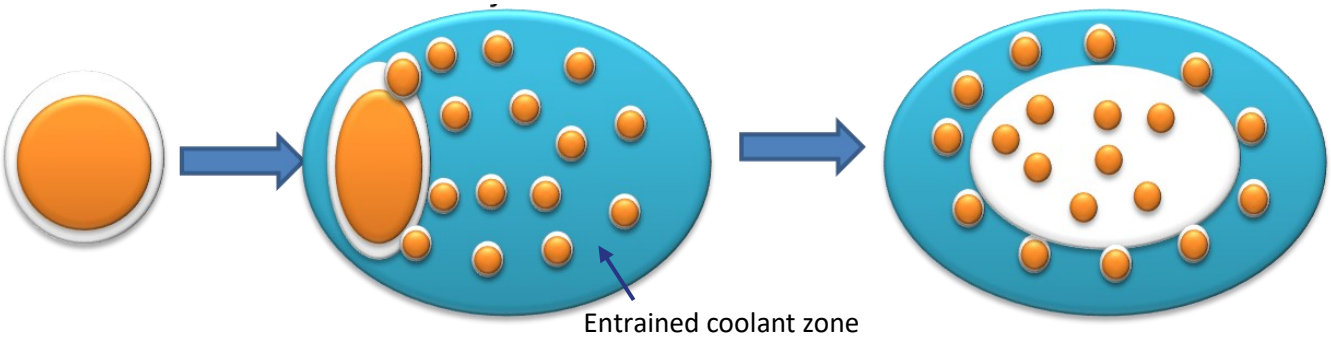

Figure 137: Non-Equilibrium Micro-Interaction concept

The NEMI concept is expected to bring serious modifications of the fragmentation behavior due, at least, to the difference in drag caused by the entrainment of water and fragments in the wake of the drops. However, if the simulations with Basilisk could bring us a quite precise picture of the fragmentation aspects (dynamics, location, size), the vapor production mechanisms remain very vague, in the absence of data. The sensitivity calculations in chapter 3 led to the following conclusions:

- The void initially present has a considerable importance on the propagation of the shock wave and should strongly mitigate the explosion due to its damping effect on the shock propagation.
- The void creation process, including interaction with the ambient (or entrained) coolant has an overwhelming impact.

Thus, the model should consider the void management as a first priority. In the absence of a data that would help us to describe a precise model, **we are led to recommend a separation in the treatment of the pre-existing void and that of the void created during the interaction**. The additional field would have a similar role as the “m-fluid” of the standard micro-interaction, except it would contain only the vapor (and H_2 in case of oxidation). It would allow to build more easily a model for the interfacial areas. This idea cannot be tested in the frame of this thesis and, in fact, may be achievable easily only in the future version 4 of the code, currently under developments. We could not sketch a simplified model different from the one already existing, which has shown its limits since we recommend imposing a large minimum bubble size (of the order of the interaction zone, similarly to the “m-fluid”) to avoid an unrealistic damping of the explosion strength.

The MC3D sensitivity analysis has also highlighted the need for a better precision concerning the fragmentation, since the kinetics of drop fragmentation has a determining effect on the kinetics of amplification and on the intensity of the explosion. In contrast with the previous points, the DNS analysis is expected to bring crucial information in order to, first, parametrize the model, and second, improve it if possible.

The sensitivity analysis has also indicated a possible deficiency of the current modeling related to the cooling of the fragments. Regardless the choice of the heat transfer correlations, the single numerical field for the fragments imposes an important uncertainty and a limit in the cooling speed. Let us remind this point: if the

cooling rate is reasonably caught in the current version, then it is likely to have a characteristic time of the same order as that of the fragmentation. This means that hot fragments, producing strong heat transfers and boiling, are generated meanwhile some are already cooled. On average, the temperature of the fragments may become low and even lower that the film boiling limit, which led to an artifact in the results. To avoid this difficulty, a lower limit in the fragment size must be set between 75 and 100 µm, depending on the conditions. This is also the order of magnitude of the smallest mean fragment size in the KROTOS experiments. It is expected that this effect is due to solidification. However, this point must be improved numerically. Ideally, we must **increase the number of fragment fields**. For this purpose, we have the MUDROPS model in which as many drop/fragments fields can be used if necessary, from a computational cost point of view. Additionally, one may reserve a field for the cold, "inactive" fragments.

5.2. Objectives of the present developments

We must highlight that we cannot in the frame of the current work propose and develop a very complex model in the MC3D code[11]. The method that we will use is developed in the next paragraph, but, due to strong complexity of the code and the numerous model interactions, we do not aim here at providing a turnkey model but rather testing ideas/proposals.

Figure 138 provides a sketch of the basic principles used in MC3D to evaluate the heat transfers during the transient phase of fragmentation. At any time, the melt is described by at least 2 numerical fields, at least one for the "drops", at least one for the "fragments", created from the fragmentation of the drops. Both types are expected to be spheres, where corrections for deformable drops may be brought to the drag coefficient or to the heat transfer. This is already done for the frictions, via the use of specific correlations for liquid drops in the "distorted" regime. The current proposals do not aim to propose new heat transfer correlations but to make reasonable improvements related to the deformation while keeping the same heat transfer modeling (see Figure 138). In other words, we are seeking for a relation of the form:

$$\Phi_d = g(We)\ \Phi_{d,0}$$

where $\Phi_{d,0}$ is the heat transfer used for non-deformable spheres, and $g(We)$ is a geometrical factor, likely function of the Weber number ($\Phi_{d,0}$ takes into account the variation due to the Reynolds number). This will be rediscussed.

The reality, as seen from the experiments or from the DNS, is clearly much more intricate since the real path for fragmentation is generally the development of 2D waves, which will be destabilized to form ligaments, which will then break up to form more or less rounded particles. **The first, crucial, point of verification is that the MC3D scheme can be used efficiently to describe the heat transfer from the melt to the coolant**.

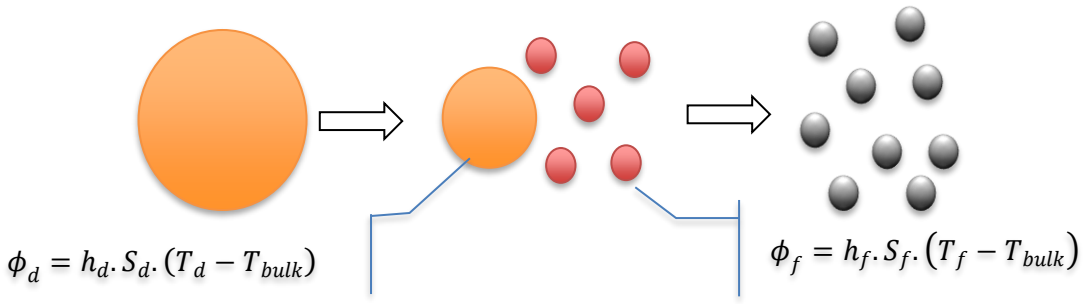

Figure 138: Scheme of the modeling for the fragmentation of liquid drops and heat transfer

The propositions made below are based on a preservation of this simple scheme and re-using as much as possible of what is already existing in the code.

[11] Unless for simple modifications, the development of the code is a complex activity that needs a strong expertise and knowledge of all parts of the codes. The development of a totally new explosion model cannot be handled in the frame of thesis.

Also, **we will limit the modifications to those that can be verified from the DNS analyses**. This means that we won't touch the boiling model (unless some few fixes of bugs found in the current version from the sensitivity analysis). However, as **we do not aim at modifying the heat transfer correlations to specifically fit the DNS results, it is believed that the modifications should also be applicable for the problem of film boiling and steam explosion**.

The next paragraph proposes a method for tuning the developments that should also be used for further tests and improvements.

The EXPLO model already has an impressive number of parameters. Indeed, none of the existing constitutive laws is considering the very transient situation of interest, starting from the drop/fragments that, for the most part, are far from being undeformable spheres. Then every law may be accompagnied by a "fitting" parameter. In fact, it is not reasonable to multiply the number of parameters, so a strategy must choose carefully the parameters to be fitted (those that are expected to have the largest range of representativity) and the set of results to be compared.

As for the parameters:

- The fragmentation model is based on two parameters (the fragmentation rate and the characteristic Weber number). Any improvment of the model should lead to only "second order" parameters, which may be set separately.
- The NEMI model assumes a mechanical equilibrium within a localized mixture of melt, a certain amount of water and void. Thus the drag model must be adapted and will lead to an additionnal parameter (that may, in tern, strongly act on fragmentation):
    - The amount of the entrained water.

Concerning the results chosen for comparison:

- Fragmentation will be mainly compared to the Sauter Mean Diameter and the fragmentation time, although this last data is very uncertain and will be used with lower priority.

- The NEMI model modifies the flow dynamics so we will compare the evolutions of the melt velocities. To do this, we will solely compare the mean velocity at 2 instants. The results from the simulation (cf., Figure 139) tend to indicate that the velocity evolves quite similarly for the fragmenting case with a first strong increase up to about 1.5 Ranger & Nicholls times, and then a slow increase. One will then **compare the melt velocity at 1 and 3 T_{RN}.**

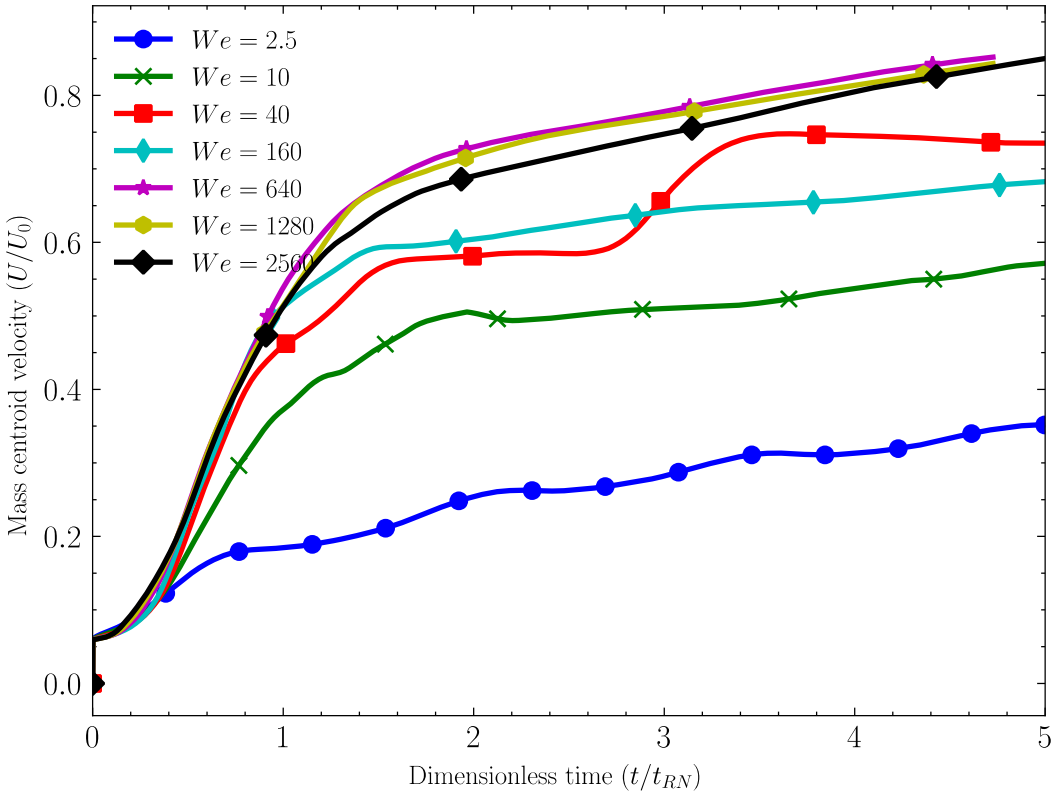

Figure 139: Mass centroid velocity for level 13 for investigated cases

The Figure 140 gives these results from the DNS simulations. One will notice an increase of the relative velocity (i.e., entrainment) up to a moderate Weber number of about 50. For larger Weber numbers, the relative velocities are almost constant, or increase only slightly.

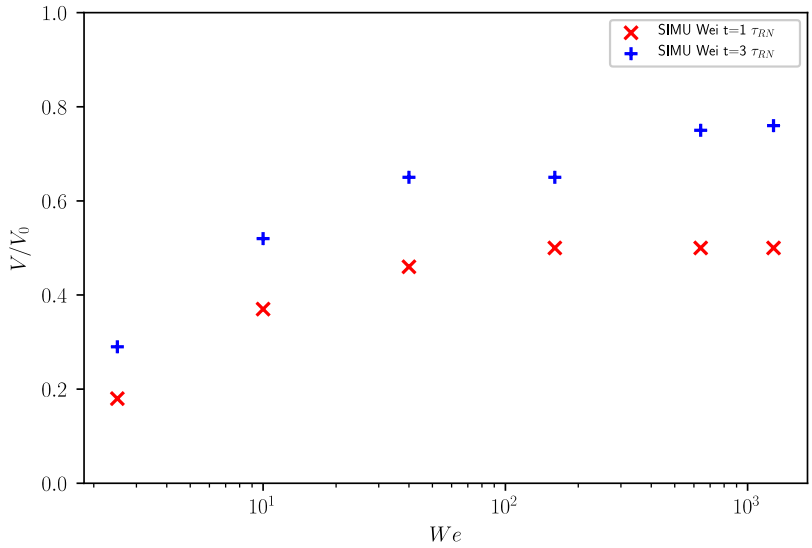

Figure 140: Relative mean melt velocity from the DNS after 1 and 3 T_{RN}. V_0 is the imposed coolant velocity.

- The most important result from the DNS is, for the first time, the characteristics of the heat transfer. In a similar way than for the velocity**, we will compare the cooling level of the melt for 2 given instants, namely 2 and 4 T_{RN}.** Figure 141 shows the results from the DNS for the cooling grade (after 1,2,3 and 4 T_{RN}):
  - $T^* = \frac{T_{mean} - T_{w,0}}{T_{m,0} - T_{w,0}}$

$T_{w,0}$ is the initial water temperature, $T_{m,0}$ the initial melt temperature. It is noticed that the cooling grade is almost constant for low Weber number cases, but it increases almost linearly with the log of the Weber number for the fragmenting cases, except at the beginning of the process ($t = 1\ \tau_{RN}$). As the SMD has the inverse trends at large We numbers (Figure 40), we may conclude that the heat transfer remains primarily linked to created interfacial area.

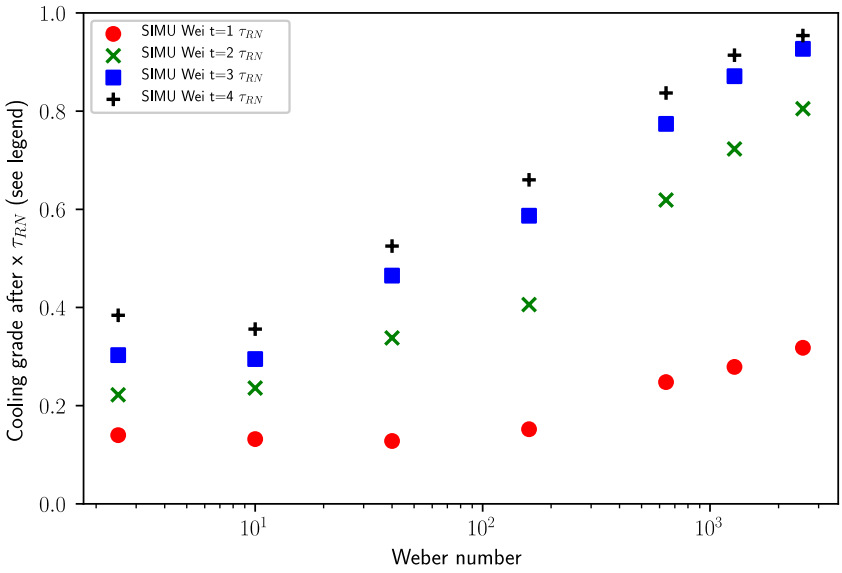

Figure 141: Cooling grade from the DNS after 1,2,3 and 4 T_{RN}

Obviously, it might be difficult to fit all the data for the same set of parameters. Then we must prioritize the points of comparison. Obviously, steam explosion is a matter of transfer of heat from the melt to the coolant, so the cooling of the melt comes as the first priority.

However, in the frame of the present work, we only set qualitatively the parameter since further work is necessary for the integration in the next version.

5.3. Data set for comparison and results of the current version (3.10)

The dataset is the same as the one used for the validation of the MC3D code, to obtain the results in Figure 40. It is a simple one-dimensional geometry with a small amount of “hot” melt with the same properties as those used for the DNS. The tube is sufficiently long to obtain a complete fragmentation before the melt is expelled out of the domain. The difference with the standard dataset is that the melt is set at a temperature of 350 K, whereas the water is set at 300 K therefore avoiding boiling conditions. Also, the Prandtl number of the water is imposed to be 1, as in the simulations. This Prandtl number is in fact only used in the heat transfer correlations.

The results from the calculations with the standard version (plus some few fixes) are illustrated in Figure 142 (the fragmentation data are already reported in Figure 40). It is seen that the general trends are not correct, although the cooling grade after 3 T_{RN}, i.e., once fragmentation is almost finished, is in a correct range.

It will also be noticed that, despite a quite correct acceleration, the case We=2.5, with a small deformation, does not fit properly the cooling grade. This may come from the heat transfer correlation used in MC3D which is not Whitaker one (Table 6) but also from the oscillations which tend to increase the heat transfer by 28 %.

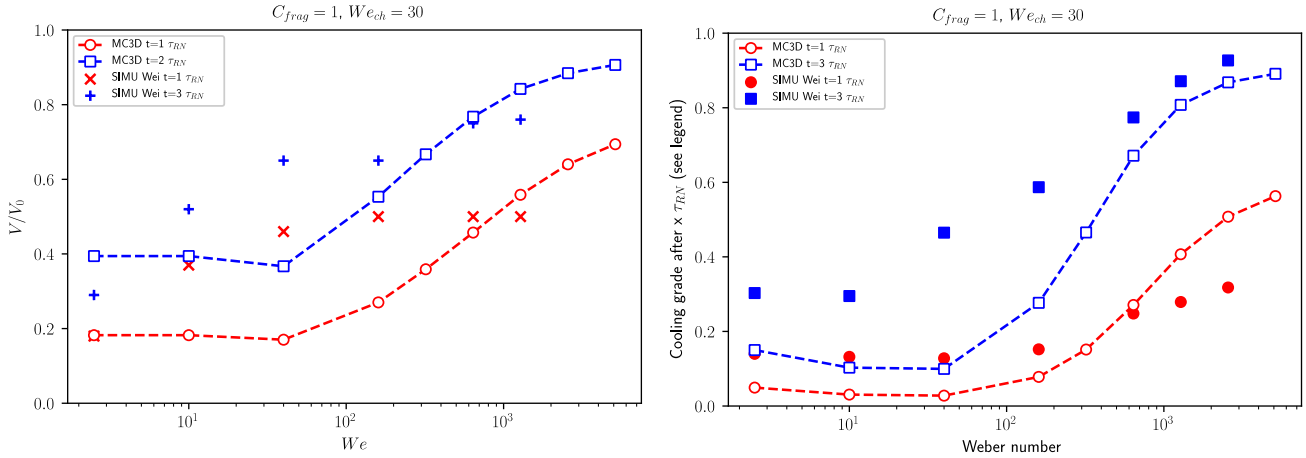

Figure 142: Comparison of the mean relative melt velocity and cooling grade between the DNS and MC3D version 3.10.2

5.4. Developments

5.4.1. Fragmentation

5.4.1.1. Improvement at low Weber numbers.

Although explosion involves very high Weber numbers, the model also aims to model the ability of a given premixing to develop a strong explosion. This means that the model must also be correct for low and moderate Weber cases.

It is reminded that diameter of the created particles (Sauter, then used in an area transport equation) is obtained from a Weber criterion (see section 2.4.4.2 for details):

$$D_f = We_{ch} \frac{\sigma}{\rho_{fluid} \Delta V_{dc}^2}$$

It is also reminded that the general phenomenology seems similar whatever the Weber number, in contrast with the LG situation. It is therefore not necessary to have a specific model, but only to adjust the parameters. There are several ways to correlate but the following form seems satisfactory:

$$We_{Ch} = \begin{cases} We_{ch,\infty} \; if \; We > 59 \\ quadratic \; interpolation \; if \; 9 \leq We \leq 59 \\ We_{ch,0} \quad if \; We < 9 \end{cases}$$

Where $We_{ch,\infty}$ and $We_{ch,0}$ are user-defined parameters. In our simulation, $We_{ch,\infty} = 30$ and $We_{ch,0} = 9$.

The results are given in Figure 143, to be compared with Figure 40.

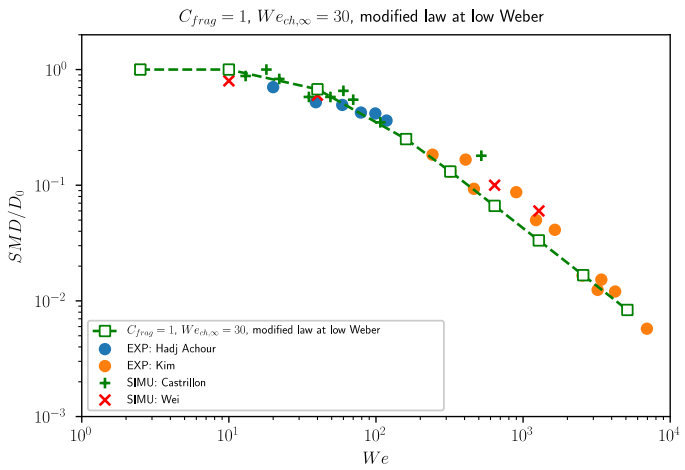

Figure 143: Results of the modification at low We numbers on the calculated SMD

5.4.1.2. Drag coefficients

The detailed inspection of the MC3D models has revealed a probable weakness concerning the drag. Beyond the viscous regime, the drag coefficient is taken by minimizing the coefficient in the so-called "distorted regime" of a falling bubble (Cd_{dist}) and a maximum value taken at 8/3 (Cd_{cap}).

$$Cd_{dist} = \frac{2}{3} D_d \sqrt{g \frac{\rho_d - \rho_l}{\sigma}}$$

$$Cd = min\left(Cd_{dist}, Cd_{cap}\right)$$

However, the distorted regime is not applicable in the context of explosion since it is supposed to represent the situation of a drop falling under the effect of gravity. It is only a function of the diameter, not of the velocity or of the real acceleration. It is remarked that the coefficient is in fact related to the gravitational Bond number as:

$$Cd_{dist} = \frac{2}{3}\sqrt{Bo} = \frac{2}{3}\sqrt{\frac{\rho_d - \rho_l}{\sigma} g D_d^2}$$

and thus, it is possible to translate the coefficient for a given acceleration a. The use of an acceleration is not convenient (on the numerical point of view), but it is possible to change Bond numbers to Weber numbers by noting that a reasonable estimation of acceleration for the melt

$$a \approx \frac{V^2}{D_d}$$

and thus:

$$Cd_{dist} = \frac{2}{3}\sqrt{\frac{\rho_d - \rho_l}{\sigma} a D_d^2} = \frac{2}{3}\sqrt{\frac{\rho_d - \rho_l}{\sigma}\frac{V^2}{D_d} D_d^2} = \frac{2}{3}\sqrt{\frac{\rho_d - \rho_l}{\rho_l} We}$$

Therefore, the distorted regime may be alternatively written as a function of the square root of the Weber number:

$$Cd_{dist} \sim \sqrt{\frac{\rho_d - \rho_l}{\rho_l} We}.$$

The precise adjustment is quite time-consuming and could not be done in the present frame.

The drag coefficient plotted in Figure 125 are seen to increase, at least in a transient way, up to nearly 8, which is much larger than the limit 8/3 usually taken for stable (non fragmentating) drops. Since the coefficients evaluated from the DNS are quite changing with time, a constant lower maximum value might be tested. In order

to determine the multiplicative coefficient for Cd_{dist} we tentatively fitted the case We=10 which should be at the limit of fragmentation with the friction coefficient equal to 8/3 approximately. Finally, we have

$$\boldsymbol{Cd = \min(Cd_{dist}, Cd_{max})}$$

$$\boldsymbol{Cd_{dist} = \frac{1}{3}\sqrt{\frac{\rho_d - \rho_l}{\rho_l} We}}$$

$$\boldsymbol{Cd_{max} = Cte = \frac{8}{3} \rightarrow 6}$$

This results in an important increase of the drag of the drops (fragments are not affected here, but they should also receive some attention). Then the differential velocity between the drops and the water is smaller, and so the diameters of the created fragments are larger. As a consequence, the fragmentation parameter setting must be adjusted. An example is given in Figure 144 where the impact for the low Weber number cases (with large proportion of drops compared to fragments) is important.

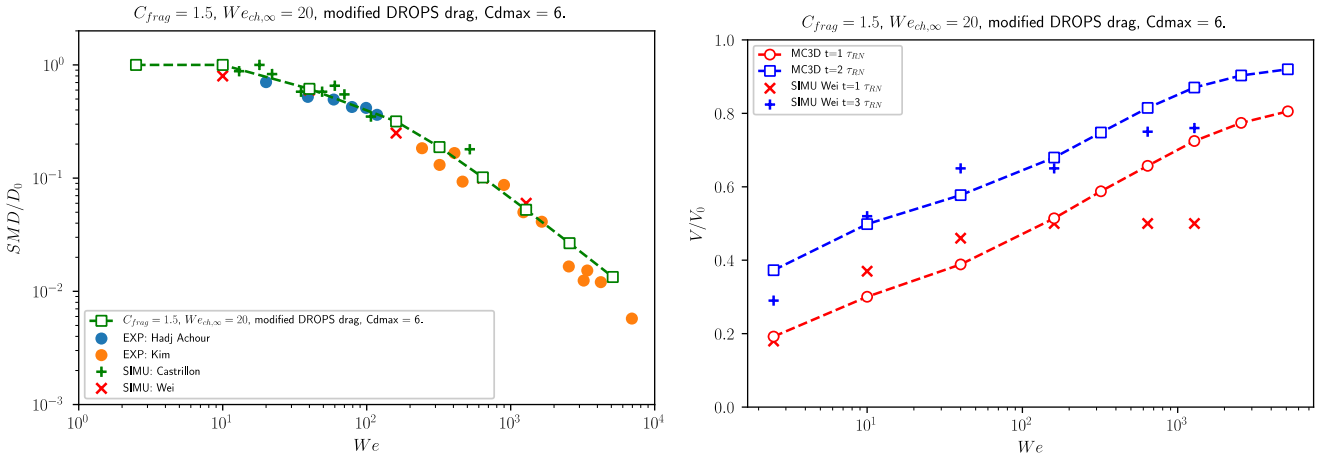

Figure 144: Example of results of the modification of the drag and a change of fragmentation parameters (figure title). The maximum drag coefficient value is 6.

Compared to the standard version (Figure 142), the behavior at We = 10 and 40 is improved, at the cost of a degradation for We=2.5. This may mean that a behavior as the square root.

Note: following the remark of N. Seiler (one of the reviewers of this thesis), there is another alternative way to link the Bond and the Weber numbers and estimate the drag coefficient: considering the drop is under steady state, we have $(\rho_d - \rho_l)\frac{\pi D^3}{6} g = \frac{C_D \rho_L \pi D^2 (U_d - U_l)^2}{8}$. The above equation can be transformed as $\frac{(\rho_d - \rho_l) D^2 g}{\sigma} = \frac{3}{4} C_D \frac{\rho_L (U_d - U_l)^2 D}{\sigma}$, which is equivalent to $Bo = \frac{3}{4} Cd\ We$.

Using the equation $Cd_{dist} = \frac{2}{3}\sqrt{Bo}$ yields to

$$Cd_{dist} = \frac{2}{3}\sqrt{Bo} = \frac{2}{3}\sqrt{\frac{3}{4} Cd_{dist}\ We}$$

and then

$$Cd_{dist} = \frac{1}{3}\ We$$

This method could also be tested in the further work to propose a better correlation for drag coefficient.

5.4.2. The NEMI description

5.4.2.1. Fragmentation, partition of the fragments in the MUDROPS description

A micro-interaction process can be designed using the MUDROPS description of the MC3D code. Recall that MUDROPS is a MUSIG (MUlti SIze Group) type model where the corium drops are separated into several fields, each corresponding to a given diameter. Within each class, the drops have all the same diameter. In an ideal steam explosion simulation, an EXPLO calculation is expected to start from a PREMIX state, with a given volume distribution of the drops. The use of MUDROPS differs in the PREMIX and in the EXPLO application. The fragmentation process using the MUDROPS description in PREMIX is explained in Figure 145**.** The fragmentation process in the EXPLO application is different because the result of the fragmentation always goes into a single field called FRAGMENTS, without predefined size (Figure 146). The size of the fragments in the F-field (i.e., the fragment field) therefore evolves over time, thanks to a transport surface equation. On the physics point of view, the fragmentation models of PREMIX and EXPLO are very similar.

In the current EXPLO application, the MUDROPS fields are all associated with the same velocity field and thus have same speed (homogeneous model). But the FRAGMENT field has its own velocity field.

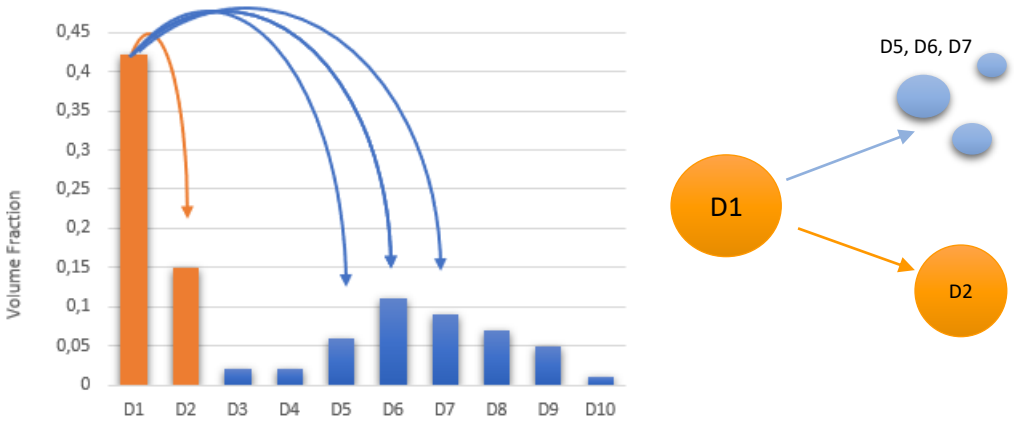

Figure 145: Illustration of the fragmentation process using the MUDROPS discretisation in PREMIX application. Each D corresponds to a class with a fixed drop size. The fragmentation process of parent drop D1 will produce small drops (D5, D6, D7) according to the Weber criteria presented in chapter 2.4.4.2. At the same time, the reduction in drop volume in class D1 due to fragmentation will yield a partial transfer of mass from D1 to D2 (closest class to D1 with smaller size)*

In the NEMI/EXPLO description, the fragments resulting from the drop fragmentation can then be "arranged" in the various MUDROPS classes according to the diameter of creation as in the case of PREMIX application (Figure 145**)**. This means that it will be probably necessary to add supplementary MUDROPS fields for small drops/fragments.

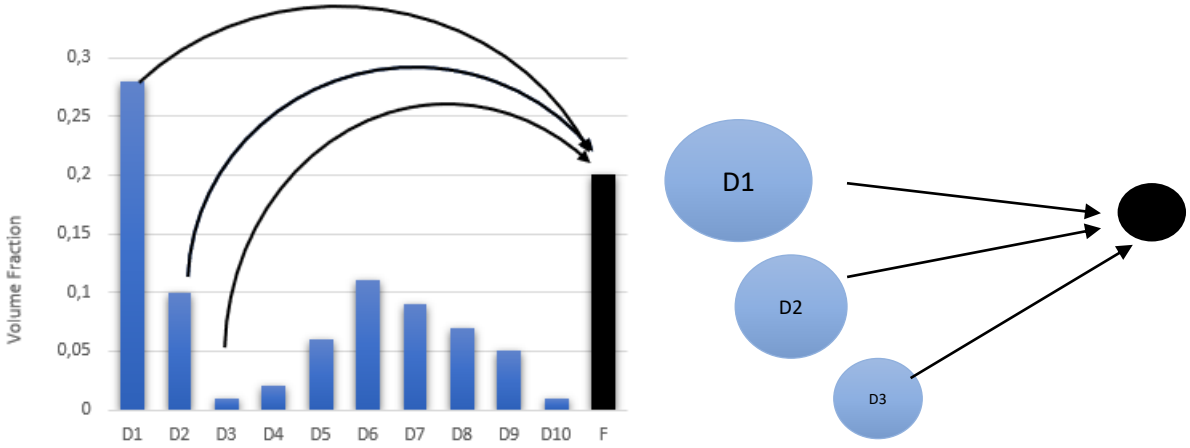

Figure 146: Illustration of the fragmentation process using the MUDROPS discretisation in standard EXPLO application. The fragmentation of drops in class D will produce fragments placed all in the same class F. Only DROPS are allowed to fragment (the fragment in class F cannot fragment further)*

The homogeneous description in momentum is preserved, thus, **drops and fragments will have the same speed, which ensures an automatic coupling (micro-interaction principle)**. Another advantage is that the difficulty related to the mean temperature pointed out in the previous chapter (reminded in 5.1) should have a reduced impact as the fragments are distributed in several specific fields. Nevertheless**, it is recommended, to keep the fragment field as a "bin" where the "cold" fragments could be placed (Figure 147). This "ultimate" procedure has not been implemented in the present code patch**.

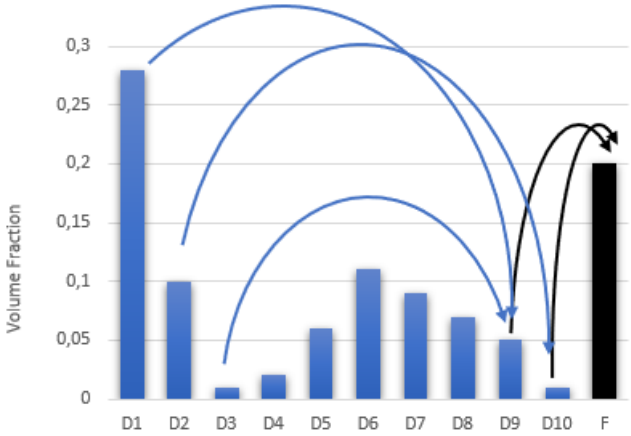

Figure 147: Proposed final scheme for the management of the melt fields in NEMI. The fragmentation process occurs within the DROPS fields (blue arrows). A supplementary transfer process is done as a function of the temperature in the DROPS field.

Note: We have to be careful with our terminology since the term "fragment" have two meanings:

- result of the physical process of fragmentation of the "drops";
- name of the numerical field (FRAGMENTS) which receives these particles.

Similarly, the term "drop" is vague, but it will most of the time refer to the particles in the DROPS field of the code. In the proposed model, the "fragments", as a result of the physical process of fragmentation, are placed, under certain conditions, in the DROPS fields. In the following, the terms fragments and drops will be understood according to the context:

- on the "physical" level, the fragments are remains from fragmentation, whether they are in a DROPS field or in the FRAGMENTS field;

- on the computational level, the "drops" are relative to the corium in the DROPS fields.

Note: The micro-interaction process is physically only compatible with fragmentation in the liquid. The fragmentation in the gas is preserved with the standard model, meaning the fragmentation will produce FRAGMENTS. However, we note that this separation is approximate once the fragments are created since the positioning of the drops and fragments in the liquid or gas remains associated with the flow map (Figure 44).

In the present verification computations of the simplified fragmentation test case, 6 classes are used with a regular size discretization following a log-scale between 4 mm and 10 µm, that is, in millimetres:

Class = [4.0000 ,1.2068, 0.3641, 0.1099, 0.0331,0.0100]

5.4.2.2. Entrainment of water

The NEMI flow configuration depicted in Figure 137 makes the hypothesis, at least of a certain time, of the formation of a local mixture of melt, a certain amount of water and vapor, homogenous on the dynamic point of view. A possibility would have been to add a specific new water field and place it in the DROPS mixture. This would imply quite complex modifications and a quite important increase of computational time (the computation of the water properties is quite time-consuming using NBS tables). This approach may however be considered with attention for version 4.

Alternatively, **the entrainment of water can be treated as an "added mass"**, a concept already implemented in the code, which must be modified. It is reminded that the "added mass" is a virtual amount of the ambient fluid that must also be accelerated when the drop is accelerated. Intuitively, since the entrained fluid behind the fragmenting drop must follow the drop, we can consider that this volume behaves as an added mass. An alternative option, much more complicated, would have been to effectively place a certain amount of water in the same velocity field as the one of the considered drops. This would yield a considerable complexity of the code since we would need:

- one new numerical water field (mass + energy);
- a specific physics associated to these water fields, in particular thermal interactions, and boiling.

Such complexity is not desirable in the first steps of modelling since the impact seems quite moderate on the dynamical point of view, and since, from the thermal point of view, we still consider the non-equilibrium hypothesis. Nevertheless, such development may be considered on the future V4 of MC3D for an improved precision on the thermal point of view.

Using the option of "added mass", the volume of the added water is associated to the entrained volume, and it is hypothesised that it is a function of the fragmentation grade as:

$$V_{added} = 0.5\, V_{drop} + C_{ma}\, V_{fragments}$$

C_{ma} is in fact similar to the "entrainment factor" f_e of the MI models. DNS suggests values in the range 10-20. In the classical MI model, f_e is generally in the range 7-12 in the MI models.

To do so, we obviously need to make a distinction between (old) drops and (new) fragments, that are all placed in DROPS fields. **A user-defined diameter (*DFC_NEMI*) criterion is proposed** for this:

- **If $D_d < DFC\_NEMI$ => fragments**
- **Else If $D_d > DFC\_NEMI$ => drops**

Here, DFC_NEMI is set to 1 mm. In the context of steam explosion in NPPs, we can estimate that corium drops smaller than 1 mm should be solidified. In the present testing, this means that the first 2 classes are considered as drops, whereas originally all the drops are placed in the first class. This situation may however be quite representative of the reactor case. Clearly, this point needs further attention.

The modification of the added mass model requires quite complex modifications in the code, and they should be verified.

5.4.2.3. Drag

The way the drag is computed must also be adjusted. Currently, every DROPS field adds its contribution to the interfacial area:

$$A_D = \sum_{d=1}^{d=ND} A_d = \sum_{d=1}^{d=ND} \frac{6\,\alpha_d}{D_d}$$

Where d refers to each individual DROPS field and D refers of ensemble of the DROPS fields, which shares all the same velocity. In the context of MC3D, D is called a "dynamic mixture". Then, the fragments will considerably add interfacial areas and thus frictions. However, the goal of the model is to consider the local mixture as an object with its own characteristics, in particular diameter D_m and area A_m.

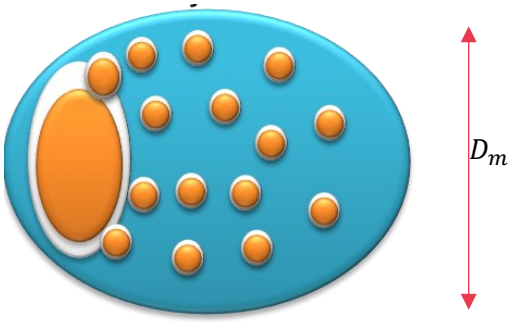

It should be better to compute it from the entrained volume of fragments and water.

However, we only tested using a specific user defined diameter, equal to the initial drop size.

The adjustments here are linked to those in the drag model (§5.4.1.2).

5.4.2.4. Heat transfer

As in the present DNS and the MC3D tests, the heating does not change the physical properties in a substantial way, heat transfers can be considered in a separate way from momentum transfers. Since the specific conditions in the DNS are not, by far, representative of the real corium case, changing specifically the heat transfer coefficient correlation is uncertain. However, in both cases, the change of the water temperature should be minor. Thus, it is expected that a global multiplicative coefficient would be representative of the changes related to velocity differences due to the changes in the drag and flow configuration. Thus, a multiplicative "configuration" coefficient C_{conf} should be applied to both situations (heat and momentum transfers).

As first approach, it is estimated that this coefficient may be related to the drag coefficient, which may be considered in fact being as a substitute to a change of the effective diameter. Considering that the drag should be 0.45 for a representative ball, the condition for which the correlations are established, the correction tested is the following:

$$C_{conf} = Cd/0.45$$

The same calculation as above provides the results in

As already pointed out, we could not make in time a precise sensitivity analysis to provide the best parameter setting (furthermore, we could not test a proposal in §5.4.3), so we only provide in Figure 148 an example of calculation with parameters providing a reasonable agreement:

$$C_f = 1.5, \qquad We_{ch,\infty} = 20, \quad Cd_{max} = 6., \quad C_{ma} = 10$$

Note that is difficult to fit the cooling grade at 1 T_{RN}, the MC3D calculation giving a too important cooling compared to the DNS. This is likely due in part to an imprecise dynamic of fragmentation. This is addressed in §5.4.3.

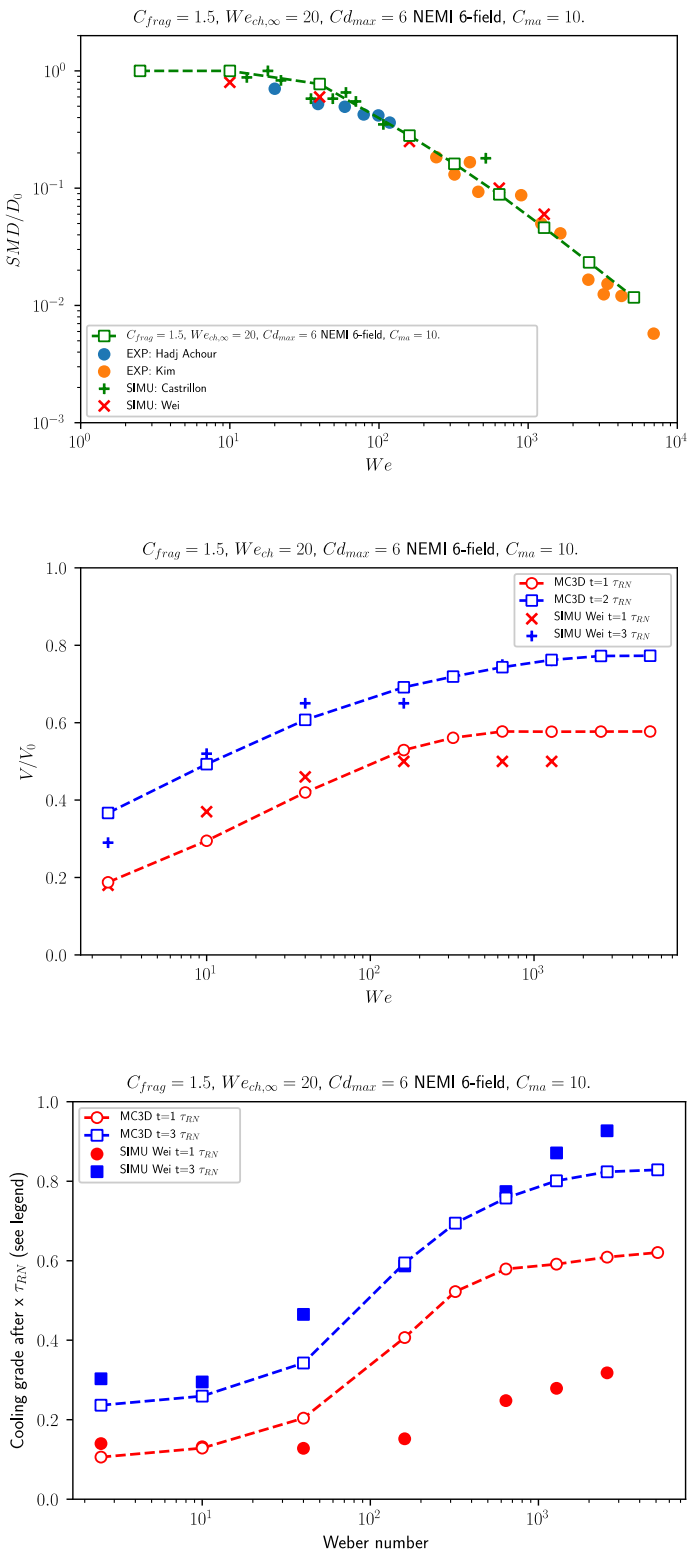

Figure 148: Example of calculation with NEMI (6 classes) representation and adjusted parameters. From top to bottom: SMD, relative melt velocity, cooling grade.

In addition, Figure 149 gives the mass partition (not to be confused with the pdf) of the melt in the 6 DROPS classes. Due to the entrainment of the melt during the fragmentation, the width of the spectrum is rather large, even for the largest We number. It is not possible to directly compare this result with the PDF of the simulations but there is a qualitative agreement with the previous DNS results.

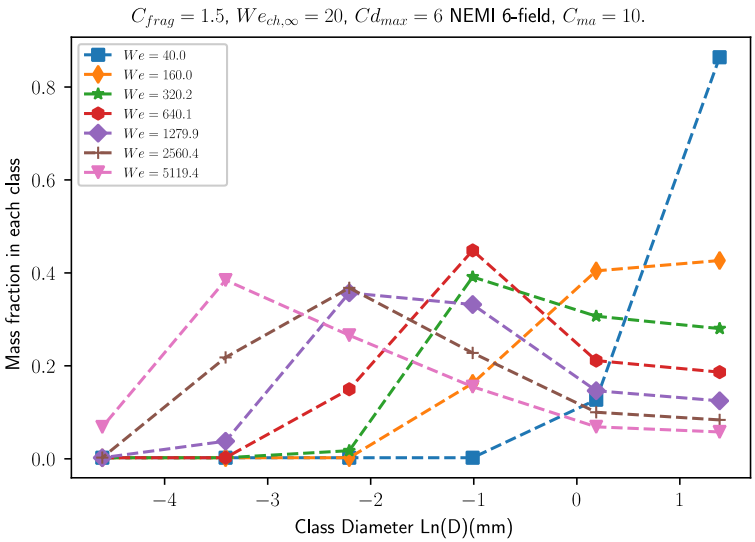

Figure 149: Mass partition of the drops/fragments in the 6 DROPS classes. Same calculation as Figure 148.

5.4.3. Other proposed modifications

5.4.3.1. Fragmentation dynamics

This modification could not be tested in time, we nevertheless provide it here as it should be tested easily by the MC3D code developers.

Due to the Eulerian modeling limitation, the fragmentation occurs in the same time scale as the explosion itself but is only roughly approximated as:

$$\Gamma_f = -\frac{d\alpha_d}{dt} \approx \frac{\alpha_d}{t_f} \approx \frac{\alpha_d}{t_f^* \tau_{RN}} = C_f \frac{\alpha_d}{\tau_{RN}}$$

$$\tau_{RN} = \frac{D_d}{\Delta V_{dc}} \cdot \sqrt{\frac{\rho_d}{\rho_c}}$$

τ_{RN} is varying with the local conditions while t_f^* is a constant of the order of unity. The problem with this formulation is that it does not fit properly the effective fragmentation kinetic, given in terms of area. In reality, the fragmentation is not instantaneous but needs some deformation of the drops to start, which takes about 1 τ_{RN}. We may then to introduce a delay. This can be done with a second order formulation such as:

$$\Gamma_f + t^{**}\tau_{RN} \frac{d\Gamma_f}{dt} = \frac{\alpha_d}{t_f^* \tau_{RN}}$$

$$\frac{d\Gamma_f}{dt} = \frac{\Gamma_f^{n+1} - \Gamma_f^n}{dt} = \frac{\alpha_d}{t_f^* t^{**} \tau_{RN}^2} - \frac{\Gamma_f^n}{t^{**}\tau_{RN}}$$

$$\Gamma_f^{n+1} = \left(\frac{\alpha_d}{t_f^* t^{**} \tau_{RN}^2} - \frac{\Gamma_f^n}{t^{**}\tau_{RN}} \right) dt + \Gamma_f^n$$

This second order equation can be easily solved. The result is shown in Figure 150 for 2 sets of parameters. Not surprisingly, the second order model leads to an oscillatory behavior, but this oscillation is not really a problem since fragmentation will simply stop when there is no more melt to fragment. It seems possible to find an adequate parameter setting to improve the behavior.

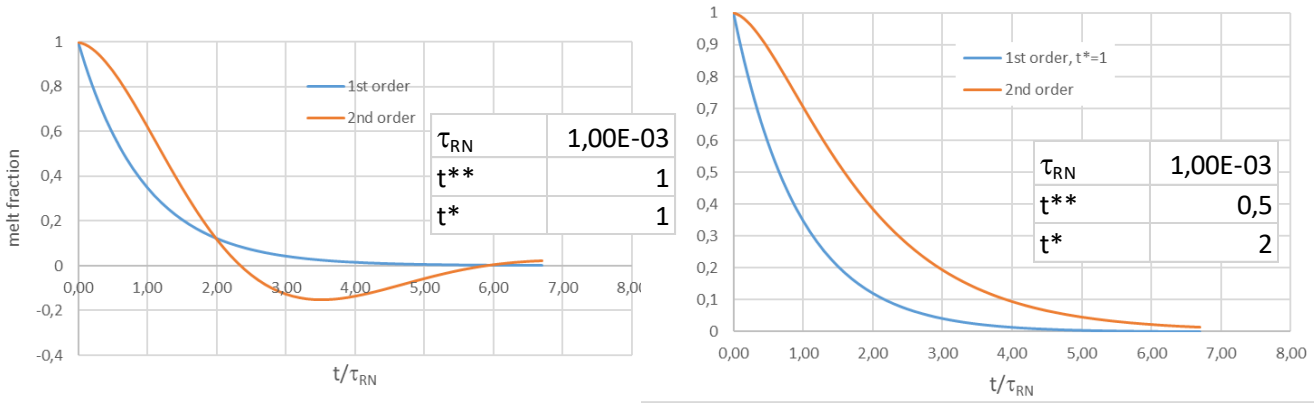

Figure 150: Examples of impact of second order formulation on the dynamic of fragmentation

The modification needs to add an array to save the fragmentation rate at the previous time step.

5.4.3.2. Relaxation of the fragments from the DROPS fields

After a given time (in the Ranger & Nicholls scale), the micro-interaction process should be less and less effective. Then the fragments should progressively leave the DROPS fields to be introduced in the FRAGMENTs fields, which is reserved at the beginning for the fragments produced in gas. It is expected then than the impact of the FRAGMENTS fields is weak (merely heating the gas).

In calculations as those analyzed here, the relaxation should not have an important effect. However, recall the discussion on chapter 3 regarding the problem of the fragment temperature in the standard modeling when the fragments are too small: they are losing their energy very fast and thus, on the mean their temperature might fall under the minimum film boiling one, with the consequence that the new-born hot fragments cannot exchange properly their heat in a boiling process.

The NEMI model as presented above has the advantage to split the fragments is several classes. However, this may not be enough. Thus, the amount of the cooled particles may be evaluated. Based maybe on a temperature criterion, the “cold” fragments can then be transferred from the DROPS field to the FRAGMENTS field.

5.4.4. Remarks

5.4.4.1. Energy associated to the fragmentation mass transfer

During their fragmentation, the drops are continuing to lose energy by direct transfer to the coolant, cf. Figure 151. Then, in a practical case, the fragmentation may be stopped due to solidification. In fact, the fragmentation modeling is such that the fragment will have exactly the drop temperature, so that the fragmentation has no impact on the drop temperatures (for the parent drop). However, in reality, as shown in Figure 133, there is a strong gradient of temperature at the interface and, at least for the high Weber cases, the fragments should then leave the drop with a temperature closer to the interface temperature than the mean one. As a consequence, the parent drop temperature should remain “liquid” much longer than it may be computed in the MC3D model.

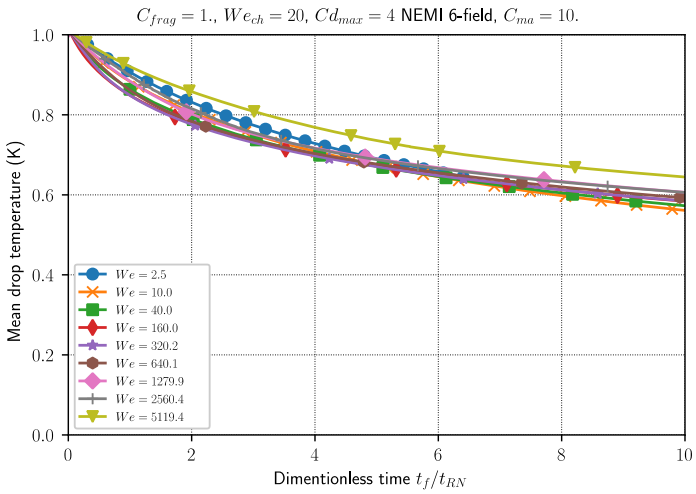

Figure 151: Example of calculation of the largest (fragmentating) drop mean temperature

5.4.4.2. Sensitivity to the number of classes

A calculation has been run with the parameters as those for Figure 148 but with 7 classes instead of 6. The min and max diameters remain the same (10 µm and 4 mm). The result for the cooling grade is given in Figure 152 and it is seen that the sensitivity is negligible.

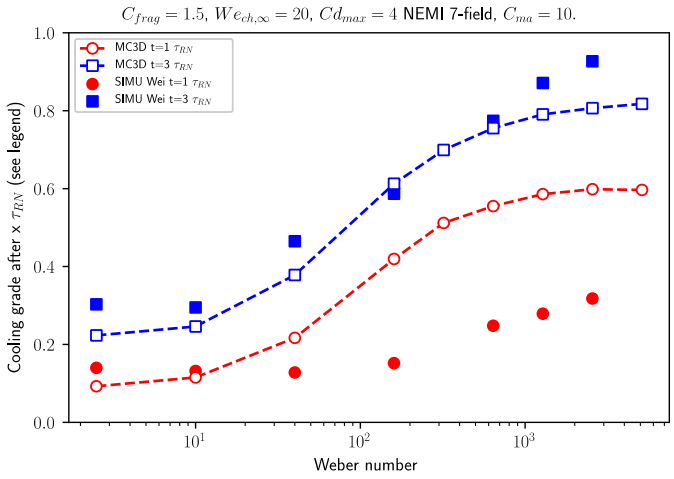

Figure 152: Cooling grade for the same calculation as the one for Figure 148, except a number of classes =7

6. Conclusion

Steam explosion is one of the most complex issues that may occur during a severe accident in a nuclear power plant. The detailed phenomena characterizing steam explosion are still not accessible by experiments and remain largely “mysterious”, due to small spatial and temporal scales of 1 mm and 1 ms, and the extreme conditions involving temperatures of several thousand degrees and pressures well above supercritical ones. The present work is a succession of simulations carried out within the framework of the RSNR-ICE project which concluded that:

- the hypotheses of film boiling heat transfer and thermal disequilibrium between phases made in the MC3D EXPLO model are reasonable;
- the fragmentation of the melt drops in the liquid coolant occurs without significant dispersion, in contrast with MC3D modeling assumptions.

It was then concluded that modifications of the MC3D-EXPLO model are necessary, although the number of modifications and their exact nature was not clarified. Such clarification is the main objective of this thesis. The major initial question was related to the role of the apparent “micro-interaction” zone, using the expression popularized by Theofanous. In order to provide such clarification, the use of a DNS model was considered, in order to study the combined effect of fragmentation and thermal exchanges, even it was clear that it would not be possible to take into account the boiling effects.

The bibliography part of the present document describes the context and phenomena involved in Steam Explosion modeling. Analysis of the experiment bibliography highlights the strong difficulties faced by the experimentalists, thus showing the numerous limitations, limited representativity compared to the reality, and the very high uncertainty in both the phenomenological representation and the results. Models are rapidly presented and discussed. Our work is done in the frame of the development of the MC3D computer code, which proposes the most detailed and mechanistic model on Fuel Coolant Interaction and Steam Explosion. It is concluded that the detailed description of drop fragmentation and the associated heat transfer are necessary and important for the explosion modeling. In this transient and rapid steam explosion process, the assumption of thermal equilibrium between the melt and coolant cannot hold. However, it seems that a part of fluid can be in mechanical equilibrium with the melt.

The impacts of the current modelling and the various parameters associated of the MC3D-EXPLO are then analyzed by a simple one-dimensional test-case, in a sensitivity study were the impact of the initial void, amount of melt was studied. Also, the impact of the bubble size and fragment size, two of the most uncertain models, are analyzed. It is found that some parameters have a significant, even crucial, influence on the behavior and reliability of the results and must be treated with care. It has led in particular to the proposal of some immediate corrections for the current code version. The most important conclusions are the following:

1. The initial void in the mixture has a considerable importance on the propagation of the shock wave due to its strong damping effect. If the corium at the front of the premixing zone is solidified, the presence of bubbles can cause a damp in pressure and prevent an explosion. This can already help to understand the behavior of some KROTOS tests.
2. The evolution and the local configuration/environment of the "bubbles" generated by the vaporization during the fine fragmentation are poorly taken into account by the current model and constitute the first axis for improvement. In some cases, this can lead to a strong condensation and a considerable underestimation of the explosion. Nevertheless, the necessary improvements seem quite complex, probably requiring the use of a dedicated additional numerical field.
3. Despite the large uncertainties due to the very small number of accurate experimental data, it seems that the fragmentation model is qualitatively correct, but may need some improvements for better accuracy, in particular the linear kinetic of the model.
4. An important result is that the assumption of a single temperature field for all fragments needs to be revised. When the fragments are small, they lose heat rapidly so that the newly generated "hot" fragments may be poorly accounted for in an averaging process: below a minimum temperature, the fragments exchange directly with water, without boiling the film.

This analysis confirms the need for further work on small-scale simulation of the fragmentation of a hot drop in another liquid to better understand the dynamic and thermal interactions during the fragmentation process. This has been done using the Basilisk solver. Calculations were run on a high-performance calculation infrastructure (TGCC, Très Grand Centre de calcul du CEA), using up to about 30 000 cores. The transient characteristics of heat transfer of a drop submitted to a velocity jump is investigated for different initial Weber numbers, the importance results of this part are:

1. Increasing the Weber number, five different regimes, so called oscillation, elongation breakup, forward-bag breakup, forward bag-ligament breakup, and sheet thinning modes are observed and identified for LL configuration. Nevertheless, beyond the elongation regime, the fundamental mechanisms of deformation and fragmentation is always the same and evolves gradually. This is contrast with the situation of drops in gas, where different mechanisms are dominant at low and high Weber numbers. In the case of drops in liquid, due to the small difference of density, the mechanisms are those of:
    - stretching and formation of a bag,
    - tangential instabilities (Kelvin-Helmholtz type) at the front with wavelengths reducing with the Weber number of the flow.
2. The resulting fragment sizes are compared with the few existing with available experimental ones and found in good agreement. At large Weber numbers, the SMD scales with the inverse of the Weber number, confirming a tangential stripping driven by Kelvin-Helmholtz type instabilities.
3. The duration of fragmentation is related to the so-called Ranger & Nicholls characteristic time. We first observe a more or less strong deformation and then fragmentation, which is contrary to the models, in particular MC3D, where fragmentation is a continuous and regular process.
4. The fragmentation of drop in liquid-liquid configuration shows a weak dispersion of the resulting fragments, in contrast with the liquid-gas situation. The fragmentation produces a melt-water mixture with a volume equals approximately to 15 times the initial drop one. This may give at first order the volume of water entrained and interacting with the melt whereas the existing micro-interaction model use typical values from 5 to 12.
5. The drag coefficient, representing globally the dynamics interaction between the melt and liquid, shows a transient behavior. In the very beginning phase of deformation, even some local instabilities are observed for high Weber number case, the mass centroid velocity (hence the drag coefficient) is quite the same for all investigated cases, which means the beginning phase is pressure-drag controlled. It's also found that the cases of low Weber number are mainly pressure-drag controlled. The deformation and expansion of the drop in the perpendicular plane contributes to the increase in drag coefficient. In addition, as we have seen in the breakup regimes, the entrained fluid within the local drop-fluid region can also increase inertia and increase the drag coefficient. Large drag coefficients are observed for high Weber cases.

The major new findings of our DNS are nevertheless related to the heat transfers. In our DNS, only two liquid phases at used, meaning that boiling is not considered. Such simplification is motivated first by the need to progress step by step, and by the probable impossibility to run 3D simulations with boiling at large Weber numbers. Thus, the results and extrapolations to the real situation of interest must be considered with care. Nevertheless, as long as the real situation involves very high pressures and then very limited void these DNS brings important conclusions for use in FCI models.

6. The simulations reveal the details of the thermal diffusion processes within the drop and the surrounding fluid. It appears that, in any case, the exchange takes place mainly in the front face and that the thin cooled layers are transported along the interface until they accumulate at the wave crests or, at moderate Weber, in the ring (or, in the absence of fragmentation, in the rear part of the drop). Similarly for the surrounding liquid, the heated layers are transported and accumulate in the bag zone behind the drop. Thus, the fragments are formed quite cold and the interaction in the bag is ultimately small, contrary to the principle of the Micro-Interaction concept. Nevertheless, in a more realistic situation, fragmentation necessarily takes place at a high temperature, otherwise it would be blocked by solidification. The exchanges between fragments and surrounding fluids should thus have a more

important part than in our simulations.

7. In the absence of fragmentation, the internal movement of the fluid seems sufficient to ensure a quite important internal mixing, which renders the hypothesis that solidification develops as a "crust " is quite fragile, not to say unrealistic. More precisely, the thermal boundary layer inside the surface is continuously moving to the drop center, cooling the drop.
8. The temperature of the entrained water in the mixture is far from homogenous, particularly at low and moderate Weber numbers, and the characteristics of heating of this volume are strongly dependent on We, in contrast with the existing micro-interaction models.
9. The drop cooling does not scale precisely with the fragmentation. The cooling is comparably more rapid as the Weber number increases. This firstly confirms that the mixture conditions should be characterized as a function of the Weber number explored.

The last part of the thesis is dedicated to modeling proposals for MC3D. In the limited time that could be devoted to this activity, only modifications that can be directly verified were handled. Furthermore, the developments already involve changes of several fitting parameters and only example calculations are undergone and presented:

1. A concept of Non-Equilibrium Micro-Interaction (NEMI) is developed. In this concept, the fragments, during a given time, are trapped in the wake of the drops that fragment, with a significant amount of water and the principles of heat transfer in disequilibrium are preserved. This is done numerically by modifying the existing MUDROPS description, where the melt drops (and then fragments) and partitioned in several numerical fields with a prescribed diameter. These fields share the same velocity (homogenous MUSIG model). The impact of the entrained water is, at first option, described as an “added mass”.
2. The drag coefficient needed in any case to be reconsidered, since the current modeling does not take into account the fragmentation effects. The DNS results are used to create a new model.
3. Concerning the thermal transfers, it was chosen not to modify the particular transfer by convection, but to carry out modifications related to the configuration of the flow.

Concerning the evolution of the void during the interaction, we can only indicate paths of development. Due to the high sensitivity of the calculations related to the bubble size, it comes that a much more precise is necessary than the one in the current model, thus involving quite complex developments. We recommend separating the numerical fields for the pre-existing gas and the one created during the interaction (steam but also hydrogen in case of oxidation). This will allow a model for the variation of area (coalescence) of the new bubbles.

REFERENCES

[1] Achour, M.H., 2017. Fragmentation de métal liquide dans l'eau (phdthesis). Université de Lorraine.

[2] Berman, M., 1982. Light water reactor safety research program semiannual report, october 1981-March1982 (No. NUREG/CR-2841). Sandia National Labs.

[3] Berman, M., 1981. light water reactor safety research program Quarterly report, January-march 1981 (Technical Report No. NUREG/CR-2163/lof4). Sandia National Labs.

[4] Berthoud, G., 2000a. Vapor explosions. Annual Review of Fluid Mechanics 32, 573–611.

[5] Berthoud, G., 2000b. Heat Transfer Modeling during a Vapor Explosion. Nuclear Technology 130, 39–58. https://doi.org/10.13182/NT00-A3076

[6] Berthoud, G., 1987. L' INTERACTION CORIUM - EAU : SYNTHESE ET ANALYSE DES RESULTATS EXPERIMENTAUX (No. STT/LPML/87/28/C). CEA.

[7] Berthoud, G., D'Aillon, L.G., 2009. Film boiling heat transfer around a very high temperature thin wire immersed into water at pressure from 1 to 210bar: Experimental results and analysis. International Journal of Thermal Sciences 48, 1728–1740. https://doi.org/10.1016/j.ijthermalsci.2009.01.012

[8] Board, S.J., Hall, R.W., Hall, R.S., 1975. Detonation of fuel coolant explosions. Nature 254, 319–321. https://doi.org/10.1038/254319a0

[9] Brackbill, J.U., Kothe, D.B., Zemach, C., 1992. A continuum method for modeling surface tension. Journal of Computational Physics 100, 335–354. https://doi.org/10.1016/0021-9991(92)90240-Y

[10] Brayer, C., Berthoud, G., 1991. APPROCHES THERMODYNAMIQUES DE L'INTERACTION THERMIQUE (No. STR/LML/91/63).

[11] Buchanan, D.J., 1974. A model for fuel-coolant interactions. J. Phys. D: Appl. Phys. 7, 1441–1457. https://doi.org/10.1088/0022-3727/7/10/318

[12] Buck, M., Bürger, M., 1997. IDEMO-A Thermal Detonation Model of Vapor Explosions: Multi-Fluid Model, Constitutive Laws and Verification Lines. Japanes-German Syposium on Multiphase Flow, Tokio 25, 27.

[13] Bürger, M., 2006. Particulate debris formation by breakup of melt jets: Main objectives and solution perspectives. Nuclear Engineering and Design 236, 1991–1997. https://doi.org/10.1016/j.nucengdes.2006.03.032

[14] Bürger, M., Buck, M., Saied-Ahmad, S., Schatz, A., 1996. experimental and Theoretical investigations on the Fragmentation of Melt Drops in Relative Flows. Report INV-MFC (98)—D016 2–135.

[15] Carachalios, C., Burger, M., Unger, H., 1983. A transient two-phase model to describe thermal detonations based on hydrodynamic fragmentation: Chapter 6, in: Proceedings of the International Meeting on Light Water Severe Accident Evaluation. Cambridge, MA (USA).

[16] Castrillon-Escobar, S., Rimbert, N., Meignen, R., Gradeck, M., Hadj-Achour, M., 2015. Direct numerical simulations of hydrodynamic fragmentation of liquid metal droplets by a water flow, in: ICLASS 2015, 13th Triennial International Conference on Liquid Atomization and Spray Systems. Presented at the ICLASS 2015, Tainan, Taiwan.

[17] Chen, X., Luo, R., Yuen, W.W., Theofanous, T.G., 1999. Experimental simulation of microinteractions in large scale explosions. Nuclear Engineering and Design 189, 163–178. https://doi.org/10.1016/S0029-5493(99)00032-1

[18] Chen, X., Yuen, W.W., Theofanous, T.G., 1997. On the constitutive description of the Microinteractions concept in steam explosions. Nuclear Engineering and Design 17.

[19] Cheng, S., Matsuba, K., Isozaki, M., Kamiyama, K., Suzuki, T., Tobita, Y., 2015. SIMMER-III Analyses of Local Fuel-Coolant Interactions in a Simulated Molten Fuel Pool: Effect of Coolant Quantity. Science and Technology of Nuclear Installations 2015, 964327. https://doi.org/10.1155/2015/964327

[20] Cherdron, W., Huber, F., Kaiser, A., Schütz, W., 2005. Eco steam explosion experiments: documentation and evaluation of experimental data. FZKA.

[21] Cho, D.H., Armstrong, D.R., Gunther, W.H., 1998. Experiments on interactions between Zirconium-containing melt and water (Technical Report No. NUREG/CR-5372). Argonne National Lab., Ill., argonne.

[22] Cho, D.H., Armstrong, D.R., Gunther, W.H., Basu, S., 1997. Experiments on interactions between zirconium-containing melt and water (ZREX): Hydrogen generation and chemical augmentation of energetics (Article No. ANL/ASD/CP--93443). Argonne National Lab., Ill., Illinois.

[23] Cho, D.H., Ivins, R.O., Wright, R.W., 1972. RATE-LIMITED MODEL OF MOLTEN FUEL/COOLANT INTERACTIONS: MODEL DEVELOPMENT AND PRELIMINARY CALCULATIONS. Argonne National Lab., Ill.

[24] Cho, D.H., Ivins, R.O., Wright, R.W., 1971. PRESSURE GENERATION BY MOLTEN FUEL-COOLANT INTERACTIONS UNDER LMFBR ACCIDENT CONDITIONS. (No. CONF-710302-(Vol.1)). Argonne National Lab., Ill.

[25] Corradini, M.L., Hohmann, H., 1993. Multi-phase flow aspects of fuel-coolant interactions in reactor safety research. Nuclear Engineering and Design 145, 207–215. https://doi.org/10.1016/0029-5493(93)90067-J

[26] Corradini, M.L., Kim, B.J., Oh, M.D., 1988. Vapor explosions in light water reactors: A review of theory and modeling. Progress in Nuclear Energy 22, 1–117. https://doi.org/10.1016/0149-1970(88)90004-2

[27] De Malmazet, E., 2009. Etude de la fragmentation de gouttes chaudes en ébullition en film dans un écoulement d'eau. Grenoble INPG.

[28] de Villiers, E., Gosman, A.D., Weller, H.G., 2004. Large Eddy Simulation of Primary Diesel Spray Atomization. SAE Transactions 113, 193–206.

[29] Delale, C.F., 2012. Bubble dynamics and shock waves. Springer Science & Business Media.

[30] Dong, Y., Yan, Y., Liu, C., 2016. New visualization method for vortex structure in turbulence by lambda2 and vortex filaments. Applied Mathematical Modelling 40, 500–509. https://doi.org/10.1016/j.apm.2015.04.059

[31] Edouard SCOTT,Berthoud G., 1978. Mutiphase thermal detonation, in: ASME. Presented at the ASME, Aan Francisco, USA.

[32] Enright, D., Fedkiw, R., Ferziger, J., Mitchell, I., 2002. A Hybrid Particle Level Set Method for Improved Interface Capturing. Journal of Computational Physics 183, 83–116. https://doi.org/10.1006/jcph.2002.7166

[33] Epstein, M., 1977. Stability of a Submerged Frozen Crust. Journal of Heat Transfer 99, 527–532. https://doi.org/10.1115/1.3450737

[34] Escobar, S.C., 2016. Instabilité et dispersion de jets de corium liquides : analyse des processus physiques et modélisation dans le logiciel MC3D (phdthesis). Université de Lorraine.

[35] Faeth, G.M., Hsiang, L.-P., Wu, P.-K., 1995. Structure and breakup properties of sprays. International Journal of Multiphase Flow 21, 99–127. https://doi.org/10.1016/0301-9322(95)00059-7

[36] Fletcher, D.F., Theofanous, T.G., 1997. Heat Transfer and Fluid Dynamic Aspects of Explosive Melt–Water Interactions, in: Advances in Heat Transfer. Elsevier, pp. 129–213. https://doi.org/10.1016/S0065-2717(08)70185-0

[37] Frolov, S.M., Avdeev, K.A., Aksenov, V.S., Borisov, A.A., Frolov, F.S., Shamshin, I.O., Tukhvatullina, R.R., Basara, B., Edelbauer, W., Pachler, K., 2017. Experimental and computational studies of shock wave-to-bubbly water momentum transfer. International Journal of Multiphase Flow 92, 20–38.

[38] Frost, D.L., Lee, J.H.S., Ciccarelli, G., 1991. The use of Hugoniot analysis for the propagation of vapor explosion waves. Shock Waves 1, 99–110. https://doi.org/10.1007/BF01414905

[39] Gelfand, B.E., 1996. Droplet breakup phenomena in flows with velocity lag. Progress in Energy and Combustion Science 22, 201–265. https://doi.org/10.1016/S0360-1285(96)00005-6

[40] Gorokhovski, M., Herrmann, M., 2008. Modeling Primary Atomization. Annu. Rev. Fluid Mech. 40, 343–366. https://doi.org/10.1146/annurev.fluid.40.111406.102200

[41] Guildenbecher, D.R., López-Rivera, C., Sojka, P.E., 2009. Secondary atomization. Experiments in Fluids 46, 371–402. https://doi.org/10.1007/s00348-008-0593-2

[42] Hadj-Achour, M., Rimbert, N., Gradeck, M., Meignen, R., 2021. Fragmentation of a liquid metal droplet falling in a water pool. Physics of Fluids 33, 103315. https://doi.org/10.1063/5.0062430

[43] Han, J., Tryggvason, G., 2001. Secondary breakup of axisymmetric liquid drops. II. Impulsive acceleration. Physics of Fluids 13, 1554–1565. https://doi.org/10.1063/1.1370389

[44] Haraldsson, H.Ó., Li, H.X., Yang, Z.L., Dinh, T.N., Sehgal, B.R., 2001. Effect of solidification on drop fragmentation in liquid–liquid media. Heat and Mass Transfer 37, 417–426. https://doi.org/10.1007/s002310000097

[45] Head, J.W., Wilson, L., 2003. Deep submarine pyroclastic eruptions: theory and predicted landforms and deposits. Journal of Volcanology and Geothermal Research 121, 155–193. https://doi.org/10.1016/S0377-0273(02)00425-0

[46] Hicks, E.P., Menzies, D.C., 1965. Theoretical studies on the fast reactor maximum accident. ANL-7120 654.

[47] Huhtiniemi, I., Hohmann, H., Magallon, D., 1997. FCI experiments in the corium/water system. Nuclear Engineering and Design 11.

[48] Huhtiniemi, I., Magallon, D., 2001. Insight into steam explosions with corium melts in KROTOS. Nuclear Engineering and Design 204, 391–400. https://doi.org/10.1016/S0029-5493(00)00319-8

[49] Huhtiniemi, I., Magallon, D., Hohmann, H., 1999. Results of recent KROTOS FCI tests: alumina versus corium melts. Nuclear engineering and design 189, 379–389.

[50] Hulin, H., Kolev, N.I., 2000. Shock waves in multiphase flow of fuel–coolant interaction. International Journal of Thermal Sciences 39, 354–359. https://doi.org/10.1016/S1290-0729(00)00213-1

[51] Iskhakov, A.S., Melikhov, V.I., Melikhov, O.I., Yakush, S.E., Chung, L.T., 2019. Hugoniot analysis of experimental data on steam explosion in stratified melt-coolant configuration. Nuclear Engineering and Design 347, 151–157. https://doi.org/10.1016/j.nucengdes.2019.04.004

[52] Jain, M., Prakash, R.S., Tomar, G., Ravikrishna, R.V., 2015. Secondary breakup of a drop at moderate Weber numbers. Proceedings of the Royal Society A: Mathematical, Physical and Engineering Sciences 471, 20140930. https://doi.org/10.1098/rspa.2014.0930

[53] Jalaal, M., Mehravaran, K., 2014. Transient growth of droplet instabilities in a stream. Physics of Fluids 26, 012101.

[54] Jeong, J., Hussain, F., 1995. On the identification of a vortex. Journal of Fluid Mechanics 285, 69–94. https://doi.org/10.1017/S0022112095000462

[55] Johnson, M., Journeau, C., Matsuba, K., Emura, Y., Kamiyama, K., 2021. Characterization of high-temperature nuclear fuel-coolant interactions through X-ray visualization and image processing. Annals of Nuclear Energy 151, 107881. https://doi.org/10.1016/j.anucene.2020.107881

[56] Joseph, D.D., Belanger, J., Beavers, G.S., 1999. Breakup of a liquid drop suddenly exposed to a high-speed airstream. International Journal of Multiphase Flow 25, 1263–1303. https://doi.org/10.1016/S0301-9322(99)00043-9

[57] Kalman, H., Letan, R., 1985. Thickness of thermal and velocity boundary layers on a mobile surface of a sphere. International communications in heat and mass transfer 12, 201–208.

[58] Khare, P., Ma, D., Chen, X., Yang, V., 2012. Phenomenology of Secondary Breakup of Newtonian Liquid Droplets. 50th AIAA Aerospace Sciences Meeting including the New Horizons Forum and Aerospace Exposition.

[59] Khare, P., Yang, V., 2013. Drag coefficients of deforming and fragmenting liquid droplets, in: ILASS Americas, 25th Annual Conference on Liquid Atomization and Spray Systems, Pittsburgh, PA. pp. 1–12.

[60] Kim, D., Desjardins, O., Herrmann, M., Moin, P., 2006. Toward two-phase simulation of the primary breakup of a round liquid jet by a coaxial flow of gas. Center for Turbulence Research Annual Research Briefs 185.

[61] Kim, D.S., Burger, M., Frohlich, G., Unger, H., 1983. Experimental investigation of hydrodynamic fragmentation of gallium drops in water flows, in: Light Water Reactor Severe Accident Evaluation.

[62] Kolev, N.I., 2015. Multiphase Flow Dynamics 1. Springer International Publishing, Cham. https://doi.org/10.1007/978-3-319-15296-7

[63] Konovalenko, A., Karbojian, A., Kudinov, P., 2012. Experimental results on pouring and underwater liquid melt spreading and energetic melt-coolant interaction, in: The 9th International Topical Meeting on Nuclear Thermal-Hydraulics, Operation and Safety (NUTHOS-9), Kaohsiung, Taiwan, September 9-13. American Nuclear Society.

[64] Krzeczkowski, S.A., 1980. Measurement of liquid droplet disintegration mechanisms. International Journal of Multiphase Flow 6, 227–239. https://doi.org/10.1016/0301-9322(80)90013-0

[65] Lamome, J., Meignen, R., 2008. On the explosivity of a molten drop submitted to a small pressure perturbation. Nuclear Engineering and Design 238, 3445–3456. https://doi.org/10.1016/j.nucengdes.2008.08.006

[66] Landau, L.D., Lifshitz, E.M., 2013. Course of theoretical physics. Elsevier.

[67] Loisel, V., Zambaux, J.-A., Hadj-Achour, M., Picchi, S., Coindreau, O., Meignen, R., 2019. Oxidation during fuel-coolant interaction: Advances and modeling. Nuclear Engineering and Design 346, 200–208. https://doi.org/10.1016/j.nucengdes.2019.02.008

[68] Magallon, D., 2006. Characteristics of corium debris bed generated in large-scale fuel-coolant interaction experiments. Nuclear Engineering and Design, Festschrift Edition Celebrating the 70th Birthday of Prof. Bal Raj Sehgal: Invited papers on - Core melt accidents in LWRs State of the art of "COOLABILITY OF POROUS DEBRIS" 236, 1998–2009. https://doi.org/10.1016/j.nucengdes.2006.03.038

[69] Manfred Burger, Song-Hak Cho, Eberhard von Berg, Alfred Schatz, 1998. Modelling of Drop Fragmentationn in Thermal Detonation Waves and Experimental Verification (No. Report INV-MFC (98)-D015). IKE.

[70] Marmottant, P., Villermaux, E., 2004. On spray formation. J. Fluid Mech. 498, 73–111. https://doi.org/10.1017/S0022112003006529

[71] Meignen, R., 2005. Comparative Review of FCI Computer Models Used in the OECD-SERENA Program 13.

[72] Meignen, R., 1995. Modelisation de la fragmentation d'un jet liquide a tres haute temperature dans un liquide froid volatil. Grenoble INPG.

[73] Meignen, R., Raverdy, B., Buck, M., Bürger, M., Pohlner, G., 2012. On the role of void on steam explosion loads 18.

[74] Mitchell, D.E., Corradini, M.L., 1981. Intermediate scale steam explosion phenomena: Experiments and analysis (Technical Report No. NUREG/CR-2145). Sandia National Labs., Albuquerque, New Mexico.

[75] Mitropetros, K., Hieronymus, H., Steinbach, J., 2006. Single bubble ignition after shock wave impact. Chemical Engineering Science 61, 397–416. https://doi.org/10.1016/j.ces.2005.07.014

[76] Morita, K., Kondo, S., Tobita, Y., Brear, D.J., 1999. SIMMER-III applications to fuel–coolant interactions. Nuclear engineering and design 189, 337–357.

[77] Moriyama, K., Maruyama, Y., Nakamura, H., 2008. Steam explosion simulation code JASMINE v. 3 user's guide. Japan Atomic Energy Agency.

[78] Moriyama, K., Takagi, S., Muramatsu, K., NAKAMURA, H., MARUYAMA, Y., 2006. KROTOS 38 to 44: Data Report KROTOS 38 to 44: Data Report, 1996. Journal of nuclear science and technology 43, 774–784.

[79] Nelson, L.S., Duda, P.M., 1985. Steam explosion experiments with single drops of iron oxide melted with a CO/sub 2/ laser. Part II. Parametric studies. Presented at the NUREG, CR-2718.

[80] Nuclear Regulatory Commission, 1975. Reactor safety study. An assessment of accident risks in US commercial nuclear power plants. Executive Summary. United States Nuclear Regulatory Commission.

[81] Pairetti, C.I., Marquez Damian, S., Nigro, N.M., Popinet, S., Zaleski, S., 2020. Mesh resolution effects on VOF simulations of primary atomization. Atomization and Sprays 30, 913–935. https://doi.org/10.1615/AtomizSpr.2020035413

[82] Paladino, D., Theerthan, S.A., Sehgal, B.R., 2002. DECOBI: investigation of melt coolability with bottom coolant injection. Progress in Nuclear Energy 40, 161–206. https://doi.org/10.1016/S0149-1970(01)00022-1

[83] Picchi, S., 2017. MC3D Version 3.9: Description of the physical models of the PREMIXING application (No. PSN-RES/SAG/2017-00073). IRSN, cadarache.

[84] Picchi, S., Meignen, R., 2021. MC3D Version 3.10 Validation report (No. Rapport n°IRSN/2020-0013). IRSN, cadarache.

[85] Pilch, M., Erdman, C.A., 1987. Use of breakup time data and velocity history data to predict the maximum size of stable fragments for acceleration-induced breakup of a liquid drop. International Journal of Multiphase Flow 13, 741–757. https://doi.org/10.1016/0301-9322(87)90063-2

[86] Plesset, M.S., Chapman, R.B., 1971. Collapse of an initially spherical vapour cavity in the neighbourhood of a solid boundary. Journal of Fluid Mechanics 47, 283–290.

[87] Pohlner, G., Vujic, Z., Burger, M., Lohnert, G., 2006. Simulation of melt jet breakup and debris bed formation in water pools with IKEJET/IKEMIX. Nuclear Engineering and Design 23.

[88] Pope, S.B., 2000. Turbulent Flows. Cambridge University Press, Cambridge. https://doi.org/10.1017/CBO9780511840531

[89] Popinet, S., 2021. http://basilisk.fr/ [WWW Document]. Basilisk Main Page. URL http://basilisk.fr/ (accessed 6.14.21).

[90] Popinet, S., 2003. Gerris: a tree-based adaptive solver for the incompressible Euler equations in complex geometries. Journal of Computational Physics 190, 572–600. https://doi.org/10.1016/S0021-9991(03)00298-5

[91] Prosperetti, A., 2015. The speed of sound in a gas–vapour bubbly liquid. Interface Focus 5, 20150024. https://doi.org/10.1098/rsfs.2015.0024

[92] Qian, L., Zhong, X., Zhu, C., Lin, J., 2021. An experimental investigation on the secondary breakup of carboxymethyl cellulose droplets. International Journal of Multiphase Flow 136, 103526.

[93] Quan, S., Schmidt, D.P., 2006. Direct numerical study of a liquid droplet impulsively accelerated by gaseous flow. Physics of Fluids 18, 102103. https://doi.org/10.1063/1.2363216

[94] Ranger, A.A., Nicholls, J.A., 1972. Atomization of liquid droplets in a convective gas stream. International Journal of Heat and Mass Transfer 15, 1203–1211.

[95] Rimbert, N., Escobar, S.C., Meignen, R., Hadj-Achour, M., Gradeck, M., 2020. Spheroidal droplet deformation, oscillation and breakup in uniform outer flow. Journal of Fluid Mechanics 904. https://doi.org/10.1017/jfm.2020.675

[96] Sairanen, R., Berthoud, G., Ratel, G., Meignen, R., Jacobs, H., Buerger, M., Buck, M., Moriyama, M., Naito, M., Song, J.H., Suh, N., Melikhov, O., Basu, S., Corradini, M., Theofanous, T., Dinh, N., Magallon, D., Royen, J., Vitanza, C., 2007. OECD research programme on fuel-coolant interaction steam explosion resolution for nuclear applications - SERENA. Final Report - December 2006 (No. NEA-CSNI-R--2007-11). Organisation for Economic Co-Operation and Development.

[97] Sazhin, S.S., 2017. Modelling of fuel droplet heating and evaporation: Recent results and unsolved problems. Fuel 196, 69–101.

[98] Song, J.H., Park, I.K., Chang, Y.J., Shin, Y.S., Kim, J.H., Min, B.T., Hong, S.W., Kim, H.D., 2002. Experiments on the interactions of molten ZrO2 with water using TROI facility. Nuclear Engineering and Design 213, 97–110. https://doi.org/10.1016/S0029-5493(01)00504-0

[99] Spencer, B.W., Wang, K., Blomquist, C.A., McUmber, L.M., Schneider, J.P., 1994. Fragmentation and quench behavior of corium melt streams in water (Technical Report No. NUREG/CR-6133; ANL-93/32 ON: TI94009042; TRN: 94:006633). Nuclear Regulatory Commission, Washington, DC (United States). Div. of …, United States.

[100] Theofanous, T.G., 2011. Aerobreakup of Newtonian and viscoelastic liquids. Annual Review of Fluid Mechanics 43, 661–690.

[101] Theofanous, T.G., Yuen, W.W., 1995. The probability of alpha-mode containment failure. Nuclear Engineering and Design 155, 459–473. https://doi.org/10.1016/0029-5493(94)00889-7

[102] Tiselj, I., Flageul, C., Oder, J., 2020. Direct Numerical Simulation and Wall-Resolved Large Eddy Simulation in Nuclear Thermal Hydraulics. Nuclear Technology 206, 164–178. https://doi.org/10.1080/00295450.2019.1614381

[103] Tobita, Y., Kondo, S., Yamano, H., Morita, K., Maschek, W., Coste, P., Cadiou, T., 2006. The development of SIMMER-III, an advanced computer program for LMFR safety analysis, and its application to sodium experiments. Nuclear Technology 153, 245–255.

[104] Tryggvason, G., Scardovelli, R., Zaleski, S., 2011. Direct Numerical Simulations of Gas–Liquid Multiphase Flows. Cambridge University Press, Cambridge. https://doi.org/10.1017/CBO9780511975264

[105] Turland, B.D., Fletcher, D.F., Hodges, K.I., Attwood, G.J., 1995. Quantification of the probability of containment failure caused by an in-vessel steam explosion for the Sizewell B PWR. Nuclear Engineering and Design 155, 445–458. https://doi.org/10.1016/0029-5493(94)00888-6

[106] Uršič, M., 2011. Modelling of solidification effects in fuel coolant interactions (Doctoral thesis). UNIVERSITY OF LJUBLJANA, Ljubljana.

[107] Uršič, M., Leskovar, M., Mavko, B., 2011. Improved solidification influence modelling for Eulerian fuel–coolant interaction codes. Nuclear Engineering and Design 241, 1206–1216. https://doi.org/10.1016/j.nucengdes.2010.05.001

[108] Uršič, M., Leskovar, M., Meignen, R., 2015. Eulerian modelling of melt solidification impact during fuel–coolant interaction. Annals of Nuclear Energy 78, 130–139. https://doi.org/10.1016/j.anucene.2015.01.003

[109] van Hooft, J.A., Popinet, S., van Heerwaarden, C.C., van der Linden, S.J.A., de Roode, S.R., van de Wiel, B.J.H., 2018. Towards Adaptive Grids for Atmospheric Boundary-Layer Simulations. Boundary-Layer Meteorol 167, 421–443. https://doi.org/10.1007/s10546-018-0335-9

[110] VonNeumann, J., Richtmyer, R.D., 1950. A Method for the Numerical Calculation of Hydrodynamic Shocks. Journal of Applied Physics 21, 232–237. https://doi.org/10.1063/1.1699639

[111] Wang, S.K., Blomquist, C.A., Spencer, B.W., 1989. Modeling of thermal and hydrodynamic aspects of molten jet/water interactions. Argonne National Lab.

[112] Whitaker, S., 1972. Forced convection heat transfer correlations for flow in pipes, past flat plates, single cylinders, single spheres, and for flow in packed beds and tube bundles. AIChE Journal 18, 361–371.

[113] Wohletz, K., 2002. Water/magma interaction: some theory and experiments on peperite formation. Journal of Volcanology and Geothermal Research 114, 19–35. https://doi.org/10.1016/S0377-0273(01)00280-3

[114] Yang, S., Gong, H., Guo, K., Li, Y., Zan, Y., Zhuo, W., Li, P., 2023. Experimental study on water injection and stratified steam explosion at the top of metal molten pool. Annals of Nuclear Energy 183, 109640. https://doi.org/10.1016/j.anucene.2022.109640

[115] Yih, C.-S., 1980. Chapter 4 - HYDRODYNAMIC STABILITY, in: Yih, C.-S. (Ed.), Stratified Flows. Academic Press, pp. 219–275. https://doi.org/10.1016/B978-0-12-771050-1.50012-7

[116] Yuen, W.W., Theofanous, T.G., 1999. On the existence of multiphase thermal detonations. International Journal of Multiphase Flow 25, 1505–1519. https://doi.org/10.1016/S0301-9322(99)00064-6

[117] Zambaux, J.-A., 2016. Projet RSNR-ICE : Simulation de l'ébullition en film en régime supercritique avec le logiciel MC3D (Technical Report No. PSN-RES/SAG/2016-00363). IRSN, cadarache, FR.

[118] Zambaux, J.A., Manickam, L., Meignen, R., Ma, W.M., Bechta, S., Picchi, S., 2018. Study on thermal fragmentation characteristics of a superheated alumina droplet. Annals of Nuclear Energy 119, 352–361. https://doi.org/10.1016/j.anucene.2018.05.029

[119] Zhdanov, S.K., 1995. Nonlinear theory of Kelvin-Helmholtz instability. Physica D: Nonlinear Phenomena 87(1–4), 375–379. https://doi.org/10.1016/0167-2789(95)00169-5

APPENDIX

1.1. KROTOS KT-4 test results (shock propagation in pure liquid)

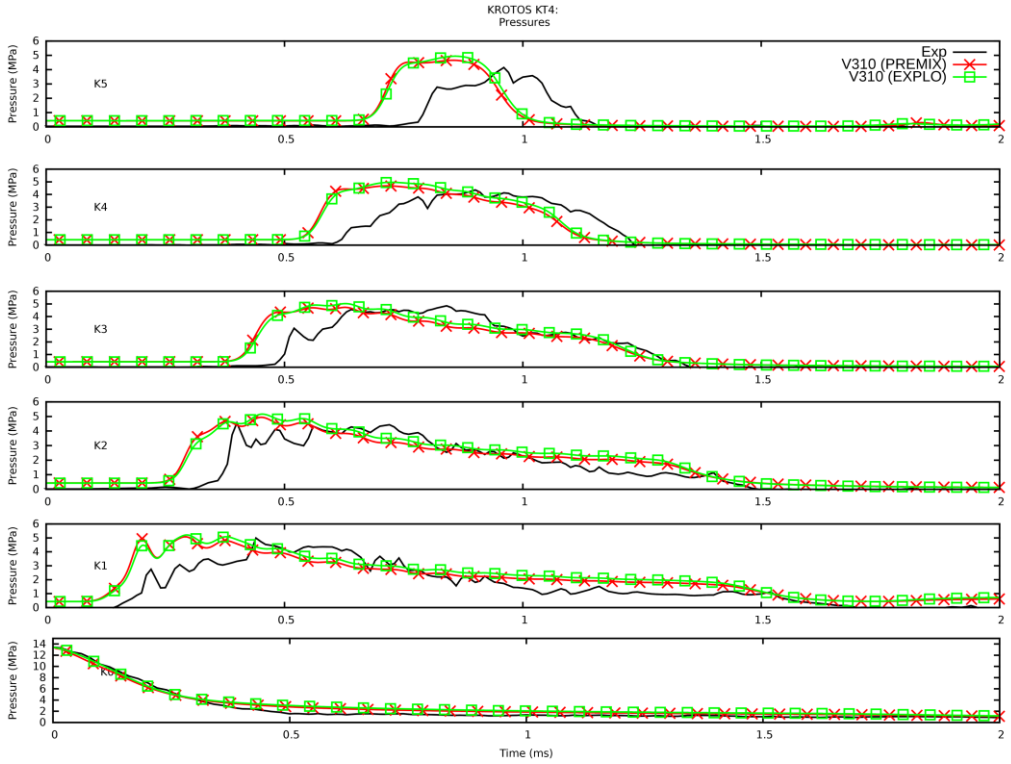

Figure 153: Propagation of the trigger wave in the validation test MC3D V3.10, compared to the experimental one (from the Validation report MC3D-3.10, IRSN-2020-00134)

1.2. Mesh convergence and role of artificial viscosity

Here, to verify the convergence of the MC3D mesh and the effect of artificial viscosity, a sensitivity analysis is performed for the explosion calculation using an initially homogeneous mixture of 1% drop, 30% vacuum and 69% liquid (volume fraction) in the column.

Figure 154 shows the pressure history at different heights for cases using different mesh size. To isolate the effect of viscosity, in all computation illustrated in Figure 154 are performed without artificial (numerical) viscosity. First, a numerical pressure peak followed by numerical oscillations are observed for all cases when the shock arrives, showing that the standard scheme (without numerical viscosity) cannot handle the strong shock cases well. Such numerical peak and oscillations are smaller with a finer mesh (the first figure comparing to the last figure). It's already known that some numerical difficulties arise for shock involved simulation. When the mesh size is larger than the shock-front thickness, such mesh cannot capture the shock behavior (the steep variation of physical properties), which will cause the numerical oscillation. As shown here (Figure 155), decreasing the mesh size can reduce this effect but very costly.

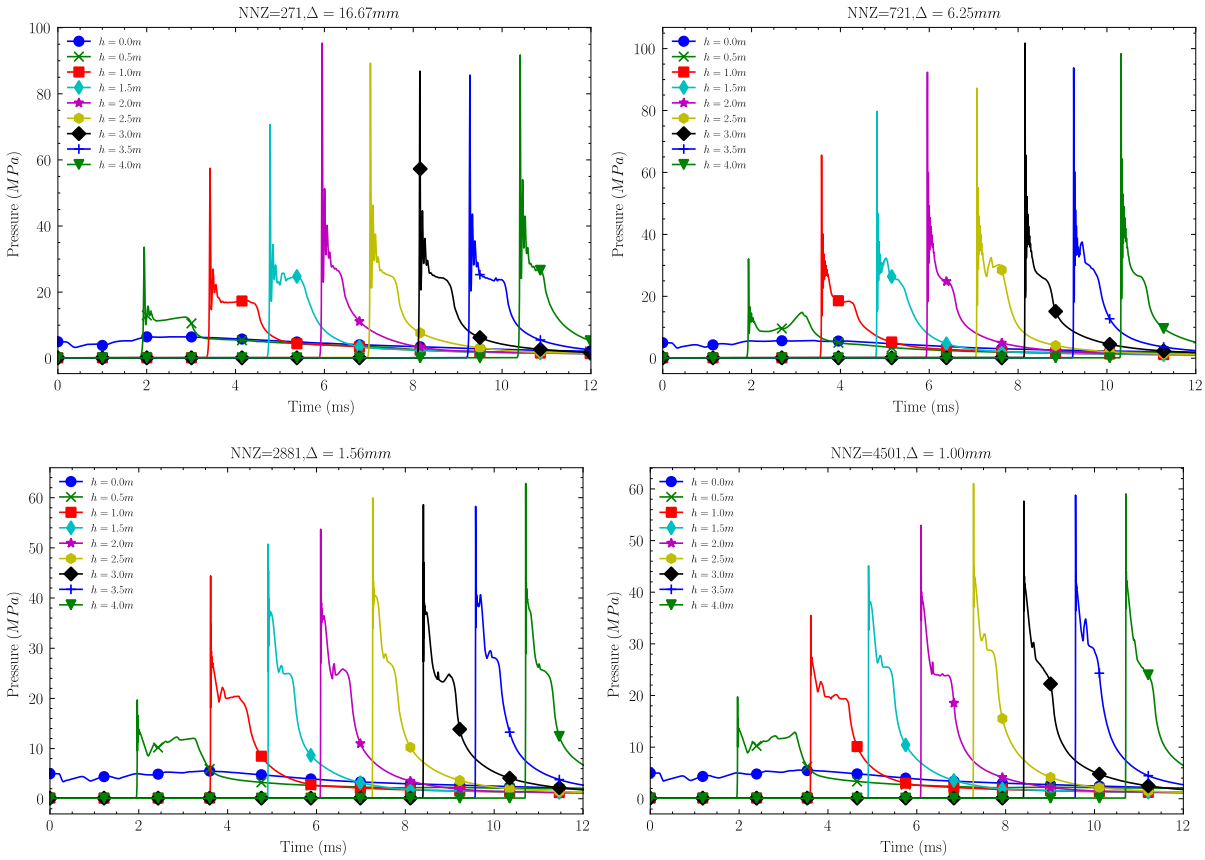

Figure 154: Pressure history at different heights. Subfigures have different mesh size, with NNZ the number of nodes and Δ the mesh size.

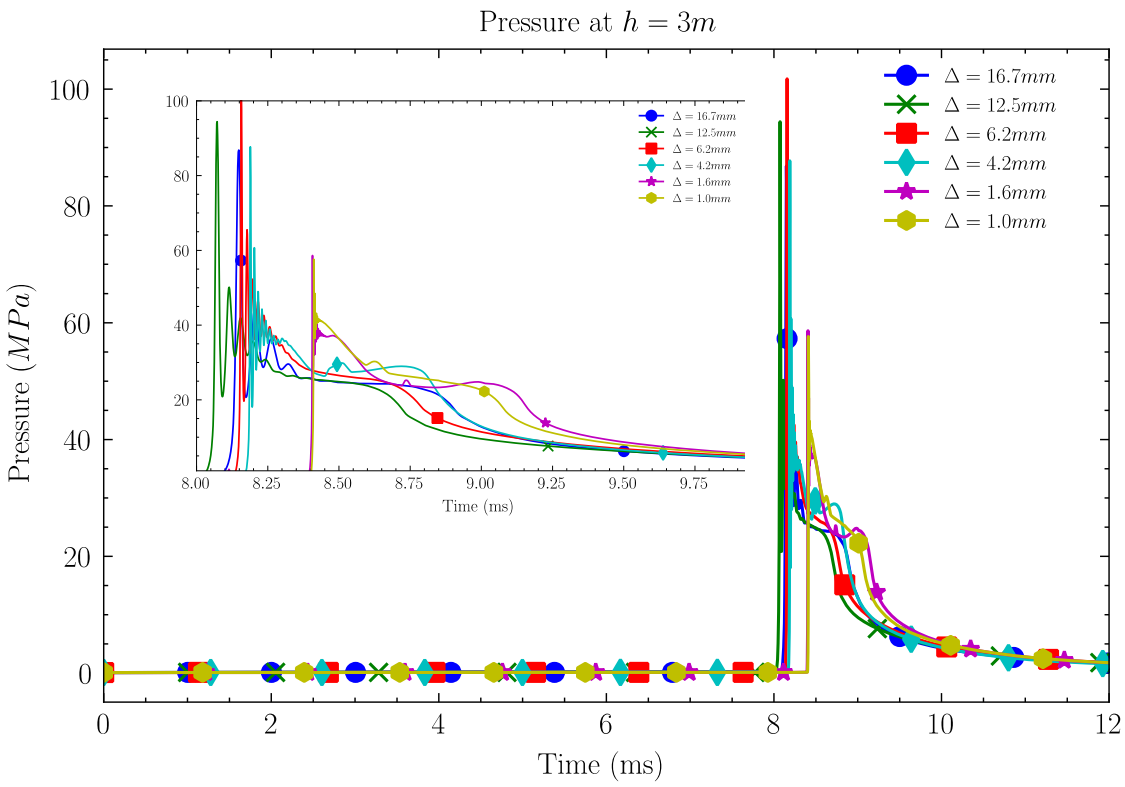

Figure 155: Comparison of different case at a fixed height h=3m, global view and a zoom view

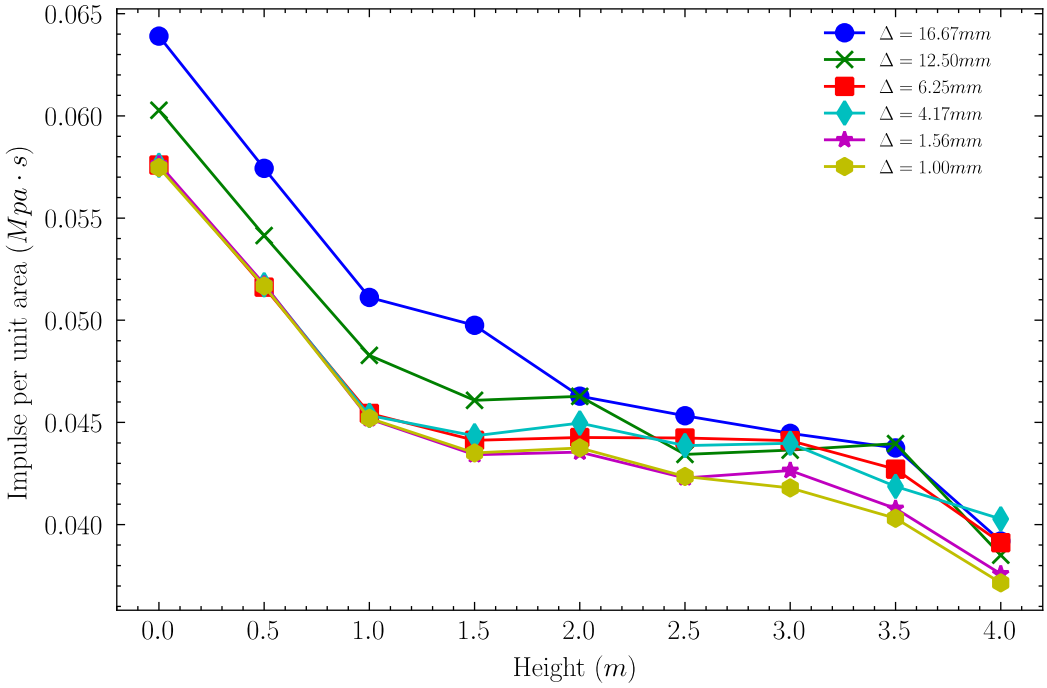

Figure 156: Impulse (integral of pressure over time) per unit area at different heights, different curves correspond to different mesh size

Regarding to the pressure profil at a fixed high (Figure 155) and the results of impulse per unit area (cf., Figure 156, the osscillations appear only in very short time segments, having almost no influence on the resultat of impulse), a strict converence reaches for mesh size smaller than 1.56mm, repsenting 2881 nodes for 4.5 meter.

To limit numerical oscillation,a well-used solution is to add a numerical/artificial viscosity (see, §2.4.5.2) where the shock front is present. Figure 157 gives the pressure history at different heights for the case of different artificial viscosity coefficients, which shows that increasing the artificial viscosity can reduce the numerical oscillation. However, this does not mean that it is always better to choose a high artificial viscosity coefficient. Too large a coefficient will smooth the pressure too much and we will lose the sharpness of the shock front. Also, since the shock case usually represents high pressure and temperature, too large a coefficient will lead to other numerical problems, i.e., too large viscosities may also lead to non-convergence of the water property table. In conclusion, the coefficient should be used carefully and should be chosen as small as possible, as long as the numerical oscillations is limited.

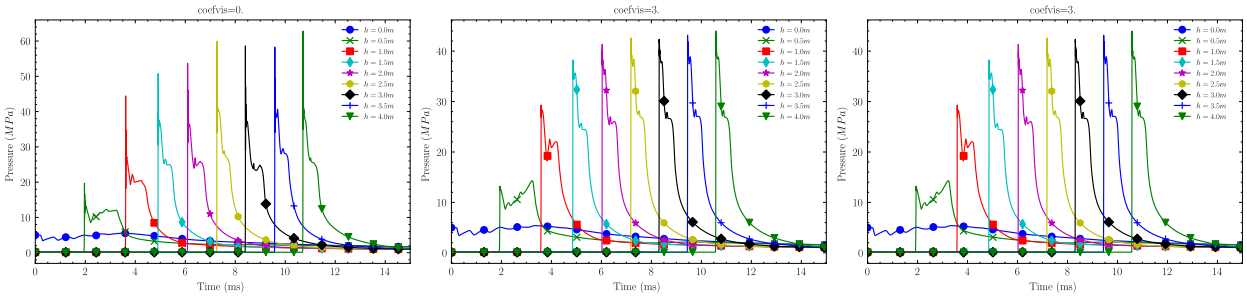

Figure 157: Pressure history at different heights. Subfigures have different coefficients of artificial viscosity

1.3. Vortex detection: criterion $\lambda 2$

The vortex structures play a key role in the turbulence involved flow because they can influence the kinetic energy production and dissipation, enhance the transport mass/area, heat and momentum. Several methods (Dong et al., 2016) have been proposed to identify the vortex in the past, but none is unanimously accepted by the scientific community. First, the vorticity is not the ideal quantity to characterize vortices because, for

example, near the boundary layers its value is large everywhere, due to the strong shear. Moreover, vortices are in most cases poorly represented because the variables used (e.g., streamlines) can be dependent on the chosen reference frame. Thus, a flow can be stationary or transient simply by changing the reference frame (e.g., the wake flow behind a sphere with a low Reynolds number). One of the difficulties defining a vortex is to guarantee the independence from the chosen Galilean reference (Galilean invariance).

To detect the vortex as well as its axis of rotation, the $\lambda 2$ criterion (Jeong and Hussain, 1995) is used due to its reliability and simplicity. We only briefly explain this criterion, however, the reader can consult a more detailed bibliography, e.g. (Jeong and Hussain, 1995), for more information. The criterion for extracting vortex regions $\lambda 2$ is based on the instantaneous velocity field and the analysis of the velocity gradient tensor.

Let $\boldsymbol{u}$ be the three-dimensional velocity field. For every grid point, $\nabla \boldsymbol{u}$ can be decomposed into a symmetric part $S = (\nabla \boldsymbol{u} + \boldsymbol{\nabla u^T})/\mathbf{2}$ and an antisymmetric part $\Omega = (\nabla \boldsymbol{u} - \boldsymbol{\nabla u^T})/\mathbf{2}$, i.e., $S = \frac{\frac{\partial \mathrm{u_i}}{\partial x_j} + \frac{\partial \mathrm{u_j}}{\partial x_i}}{\mathbf{2}}$ and $\Omega = \frac{\frac{\partial \mathrm{u_i}}{\partial x_j} - \frac{\partial \mathrm{u_j}}{\partial x_i}}{\mathbf{2}}$

The matrix $S^2 + \Omega^2$ is real and symmetric and thus has exactly three real eigenvalues. These eigenvalues are sorted in the decreasing order: $\lambda_1 \gg \lambda_2 \gg \lambda_3$. A vortex is defined as a connected region where two of the eigenvalues are negative, which is equivalent to the condition $\lambda_2 < 0$.